Characterization of barren and mineralized hydrothermal systems in an impact structure: the granophyre unit and footwall of the Sudbury Igneous Complex, Ontario, Canada

by

Robert Craig Stewart

A thesis submitted in partial fulfillment of the requirements for the degree of Doctor of Philosophy (PhD) in Mineral Deposits and Precambrian Geology

The Faculty of Graduate Studies

Laurentian University

Sudbury, Ontario, Canada

THESIS DEFENCE COMMITTEE/COMITÉ DE SOUTENANCE DE THÈSE
Laurentian Université/Université Laurentienne
Faculty of Graduate Studies/Faculté des études supérieures

Title of Thesis Titre de la thèse	Characterization of barren and mineralized hydrothermal systems in an impact structure: the granophyre unit and footwall of the Sudbury Igneous Complex, Ontario, Canada
Name of Candidate Nom du candidat	Stewart, Robert (Craig)
Degree Diplôme	Doctor of Philosophy Science
Department/Program Département/Programme	Date of Defence April 3, 2017 PhD Mineral Deposits and Pre-Cambrian Geology

APPROVED/APPROUVÉ

Thesis Examiners/Examinateurs de thèse:

Dr. Daniel Kontak
(Supervisor/Directeur(trice) de thèse)

Dr. Pedro Jugo
(Committee member/Membre du comité)

Dr. Jacob Hanley
(Committee member/Membre du comité)

Dr. Joel Gagnon
(External Examiner/Examinateur externe)

Approved for the Faculty of Graduate Studies
Approuvé pour la Faculté des études supérieures
Dr. David Lesbarrères
Monsieur David Lesbarrères
Dean, Faculty of Graduate Studies
Doyen, Faculté des études supérieures

ACCESSIBILITY CLAUSE AND PERMISSION TO USE

Abstract

The Sudbury Igneous Complex (SIC) is the product of a differentiated impact melt sheet and one of the best preserved impact sites globally. The top 1.5 km of the 2.5 km-thick crystallized melt sheet, referred to as the granophyre unit (GR), exhibits strong textural, mineralogical, geochemical, fluid inclusion, and oxygen isotopic evidence for a long and complex hydrothermal history. This hydrothermal system has not previously been documented, and is characterized by an early magmatic-hydrothermal stage that has been overprinted by a later hydrothermal stage. The magmatic-hydrothermal stage was dominated by fluids exsolved from the GR and resulted in pervasive saussuritization of plagioclase, alteration of alkali feldspar and plagioclase to end-member compositions, and precipitation of epidote and muscovite in pits and void spaces. The overprinting hydrothermal stage was dominated by modified seawater sourced from the hydrothermal system in the overlying Onaping Formation and produced a pervasive alteration assemblage characterized by epidote, ferro-actinolite, stilpnomelane, biotite, and titanite with lesser muscovite, chlorite, and ferrotschermakite. The results from this study record a previously unidentified complex and protracted post-crystallization history of fluid-rock interaction for the GR that is related to the ore-forming hydrothermal system in the overlying Onaping Formation.

The relationship between the hydrothermal system in the GR and the mineralized systems in the footwall to the Sudbury Structure (SS) has not previously been established. The Nickel Rim South (NRS) Cu-Ni-PGE deposit, located in the east range of the Sudbury Structure, Ontario, records textural and geochemical evidence of a complex, multi-stage hydrothermal history and provides an excellent comparison to the GR. Results from fluid inclusion petrography and microthermometry are used in conjunction in order to characterize the hydrothermal system at

NRS. The combined results of fluid inclusion petrography and microthermometry, evaporate mound analysis, oxygen isotopic values of quartz, and trace element chemistry of alteration minerals reveal a complex hydrothermal history at NRS related to the cooling SIC, which contributed to hydrothermal remobilization of metals into the footwall. The hydrothermal fluids are notably different from fluids documented in other mineralized footwall systems that are represented by high temperature, multi-solid fluid inclusions inferred to be critical for ore remobilization. Instead, the hydrothermal system at NRS shares more similarities with the GR hydrothermal system, bringing into question the role of fluids represented by high temperature, multi-solid inclusions in ore remobilization.

Keywords: hydrothermal systems; Sudbury Igneous Complex; granophyre; Ni-Cu-PGE mineralization; fluid inclusion; oxygen isotope; evaporate mound

Statement of co-authorship

This thesis consists of three manuscripts prepared for publication in peer-reviewed scientific journals. Chapters two to four were co-authored by the candidate and additional collaborators. The design of the thesis was conceived by Dr. Daniel Kontak as part of an industry-supported research initiative designed by Dr. Kontak, Dr. Bruno Lafrance, Dr. Doug Tinkam, and Dr. Pedro Jugo. The execution and completion of field work, sample collection and preparation, petrography, analyses of the results and conclusions are the work of the candidate with guidance and supervision of Dr. Kontak. However, other collaborators, listed as co-authors, provided additional samples, expertise, and guidance and contributed to the work presented herein. Chapter 2 is co-authored by Dr. Daniel Kontak and Dr. Doreen Ames. Field work and sample selection were completed by the candidate. Additional samples used for comparison but not incorporated in the text were provided by Dr. Ames, Dr. Ann Therriault, and Galen McNamara. Chapter 3 is co-authored by Dr. Kontak. Dr. Mostafa Fayek assisted with collection and interpretation of quartz secondary ion mass spectroscopy data. Chapter 4 is co-authored by Dr. Kontak and Dr. Jacob Hanley. Samples were provided by Sudbury Integrated Nickel Operations – A Glencore Company under the supervision of Mike Sweeny. All papers were edited by Dr. Kontak, Dr. Jugo, Dr. Hanley, and Margaret Stewart.

Acknowledgements

I thank Dr. Dan Kontak for his guidance as primary supervisor, Dr. Pedro Jugo for his contribution as co-supervisor, and Dr. Jacob Hanley for his input and support as committee member. It has been a pleasure to work with all three of these individuals and they have made me a better geologist. I would also like to thank Dr. Dean Millar for acting as internal examiner and Dr. Joel Gagnon for acting as external examiner and providing me with thoughtful feedback.

I thank the Centre of Excellence in Mining Innovation (CEMI), Natural Sciences and Engineering Research Council of Canada (NSERC), and Sudbury Integrated Nickel Operations – A Glencore Company for their logistical and financial support of this project.
I thank Dr. Doreen Ames and Dr. Alan Galley for their support of the project and for graciously providing their knowledge of my field area. I thank Willard Desjardins, Dave Crabtree, Sandra Clarke, John Hechler, Dr. William Zhe, Dr. Joe Petrus, Dr. Mostafa Fayek, and Ryan Sharpe for their contributions and support of analytical techniques throughout the project

I thank the professors in the Harquail School of Earth Science, in particular Dr. Harold Gibson and Dr. Doug Tinkham, for their support and advice. I thank my colleagues Taus Jorgensen, Dr. Fabio Cafagna, Dr. Katie Hahn, Dr. Omid Mahmoodi, Michael Burns, Dr. Geoff Baldwin, and all the other graduate students in the Harquail School of Earth Sciences for their valued friendship.

I would not have been able to reach this point without the support and encouragement of my family and close friends. In particular, I thank my mother Louise, father Michael, brother Kyle,

sister Lindsay, sister in-law Candace, niece Maya, nephew Reid, and my parents-in-law Marilyn and Peter Engelbert. You have all supported me in my academic endeavours and for this I am extremely grateful. I would also like to thank Joe Currie, Melissa Render, Adam Parker, Carlo Castrochino, and Johanne Roux for their friendship and support.

Lastly, I thank my wife Margaret. She has provided love and support throughout every stage of this project and for this I am forever grateful. I am excited for the next chapter of our life together.

Table of Contents

List of Figures

List of Tables

Chapter 1

1 Introduction to thesis

1.1 Background

Hydrothermal ore deposits, including porphyry, epithermal, volcanogenic massive sulfide (VMS), and orogenic and Carlin-type gold constitute a significant global resource. The hydrothermal systems that form these deposits can be long-lived and produce significant concentrations of base and precious metals by leaching, mobilizing, and depositing these metals through fluid-rock interaction. Hydrothermal systems require three essential components: (i) a source of sustained heat; (ii) a fluid phase, typically aqueous solutions of variable dissolved solute content; and (iii) a rock to host the system (Kesler 2005; Pirajno 2009).

Impact sites can be ideal settings for hydrothermal cell formation due to the presence of a heat source and host (the cooling impact site) that can drive fluids sourced from either the melt sheet, surficial fluids, or metamorphic fluids (Osinski et al. 2005) provided that fluids are available to initiate a hydrothermal convection cell (Naumov 2002; Osinski et al. 2013). Impact-generated hydrothermal systems have been studied at various sites (e.g., Naumov 1993; Ames et al. 1998; Reimold et al. 1999; Grieve and Therriault 2000; Molnár et al. 2001; Osinski et al. 2005, 2013). This work has shown that hydrothermal circulation can extend to depths up to several km (Komor et al. 1988; Zurcher and Kring 2004), and the potential for fluid flow is enhanced by zones of fracturing and brecciation related to impact and if the impact occurs in a marine setting (Goto et al. 2004; Pirajno 2005). The duration of such hydrothermal systems is poorly understood; however, their longevity increases with crater size (Osinski et al. 2013).

The 1.85 Ga Sudbury Igneous Complex (SIC) in Ontario, Canada is the product of a differentiated impact melt sheet (Dietz 1960; Grieve et al. 1991) and is part of the mineralized environment of one of the largest Ni(-Cu-PGE) districts globally (Naldrett 2004; Boutroy et al. 2014). A considerable amount of research has been conducted on the units directly related to mineralization, such as the lowermost part of the SIC and its immediate footwall, which hosts magmatic Ni-Cu-PGE ores (Ames et al. 2008 and references therein), and the overlying Whitewater Group, which hosts Zn-Cu-Pb hydrothermal ores (Rousell 1984). The magmatic ores occur as three distinct deposit types (Morrison et al. 1994; Lightfoot and Farrow 2002; Ames and Farrow 2007): (i) contact; (ii) offset; and (iii) footwall. Relative to magmatic processes, the importance of hydrothermal fluids for the genesis of footwall-type Cu-Ni-PGE deposits in the Sudbury district, and the sources of such fluids is controversial. An integrated model involving both magmatic and hydrothermal stages has been proposed (Farrow and Watkinson 1992, Li and Naldrett 1993, Jago et al. 1994, Morrison et al. 1994, Watkinson 1999, Molnár and Watkinson 2001, Hanley et al. 2005). In contrast to the magmatic ores, syn-genetic massive sulfide ore (Zn-Cu-Pb) formed at the top of the crater fill Onaping Formation and as replacement of carbonates (Ames et al. 1998).

The hydrothermal system in the Onaping Formation, referred to as the hanging wall hydrothermal system, records fluid temperatures ranging from ambient up to 250° to 300°C (Ames et al. 2006). Fluid-rock interaction throughout the duration of the hydrothermal system produced semi-conformable alteration zones throughout the Sudbury basin. The alteration assemblages of these alteration zones vary vertically through the basin and are defined by an upper calcite-chlorite zone, transition zone, ferro-actinolite-chlorite zone, albite zone, and lower

silicified zone (Ames and Gibson 1995; Ames et al. 1998; Ames 1999). This hydrothermal system is considered to be responsible for the Errington and Vermillion Zn-Pb-Cu rich massive sulphide deposits (Ames 1999).

The hydrothermal system in the footwall of the SIC also produced distinct alteration zones, and these zones are observed to be both related and unrelated to Cu(-Ni)-PGE mineralization in Sudbury breccia or other impact-related breccias. Alteration zones containing variable amounts of amphibole, biotite, epidote, albite, quartz, scapolite, magnetite, biotite, alkali feldspar, and titanite border the sulfide bodies (Farrow and Watkinson 1992; Molnár et al. 1997, 1999, 2001; Ames et al. 2006). Fluid inclusion and isotope studies provide evidence for multiple fluid events in these footwall settings resulting from cooling of the SIC and later tectonic events (e.g., Farrow 1994; Molnár et al. 2001; Marshall et al. 1999; Ames et al. 2006; Tuba et al. 2010; Tuba et al. 2014). Hanley and Mungall (2003) describe hydrothermal alteration related to Cu-Ni-PGE footwall deposits as being characterized by zone enrichment in hydrosilicates (e.g., chlorite, amphibole) and large (200 m) halogen-rich halos surrounding ore deposits.

1.2 Research problems

Of the research focused on the Sudbury impact structure, relatively little work has been done on the upper 1.5 km of the 2.5 km-thick crystallized melt sheet referred to as the felsic granophyre unit (GR). Compositionally the GR is a two-feldspar monzogranite that is characterized by variably developed (0 to 65 vol. %) granophyre, hence the widespread use of this term. The limited historical work done on this unit has shown that the unit contains hydrothermal alteration minerals (Naldrett et al. 1970; Therriault et al. 2002), though no work has been done to establish

the distribution and source of these minerals. Therefore, there is a hydrothermal system in the GR that is underdocumented. Work has been done to characterize the hydrothermal systems in the footwall to the SIC and in the Sudbury basin overlying the SIC, but there is currently no understanding of how these systems are related, if at all, and of the nature of the hydrothermal environment separating these two systems. Therefore, an integrated study investigating the nature, distribution, and source of alteration in the GR is necessary in order to develop a complete understanding of the hydrothermal system in the post-impact Sudbury structure.

The role of hydrothermal fluids in the remobilization of metals into the Sudbury footwall remains controversial, and an integrated model involving both magmatic and hydrothermal stages has been proposed (Farrow and Watkinson 1992, Li and Naldrett 1993, Jago et al. 1994, Morrison et al 1994, Watkinson 1999, Molnár and Watkinson 2001, Hanley et al 2005). In order to investigate the hydrothermal processes that are critical for metal remobilization, it is important to compare the mineralized footwall system to a barren system, and the hydrothermal system in the GR provides an excellent comparison. Methods used in previous studies to document the footwall hydrothermal system are highly variable and include petrography, fluid inclusion studies, and oxygen isotopes (e.g., Farrow and Watkinson 1992; Marshall et al. 1999; McCormick et al. 2002; Hanley et al. 2011). The techniques used to document and assess the fluid inclusion record in the Sudbury footwall are variable, making it difficult to make direct comparisons between studies. Furthermore, comparison of fluid inclusion results between two separate studies can be challenging given the multitude of fluid inclusion types documented throughout both the North Range (NR) and South Range (SR) footwall. Therefore, it is important to apply the same techniques used in the GR to a mineralized footwall system in order to

maintain consistency in the data and provide context for comparison with other footwall types. The Nickel Rim South deposit (NRS) was selected for this comparison because it has not previously been studied and it is located in the East Range (ER) of the Sudbury structure. An ER deposit was selected because it represents the transition between the processes dominating the NR and those in the SR, providing an important link and comparison to these deposit types. Furthermore, NRS contains both Ni(-Cu)-rich contact-type ore and Cu(Ni-)-PGE-rich footwall-type ore, and it is currently producing, which facilitates sampling.

1.3 Thesis objectives

The primary objective of this thesis is to document and characterize the hydrothermal systems in the GR and NRS in order to compare hydrothermal processes in a barren versus mineralized system. In doing so, the following research questions are established:

1. How do the textural and mineralogical characteristics of the GR vary throughout the unit and are the observed mineral assemblages magmatic or related to alteration?
2. What is the fluid history of the GR?
3. Is there evidence for hydrothermal remobilization of metals at NRS?
4. What is the fluid history of NRS?
5. How do the fluid histories of the GR and NRS compare?

1.4 Structure of thesis

This dissertation is divided into five chapters. Chapters two to four are written in manuscript format and represent versions intended for refereed journal submission. Therefore, some

repetition of text occurs between chapters two and three with respect to background and petrographic description of the granophyre unit.

Chapter two is written in manuscript form entitled "**Petrographic and geochemical evidence for extensive post-crystallization metasomatism in an impact generated melt sheet: the granophyre unit of the Sudbury Igneous Complex revisited**". This manuscript presents a detailed description and characterization of the granophyre unit of the SIC by incorporating field data (i.e., outcrop and hand specimen description), petrography, and whole rock and mineral chemistry (i.e., SEM-EDS and EPMA) to establish the evolution of the granophyre unit from its late-stage formation during crystallization of the SIC through its hydrothermal history to its present data altered state.

Chapter three is written as a manuscript entitled "**Evidence for generation and collapse of a large-scale hydrothermal system in a cooling impact melt sheet: the granophyre unit of the Sudbury Igneous Complex, Ontario, Canada**"**.** This manuscript presents results from a multifaceted study integrating fluid inclusion petrography and microthermometry, evaporate mound analysis, cathodoluminescence of quartz, and whole rock and quartz oxygen isotope analysis to document the nature of fluid-rock interaction in the granophyre unit and how it relates to post-impact cooling history of the Sudbury Igneous Complex and overlying rocks.

Chapter four is written as a manuscript entitled "**Documenting the nature and implications of hydrothermal processes on a magmatic Ni-Cu-PGE deposit at Nickel Rim South, Sudbury,**

Ontario, Canada". This manuscript describes the hydrothermal record preserved in the Nickel Rim South deposits by incorporating petrography, mineral chemistry, fluid inclusion petrography and microthermometry, evaporate mound analysis, and stable isotopes for mineralized and barren samples. The goal of the study was to identify the composition, role, and source of fluids within the Nickel Rim South deposit.

1.5 Statement of original contributions

The following is a summary of original contributions presented by the candidate in this study:

1. Documentation of the primary mineralogy and petrographic characteristics of the granophyre unit in the North Range and South Range
2. Documentation of a hydrothermal system in the granophyre unit as evidenced by alteration assemblages, whole rock and mineral chemical data, fluid inclusions microthermometry and evaporate mound chemistry, oxygen isotopes, and cathodoluminescence imaging.
    a. The first fluid inclusion study conducted in the SIC proper (granophyre unit)
    b. First whole rock oxygen isotope study on the SIC proper
3. Trace element chemistry for epidote in the Nickel Rim South deposit.
4. A detailed description of mineralogy and lithologies at NRS and documentation of alteration assemblages both related and unrelated to mineralization.
5. First fluid inclusion study of the Nickel Rim South deposit.

1.6 References

Ames, D. E. (1999): Geology and regional hydrothermal alteration of the crater-fill, Onaping formation: association with Zn-Pb-Cu mineralization, Sudbury Structure, Canada. Unpublished Ph.D. thesis Carleton University, Ottawa, Ontario, 460 p.

Ames, D. E., and Farrow, C. E. G. (2007): Metallogeny of the Sudbury Mining Camp, Ontario, in Goodfellow, W. D., ed., Mineral Deposits of Canada: A Synthesis of Major Deposit-Types, District Metallogeny, the Evolution of Geological Provinces, and Exploration Methods: Geological Association of Canada, Mineral Deposits Division, Special Publication 5, p. 329-350.

Ames, D. E. and Gibson, H. L. (1995): Controls on geological setting of regional hydrothermal alteration within the Onaping Formation, footwall to the Errington and Vermillion base metal deposits, Sudbury Structure, Ontario. Current Research 1995-E. Geological Survey of Canada, 161-173.

Ames, D. E., Watkinson, D. H. and Parrish, R. R.(1998): Dating of a regional hydrothermal system induced by the 1850 Ma Sudbury impact event. Geology 26, 447-450.

Ames, D. E., Jonasson, I. R., Gibson, H. L., and Pope, K. O. (2006): Impact-generated hydrothermal system – constraints from the large Paleoproterozoic Sudbury crater, Canada, in Biological processes associated with impact events, eds. C. Cockell, C. Koeberl, I. Gilmour: Springer.

Ames, D. E., Davidson, A., and Wodicka, N. (2008): Geology of the Giant Sudbury Polymetallic Mining Camp, Ontario, Canada. Economic Geology 103, 1057-1077.

Boutroy, E., Dare, S. A. S., Beaudoin, G., Barnes, S.-J., and Lightfoot, P. C. (2014): Magnetite composition in Ni-Cu-PGE deposits worldwide: application to mineral exploration. Journal of Geochemical Exploration 145, 64-81.

Dietz, R.S. (1960): Meteorite impact suggested by shatter cones in rock. Science 73, 1781-1784.

Farrow, C. E. G. (1994): Geology, alteration, and the role of fluids in Cu-Ni-PGE mineralization of the footwall rocks to the Sudbury Igneous Complex, Levack and Morgan Townships, Sudbury District, Ontario. Unpublished Ph.D. thesis, Ottawa, Canada, Carleton University, 373.

Farrow, C. E.G. and Watkinson, D. H. (1992): Alteration and the role of fluids in Ni, Cu and platinum-group deposition, Sudbury Igneous Complex contact, Onaping-Levack area, Ontario. Mineralogy and Petrology 46, 67-83.

Goto, K., Tada, R., Bralower, T. J., Hasegawa, T., and Matsui, T. (2004): Evidence for ocean water invasion into the Chicxulub crater at the Cretaceous/Tertiary boundary. Meteoritics and Planetary Sciences 39, 1233-1247.

Grieve, R. A. F. and Therriault, A. (2000): Vredefort, Sudbury, Chicxulub: Three of a kind?. Annual Review of Earth and Planetary Sciences 28, 305-338.

Grieve, R. A. F., Stoffler, D., and Deutsch, A (1991): The Sudbury structure: Controversial or misunderstood? Journal of Geophysical Research 96, 22 753- 22 764.

Hanley, J. J. and Mungall, J. E. (2003): Chlorine enrichment and hydrous alteration of the Sudbury breccia hosting footwall Cu-Ni-PGE mineralization at the Fraser mine, Sudbury, Ontario, Canada. The Canadian Mineralogist 41, 857-881.

Hanley, J. J., Mungall, J. E., Pettke, T., Spooner, E. T. C., and Bray, C. J. (2005): Ore metal redistribution by hydrocarbon-brine and hydrocarbon-halide melt phases, North Range

footwall of the Sudbury Igneous Complex, Ontario, Canada. MineraliumDeposita40, p. 237-256.

Hanley, J. J., Ames, D. E., Barnes, J., Sharp, Z., and Guillong, M. (2011): Interaction of magmatic fluids and silicate melt residues with saline groundwater in the footwall of the Sudbury Igneous Complex, Ontario, Canada: new evidence from bulk rock geochemistry, fluid inclusions and stable isotopes. Chemical Geology 281.1-25.

Jago, B. C., Morrison, G. G., and Little, T. L. (1994): Metal zonation patterns and microtextural and micromineralogical evidence for alkali- and halogen-rich fluids in the genesis of the Victor Deep and McCreedy East footwall copper ore bodies, Sudbury Igneous Complex. Ontario Geological Survey Special Volume 5, 65-75.

Kesler, S. E. (2005): Ore-Forming Fluids. Elements 1, 13-18.

Komor, S. C., Valley, J. W., and Brown, P. E. (1988): Fluid-inclusion evidence for impact heating at the Siljan Ring, Sweden. Geology 16, 711-715.

Li, C. and Naldrett, A.J. (1993): High chlorine alteration minerals and calcium-rich brines in fluid inclusions from the Strathcona Deep Copper zone, Sudbury, Ontario. Economic Geology 88, 1780–1796.

Lightfoot, P. C. and Farrow, C. E. (2002): Geology, geochemistry and mineralogy of the Worthington Offset Dike: a genetic model for offset dike mineralization in the Sudbury Igneous Complex. Economic Geology 97, 1419-1446.

Marshall, D. D., Watkinson, D. H., Farrow, C. E. G., Molnár, F., and Fouillac, A. M. (1999): Multiple fluid generations in the Sudbury Igneous Complex: fluid inclusions, Ar, O, H, Rb, and Sr evidence. Chemical Geology 154, 1-19.

McCormick, K.A., Fedorowich, J.S., McDonald, A.M., and James, R.S. (2002): A textural, mineralogical, and statistical study of the footwall breccia within the Strathcona embayment of the Sudbury Structure. Economic Geology 97, 125–143.

Molnár, F., Watkinson, D. H., Jones, P. C., and Gatter, I. (1997): Fluid inclusion evidence for hydrothermal enrichment of magmatic ore at the contact zone of the Ni-Cu-platinum group element 4b deposits, Linsley mine, Sudbury, Canada. Economic Geology 92, 674-685.

Molnár, F. and Watkinson, D.H. (2001): Fluid-inclusion data for vein type Cu–Ni–PGE footwall ores and their use in establishing an exploration model for hydrothermal PGE-enrichment around mafic ultramafic intrusions. Exploration and Mining Geology 10, 125–141.

Molnár, F., Watkinson, D.H., Jones, P.C. (2001): Multiple hydrothermal processes in footwall units of the North Range, Sudbury igneous complex, Canada, and implications for the genesis of vein-type Cu–Ni–PGE deposits. Economic Geology 96, 1645–1670.

Morrison, G. G., Jago, B. C., and White, T. L. (1994): Footwall mineralization of the Sudbury Igneous Complex, in: Lightfoot, P. C., Naldrett, A. J. (eds.) Proceedings of the Sudbury-Noril'sk symposium. Ontario Geological Survey Special Volume5, 57-64.

Naldrett, A. J. (2004): Magmatic Sulfide Deposits: Geology, geochemistry and exploration. Spring Verlag, Heidelberg, Berlin, 728.

Naldrett, A. J., Bray, J. G., Gasparrini, E. L., Podolsky, T., and Rucklidge, J. C. (1970): Cryptic variation and the petrology of the Sudbury Nickel Irruptive. Economic Geology 65, 122-155.

Naumov, M. V. (1993): Zonation of hydrothermal alteration in the central uplift of the Puchezh-Katunkiastrobleme. Metoritics 28, 408-409.

Naumov, M. V. (2002): Impact-generated hydrothermal systems: Data from Popigai, Kara, and Puchezh-Katunki impact structures. In: Plado, J., and Pesonen, L. J. (Eds.), Impacts in Precambrian Shields. Springer-Verlag, Berlin, 117-171.

Osinski, G. R., Lee, P., Parnell, J., Spray, J. G., and Baron, M. (2005): A case study of impact-induced hydrothermal activity: The Haughton impact structure, Devon Island, Canadian High Arctic. Meteoritics and Planetary Science 40, 1859-1878.

Osinski, G. R., Tornabene, L. L., Banerjee, N. R., Cockell, C. S., Flemming, R., Izawa, M. R. M., McCutcheon, J., Parnell, J., Preston, L. J., Pickersgill, A. E., Pontefract, A., Sapers, H. M., and Southam, G. (2013): Impact-generated hydrothermal systems on Earth and Mars. Icarus 224, 347–363.

Pirajno, F. (2005): Hydrothermal processes associated with meteorite impact structures: evidence from three Australian examples and implications for economic resources. Australian Journal of Earth Sciences 52, 587-605.

Pirajno, F. (2009): Hydrothermal Processes and Mineral systems. Springer-Science and Business Media B. V.

Reimold, U., Koeberl, W., Fletcher, P., Killick, A. M., and Wilson, J. D. (1999): Pseudotachylite breccias from fault zones in the Witwatersrand Basin, South Africa: evidence of autometasomatism and post-brecciation alteration processes. Mineralogy and Petrology 66, 25-53.

Rousell, D. H. (1984): Mineralization in the Whitewater Group. In The geology and ore deposits of the Sudbury structure, (eds.) Pye, E. G., Naldrett, A. J., and Giblin, P. E. Ontario Geological Survey Special Volume 1, 219-232.

Therriault, A. M., Fowler, A. D., and Grieve, R. A. F.(2002): The Sudbury Igneous Complex: A Differentiated Impact Melt Sheet. Economic Geology 97, 1521-1540.

Tuba, G., Molnár, F., Watkinson, D. H., Jones, P. C., and Mogessie, A. (2010): Hydrothermal vein and alteration assemblages associated with low-sulfide footwall Cu-Ni-PGE mineralization and regional hydrothermal processes, North and East Ranges, Sudbury structure, Canada. SEG Special Publication 15, 573-598.

Tuba, G., Molnár, F., Ames, D. E., Péntek, A., Watkinson, D. H., and Jones, P. C. (2014): Multi-stage hydrothermal processes involved in "low-sulfide" Cu(-Ni)-PGE mineralization in the footwall of the Sudbury Igneous Complex (Canada): Amy Lake PGE zone, East Range. Mineralium Deposita 49, 7-47.

Watkinson, D. H. (1999): Platinum-group-element enrichment in Cu-Ni-rich sulfides from footwall deposits, Sudbury Igneous Complex, Canada. Chronique de la Recherchemineire 535, 55-69.

Zurcher, L. and Kring, D. A. (2004): Hydrothermal alteration at the core of the Yaxcopoil-1 borehole, Chicxulib impact structure, Mexico. Meteoritics and Planetary Sciences 38, 1199-1222.

Chapter 2

Petrographic and geochemical evidence for extensive post-crystallization metasomatism in an impact generated melt sheet: the granophyre unit of the Sudbury Igneous Complex revisited

2.1 Abstract

The Sudbury Igneous Complex (SIC) is the product of a differentiated impact melt sheet and one of the best preserved impact sites globally. The top 1.5 km of the 2.5 km-thick crystallized melt sheet, referred to as the granophyre unit (GR), exhibits strong textural, mineralogical, and geochemical evidence for a long and complex alteration history. The unit is divided into a North Range (NR) and South Range (SR), both of which consist of two-feldspar (i.e., subsolvus) monzogranite characterized by variably developed granophyre(0 to 35 vol. % SR; 7 to 63 vol. % NR). The alteration assemblages of the GR vary between the NR and SR. The SR is characterized by biotite-epidote-titanite with lesser muscovite-stilpnomelane-chlorite-ferrotschermakite, whereas the NR is characterized by epidote-ferro-actinolite-stilpnomelane with lesser chlorite. The alteration intensity varies considerably throughout both the NR and SR, but the SR exhibits slightly stronger alteration than the NR. There is both extensive textural and chemical evidence for metasomatism and re-equilibration of the GR, including the strongly pitted texture of plagioclase and K-feldspar, which may indicate dissolution and precipitation reactions. The two feldspar phases (50 to 70 vol. %) record equilibration to <350ºC based on their bulk chemistry (Ab_{98-100} and Or_{95-100}). Furthermore, Fe-Ti oxides record variable degrees of re-equilibration both texturally and chemically. Primary Ca-rich amphibole (Fe# = 0.40 to 0.48) is extensively replaced by a Fe-rich amphibole (Fe# = 0.51 to 0.74) and also Fe-rich chlorite

(Fe#= 0.66 to 0.88). Accessory phases such as zircon contain inclusions of baddeleyite, uraninite, and thorite, indicating that it also has undergone fluid-mediated alteration. Whole rock geochemical data and mass balance calculations indicate that the observed alteration is the product of minimal elemental gains and losses with the exception of Fe, which is reflected by the high Fe# in secondary mineral phases and cannot be accounted for by loss of Fe in primary phases of the GR. The GR hydrothermal system therefore involved ingress of an external source of Fe, and the source of this Fe is proposed to be either the overlying Onaping Formation or the underlying quartz gabbro and norite units. The results from this study record a complex and protracted post-crystallization history of fluid-rock interaction for the GR that may be related to the ore deposit-forming hydrothermal fluids elsewhere in the Sudbury Structure.

2.2 Introduction

Hydrothermal alteration in upper level crustal settings is often associated with large intrusive centres that are frequently felsic in nature (e.g., porphyry deposits; Seedorf et al. 2005). Such settings have the ability to alter large volumes of rock (Plumper and Putnis 2009) with this alteration being produced by coupled dissolution-precipitation (CDP; Putnis 2002), which is a reaction mechanism often being overlooked in the study of these systems. In addition, many of these settings are associated with a variety of ore deposits (e.g., hydrothermal Au-Ag, IOCG-U-Ag, Fe-Cu-REE; Bigot and Jebrak 2015; Li and Zhou 2015; MacMillan et al. 2016;Wu et al. 2016). Long-lived, large-scale hydrothermal circulation has the ability to chemically re-equilibrate the host rock towards that of the circulating fluid and can result in a new rock that is altered both texturally and chemically (i.e., mineral replacement). The end result of the alteration process is to produce a new mineral assemblage that is indicative of the relict hydrothermal

system (i.e., composition of the fluid, P-T conditions; Farmer 2000). The products of these systems can be observed from the macroscopic (i.e., outcrop and hand sample) to microscopic scales. As the latter may provide vectors in some ore deposit settings, the recognition, characterization and understanding of the processes and products are useful not just in ore deposit studies but many other aspects of the earth sciences.

Hydrothermal systems require three essential components: a fluid (or combination of different fluids), a heat source, and rock to host the system (Pirajano 2009). Impact sites can be ideal settings for formation of hydrothermal cells due to the presence of a heat source and host rocks (the cooling impact site), provided that fluids are available to initiate a hydrothermal convection cell (Naumov 2002; Osinski et al. 2013). The 1.85 Ga Sudbury Igneous Complex (SIC) in Ontario, Canada is the product of a differentiated impact melt sheet (Dietz 1960; Grieve et al. 1991) and is part of the mineralized environment of one of the largest Ni(-Cu-PGE) districts globally (Naldrett 2004; Boutroy et al. 2014). Due to the global significance of the Ni(-Cu-PGE) mineralization within the SIC and its immediate surroundings, a considerable amount of research has been conducted on the units directly related to mineralization, such as the lowermost part of the SIC and its immediate footwall, which hosts the Ni-Cu-PGE ores (Ames et al. 2008 and references therein). In contrast, relatively little attention has been focused on the upper 1.5 km of the 2.5 km-thick crystallized melt sheet, that is the felsic granophyre unit (GR). Compositionally the GR is a two-feldspar monzogranite that is characterized by variably developed (0 to 65 vol. %) granophyre, hence the widespread use of this term. Historical work has provided minimal recognition of any hydrothermal alteration in the GR, the most authoritative references being Naldrett et al. (1970) and Therriault et al. (2002). This is in contrast with what would be

expected for such a large felsic body emplaced into the upper crust and in close proximity to a large body of water, as evidenced from the sub-aqueous setting of the overlying sedimentary strata and widespread alteration within these and underlying volcanic rocks (Ames et al. 1998; Huber et al. 2014).

The results of this study provide substantial textural and chemical evidence for the extensive and pervasive alteration of the GR. In this paper a complete description and characterization of the GR is presented using data from field traverses, macroscopic (outcrop and hand specimen) to microscopic (petrography, scanning electron microscope imaging, cathodoluminescence) observations, and whole rock and mineral chemistry (SEM-EDS, EPMA). These data are integrated to establish the evolution of the GR from the onset of its late-stage crystallization in the SIC to its present altered state. This study provides evidence for large-scale, pervasive alteration in a high-level felsic setting and the results can be used as an analogue to other high-level intrusive settings and various ore-hosting environments (e.g., VMS, porphyry). This work is also of particular importance to furthering the understanding of processes leading to Cu-Ni-PGE mineralization in the footwall environment of the SIC (e.g., Levack, Broken Hammer, Nickel Rim South deposits).

2.3 Geological Background

2.3.1 Geological Setting

The Sudbury Structure (SS; Fig. 1A) is located at the junction of three major structural provinces of the Canadian Shield (Superior, Southern, Grenville) and comprises the SIC, the Whitewater Group overlying the SIC, and Archean and Proterozoic footwall rocks that underlie the SIC

(Dressler 1984). The basement rocks are divided into two main domains: (i) Archean rocks of the North Range (NR; i.e., Superior Province); and (ii) Proterozoic rocks of the South Range (SR; i.e., Southern Province; Dressler 1984). The NR basement rocks consist of gneissic, metavolcanic, metasedimentary, and granitic rocks. The gneisses (Levack Gneiss Complex), which dominate large parts of the NR, are grey banded rocks of granodioritic, tonalitic and quartz-dioritic composition (Dressler 1984; Lafrance et al. 2008). In contrast, the SR is underlain by Paleoproterozoic metavolcanics and metasedimentary rocks of the Huronian Supergroup. Most evidence is consistent with the SS being the result of an impact event at 1.85 Ga (Dietz 1960; Card et al. 1984; Naldrett and Hewins 1984; Grieve et al. 1991; Ames et al. 1998; Mungall et al. 2004) and that the SIC represents the crystallized product of an impact-generated melt sheet (Krough et al. 1984; Peredery and Morrison 1984; Golightly 1994). The geology of the Sudbury area is the result of large-scale tectonic and magmatic events pertaining to the meteorite impact, the subsequent fill of the impact crater, and associated pre-, syn- and post-impact deformational processes.

The SIC contains several units that are the result of differentiation and crystallization of the melt sheet. From bottom to top these units are: (i) the sublayer and associated quartz diorite offset dikes; (ii) norite (mafic and felsic); (iii) quartz gabbro; and (iv) GR (Coats and Snajdr 1984; Lightfoot et al. 1997). Overlying the GR is the Basal Onaping Intrusion, a semi-conformable, clast-rich melt body interpreted to be of intrusive origin. This unit has been interpreted to also be part of the impact melt sheet (Ames et al. 2005; Anders et al. 2015). Above the Basal Onaping Intrusion is the Whitewater Group, also referred to as the basin fill, which consists of the

Onaping Formation - a fallback breccia unit - and the shallow marine sedimentary rocks of the Onwatin and Chelmsford formations.

The Sudbury environment has been affected by several pre-, syn-, and post-impact regional tectonic events, including the 2.4 to 2.3 Ga Blezardian orogeny (Stockwell 1982; Riller and Schwerdtner 1997), the 1.89 to 1.83 Penokean orogeny (Hoffman 1989; Sims et al. 1989), a 1.45 Ga NW-thrusting event (Krough 1994), and the 1.0 Ga Grenvillian orogeny (Brocoum and Dalziel 1974). Post-impact deformation was particularly strong in the SR due to the development of the South Range Shear Zone (Peredery and Morrison 1984; Milkereit and Green 1992).

The Sudbury area is known for its magmatic Ni-Cu-PGE deposits. The magmatic ores occur as three distinct deposit types (Morrison et al. 1994; Lightfoot and Farrow 2002; Ames and Farrow 2007): (i) contact-type deposits found at or near the basal contact of the SIC with the Proterozoic and Archean basement. These deposits have high Ni/Cu ratios (≥1 and Pt + Pd + Au <1 g/t); (ii) offset deposits which are hosted by offset dike rocks (e.g., inclusion-rich quartz diorite) that intrude the Archean basement rocks. These deposits have high but variable Cu/Ni ratios (about 1) and Pt + Pd + Au >2.5 g/t; and (iii) footwall-type deposits which are present as stringers, disseminations, and sheet-like veins in the basement up to 2 km outside the SIC. In addition to the magmatic ores, syngenetic massive sulfide ore deposits (Zn-Cu-Pb-Ag) are also present at the top of the Onaping Formation where they replace carbonates of the Vermillion Formation (Ames et al. 1998). These deposits are significant in that they reflect the formation of a large hydrothermal cell developed above the cooling SIC, akin to SEDEX-type mineralization (Ames 1999).

2.3.2 Characteristics of Granophyre

Granophyre is an intergrowth of quartz and alkali feldspar on a macroscopic (>1 mm) to microscopic (mm) scale (Barker 1970). It is not to be confused with graphic texture, which ranges in size from 1 mm to 1 m and is characterized by subhedral skeletal quartz hosted in alkali feldspar or sodic plagioclase (Barker 1970). Most granophyres are inferred to form by rapid, simultaneous growth (i.e., eutectic crystallization) of alkali feldspar and quartz from a silica-rich melt (Smith 1974), although a replacement origin is also suggested (Augustithis 1973). The intergrowths occur primarily as mesostasis, groundmass, and occasionally as megacrysts in plutonic rocks, and they form as irregular or vermicular crystal habits. Most models for the formation of granophyre involve magmatic undercooling, whereby quartz and alkali feldspar crystals form at a temperature below the liquidii as a result of sudden loss of volatiles (e.g., due to pressure release) which induces crystallization and granophyre formation due to undercooling (Tuttle and Bowen 1958; Swanson 1977, 1986; Morgan and London 2012). Granophyre occurs most commonly in felsic systems, but it can also be found in late differentiates of mafic systems, such as in the Pallisades sill in New York State (Block et al. 2015).

2.3.3 Granophyre in the Sudbury Igneous Complex

2.3.3.1 Petrographic Characteristics and Models

Although substantial work has been done on the lowermost portions of the SIC (i.e., norites) and its footwall rocks (e.g., Naldrett et al. 1970; Naldrett and Hewins 1984; Farrow 1994; Therriault 2001; Murphy and Spray 2002; Therriault et al. 2002; Hanley and Mungall 2003; Mungall and Hanley 2004; Péntek et al. 2008; Hanley and Bray 2009; Tuba et al. 2010; Tuba et al. 2014), relatively few studies have focused on the GR. In one of the first detailed descriptions of the unit,

Naldrett et al. (1970) described it as having an average mode of 70% granophyre (i.e., quartz-K-feldspar intergrowth), 20% plagioclase, and 10% augite, biotite, hornblende, and secondary minerals. Furthermore, these authors recognized that samples from the NR differ slightly from those of the SR with the former showing three parts granophyre to one part plagioclase, and the plagioclase is saussuritized in the bottom 25% of the unit. In contrast, these authors observed that SR GR contains quartz and plagioclase with rare rims of antiperthite, and most of the original granophyre consists of granulated quartz and more fine-grained, irregular masses of feldspar. They also noted that biotite is the most common mafic phase in the SR whereas in the NR green hornblende, stilpnomelane, and chlorite are the dominant mafic phases. Lastly, they attributed the presence of a pronounced gneissic foliation defined by oriented biotite to later deformation centred on the SR. Bennett et al. (1991) also described deformation in the SR GR and attributed it to the Penokean Orogeny.

A plagioclase-rich upper portion of the GR present in both ranges has been proposed (Stevenson 1961; Stevenson 1963; Peredery and Naldrett 1975; Naldrett and Hewins 1984). A study by Ames et al. (2002) indicated that the plagioclase-rich GR may relate to melting and incorporation of some overlying Onaping Formation by the superheated melt sheet. This hypothesis is supported by whole-rock chemical affinities between the GR and Onaping Formation (Ames et al. 2002). Evidence for a separate, post-SIC intrusion has also been suggested (Peredery and Naldrett 1975; Peredery and Morrison 1984). Therriault et al. (2002) described the GR as a coarse-grained, texturally heterogeneous unit lacking layering and composed mainly of micrographic/granophyric intergrowths (55 to 60 modal%) of quartz and K-feldspar (i.e., perthite or microcline) cored by albite laths ($An_{<5}$) ≤4 mm in length with additional anhedral quartz and

perthitic feldspar, epidote, biotite, and amphibole with minor apatite, calcite, and chlorite. As documented in other studies, these authors noted the GR consists of three parts: a lower, middle, and upper domain, which are marked by changes in colour and appearance of acicular amphibole in the middle part and an increase in modal % plagioclase in the upper part. Therriault et al. (2002) attributed the formation of the GR to undercooling caused by exsolution of a volatile phase.

2.3.3.2 Whole rock geochemistry

A detailed review on the geochemistry of the GR and main mass SIC was provided by Lightfoot et al. (1997) and Lightfoot et al. (2001). This work related the compositional differences between the norite and GR units to in situ differentiation of a single magma of quartz dioritic composition, as represented by the offset dyke rocks of the same composition. These studies described the GR as exhibiting an upward decrease in SiO_2 (73 to 63 wt. %) and increase in MgO (0.7 to 2.0 wt. %) and TiO_2 (0.7 to 1.1 wt. %) with little change in its Fe# (Fe/(Fe+Mg)) (0.6 to 0.8 but variable). These features are considered to reflect a top-down crystallization of the melt sheet. It was also noted that there might have been a hydrothermal imprint on the GR, as recorded by the variability of mobile elements such as K_2O, Na_2O, and Rb. However, that most of the major elements and ratios of the incompatible elements remain constant in vertical chemical profiles was interpreted to indicate that these elements had likely not been affected by later hydrothermal alteration (Lightfoot et al. 1997). Therriault et al. (2002) noted that major and trace elements and REE abundances vary continuously and gradationally between units in the SIC and that the GR exhibits an overall decrease in ΣREE and increase in negative Eu anomaly between the middle and upper portions. Zieg and Marsh (2005) also conducted a whole-rock

geochemical study and concluded that variability in some elements (K_2O, Na_2O, Rb) could be attributed to hydrothermal alteration experienced by the GR and quartz gabbro unit. They also noted an increase in SiO_2 and Zr near the top of the unit in both ranges.

2.3.4 Mineral Replacement Processes

Mineral replacement reactions during sub-solidus equilibration in felsic igneous rocks are common, but sometimes overlooked (e.g., Putnis 2002, 2009; Putnis and Putnis 2007; Putnis and John 2010; Ruiz-Agudo et al. 2014). These reactions record the equilibration of minerals with fluids of mixed origin, such as orthomagmatic, meteroric, basinal, or metamorphic. This fluid infiltration and interaction has occurred on a large scale in Earth's crust (Plumper and Putnis 2009), and therefore in the context of fluid-rock interaction a truly "fresh" or unaltered rock is rare. In order to better understand processes associated with fluid-rock interaction, detailed textural and chemical studies have been carried out in both natural and laboratory settings (Worden et al. 1990; Putnis 2002; Niedermeier et al. 2009; Plumper and Putnis 2009; Putnis and John 2010). Included in this work is a large range of minerals such as carbonates (Sabbides et al. 1992), zircon (Geisler et al. 2003; Geisler et al. 2007), zeolite (Dunkel and Putnis 2014), fluorapatite (Harlov et al. 2002), fluorite (Godinho et al. 2014), and cerrusite (Wang et al. 2013).

In settings with high fluid:rock ratios, such as hydrothermal ore-forming environments, processes facilitating mineral replacement reactions via coupled dissolution-precipitation (CDP) include chemical weathering, diagenesis, metamorphism, and metasomatism. In all cases an earlier mineral assemblage is replaced by a thermodynamically more stable assemblage (Putnis 2002; Ruiz-Agudo et al. 2014). An important aspect in CDP is the transfer of crystallographic

information or structure while cations exchange freely through interconnected channels (Putnis 2002; Niedermeier et al. 2009). In this process a parent mineral is dissolved by an aqueous solution and a new, more stable phase is precipitated on an atomic monolayer scale. The kinetics of the reaction is controlled by the rate of mass transfer through the fluid at high solubilities and by the rate of dissolution and precipitation at low solubilities (Putnis 2002). Therefore, relative solubility of the reactant compared to the product is more important than their absolute solubilities. Significantly, CDP commonly produces pit-textured pseudomorphs, thus providing important petrographic evidence of mass change. In addition, the crystallographic configuration of primary minerals may be partially preserved in the product due to the fact that the replacement occurs on an atomic monolayer scale (Plumper and Putnis 2009).

2.4 Methods

2.4.1 Sample collection, modal analysis, and rock staining

A suite of samples from the GR was collected from two geological traverses (Fig. 1B, C) near the city of Sudbury along highway #144, which cuts through the SIC, and from diamond drill core (drill hole 70011) provided by D. Ames (see Fig. 1A). Of the two traverses, one was through the SR (n=82) and the second was through the NR (n=52). In both cases, a systematic sampling approach was used with samples collected, where possible, along ~10 m spacing in order to ensure representative coverage. However, sampling was restricted to roadside outcrop exposure and was thus affected by road direction, which limited sampling coverage when recalculated to true stratigraphic depths. Additional samples were obtained from the sample suites of A. Therriault (n=12; Therriault et al. 2002), G. McNamera (n=7; McNamera 2011) and

D. Ames (n=41; personal collection)and were used as a comparison to the samples collected in this study.

A digital point counting method was used to estimate the proportions of granophyre in each sample collected. Whole polished thin sections (27 mm by 46 mm) were scanned in plane polarized light at high resolution and the resulting images were overlain with a grid used to perform a 400-spot manual point count to estimate the modal % granophyre for each sample. The grid point density was determined by trial and error whereby grids of different densities (100, 200 and 800 points) were tested. A grid density of 400 points/slide provided reproducible results whereas a higher density grid gave the same results but required more time.

To estimate the proportion of quartz and of the different feldspar phases in the samples, cut slabs of each sample were stained using the methods of Bailey and Stevens (1960) and Reid (1969). This method involves etching the cut surface of each slab with hydrofluoric acid and exposing the etched surface to reagents which produce purple (plagioclase) and yellow (alkali feldspar) colouration related to the calcium and potassium concentrations, respectively. This staining was done for three purposes: (i) to better reveal and examine the textures in the samples on a macroscopic scale; (ii) to provide a better estimate of the modal abundance of quartz, K-feldspar, and plagioclase in the original rock using imaging analysis software (Gimp 2.0); and (iii) to get an idea of the composition of the plagioclase based on its resultant colour from staining. As it became apparent during the course of this work that no remnant calcic plagioclase was present in any of the samples, slabs of an in-house reference granite with calcic plagioclase were stained to ensure that the solution being used was working properly.

2.4.2 Whole rock geochemistry

Twenty samples selected for whole rock analysis (n=11 from SR; n=9 from NR) were submitted to Activation Laboratories in Ancaster, Ontario, Canada. Whole rock major and minor oxides (SiO_2, TiO_2, Al_2O_3, Fe_2O_3, FeO, MnO, MgO, CaO, Na_2O, K_2O, P_2O_5, SrO, BaO) and loss on ignition (LOI) were determined using lithium metaborate/lithium tetraborate ($LiBO_2/Li_2B_4O_7$) fusion and analyzed by inductively coupled plasma atomic emission spectroscopy (ICP-AES). Loss on ignition was determined by placing 1 g of sample in an oven at 1000°C for one hour. Trace element concentrations were determined using inductively coupled plasma mass spectrometry (ICP–MS). Prepared samples (0.2 g) were added to lithium metaborate flux (0.9 g), mixed, and fused in a furnace at 1000°C. The resulting melt was cooled and dissolved in 100 mL of 4% nitric acid and then analyzed. The trace elements As, Bi, Hg, Sb, Se, and Te were analyzed by ICP–MS after aqua regia digestion. The elements Ag, As, Cd, Co, Cu, Mo, Ni, Pb, Zn, and REEs were measured by ICP-AES following digestion with perchloric, nitric, hydrofluoric, and hydrochloric acids. Fluorine and chlorine were measured by ion chromatography following decomposition of the sample by potassium hydroxide fusion. Carbon was determined by combusting the sample in a LECO induction furnace and quantifying the generated CO_2 by infrared spectrometry.

2.4.3 Mineralogy, textures, and mineral chemistry

After petrographic examination of all samples, a suite of 22 samples (n=12 from SR; n=10 from NR) was selected to further assess mineralogy, textural features at different scales, and mineral chemistry of all phases. Qualitative mineralogy work was done by transmitted and reflected light microscopy and using a scanning electron microscope (SEM) in the Central Analytical Facility

(CAF) laboratory, Laurentian University. An Oxford S-Sight energy dispersive spectrometer (EDS) mounted on a JEOL6400 SEM was used with a 15 kV accelerating voltage, a 1.005 nA beam current, acquisition count times between 10 and 30 seconds and a working distance of 15 mm. The SEM was also equipped with a GatanChromaCL mirror-type cathodoluminescence (CL) detector and a linear array photomultiplier tube with 16 separate photocathodes.

Twelve samples were selected for additional mineral chemistry using a Cameca SX-100 Electron Probe Micro Analyzer (EPMA) at the Ontario Geological Survey Geo Labs. This EPMA is equipped with 5 wavelength dispersive (WD) spectrometers and the instrument operating conditions were a beam current of 20 nA with an accelerating voltage of 20 kV, a count time between 10 and 25 seconds, and a beam diameter of 8 to 10 μm where possible but focused beam when required. Detection limits for the major elements (e.g., SiO_2, TiO_2, Al_2O_3, FeO, Cr_2O_3, MnO, MgO, CaO, Na_2O, K_2O) and halogens (F, Cl)reported are in the order of 0.1 wt. %.

2.5 Results

2.5.1 Field observations

A summary of the most relevant field observations is presented in Figure 2 and includes the variability in the modal abundance of K-feldspar, quartz, and plagioclase, the volume proportion of granophyre, the presence of miaroles, and the amphibole crystal habit (acicular/skeletal). Typical examples of GR in outcrop and in stained and unstained slabs for both the NR and SR traverses are shown in Figures 3 and 4.

During the field traverses and sample collection, important features visible in outcrop were described including macroscopic textures, presence of mafic phases, miaroles, and abundance and style of quartz and epidote veins. As will be described in detail in this section, the SR GR exhibited a greater degree of textural heterogeneity than the NR GR. The following features are noted:

1) The SR, in particular the bottom portion, contains discontinuous shear zones that coincide with an absence of granophyre. An example of SR GR in outcrop is shown in Figure 3A, where quartz and K-feldspar grains are visible and biotite is present as small clusters (0.2 to 0.5 cm).
2) Amphibole is the dominant mafic phase in the NR. In the lower portion of the NR it has an acicular texture (Fig. 3B) and typically varies from 8 to 15 modal %, but it decreases in abundance above this portion and is not of the acicular variety.
3) Miarolitic cavities are observed in both the SR (Fig. 3C) and NR (Fig. 3D). Miarolitic cavities, where present, are concentrated in the middle of the GR over an interval of approximately 200 m, but overall they are rare. They vary in size from 1 to 4 cm, are spherical to oval in shape, and contain quartz and/or epidote and in rare cases K-feldspar (Fig. 3C, D).
4) Coarse-grained felsic domains occur in the lower portion (bottom ~300 m) of the NR and contain quartz, K-feldspar (Fig. 3E), and occasionally acicular amphibole (Fig. 3F).
5) Both the NR and SR contain variable amounts of quartz and epidote veins that are unevenly distributed. In the SR, epidote veins are most abundant in the bottom ~400 m, decrease slightly in the middle portion, and increase in abundance in the upper portion. In the NR epidote veins are evenly distributed in the bottom and middle portions and decrease

slightly in the upper portion. Quartz veins are also present but less abundant than epidote veins. The abundance of quartz veins is uniform in the bottom and middle portions of the SR and increases in the upper portion of the SR, whereas quartz veins are less abundant in the NR and no correlation was observed with respect to depth.

2.5.2 Macroscopic features of the granophyre

Each stained slab from the GR was examined in detail in order to assess the type and abundance of the feldspar present and to determine macroscopic features not easily observed on outcrop surfaces, such as mineral and textural relationships. As the representative images in Figures 3G and H illustrate, the use of staining enhances textures that are not otherwise easily seen. Based on these samples, distinct compositional and textural differences are observed between and within the NR and SR. Given that the granophyre is primary, it is preserved in all samples unless a locally developed intense overprinting fabric has destroyed the feature (i.e., shear zones in the SR). Thus, the observed differences in the presence of granophyre may indicate intrinsic differences between the NR and SR.

The bottom portion of the SR (lower 800 m) contains 0 to 5 volume % granophyre (Figs. 2, 4A) except for a short interval (~25 m; 600 m from base) with up to 35 volume %. Although the latter interval is bounded above and below by shear zones, samples in this section void of granophyre do not record deformational fabrics and instead retain primary igneous textures, much like the sample in Figure 4A. Within the lowermost 100 m of the SR GR, euhedral and granophyre-hosted quartz coarsen upwards from the transitional contact between the quartz gabbro and GR. Small (<0.5 cm) quartz veinlets also occur. The middle portion of the unit contains variable

amounts of granophyre (5 to 32 vol. %; Figs. 2, 4B) and exhibits the coarsest quartz grains (<1.5 cm). In contrast, plagioclase grains, either as laths coring granophyre or as individual, euhedral grains, becomes more fine-grained. The top part of the unit contains highly variable proportions of granophyre (0 to 35 vol. %) and lacks evidence of deformation. Overall the upper portion of the SR GR marks a reduction in grain size of all phases and the appearance of recrystallized quartz domains.

The bottom ~50 m of the NR traverse contains 7 to 15 volume % granophyre which increases to a maximum of 63 volume % at 600 m from its base (Fig. 2). The transition between the quartz gabbro and GR contains coarse-grained, euhedral plagioclase, as was noted for the SR. This grain morphology is consistent throughout the NR samples although the grain size of plagioclase decreases away from the quartz gabbro. Small quartz pods are present between granophyre domains and are void of K-feldspar. A few samples contain epidote veinlets. In the middle part of the unit occurs the highest proportion and most consistent amount of granophyre (23 to 66 vol. %) and the grain size coarsens. The uppermost part of the unit contains between 25 to 42 volume % granophyre and is slightly more fine-grained in comparison to the lower part. The top ~200 m shows an increase in plagioclase which is commensurate with a decrease in quartz. Two samples are noted for their presence of a weak fabric (oriented plagioclase). Within the unit occur minor veins of chlorite, epidote, quartz, and rare carbonate and importantly the presence of recrystallized quartz is nearly absent in the NR samples.

The staining of rock slabs (Fig. 3G) provides a means of examining not only textures, but also the change in bulk composition of samples based on the proportions and compositions of the

feldspars (Brown and Parsons 1981, 1985). In granitoid rocks where the primary chemistry of feldspars is retained, plagioclase stains shades of purple whereas K-feldspar stains yellow and in addition may show perthitic textures (i.e., purple flames). For the GR, all the samples stained yellow and white, the former indicating the K-feldspar lacked perthite lamellae and the plagioclase approached or was near end-member albite. Furthermore, in many samples the mineral domains were not well defined, in contrast to the stained reference sample (see above), which may indicate development of a pervasive porous texture to the samples.

2.5.3 Petrographic features and mineral paragenesis

Granophyre in the GR typically exhibits a uniform fine-grained growth away from a central plagioclase lath, or coarsening of grains away from a lath (Fig. 4C, D). Detailed examination of granophyre in samples from the NR and SR indicate differences in the grain size and abundance and degree of preservation of the texture. Thus, overall the texture is more fine-grained and the degree of preservation is much lower in the SR. There is no apparent association between the degree of alteration per sample and location. Plagioclase laths from both ranges are pitted (Fig. 6), but this texture is more common in the NR. Additionally, in the NR granophyre becomes more coarse-grained away from its plagioclase nucleus, much like features that typify unidirectional solidification textures (e.g., Erdenebayar et al. 2014) whereas in the SR it is generally more fine-grained and does not coarsen away from the central plagioclase. The NR has retained its primary textures in contrast to the SR GR which not only exhibits different magmatic textures, but also reflects local deformation. The modal proportions of quartz and K-feldspar within granophyre vary outwards from plagioclase laths; in some instances K-feldspar is more abundant in the outer, coarser-grained domains whereas in other instances quartz is the dominant

phase. Pitted textures are common, but vary in intensity in plagioclase (Fig. 5C, D) and K-feldspar (Fig. 6A, B).

Detailed petrographic study of GR samples using transmitted and reflected light microscopy and data collection using SEM-EDS indicates that there are significant textural and mineralogical differences between the SR and NR; hence results of this work are presented separately. As already noted, a graphical representation of the modal abundances of the three primary phases (i.e., quartz and two feldspars) is shown in Figure 2. In addition, a mineral paragenesis for the GR is shown in Figure 7 and was constructed using observations collected during detailed petrographic examination of all hand samples and polished thin sections collected in this study. The sequence is not a continuum. The first stage, magmatic in origin, is similar for the NR and SR and includes the formation of plagioclase and the associated granophyre growth, as well as the formation of primary amphibole (NR only), apatite, zircon, ilmenite, and subhedral to anhedral quartz not associated with granophyre. The second stage represents the equilibration of the magmatic assemblage with a fluid and development of secondary minerals. This stage is represented by the formation of biotite (SR), ferro-actinolite (NR), stilpnomelane, epidote, chlorite, titanite, ferrotschermakite (SR) rutile, hematite, baddeleyite, galena, thorite, allanite, calcite and muscovite.

South Range

Plagioclase, 10 to 37 modal % (avg. 24 modal %) and 0.15 to 4 mm, is present as large, euhedral laths with aspect ratios of approximately 1:4. Where granophyre is present it surrounds these large plagioclase laths, indicating that the plagioclase nucleated granophyre (Fig. 5D). K-feldspar

constitutes 15 to 45 modal % (avg. 31 modal %), ranges from 0.1 to 3 mm, and typically lacks perthite with the exception of rare occurrences in the bottom of the SR (Fig. 6A). At the top of the SR, K-feldspar is contained in granophyre and is also present as individual, subhedral grains. Quartz is present in granophyre (0.1 to 1.5 mm; Fig. 4A, C, D), as interstitial infill (0.2 to 2 mm; Fig. 8A), and as isolated subhedral to euhedral grains (0.5 to 2 mm) and constitutes 27 to 60 modal % (avg. 45 modal %) of the GR. Ilmenite, as euhedral to subhedral grains of 0.1 to 0.35 mm, constitutes trace to 2 modal % and is slightly more abundant at the bottom and top of the unit (Fig. 9A). This phase has a variable internal texture with homogeneous domains or complex intergrowths of titanite, rutile, magnetite and hematite (Fig. 9E). Apatite is present as a minor to trace phase and is slightly more abundant at the bottom of the SR (Fig. 10A). It occurs as primary, intergranular crystals of 0.1 to 1.0 mm with an aspect ratio of up to ~20:1 and texturally predates most other primary phases. Zircon, 20 to 250 μm size (Fig. 10E, F), is a minor constituent and present as an early phase. Pyrrhotite is very rare, irregularly distributed, and very fine grained (~100 μm).

North Range

Plagioclase constitutes 20 to 39 modal % (avg. 30 modal %) of the NR GR and ranges in size from 0.2 to 6 mm with its average grain size being greater than that in the SR. Similar to the SR, the associated granophyre textures indicate that plagioclase nucleated granophyre growth. K-feldspar constitutes 19 to 46 modal % (avg. 35 modal %) of the GR and ranges in size from 0.1 to 2 mm (Fig. 6C). The majority is contained within granophyre, but some is present as small, subhedral to anhedral grains 0.3 and 1.5 mm in size. As in the SR, K-feldspar lacks perthitic texture. Primary quartz constitutes 21 to 55 modal % (avg. 35 modal %) of the GR, mostly

occurs in granophyre, and is typically more coarse-grained than in the SR (0.1 to 3 mm). It is also present as individual, euhedral to subhedral grains, but this texture is much less common than in the SR (≤2 modal %). Primary amphibole occurs as subhedral to euhedral 0.4 to 1.5 mm grains and constitutes up to ~4 modal % of the NR GR (Fig. 11A, B). Like plagioclase, amphibole is an early phase of the GR and pre-dates granophyre growth. Ilmenite is the only primary oxide phase (Fig. 9B), is generally euhedral and 100 to 250 μm, and constitutes up to 2 modal % of the NR GR, but is generally much less abundant than in the SR. Apatite is present in the NR with a similar texture and abundance to the SR. Zircon is also present as a trace phase, and texturally is the same as in the SR (Fig. 10G).

2.5.4 Alteration mineral assemblages

A summary of observations of secondary mineralogy in the GR is presented in Table 1 where grain size, shape, habit, and associated relevant observations are noted. In the following section details pertaining to the nature of the alteration are summarized.

South Range

The SR GR is characterized by the assemblage biotite-epidote-titanite with lesser muscovite-stilpnomelane-chlorite; trace ferrotschermakite and calcite also occur. Pits in plagioclase are lined with a variety of secondary minerals that include epidote, muscovite, and chlorite with baddeleyite, uraninite, and galena. K-feldspar is also pitted (Fig. 6B), but to a lesser degree, and the pits have fewer phases including epidote and rarely biotite and contain abundant L-V aqueous type fluid inclusions (Fig. 6D). Recrystallized quartz is common in the SR (Fig. 8A) and, along with granophyre-hosted quartz, contains abundant secondary fluid inclusions (Fig.

8B). Quartz was examined using CL to determine if it experienced alteration, a texture not obvious using standard petrography. Representative CL images with accompanying back-scattered electron images (BSE; Fig. 8C-F) indicate the CL intensity of quartz re-equilibration varies from weakly (i.e., mottled texture; Fig. 8C, D) to strongly (Fig. 8E, F) altered.

Secondary biotite (5 modal %, Fig 12A) is present as aggregates (Fig. 12B) and is the most abundant and pervasive alteration phase throughout the SR GR. It exhibits a brown pleochroism, is occasionally rimmed by epidote (Fig. 12C), and is present along grain boundaries between plagioclase and granophyre. In some samples biotite exhibits a weak to strong foliation (Fig. 12A). These samples contain little to no granophyre and this may be due to discontinuous shear zones. Biotite also occurs with ilmenite and titanite (Fig. 12D).

Epidote is a common alteration phase and is present as three varieties: (i) in pits in plagioclase (Fig. 5) and K-feldspar (Fig. 6B); (ii) as intergranular, subhedral to euhedral grains occurring within and around granophyre (Fig. 13A, B); and (iii) as veins (Fig. 13C). Epidote is noted to increase as metasomatic textures become more abundant. Allanite (0.5 to 1 mm), a LREE- rich epidote, is rare and, where observed, forms a core to an epidote rim (Fig. 13D). Chlorite is restricted to the bottom of the SR (two samples) and is often associated with or forms pseudomorphs of biotite (Fig. 14A, B). Ferrotschermakite is a rare phase and is only present as an alteration phase near the lower GR contact of SR (Fig. 11E). Muscovite is sparsely distributed and is discontinuous and more abundant at the top of the unit (less than 2 modal %; Fig. 10B). Primary ilmenite (Fig. 9A) is variably altered to titanite, hematite, and rutile (Fig. 9E). Where ilmenite is altered to titanite, the texture varies from titanite rims on ilmenite grains to complete

replacement of ilmenite by titanite (Fig. 9c), and these textures are often associated with biotite (Fig. 12D). Secondary titanite unrelated to ilmenite-titanite reactions is rare. Zircon is variably altered and typically exhibits a pitted texture with secondary phases such as thorite and galena observed in these pits (Fig. 10D-F). Carbonate occurs in only one sample where it is present as a replacement after plagioclase (Fig. 10C).

North Range

Alteration in the NR GR is characterized by an epidote-ferro-actinolite-stilpnomelane assemblage with varying amounts of chlorite. Similar to the SR, plagioclase is pitted (Fig. 5AB) and these pits are lined with ferro-actinolite, epidote, and lesser stilpnomelane and chlorite. The latter phases are more abundant than in the SR samples. K-feldspar is pitted, with epidote and ferro-actinolite hosted in the pits, and contains fluid inclusions. Epidote, the most common alteration product in the NR, is present as either medium-grained aggregates or in pitted areas of plagioclase and more rarely K-feldspar. A weak correlation exists between the abundance of epidote and the development of pitted plagioclase. Similar to the SR, allanite is rare.

Secondary ferro-actinolite in the NR is present as radiating aggregates and clearly overprints primary mineral phases (Fig. 11F). Chlorite is less abundant in the NR than in the SR and is present in clots, in late veins with epidote, as rims around plagioclase laths, along grain boundaries, or as a replacement of primary amphibole (Fig. 11C, D, G, H). Chlorite also occurs intergrown with other secondary phases such as carbonate, fibrous quartz and rarely thorite (Fig. 10H, I).

The re-equilibration of ilmenite to titanite is more consistent in the NR than the SR. Very rarely titanite is replaced by ilmenite (Fig. 9D). Ilmenite grains from the NR are subhedral to euhedral and replacement is controlled by partings (Fig. 9B, F, G), which is significantly different from the concentric replacement of ilmenite by titanite in the SR (Fig. 9C). Stilpnomelane is present as a late infilling phase, replacing hornblende, and intergrown with secondary ferro-actinolite and rarely chlorite (Fig. 19C). Similar to the SR, zircon has a pitted texture and contains secondary galena. (Fig. 10G). Carbonate is rare and was only seen in one sample (Fig. 14D).

2.5.5 Alteration index

An alteration index (AI) was assigned to each sample to assess its degree, extent and distribution of alteration in the NR and SR GR. A weighting system was designed using the following factors assigned to each of the alteration phases: (1) epidote, biotite, secondary amphibole, chlorite, stilpnomelane, and titanite were each given a weight of two; and (2) carbonate and muscovite were each given a weight of one. This weighting system was based on the pervasiveness and distribution of each phase. These weights were then multiplied by a factor between 1 and 3 based on modal abundances of less than 1% (1), between 1 and 5% (2), and greater than 5% (3). These values were then added to yield an AI for each sample. For example, a rock with biotite, epidote, titanite and carbonate each present as ≤1% would be given an AI of 7.

The results for the AI study are summarized in Figure 15 along with the location of shear zones in the SR (angled black lines) and the percentage of recrystallized quartz in the SR samples. As seen in this figure, the average AI is slightly higher in the SR versus the NR (10.8 and 8.6, respectively), but in each case there is large variability ($1\sigma = 4.2$ and 3.4, respectively).

2.5.6 Mineral chemistry

Mineral chemistry data are divided into primary and secondary phases based on the petrographic summary above. Here the term primary refers to magmatic phases produced by crystallization, and the term secondary refers to mineral phases produced by hydrothermal alteration or metamorphism. Qualitative mineral chemistry was determined by SEM-EDS analysis for plagioclase, alkali feldspar, ilmenite, and apatite and by EPMA for all other mineral phases. Data collected by EPMA is summarized in Tables 2 to 7.

South Range magmatic phases

Plagioclase grains analyzed in six samples (n=91) have a uniform chemistry of An_9Ab_{91} to An_0Ab_{100} except for a small portion (~5 %) in two samples with compositions of $An_{23}Ab_{77}$ to $An_{15}Ab_{85}$. As noted above, alkali feldspar is texturally uniform based on petrographic and SEM-BSE imaging. It has little to no perthite, and point and raster analyses for five samples (n=56) through the SR GR indicate that it is chemically uniform ($Or_{97}Ab_3$ to Or_{100}).

Ilmenite chemistry was determined by both point analysis for texturally uniform grains and by raster analysis for texturally complex grains on a total of five samples (n=21). The following chemistry is noted: 29.6 to 33.5 wt. % Ti, 28.8 to 31.6 wt. % Fe, 2.9 to 4.0 wt. % Mn, and 0.5 to 1.6 wt. % Ca.

Apatite from six samples (n=32) has a uniform chemistry that is near stoichiometric with 36.4 wt. % Ca and 19.2 wt. % P with Na, Si and Fe below the detection limit of 0.1 wt. %. Apatite is enriched in F (averaging 4.9 wt. %).

North Range magmatic phases

Plagioclase grains in six samples (n=76) through the NR GR have a uniform chemistry of An_6Ab_{94} to An_0Ab_{100}. K-feldspar with a uniform texture and lacking perthite was analyzed in six samples (n=72) and is chemically uniform with a composition of $Or_{97}Ab_3$ to $Or_{100}Ab_0$.

Mineral chemistry data for texturally early amphibole are scattered (Fig. 16A) due to variable degrees of chloritization, and this is reflected by a trend towards lower Si (a.p.f.u.) and Fe# on the classification diagram for monoclinic amphiboles (Leake et al. 1997; Fig. 16A). In order to address this issue, primary amphibole grains with the least amount of visible alteration were selected for analysis, and of these analyses, the five that plot at the upper end of the chloritization trend on the amphibole classification diagram were identified as being most representative of the least altered values. The mineral chemistry of least altered primary hornblende indicates that it is magnesiohornblende, but it plots close to the boundary between ferro- and magnesiohornblende.

Ilmenite from five samples (n=38) was analyzed using point and raster analyses as for the south range and the data indicate the following chemistry: 26.6 to 33.0 wt. % Ti, 27.8 to 36.8 wt. % Fe, 1.3 to 3.7 wt. % Mn.

Results for analyses of apatite in six samples (n=37) are similar to the SR, with a uniform stoichiometric chemistry and other elements such as Na, Si, and Fe falling below detection limit (0.1 wt. %). Apatite in the NR is also enriched in F (averaging 4.8 wt. %).

South and North Range secondary phases

Epidote is texturally divided into three styles: (i) pervasive blocky; (ii) pit-filling; and (iii) as a vein, with all three textures occurring in both ranges. Blocky epidote was analyzed in eight samples (SR = 3; NR = 5), pit-filling epidote was analyzed in five samples (SR = 4; NR = 1), and representative vein style epidote was analyzed in one sample in the NR (Fig. 16B; Table 3). Results for pit-filling and blocky epidote in the SR exhibit some scatter with respect to FeO (8.2 to 13.2 and 8.6 to 15.2 wt. %, respectively) and very little scatter in CaO values (21.6 to 23.8 and 22.9 to 23.6 wt. %, respectively) with the exception of one outlier, whereas in the NR these epidote textures exhibit slightly less scatter than the SR with respect to FeO (12.8 to 13.8 and 11.8 to 16.3 wt. %, respectively) and more significant scatter in CaO values (22.0 to 23.0 and 21.6 to 23.6 wt. %, respectively). Results for vein style epidote indicate that it contains less CaO than the majority of analyses for pit-filling and blocky epidote and exhibits some scatter with respect to CaO (22.0 to 22.8 wt. %) and FeO (13.7 to 15.4 wt. %).

Petrographic analysis of secondary amphibole in the NR and SR suggests that it is distinctly different in each range and this is confirmed by the mineral chemistry from two samples in the NR and one sample in the SR (Fig. 16A; Table 2). In the NR, chemical analyses of secondary amphibole indicate that it is ferro-actinolite, whereas in the SR secondary amphibole is ferrotschermakite. This indicates that, although the amphibole species in both ranges are similar with respect to Fe#, the Si (a.p.f.u.) values, and by corollary Al contents, are distinctly different. The Fe# of secondary amphibole that has replaced the least altered amphibole (0.51 to 0.74) and secondary, acicular amphibole (0.54 to 0.70) in the NR, and of ferrotschermakite (0.69 to 0.73) in the SR, is notable because it is higher than the Fe# of least altered amphibole (0.40 to 0.48).

In the SR, chlorite analyses were performed on individual grains (six samples) and vein-hosted chlorite (one sample), whereas in the NR individual grains of chlorite and chlorite replacement of primary amphibole were analyzed (four samples; Table 4). All analyses for both ranges plot as pseudothuringite on the chlorite classification diagram (Fig. 17A). There is limited scatter within each of the two ranges, with the NR data plotting as a continuous scatter and the SR data plotting as two distinct clusters. The cluster of SR data with the higher Fe# is from the middle of the unit, whereas the cluster with the lower Fe# is from the bottom and top of the unit.

Stilpnomelane is present in both the NR and SR and five samples containing representative stilpnomelane were analyzed in the NR (Table 5). Semi-qualitative data collected by SEM for stilpnomelane in the SR indicates that the mineral chemistry is very similar for both ranges and the microprobe analyses in the NR are therefore also likely representative of the SR. The EPMA results for stilpnomelane indicate that is has an average Fe# of 0.87 and the chemistry of stilpnomelane is consistent from the bottom to the top of the GR.

In the NR, titanite is present as a fracture controlled replacement of ilmenite, and in the SR titanite occurs as rims surrounding individual grains of ilmenite. Both of these textural variations were analyzed for three samples from each range (Table 6), and the data indicate that the chemistry of titanite varies between the NR and SR. The FeO content of titanite in the NR has a range of 1.10 to 4.96 wt. %, which is higher than the SR titanite, with a range of 0.46 to 0.69 wt. %. Titanite in the SR has higher TiO_2 and CaO contents (36.1 to 37.4 and 28.02 to 29.26 wt. %, respectively) than NR titanite (26.37 to 35.82 and 27.83 to 28.68 wt. %, respectively).

Biotite is only present in the SR and was analyzed in six samples (Table 7). The average Fe# for each samples ranges from 0.69 to 0.85, indicating that the composition of biotite is closer to the annite-siderophyllite solid solution series (Fig. 17B). Similarly to chlorite, biotite exhibits higher Fe# in the middle of the unit (average Fe# 0.79 to 0.85) than in the bottom and top (average Fe# 0.69 to 0.74).

2.5.7 Whole rock geochemistry

The results of 20 analyses of the GR for the NR (n=9) and SR (n=11) are presented in Table 8 and selected elements and elemental ratios are plotted in Figures 18 and 19. The samples show a similar chemistry except for three samples (indicated outlier samples) from the bottom part of the SR that are depleted in SiO_2(55.7 to 60.8 wt. %) and enriched in Al_2O_3 (13.6 to 17.4 wt. %), Fe_2O_3 (8.8 to 9.7 wt. %), FeO (6.1 to 7 wt. %), MgO (1.9 to 2.3 wt. %), and CaO (0.7 to 4.3 wt. %) compared to the other GR samples. With the exception of the three outliers, the samples have a typical granite chemistry with ~67.5 to 73.5 wt. %SiO_2 and, as expected based on their point-count QAP plot, fall in the field for granites (Fig. 19A). More specifically in terms of these data, it is noted that the SR exhibits greater variation than the NR in FeO_{total} (6.96 to 15.74 and 8.62 to 11.71wt. %, respectively), TiO_2 (0.42 to 1.83 and 0.69 to 0.97 wt. % respectively), and CaO (0.23 to 4.35 and 0.92 to 3.0 wt. % respectively). Both the SR and NR have low concentrations of MnO (0.05 to 0.14 and 0.06 to 0.1 wt. % respectively). The NR has higher LOI than the SR (1.27 to 2.45 and 0.69 to 1.63 wt. %, respectively). In contrast MgO is similar in both units with respect to concentration and variation (SR=0.27 to 2.27; NR=0.48 to 2.21 wt. %).

Trace element data are shown in Table 8 and a subset of these data that were also analyzed in other studies (i.e., Lightfoot et al. 1997; Therriault et al. 2002) is presented in Figure 20. These data have been divided into rare earth elements (REE; Fig. 20A) and additional trace elements (Fig. 20B). Data for GR samples are shown as fields representing the minimum and maximum values. There are minimal variations in all trace element chemistry between the NR and SR. The trace element and REE values for the three SR outlier samples described above are similar to all GR samples.

Chondrite-normalized REE patterns (Fig. 20A) show LREE (light rare earth elements; La, Ce, Pr, Nd, Sm, Eu, and Gd) enrichment($(La/Yb)_N$ = 8.5 to 15.3 in SR and 8.8 to 17.8 in NR) with a uniform decrease from the LREE to HREE (heavy rare earth elements; Tb, Dy, Ho, Er, Tm, Yb, Lu, and Y). Most samples exhibit a negative Eu anomaly (*Eu = 0.55 to 1.14 in SR and 0.44 to 0.85 in NR) with two samples from the SR exhibiting a positive anomaly (GNa-21 and GNa-52). Overall the NR GR exhibits more consistent REE patterns. Total REE concentrations range from 150 to 298 ppm in the SR and 141 to 286 ppm in the NR.

Additional trace element data are plotted on a primitive mantle-normalized diagram (Fig. 20B) and these data are summarized in Table 8. The outlier samples in the SR are enriched in Rb, Sc, V, and Co and depleted in Sr and Ba compared to the other SR samples. The NR data show an increase in V and Co in samples from the upper half of the unit; however, overall trace element data from the NR and SR are similar. Primitive mantle-normalized patterns for the NR and SR are similar (Fig. 20B) and exhibit negative Cs, Nb, Ta, Sr, and Y and positive Pb anomalies.

2.6 Discussion

Evidence for hydrothermal circulation has been described in the Onaping Formation (Ames et al. 1998, Ames et al. 2006, Campos-Alvarez et al. 2010) and in the footwall to the SIC (Farrow and Watkinson 1992; Farrow 1994; Farrow and Watkinson 1996; Marshall et al. 1999; Molnár et al. 2001; Hanley and Mungall 2003; Péntek et al. 2013; Tuba et al. 2014), but only rarely in the SIC (Campos-Alvarez et al. 2010; Tuba et al. 2010) and GR proper. A large zone of hydrothermal-related alteration in the Onaping Formation (Ames et al. 2006) overlying the SIC suggests that the cooling SIC itself created a hydrothermal system. The model proposed and discussed below for the formation and alteration of the GR, which is suggested to be similar to that developed in high-level intrusive settings, is supported by the presence of pervasive alteration and associated alteration assemblages (e.g., saussuritized plagioclase), the Fe-rich nature of most of the secondary mineral phases, the textural and chemical re-equilibration of feldspar, amphibole, and ilmenite phases, formation of secondary accessory phases (e.g., baddeleyite, thorite, uraninite in zircon), and abundance of secondary fluid inclusions in feldspars and quartz. The development and implications of this alteration, the source of the altering fluid, and comparison between the GR and similar environments are discussed.

2.6.1 Magmatic characteristics of the granophyre unit

The results of this detailed petrological study of the NR and SR GR show that these units have contrasting features and each is internally heterogeneous. Modal mineralogical data derived from point counting of the primary phases (plagioclase, K-feldspar, quartz) plot in the granite field using the QAP diagram (Fig. 19A) but are scattered within the field. The most significant differences between the two units include their different primary modal mineralogy variation in

both the volume % and grain size of granophyre. These differences can be explained by variations in the volatile content and resulting P_{H2O} between the melts in the two ranges and this is explained in detail below.

There are three important differences in the primary modal mineralogy of the GR between the two ranges: (i) the presence of primary amphibole in the NR and absence of primary amphibole in the SR; (ii) a greater modal abundance of quartz in the SR than in the NR; and (iii) a greater modal abundance of plagioclase in the NR than in the SR. In spite of these differences, the chondrite-normalized REE patterns for the two ranges are nearly identical, suggesting that the two ranges were derived either from two melts with very similar compositions or from the same melt. This is further supported by similar ratios of immobile trace elements between the two ranges (e.g., Zr/TiO_2; Fig. 19F). This similarity in whole rock geochemical data negates the potential effects of the viscous emulsion model of Zieg and Marsh (2005), which suggested that the primary impact melt sheet produced a heterogeneous distribution of liquids corresponding to the spectrum of the surrounding target lithologies. This model would also require that the SR have a more mafic character than the NR because of the mafic-rich footwall units in the SR (Elsie Mountain and Stobie formations and Nipissing mafic intrusives), but instead the NR appears to have a greater primary mafic component than the SR. Therefore, the data from this study suggest that the GR melt had a more homogenous character and the mineralogical differences must be the product of variable melt conditions rather than compositions.

The modal mineralogy during granitoid formation changes in response to changes in P_{total}, P_{H2O}, and a_{H2O} in a magma at a given time during crystallization (Morgan and London 2012). In

general, a decrease in P_{Total} and P_{H2O} during melt evolution will move the alkali feldspar-quartz cotectic towards quartz in the hydrous haplogranite (Ab-Or-Qtz-H_2O) system (Nekvasil 1988), thereby crystallizing a greater proportion of quartz. An increase in a_{H2O} during crystallization will result in a greater proportion of plagioclase to alkali feldspar (Lowenstern et al. 1997). Therefore, the differences in quartz and feldspar content between the NR and SR GR may be the product of variations in P_{total}, P_{H2O}, and a_{H2O}. The GR is assumed to have remained at constant depth, and therefore constant P_{total}, during crystallization, and the effects of differences in P_{total} between the two ranges would have been negligible to non-existent. At constant P_{total} an increase in a_{H2O} corresponds to an increase in the H_2O content of the melt (Nekvasil 1988). Given the greater proportion of plagioclase in the NR than in the SR, it is therefore possible that the NR melt contained a greater concentration of H_2O during crystallization. This would also correspond to a greater P_{H2O} in the NR, resulting in a lower modal abundance of quartz in the NR than in the SR. Variations in the H_2O content between the two ranges during crystallization may also explain the absence of primary hornblende in the SR, as it is a hydrous mineral and more likely to crystallize where there is a greater concentration of H_2O.

A variation in the volatile content of the melt between the NR and SR GR is further supported by the variations in the volume % and grain size of granophyre. Granophyre forms by rapid simultaneous crystallization of quartz and alkali feldspar (Barker 1970) and is usually the result of magmatic undercooling (e.g., Lowenstern et al. 1997; Morgan and London 2012). This can be achieved in several ways, the most common of which are intrusion of felsic magma into shallow upper crust to cause isothermal depressurization and associated degassing (Lowenstern et al. 1997; Morgan and London 2012) and adiabatic cooling by outgassing of magmatic volatiles.

Isothermal depressurization cannot account for the formation of granophyre in the GR because it is assumed to have remained at constant pressure during crystallization. There is evidence for volatile saturation and exsolution in the GR during its crystallization given the presence of miarolitic cavities and bubble trains, the latter representing the coalescence of the former. It is therefore possible that adiabatic cooling by outgassing of volatiles contributed to magmatic undercooling and the resulting granophyre formation in the GR. Additionally, although the miarolitic cavities and bubble trains are rare in the GR and, where present, constitute a very small volume percent of exposed outcrop, they are generally concentrated towards the centre of the unit (Fig. 2), which supports the idea of top-downward and bottom-upward crystallization (Zieg and Marsh 2005). This process of crystallization would have enhanced magmatic undercooling through cyclical volatile saturation and release. As the melt crystallized, the restite would have become saturated in volatiles, thereby increasing the solidus temperature and promoting magmatic undercooling. Volatile saturation of this restite led to volatile release and the production of the observed miarolitic cavities. Continued crystallization returned the system to saturated conditions, again increasing the solidus temperature and maintaining the cycle. Candela (1991) also proposed that a connectivity of magmatic volatile phases in such crystallizing intervals might promote additional flow of magmatic volatile phases near the crystallizing front. The bubble trains may reflect such an interconnectivity of magmatic volatiles, thus allowing for volatile migration and enhancement of local melt undercooling. The formation of miarole connectivity is favoured in systems with high initial water content and lower pressures features (Candela and Blevin 1995), which likely applied to the crystallizing GR. Therefore, magmatic volatile exsolution is likely the most important mechanism to drive magmatic undercooling and produce granophyre in the GR. Given that the NR contains a greater volume %

of granophyre, it follows that there was a greater degree of volatile exsolution, and thus a greater P_{H2O} and a_{H2O}, in the NR than in the SR.

2.6.2 Mass balance calculations and implications

In order to assess the chemical changes induced by hydrothermal alteration in the GR and the chemistry of the fluid(s) responsible for this alteration, mass balance calculations are required. Given the uncertainty in the composition of the least altered precursor to the SR GR due to the ambiguous origin of biotite, the mass balance calculations can only confidently be applied to the NR GR. Given that the whole rock geochemical data for the two ranges are very similar, it is likely that post-crystallization processes for the two ranges were also similar, and the mass balance calculations for the NR GR are therefore inferred to broadly reflect the SR GR as well. It is not possible to sample a least altered precursor to the altered GR due to the pervasive nature of the alteration observed throughout the unit, and the least altered composition must therefore be calculated using the mineral chemistry of the primary phases. Two important assumptions must be made for these calculations. First, although the mineral chemistry has been altered throughout the GR, the primary relative proportions of quartz, feldspar, and primary amphibole have been preserved. Second, the initial feldspar compositions in the GR can be determined by using estimates of the crystallization temperature of the GR from Darling et al. (2009; 700° to 750°C) in conjunction with two-feldspar thermometry (Fuhrman and Lindsley 1988). Texturally primary hornblende is incorporated into the mass balance calculations using EPMA data collected from grains that show little to no evidence of re-equilibration. Apatite and ilmenite are also texturally primary and trace amounts of these minerals are incorporated into the calculations. The modal abundances of quartz, plagioclase, alkali feldspar, hornblende, apatite, and ilmenite are then

normalized to 100% in order to calculate the least altered whole rock composition of the NR GR. Three samples were selected for mass balance calculations from the bottom (GNb-8), middle (GNb-35), and top (GNb-50) of the NR GR. These samples were selected due to their low modal abundances of secondary minerals, minimizing any error that may arise by normalizing the abundances of the primary phases to 100%.

Mass balance calculations were applied for the major elements using the MacLean method (1990) and the results of these calculations are summarized in Table 9. There are no apparent differences between the bottom, middle, and top of the unit. Most of the elements are conservative and the calculated mass changes are negligible; however, there are notable mass gains in SiO_2 and FeO (Fig. 21). This indicates that an external source of SiO_2 and FeO was necessary to produce the alteration mineral assemblage observed in the GR. This addition of FeO is also reflected by high Fe# in biotite (0.69 to 0.85) in the SR and secondary ferro-actinolite (0.51 to 0.74) in the NR.

A plausible explanation for this Fe enrichment is that the hydrothermal cell was vertically extensive through the SIC, allowing for interaction with the overlying Onaping Formation and/or the underlying quartz gabbro or norite units to provide a source of Fe. The Onaping Formation, the bulk composition of which has 5.07 to 6.32 wt. % FeO (Ames et al. 2002), is a more plausible source of Fe given that incurring would have interacted with it as part of the developing convective hydrothermal cell related to the cooling SIC. Evidence for the effects of hydrothermal circulation throughout the entire Onaping Formation is present as alteration minerals that are pseudomorphs of glass fragments, matrix replacement, and alteration of local lithic fragments

(Ames et al. 2002). It is suggested that fluid-rock interaction resulting from this alteration could have therefore incorporated Fe into the hydrothermal fluid.

The mass balance calculations also have implications for feldspar alteration in the GR. The K-feldspar in the GR presently has a composition of Or_{100} but in the least altered precursor GR its composition is inferred to have been Or_{70}. In order for alkali feldspar to be altered to end-member orthoclase, K must replace Na in the crystal structure. If this were the process by which Or_{70} was altered to Or_{100} in the GR, it would be reflected by a mass gain in K_2O because there are no primary mineral phases present in the GR that could have provided an internal source of K_2O. Instead, there are negligible changes in K_2O between the least altered and altered GR, indicating that Na was removed from the alkali feldspars and was not replaced by K. This process would require that the alkali feldspars undergo a mass loss, and this is reflected by the pitted texture of the alkali feldspars throughout the GR. This reaction would therefore have added Na, Al, Si, and O to the altering hydrothermal fluid. The addition of Na to the fluid is especially relevant for forming albitic plagioclase, which presently has a composition of An_0 and had an initial composition of An_{30}. This compositional change indicates that Na replaced Ca in the crystal structure, but again the mass balance calculations indicate negligible changes in Na_2O. It is therefore likely that the Na removed from alkali feldspar was added to plagioclase, which in turn lost Ca to the altering fluids. This Ca was incorporated into epidote (NR and SR) and ferro-actinolite (NR only) and some was removed from the rock altogether, as the mass balance calculations indicate either negligible changes or losses in CaO.

2.6.3 Textural and mineral-chemical evolution of the granophyre unit

This study provides textural and mineral-chemical evidence to suggest that the GR has experienced a history of metasomatism. The effect of this has been to drastically modify both the texture and chemistry of the majority of the rock as reflected by the chemistry of the feldspar (60 to 70 modal %), amphibole, and oxide phases and by the development of secondary minerals (e.g., ferro-actinolite, biotite). Variations in the CL signature of quartz are also attributed to this alteration and are likely due to modifications of its trace element composition, as has been documented in other systems (e.g., Rusk et al. 2006; Allan and Yardley 2007). Thus the only primary feature of the GR that has survived this protracted history of metasomatism is the granophyre itself. The processes whereby such transformation occurs have been studied in a variety of environments, including both natural (Harlov and Forster 2002; Geisler et al. 2003; Plumper and Putnis 2009; Morad et al. 2010) and laboratory (Putnis et al. 2007a, 2007b; Hovelmann et al. 2010; Dunkel and Putnis 2014; Ruiz-Agudo et al. 2015) settings. These studies have focused on feldspar phases due to their highly favourable reactivity with hydrothermal fluids, providing a record of the development of metasomatism. Discussed below is the transformation of the original GR as reflected by the textures noted above and the mineral chemical data presented.

As outlined in the mass balance section above, metasomatism of the GR resulted in alteration of primary plagioclase from An_{30} to An_0 and primary alkali feldspar from Or_{70} to Or_{100}. Etched and stained NR and SR GR samples indicate that this chemical change is uniform throughout all feldspar grains. It is not possible that these end member feldspar compositions represent primary values based on the crystallization temperature of the GR (700° to 750°C; Darling et al. 2009)

used in conjunction with ternary feldspar modelling (Fuhrman and Lindsley 1988). Therefore, the uniform chemical changes reflected by plagioclase and alkali feldspar must be the product of pervasive metasomatism. This is further supported by the pitted texture in both feldspars, indicating that they were equilibrated with the altering fluid(s), and this reaction resulted in mass loss. The process of uniform plagioclase re-equilibration to endmember albite has been documented in other systems where it has been attributed to CDP reactions (Engvik et al. 2008). CDP reactions result in the wholesale dissolution of a parent mineral followed by precipitation of a more stable phase on an atomic monolayer scale (Putnis 2002). These reactions commonly produce pit-textured pseudomorphs due to the mass change associated with the mineral replacement and the porosity created enhances fluid infiltration to facilitate further CDP reactions (Plumper and Putnis 2009). It is therefore possible that CDP reactions were responsible for the alteration of An_{30} to An_0 in the GR. Coupled dissolution-precipitation reactions have also been suggested for K-feldspar in other systems (e.g., Nishimoto and Yoshida 2010; Schepers and Milsch 2013), and, given the pitted texture and uniform chemistry of altered alkali feldspar in the GR, it is possible that these reactions also altered Or_{70} to Or_{100}. Furthermore, primary zircon exhibits a pitted texture, which has been attributed in other systems to CDP reactions (e.g., Geisler et al. 2003, Geisler et al. 2007), and ilmenite exhibits complex replacement textures of titanite, hematite, and rutile that cannot be attributed to oxidation and have been experimentally related to CDP reactions (Putnis et al. 2007b).

The alteration of plagioclase and alkali feldspar to endmember albite and orthoclase involved a loss of Ca and Na, respectively, to the altering fluid. The implications of this alteration with respect to the mass balance calculations and feldspar compositions were described in the mass

balance section above. This process also has implications for the formation of several Ca-bearing secondary minerals, including epidote, ferro-actinolite (NR only), and ferrotschermakite (SR only), as a source of Ca was required for their formation. Zircon also provides evidence for interaction with a fluid as it has rims characterized by pits that are typically lined by secondary baddeleyite, thorite, galena, and uraninite. The formation of baddeleyite is unexpected for the GR given its Si-rich nature; however, it has been noted that in the presence of a Ca-rich fluid its formation is favoured over that of zircon (Harlov and Dunkley 2011; Harlov et al. 2014). Replacement of primary ilmenite by titanite and to a lesser extent hematite and rutile is also indicative of interaction with a Ca-bearing fluid. Some ilmenite in the SR exhibits titanite rims that appear to be reaction rims or coronas and these are associated with the presence of biotite. This suggests that the formation of titanite in the SR may involve the interaction of biotite with ilmenite in the presence of a Ca-rich hydrothermal fluid. It is also possible that these titanite reaction rims may be associated with metamorphism and represent a very late stage in the history of the GR, as they are the last phase to form in the paragenesis of the SR GR (Fig. 7). Similar ilmenite-titanite-biotite textures have been documented in amphibolite facies metamorphic rocks where they are attributed to metamorphism (Harlov et al. 2006).

Mass balance calculations for the GR indicate that post-crystallization processes resulted in a gain of Fe and therefore an external source of Fe is required. This is further supported by the presence of Fe-bearing secondary mineral phases with high Fe#, these being chlorite, epidote, stilpnomelane, and biotite. The chemistry of epidote is notable because it occupies two apparent positions in the paragenesis of the GR, the first being as early saussuritization of plagioclase and the second being as later void space filling around grain boundaries. The chemistry of these two

styles of epidote is very similar in spite of the differences in timing of formation (Fig. 16B). There are two possible explanations for the similar chemistry: (i) the fluid was enriched in Fe early in the alteration history of the GR; or (ii) epidote currently observed in the GR represents a replacement of an earlier-formed mineral. It is not possible to determine which of these options is more plausible given the available data. There is also a clear distinction in Fe# for epidote between the NR and SR, with the NR epidote having a higher Fe#, and this may be indicative of a heterogeneous fluid composition.

Although it is not possible to track alteration-induced trace element changes in quartz, its CL signature indicates that it has equilibrated with a fluid. Magmatic quartz typically produces a uniform signature or showing concentric growth zones (Vasyukova et al. 2013), whereas the CL signature of quartz throughout the GR is not uniform and is either dark or exhibits strong fluctuations between bright and dark signatures. Variations in the CL signature of quartz have been attributed to variations in its trace element composition resulting from substitutions of Al^{3+}, Ti^{4+}, Fe^{3+}, Ge^{4+}, or P^{5+} for Si^{4+} (Gotze et al. 2001), and it is possible that this is also the case in the GR. The CL images reveal microfractures throughout quartz that were not easily identifiable by standard microscopy (Fig. 8F), with the areas along these microfractures having dark CL signatures and the areas absent of microfracturing having bright CL signatures (Fig. 8D). This relationship suggests that fluid infiltration along these microfractures altered the trace element signature of quartz and the resulting CL signature.

Muscovite is present in the NR and SR as saussuritization of plagioclase, and biotite is present in the SR. The formation of these phyllosilicate minerals would have required an internally derived

source of K based on the mass balance calculations. The only possible source for K is alkali feldspar, as there are no other significant primary sources of K in the GR. It is therefore likely that reaction of K-feldspar from Or_{70} to Or_{100} also resulted in a loss of K to the altering fluid.

The origin of biotite is of particular interest as it dominates the SR secondary mineral assemblage and is absent in the NR. A variation in the metamorphic and deformation history between the NR and SR has been well documented (Peredery and Morrison 1984; Rousell 1984), and this may provide the best explanation for the difference in biotite content between the two ranges. In the SR, biotite represents a late stage in the mineral paragenesis, does not appear to be the product of replacement reactions, and there is no clear evidence that it has a hydrothermal origin. Biotite defines a foliation in some samples, indicating that it is associated with later deformation superimposed on the SR GR. However, domains containing foliated biotite are discontinuous and are less abundant than unfoliated biotite. Furthermore, biotite exhibits textural relationships with alteration minerals of hydrothermal origin in some samples (i.e., chlorite, ferrotschermakite, epidote), but it typically appears to be overprinting these minerals. It is therefore not possible to unequivocally demonstrate that the biotite in the SR GR has a metamorphic rather than hydrothermal origin and its origin remains ambiguous.

2.6.4 Comparison to current models for the Sudbury Igneous Complex

In general, three models of formation have been proposed for the igneous history of the SIC: (i) crystal fractionation and settling (Naldrett and Hewins 1984); (ii) multiple influxes of magma whereby the felsic norite and GR melts were derived from different sources (Chai and Eckstrand 1994); and (iii) crystallization of a compositionally zoned magma with two or more layers, or in

situ crystallization of a density-stratified melt (Golightly 1994; Marsh and Zieg 1999). In the latter model it is suggested that the transition zone gabbro was the last phase to crystallize and that the norite crystallized from the base-upwards and the GR from the top-downwards.

The data from this study agree with the third model and the hypothesis that the GR crystallized from the top-downward and originated as part of a single homogeneous magma. This conclusion is supported by the increased abundance of miarolitic cavities and bubble trains toward the centre of the GR, indicating that fluids and/or volatiles accumulated towards the centre and crystallization was downward until volatile saturation was reached. Additionally, similar incompatible trace element ratios between the GR and transition zone gabbro and norite support the third model and eliminate the potential for the Chai and Eckstrand (1994) model that invokes multiple influxes of magma (Lightfoot et al.1997). The implication of similar trace element ratios in these units is that the melt sheet had to be homogenous prior to crystallization. This phenomenon, along with the lack of mafic target rocks in the NR and their abundance in the SR, contradicts the hypothesis that a mafic component and a lack of complete homogenization can account for the paucity of primary mafic minerals in the SR. While heterogeneous volatile distribution in the GR magma may account for the differences in volume % granophyre between the NR and SR (see *Magmatic characteristics of the granophyre unit*), it cannot account for the greater abundance of biotite and lesser abundance of amphibole in the SR as compared to the NR.

2.7 Conclusions

Results from this study demonstrate that the GR of the SIC has experienced pervasive metasomatism via fluid-induced re-equilibration that has not been sufficiently described in previous work. We provide evidence that the NR and SR are distinct with respect to volume proportion of primary mafic phases and granophyre and with respect to granophyre grain size, and these differences may be the result of a greater volatile content in the NR. The whole rock chemistry is similar for the NR and SR, suggesting that the two ranges underwent similar post-crystallization processes. The chemistry of texturally primary plagioclase and alkali feldspar indicates that the only primary component preserved in the GR is the granophyre itself, and pervasive metasomatism may have induced CDP reactions in the highly reactive feldspars. The textural and chemical evidence for metasomatism indicates an influx and circulation of a large volume of fluid that transported significant amounts of Ca from re-equilibrated plagioclase to form secondary minerals. The distinctly high Fe# in secondary Fe-bearing mineral phases cannot be accounted for by Fe-loss of primary phases within the GR. The fluid therefore must have interacted with either the overlying Onaping Formation or possibly the underlying quartz gabbro and norite units to derive an external source of Fe. This implies that the hydrothermal system responsible for the pervasive metasomatism was vertically extensive and may have been related to the ore deposit-forming hydrothermal fluids in the overlying Onaping Formation.

2.8 References

Allan, M. M. and Yardley, B. W. D. (2007): Tracking meteoric infiltration into a magmatic-hydrothermal system: A cathodoluminescence, oxygen isotope and trace element study of quartz from Mt. Leyshon, Australia. Chemical Geology 240, 343-360.

Ames, D. E., Watkinson, D. H. and Parrish, R. R.(1998): Dating of a regional hydrothermal system induced by the 1850 Ma Sudbury impact event. Geology 26, 447-450.

Ames, D. E. (1999): Geology and regional hydrothermal alteration of the crater-fill, Onaping formation: association with Zn-Pb-Cu mineralization, Sudbury Structure, Canada. Unpublished Ph.D. thesis Carleton University, Ottawa, Ontario, 460 p.

Ames, D. E., Golightly, J. P., Lightfoot, P. C., and Gibson, H. L. (2002): Vitric compositions in the Onaping formation and their relationship to the Sudbury Igneous Complex, Sudbury Structure. Economic Geology 97, 1541-1562.

Ames, D. E., Davidson, A., Buckle, J., and Card, K. D. (2005): Sudbury bedrock compilation; Geology. Geological Survey of Canada Open File 4570.

Ames, D. E., Jonasson, I. R., Gibson, H. L., and Pope, K. O. (2006): Impact-generated hydrothermal system – constraints from the large Paleoproterozoic Sudbury crater, Canada, in Biological processes associated with impact events, eds. C. Cockell, C. Koeberl, I. Gilmour: Springer.

Ames, D. E., and Farrow, C. E. G. (2007): Metallogeny of the Sudbury Mining Camp, Ontario, in Goodfellow, W. D., ed., Mineral Deposits of Canada: A Synthesis of Major Deposit-Types, District Metallogeny, the Evolution of Geological Provinces, and Exploration Methods. Geological Association of Canada, Mineral Deposits Division, Special Publication 5, 329-350.

Ames, D. E., Davidson, A., and Wodicka, N. (2008): Geology of the Giant Sudbury Polymetallic Mining Camp, Ontario, Canada. Economic Geology 103, 1057-1077.

Anders, D., Osinski, G. R., Grieve, R. A. F., and Brillinger, D. T. M. (2015): The Basal Onaping Intrusion in the North Range: Roof rocks of the Sudbury Igneous Complex. Meteoritics and Planetary Sciences 50, 1577-1594.

Augustithis, S. S. (1973): Atlas of the Textural Patterns of Granites, Gneisses and Associated Rock Types. Amsterdam: Elsevier, 378 p.

Bailey, E. H. and Stevens, R. E. (1960): Selective staining of K-feldspar and plagioclase on rock slabs and thin sections. American Mineralogist 45, 1020-1025.

Bailey, S. W. (ed.): Micas. Mineralogical Society of America, Reviews in Mineralogy 13, 357-456.

Barker, D. S. (1970): Compositions of granophyre, myrmekite, and graphic granite. Geological Society of America Bulletin 81, 3339-3350.

Bennett, G., Dressler, B. O., and Robertson, J. A. (1991): The Huronian Supergroup and associated intrusive rocks, in Geology of Ontario, eds. P.C. Thurston , H.R. Williams, R.H. Stucliffe, and G.M. Stott. Ontario Geological Survey 4, part 1, 549-591.

Bigot, L. and Jebrak, M. (2015): Gold mineralization at the syenite-hosted Beattie gold deposit, Duparquet, Neoarchean Abitibi Belt, Canada. Economic Geology 110, 315-335.

Block, K. A., Steiner, J. C., Puffer, J. H., Jones, K. M., and Goldstein, S. L. (2015): Evolution of late stage differentiates in the Palisades Sill, New York and New Jersey. Lithos 230, 121-132.

Boles, J. R. (1982): Active albitization of plagioclase, Gulf Coast Tertiary. American Journal of Science 282, 165-180.

Brocoum, S. T. and Dalziel, I. W. D.(1974): The Sudbury Basin, the Southern Province, the Grenville Front and the Penokean Orogen. Geological Society of America Bulletin 85, 1571-1580.

Brown, E. H. (1971): Phase relations of biotite and stilpnomelane in the greenschist facies. Contributions to Mineralogy and Petrology 31, 275-299.

Brown, W. L. and Parsons, I. (1981): Towards a more practical two-feldspar geothermometer. Contributions to Mineralogy and Petrology 76, 369-377.

Brown, W. L. and Parsons, I. (1985): Calorimetric and phase-diagram approaches to two-feldspar geothermometry: a critique. American Mineralogist 70, 356-361.

Boutroy, E., Dare, S. A. S., Beaudoin, G., Barnes, S.-J., and Lightfoot, P. C. (2014): Magnetite composition in Ni-Cu-PGE deposits worldwide: application to mineral exploration. Journal of Geochemical Exploration 145, 64-81.

Campos-Alvarez, N. O., Samson, I. M., Fryer, B. J., and Ames, D. E. (2010): Fluid sources and hydrothermal architecture of the Sudbury Structure: constraints from femtosecond LA-ICP-MS Sr isotopic analysis of hydrothermal epidote and calcite. Chemical Geology 278, 131-150.

Candela, P. A. (1991): Physics of aqueous phase evolution in plutonic environments. American Mineralogist 76, 1081-1091.

Candela, P. A., and Blevin, P. L. (1995): So some miarolitic granites preserve evidence of magmatic volatile phase permeability? Economic Geology 90, 2310-2316.

Card, K. D., Gupta, V. K., McGrath, P. H., and Grant, F. S.(1984): The Sudbury Structure: Its regional Geological and Geophysical Setting: The Geology and Ore Deposits of the Sudbury Structure. O.G.S. Special Volume 1, 25-44.

Chai, G. and Eckstrand, R. (1994): Rare-earth element characteristics and origin of the Sudbury Igneous Complex, Ontario, Canada. Chemical Geology 113, 221-244.

Coats, C. J. A. and Snajdr, P.(1984): Ore Deposits of the North Range, Onaping-Levack area, Sudbury, in The Geology and Mineral Deposits of the Sudbury Structure, eds. E. G. Pye, A. J. Naldrett, P. Giblin. Ontario Geological Survey, Special Publication 1, 328-346.

Darling, J., Storey, C., and Hawkesworth, C. (2009): Impact melt sheet zircons and their implications for the Hadean crust. Geology 37, 927-930.

Deer, W. A., Howie, R. A., and Zussman, J. (1966): An introduction to the rock-forming minerals. Longman, London, 528 p.

Dietz, R.S. (1960): Meteorite impact suggested by shatter cones in rock. Science 73, 1781-1784.

Dressler, B. O. (1984): General Geology of the Sudbury Area, in The Geology and Mineral Deposits of the Sudbury Structure, eds. E. G. Pye, A. J. Naldrett, P. Giblin, Ontario Geological Survey, Special Publication 1, 57-82.

Dunkel, K. G. and Putnis, A. (2014): Replacement and ion exchange reactions of scolecite in a high pH aqueous solution. European Journal of Mineralogy 26, 61-69.

Engvik, A. K., Putnis, A., Fitz, J. D., and Austrheim, H. (2008): Albitization of granitic rocks: the mechanism of replacement of oligoclase by albite. The Canadian Mineralogist 46, 1401-1415.

Erdenebayar, J., Ogata, T., Imai, A., and Sereenen, J. (2014): Textural and chemical evolution of unidirectional solidification textures in highly differentiated granitic rocks at Kharaatyagaan, Central Mongolia. Resource Geology 64, 283-300.

Farmer, J. D.(2000): Hydrothermal systems: Doorways to early biosphere evolution. GSA Today 10, 1-9.

Farrow, C. E. G. (1994): Geology, alteration, and the role of fluids in Cu-Ni-PGE mineralization of the footwall rocks to the Sudbury Igneous Complex, Levack and Morgan Townships, Sudbury District, Ontario. Unpublished Ph.D. thesis, Ottawa, Canada, Carleton University, 373.

Farrow, C. E.G. and Watkinson, D. H. (1992): Alteration and the role of fluids in Ni, Cu and platinum-group deposition, Sudbury Igneous Complex contact, Onaping-Levack area, Ontario. Mineralogy and Petrology 46, 67-83.

Farrow, C. E. G. and Watkinson, D. H. (1996): Geochemical evolution of the Epidote Zone, Fraser mine, Sudbury, Ontario: Ni-Cu-PGE remobilization by saline fluids. Exploration and Mining Geology 5, 17-31.

Farrow, C. E. G. and Watkinson, D. H. (1999): An evaluation of the role of fluids in Ni-Cu-PGE-bearing, mafic-ultramafic systems: dynamic processes in magmatic ore deposits and their application to mineral exploration. Geological Association of Canada Short Course Notes 13, 31-67.

Ferry, J. M. (1979): Reaction mechanisms, physical conditions and mass transfer during hydrothermal alteration of mica and feldspar in granitic rocks from south-central Maine, USA. Contributions to Mineralogy and Petrology 68, 125–139.

Fuhrman, M. L. and Lindsley, D. H. (1988): Ternary-feldspar modeling and thermometry. American Mineralogist 73, 201-215.

Geisler, Rashwan, A. A., Rahn, M. K. W., Poller, U., Zwingmann, H., Pidgeon, R. T., Schleicher, H., and Tomaschek, F.(2003): Low-temperature hydrothermal alteration of natural metamict zircons from the Eastern Desert, Egypt. Mineralogical Magazine 67, 485-508.

Geisler, Rashwan, Schaltegger, U., and Tomaschek, F.(2007): Re-equilibration of Zircon in Aqueous Fluids and Melts. Elements 3, 43-50.

Golightly, J. P. (1994): The Sudbury Igneous Complex as an Impact Melt: Evolution and Ore Genesis, in Proceedings of the Sudbury – Noril'sk Symposium. O.G.S. Special Volume 5, 105-117.

Godinho, J. R. A., Putnis, C. V., and Piazolo, S. (2014): Direct observations of the dissolution of fluorite surfaces with different orientations. Crystal Growth and Design 14, 69-77.

Gotze, J., Plotze, M., and Habermann, D. (2001): Origin, spectral characteristics and practical applications of the Cathodoluminescence (CL) of quartz – a review. Mineralogy and Petrology 71, 225-250.

Grieve, R. A. F., Stoffler, D., and Deutsch, A. (1991): The Sudbury Structure: Controversial or Misunderstood?. Journal of Geophysical Research 96, 753-764.

Hanley, J. J. and Mungall, J. E. (2003): Chlorine enrichment and hydrous alteration of the Sudbury breccia hosting footwall Cu-Ni-PGE mineralization at the Fraser mine, Sudbury, Ontario, Canada. The Canadian Mineralogist 41, 857-881.

Hanley, J. J. and Bray, C. J. (2009): The trace metal content of amphibole as a proximity indicator for Cu-Ni-PGE mineralization in the footwall of the Sudbury Igneous Complex, Ontario, Canada. Economic Geology 104, 113-125.

Harlov, D. E. and Forster, H.-J. (2002): High-grade fluid metasomatism on both a local and regional scale: the Seward Peninsula, Alaska, and the Val Strona di Omengna, Ivrea-Vrebano, Northern Italy. Part I: Petrography and silicate mineral chemistry. Journal of Petrology 43, 769-799.

Harlov, D. E. and Dunkley, D. J. (2011): Experimental high-grade alteration of zircon using alkali- and Ca-bearing solutions. Mineralogical Magazine 75, p. 980.

Harlov, D. E. (2012): The potential role of fluids during regional granulite-facies dehydration in the lower crust. Geoscience Frontiers 3, 813-827.

Harlov, D. E., Anczkiewicz, R., Lewerentz, A., Dunkley, D. J., and Schersten, A. (2014): Experimental alteration of zircon using alkali- and Ca-bearing solutions: Metasomatic resetting of the zircon geochronometer during high-grade metamorphism. GAC-MAC Meeting Fredericton 2014, 37, 113-114.

Hoffman, P. F.(1989): Precambrian geology and tectonic history of North America; in The geology of North America – An overview: eds. Bailey, A. W., and Palmer, A. R. Geological Society of America, Geology of North America, 447-512.

Hovelmann, J., Putnis, A., Geisler, T., Schmidt, B. C., and Golla-Schindler, U. (2010): The replacement of plagioclase feldspars by albite: observations from hydrothermal experiments. Contributions to Mineralogy and Petrology 159, 43-59.

Huber, M. S., McDonald, I., and Koeberl, C. (2014): Petrography and geochemistry of ejecta from the Sudbury impact event. Meteoritics and Planetary Science 49, 1749-1768.

Kontak, D. J. (1995): A study of feldspar phases in the high-silica, high-level Ackley granite, southeastern Newfoundland. The Canadian Mineralogist 33, 985-1010.

Kontak, D. J. and Martin, R. F. (1997): Alkali feldspar in the peraluminous South Mountain Batholith, Nova Scotia: trace-element data. The Canadian Mineralogist 35, 959-977.

Krough, T. E.(1994): Precise U-Pb ages for Grenvillian and pre-Grenvillian thrusting of Proterozoic and Archean metamorphic assemblages in the Grenville Front tectonic zone, Canada. Tectonics 13, 963-982.

Krough, T. E., Davis, D. W., and Corfu, F. (1984): Precise U-Pb Zircon and Baddeleyite Ages for the Sudbury Area, in The Geology and Mineral Deposits of the Sudbury Structure, eds. E. G. Pye, A. J. Naldrett, P. Giblin. Ontario Geological Survey, Special Publication 1, 431-446.

Lafrance, B., Legault, D., and Ames, D. E.(2008): The formation of the Sudbury breccia in the North Range of the Sudbury impact structure. Precambrian Research 165, 107-119.

Lee, M. R. and Parsons, I. (1997): Dislocation formation and albitization in alkali feldspars from the Shap granite. American Mineralogist 82, 557–570.

Leake, B. E., Woolley, A. R., Arps, C. E. S., Birch, W. D., Gilbert, M. C., Grice, J. D., Hawthorne, F. C., Kato, A., Kisch, H. J., Krivovichev, V. G., Linthout, K., Laird, J., Mandarino, J. A., Maresch, W. V., Nickel, E. H., Rock, N. M. S., Schumacher, J. C., Smith, D. C., Stephenson, N. C. N., Ungaretti, L., Whittaker, E. J. W., and Youzhi, G. (1997): Nomenclature of amphiboles: Report of the Subcommittee on Amphiboles of the International Mineralogical Association, Commission on New Minerals and Mineral Names. American Mineralogist 82, 1019-1037.

Li, X. and Zhou, M.-F. (2015): Multiple stages of hydrothermal REE remobilization recorded in fluorapatite in the Paleoproterozoic Yinachang Fe-Cu-(REE) deposit, Southwest China. Geochimica et Cosmochimica Acta 166, 53-73.

Lightfoot, P. C., Doherty, W., Farrell, K., Keays, R. R., Moore, M., and Pekeski, D. (1997): Geochemistry of the main mass, sublayer, offsets, and inclusions from the Sudbury Igneous Complex, Ontario. Ontario Geological Survey, Open File Report 5959, 231.

Lightfoot, P. C., Keays, R. R., and Doherty, W. (2001): Chemical evolution and origin of Nickel Sulfide Mineralization in the Sudbury Igneous Complex, Ontario, Canada. Economic Geology 96, 1855-1875.

Lightfoot, P. C. and Farrow, C. E. (2002): Geology, geochemistry and mineralogy of the Worthington Offset Dike: a genetic model for offset dike mineralization in the Sudbury Igneous Complex. Economic Geology 97, 1419-1446.

Lowenstern, J. B., Clynne, M. A., and Bullen, T. D. (1997): Comagmatic A-type granophyre and rhyolite from the Alid volcanic center, Eritrea, northeast Africa. Journal of Petrology 38, 1707-1721.

MacLean, W. H. (1990): Mass changes in altered rock series. Mineralium Deposita 25, 44-49.

MacMillan, E., Cook, N. J., Ciobanu, C. L., and Pring, A. (2016): Uraninite from the Olympic Dam IOCG-U-Ag deposit: Linking textural and compositional variation to temporal evolution. American Mineralogist 101, 1295-1320.

Marsh, B. D. and Zieg, M. J. (1999): Solidification fronts of the Sudbury melt sheet. Geological Association of Canada and Mineralogical Association of Canada, Field Trip Guidebook B9, 34.

Marshall, D. D., Watkinson, D. H., Farrow, C. E. G., Molnár, F., and Fouillac, A. M. (1999): Multiple fluid generations in the Sudbury Igneous Complex: fluid inclusions, Ar, O, H, Rb, and Sr evidence. Chemical Geology 154, 1-19.

McDonough, W. F. and Sun, S.-S. (1995): Composition of the Earth. Chemical Geology 120, 223-253.

McNamera, G. (2011): Lead isotope and trace element variations in the Sudbury Igneous Complex, Canada: Interplays between ores, overlying magmatic silicates, and underlying country rock lithologies. PhD Thesis, Laurentian University.

Milkereit, B. and Green, J. R. (1992): Deep geometry of the Sudbury Structure from seismic reflection profiling. Geology 20, 807-811.

Molnár, F., Watkinson, D. H., and Jones, P. C. (2001): Multiple hydrothermal processes in the footwall units of the North Range, Sudbury Igneous Complex, Canada, and implications for the genesis of vein-type Cu-Ni-PGE deposits. Economic Geology 96, 1645-1670.

Mora, C. I. and Valley, J. W. (1989): Halogen-rich scapolite and biotite: Implications for metamorphic fluid-rock interaction. American Mineralogist 74, 721-737.

Morad, S., El-Ghali, M. A. K., Caja, M. A., Sirat, M., Al-Ramadan, K., and Mansurbeg, H. (2010): Hydrothermal alteration of plagioclase in granitic rocks from Proterozoic basement of SE Sweden. Geological Journal 45, 105-116.

Morgan, B. M. IV and London, D. (2012): Process of granophyre crystallization in the Long Mountain Granite, southern Oklahoma. Geological Society of America Bulletin 124, 1251-1261.

Morrison, G. G., Jago, B. C., and White, T. L. (1994): Footwall mineralization of the Sudbury Igneous Complex, in: Lightfoot, P. C., Naldrett, A. J. (eds.) Proceedings of the Sudbury-Noril'sk symposium. Ontario Geological Survey Special Volume 5, 57-64.

Mungall, J. E., Ames, D. E., and Hanley, J. J.(2004): Crustal redistribution in large bolide impacts: geochemical evidence from the Sudbury Structure. Nature 6990, 546-548.

Mungall, J. E. and Hanley, J. J. (2004): Origins of outliers of the Huronian Supergroup within the Sudbury Structure. Journal of Geology 112, 59-70.

Murphy, A. J. and Spray, J. G. (2002): Geology, mineralization, and emplacement of the Whistle-Parkin Offset Dike, Sudbury. Economic Geology 97, 1399-1418.

Naumov, M. V. (2002): Impact-generated hydrothermal systems: Data from Popigai, Kara, and Puchezh-Katunki impact structures. In: Plado, J., and Pesonen, L. J. (Eds.), Impacts in Precambrian Shields. Springer-Verlag, Berlin, 117-171.

Naldrett, A. J., Bray, J. G., Gasparrini, E. L., Podolsky, T., and Rucklidge, J. C.(1970): Cryptic variation and the petrology of the Sudbury Nickel Irruptive. Economic Geology and Bulletin of the Society of Economic Geologists 65, 122-155.

Naldrett, A. J. (2004): Magmatic Sulfide Deposits: Geology, geochemistry and exploration. Spring Verlag, Heidelberg, Berlin, 728.

Naldrett, A. J. and Hewins, R. H. (1984): The Main Mass of the Sudbury Igneous Complex, in The Geology and Mineral Deposits of the Sudbury Structure, eds. E. G. Pye, A. J. Naldrett, P. Giblin. Ontario Geological Survey, Special Publication 1, 235-251.

Nekvasil, H. (1988): Calculated effect of anorthite component on the crystallization paths of H_2O-undersaturated haplogranite melts. American Mineralogist 73, 966-981.

Niedermeier, D. R. D., Putnis, A., Geisler, T., Golla-Schindler, U. and Putnis, C. V.(2009): The mechanism of cation and oxygen isotope exchange in alkali feldspars under hydrothermal conditions. Contributions to Mineralogy and Petrology 157, 65-76.

Nishimoto, S. and Yoshida, H. (2010): Hydrothermal alteration of deep fractured granite: Effects of dissolution and precipitation. Lithos 115, 153-162.

Osinski, G. R., Tornabene, L. L., Banerjee, N. R., Cockell, C. S., Flemming, R., Izawa, M. R. M., McCutcheon, J., Parnell, J., Preston, L. J., Pickersgill, A. E., Pontefract, A., Sapers, H.

M., and Southam, G. (2013): Impact-generated hydrothermal systems on Earth and Mars. Icarus 224, 347–363.

Parsapoor, A., Khalili, M., Tepley, F., and Maghami, M. (2015): Mineral chemistry and isotopic composition of magmatic, re-equilibrated and hydrothermal biotites from Darreh-Zar porphyry copper deposit, Kerman (Southeast of Iran). Ore Geology Reviews 66, 200-218.

Péntek, A., Molnár, F., Watkinson, D. H., and Jones, P. C. (2008):Footwall-type Cu-Ni-PGE mineralization in the Broken Hammer area, Wisner Township, North Range, Sudbury Structure. Economic Geology 103, 1005-1028.

Péntek, A., Molnár, F., Tuba, G., Watkinson, D. H., and Jones, P. C. (2013): The significance of partial melting processes in hydrothermal low sulfide Cu-Ni-PGE mineralization within the footwall of the Sudbury Igneous Complex, Ontario, Canada. Economic Geology 108, 59-78.

Peredery, W. V. and Morrison, G. G. (1984): Discussion of the Origin of the Sudbury Structure, in The Geology and Mineral Deposits of the Sudbury Structure, eds. E. G. Pye, A. J. Naldrett, P. Giblin. Ontario Geological Survey, Special Publication 1, 491-511.

Peredery, W. V. and Naldrett, A. (1975): Petrology of the Upper Irruptive Rocks, Sudbury, Ontario. Economic Geology 70, 164-175.

Pirajano, F. (2009): Hydrothermal Processes and Mineral systems. Springer-Science and Business Media B. V.

Plumper, O. and Putnis, A. (2009): The Complex Hydrothermal History of Granitic Rocks: Multiple Feldspar Replacement Reactions under Subsolidus Conditions. Journal of Petrology 50, 967-987.

Putnis, A. (2002): Mineral replacement reactions: from macroscopic observations to microscopic mechanisms. Mineralogical Magazine 66, 689-708.

Putnis, A. (2009): Mineral replacement reactions, in: Oelkers, E. H., J. (Eds.), Thermodynamics and kinetics of water-rock interaction. Review in Mineralogy and Geochemistry 30, 87-124.

Putnis, A. (2015): Transient porosity resulting from fluid-mineral interaction and its consequences. Reviews in Mineralogy and Geochemistry 80, 1-23.

Putnis, A., Heinrich, R., Putnis, C.V., Golla-Schindler, U., and Collins, L.G. (2007a): Hematite in porous red-clouded feldspars, evidence of large-scale crustal fluid-rock interaction. Lithos 95, 10–18.

Putnis, A., Janssen, T., and Putnis, C. V. (2007b): The mechanism of hydrothermal alteration of ilmenite. Geophysical Research Abstracts 9, 06889.

Putnis, A. and Putnis, C. V. (2007): The mechanism of reequilibration of solids in the presence of a fluid phase. Journal of Solid State Chemistry 180, 1783-1786.

Putnis, A. and John, T. (2010): Replacement Processes in the Earth's Crust. Elements 6, 159-164.

Reid, W. P. (1969): Mineral Staining Tests. Colorado School of Mines Industries Bulletin 12, 1-20.

Riller, U. and Schwerdtner, W. M. (1997): Mid-crustal deformation at the southern flank of the Sudbury Basin, central Ontario, Canada. Geological Society of America Special Bulletin 109, 841-854.

Rousell, D. H. (1984): Structural Geology of the Sudbury Basin, in The Geology and Mineral Deposits of the Sudbury Structure, eds. E. G. Pye, A. J. Naldrett, P. Giblin. Ontario Geological Survey, Special Publication 1, 83-95.

Ruiz-Agudo, E., Putnis, C. V., and Putnis, A. (2014): Coupled dissolution and precipitation at mineral-fluid interfaces. Chemical Geology 15, 132-146.

Ruiz-Agudo, E., Putnis, C. V., Hovelmann, J., Alvarez-Lloret, P., Ibanez-Velasco, A., and Putnis, A. (2015): Experimental study of the replacement of calcite by calcium sulphates. Geochimica et Cosmochimica Acta 156, 75-93.

Rusk, B. G., Reed, M. H., Dilles, J. H., and Kent, A. J. R. (2006): Intensity of quartz cathodoluminescence and trace-element content in quartz from the porphyry copper deposit at Butte, Montara. American Mineralogist 91, 1300-1312.

Sabbides, T., Giannimaras, E., and Koursoukos, P. G. (1992): The precipitation of calcium carbonate in artificial seawater and sustained supersaturation. Environmental Technology 13, 73-80.

Schepers, A. and Milsch, H. (2013): Dissolution-precipitation reactions in hydrothermal experiments with quartz-feldspar aggregates. Contributions to Mineralogy and Petrology 165, 83-101.

Seedorf, E., Dilles, J. H., Profess, J. M., Einaudi, M. T., Zurcher, L., Stavast, W. J. A., Johnson, D. A., and Barton, M. D. (2005): Porphyry deposits: characteristics and origin of hypogene features. Economic Geology 100th Anniversary Volume, 251-298.

Sims, P. K., Van Schmus, W. R., Schulz, K. J., and Peterman, Z. E. (1989): Tectonostratigraphic evolution of the Early Proterozoic Wisconsin magmatic terranes of the Penokean Orogen. Canadian Journal of Earth Sciences 26, 2145-2158.

Smith, J. V. (1974): Feldspar Minerals, Volume 12, Chemical and Textural Properties. New York: Springer-Verlag.

Spencer, K. J., Hacker, B. R., Kylander-Clark, A. R. C., Andersen, T. B., Cottle, J. M., Stearns, M. A., Poletti, J. E., and Seward, G. G. E. (2013): Campaign-style titanite U-Pb dating my laser-ablation ICP: Implications for crustal flow, phase transformations and titanite closure. Chemical Geology 341, 84-101.

Stewart, R. C. (2011): Halogen geochemistry of footwall breccia and associated units of the Main Mass of the Sudbury Igneous Complex, Ontario. Unpublished MSc Thesis, Saint Mary's University, 162 p.

Stevenson, J. S. (1961): Recognition of the quartzite breccia in the Whitewater Series, Sudbury. Transactions of the Royal Society of Canada 3rd Series 55, section 4, 57-65.

Stevenson, J. S. (1963): The upper contact phase of the Sudbury micropegmatite. The Canadian Mineralogist 7, 413-419.

Stockwell, C. H. (1982): Proposals for the time classification and correlation of Precambrian rocks and events in Canada and adjacent areas of the Canadian Shield. Geological Survey of Canada Paper 80-19, 135 p.

Streckeisen, A. (1974): Classification and nomenclature of plutonic rocks: Recommendations of the IUGS Subcommission on the Systematics of Igneous Rocks. Geologische Rundschau Internationale Zeitschrift für Geologie: Stuttgart 63, 773–785.

Swanson, S. E. (1977): Relation of nucleation and growth rate on the development of granitic texture. The American Mineralogist 62, 966-978.

Swanson, S. E. (1986): Quartz crystallization in igneous rocks. The American Mineralogist 71, 331-342.

Therriault, A. M. (2001):Petrogenesis of the Sudbury Igneous Complex: A Shocking Story. Unpublished PhD Thesis, University of Ottawa.

Therriault, A. M., Fowler, A. D., and Grieve, R. A. F.(2002): The Sudbury Igneous Complex: A Differentiated Impact Melt Sheet. Economic Geology 97, 1521-1540.

Tuba, G., Molnár, F., Watkinson, D. H., Jones, P. C., and Mogessie, A. (2010): Hydrothermal vein and alteration assemblages associated with low-sulfide footwall Cu-Ni-PGE mineralization and regional hydrothermal processes, North and East Ranges, Sudbury structure, Canada. SEG Special Publication 15, 573-598.

Tuba, G., Molnár, F., Ames, D. E., Péntek, A., Watkinson, D. H., and Jones, P. C. (2014): Multi-stage hydrothermal processes involved in "low-sulfide" Cu(-Ni)-PGE mineralization in the footwall of the Sudbury Igneous Complex (Canada): Amy Lake PGE zone, East Range. Mineralium Deposita 49, 7-47.

Tuttle, O. F. and Bowen, N. L. (1958): Origin of granite in the light of experimental studies in the system $NaAlSi_3O_8$-$KAlSi_3O_8$-SiO_2-H_2O. Geological Society of America Memoir 74, 1-153.

van den Kerkhof, A. M., Kronz, A., Simon, K., and Scherer, T. (2004): Fluid-controlled quartz recovery in granulite as revealed by Cathodoluminescence and trace element analysis (Bamble sector, Norway). Contributions to Mineralogy and Petrology 146, 637-652.

Vasyukova, O. V., Goemann, K., Kamenetsky, V. S., MacRae, C. M., and Wilson, N. C. (2013): Cathodoluminescence properties of quartz eyes from porphyry-type deposits: Implications for the origin of quartz. American Mineralogist 98, 98-109.

Wang, L., Putnis, C. V., Ruiz-Agudo, E., King, H. E., and Putnis, A. (2013): Coupled dissolution and precipitation at the cerrusite-phosphate solution interface: Implications for immobilization of lead in soils. Environmental Science and Technology 47, 13502-13510.

Wark, D. A. and Spear, F. S. (2005): Titanium in quartz: Cathodoluminescence and thermometry. Geochimica et Cosmochimica Acta 69, supplement S, A592-A592.

Wood, S. A. (2002): Behaviour of rare earth elements in geothermal systems: A new exploration tool?. Final project report, DOE Geothermal reservoir technology research, 1-36.

Worden, R. H., Walker, F. D. L., Parsons, I., and Brown, W. L. (1990): Development of microporosity, diffusion channels and deuteric coarsening in perthitic alkali feldspar. Contributions to Mineralogy and Petrology 104, 507-515.

Wu, Z., Sun, X., Xu, H., Konishi, H., Wang, Y., Wang, C., Dai, Y., Deng, X., and Yu, M. (2016): Occurrences and distribution of "invisible" precious metals in sulfide deposits from the Edmond hydrothermal field, Central Indian Ridge. Ore Geology Reviews 79, 105-132.

Zieg, M. J. (2001): Cooling and crystallization of the Sudbury Igneous Complex. Unpublished PhD Thesis, The Johns Hopkins University, 331 p.

Zieg, M. J. and Marsh, B. D. (2005): The Sudbury Igneous Complex: Viscous emulsion differentiation of a superheated impact melt sheet. Geological Society of America Bulletin 117, 1427-1450.

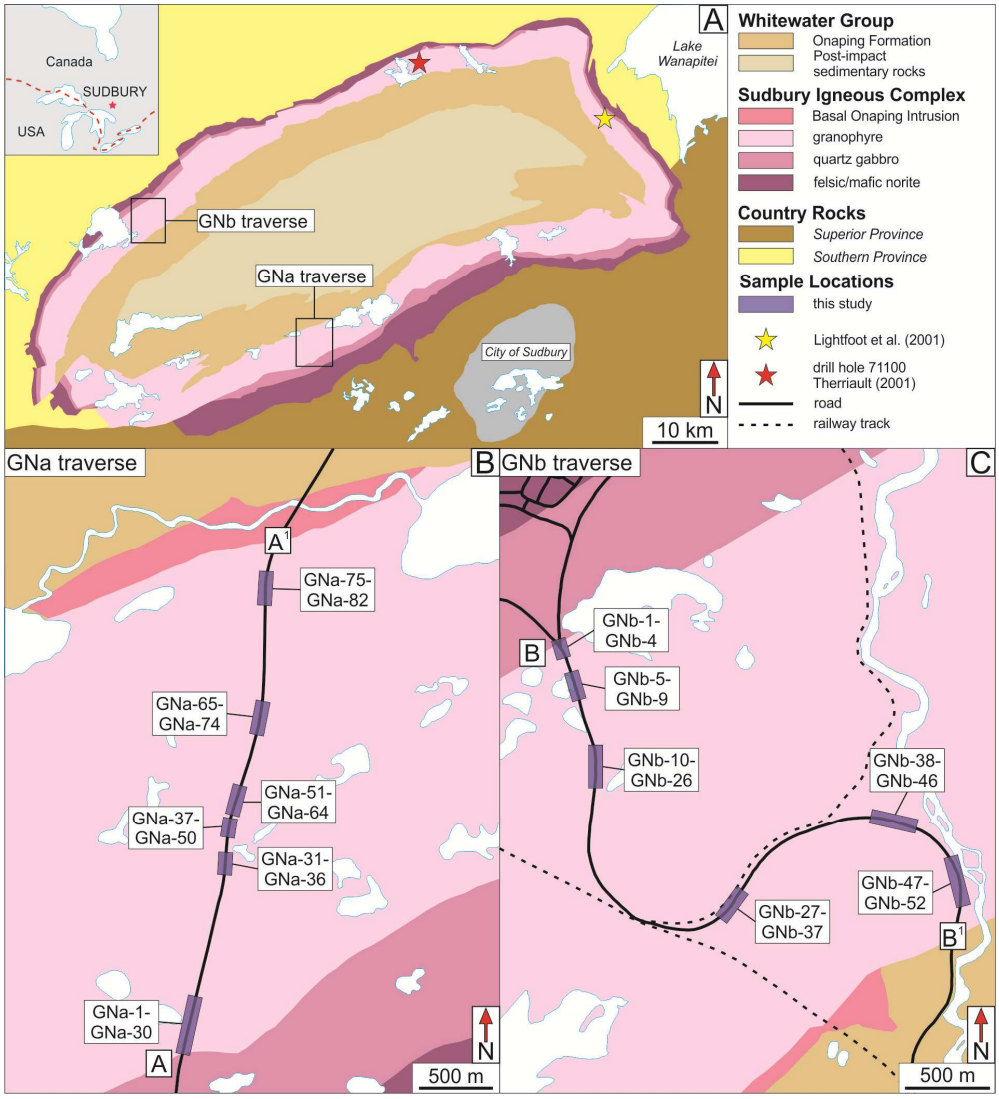

Figure 2-1. Geological setting of the area of study. (A) Regional geology of the Sudbury Structure and footwall rocks (modified after Ames and Farrow 2007). Inset map in upper left corner shows the location of the Sudbury Structure within Canada. Sample locations from other collections are indicated by a yellow star (Lightfoot et al. 2001) and red star (Therriault et al. 2002). The two black boxes indicate the locations of two traverses used for sample collection along highway #144 (shown in B and C). (B) South Range traverse (GNa, n = 82). (C) North Range traverse (GNb; n = 52). Sample locations from this study are indicated by blue boxes.

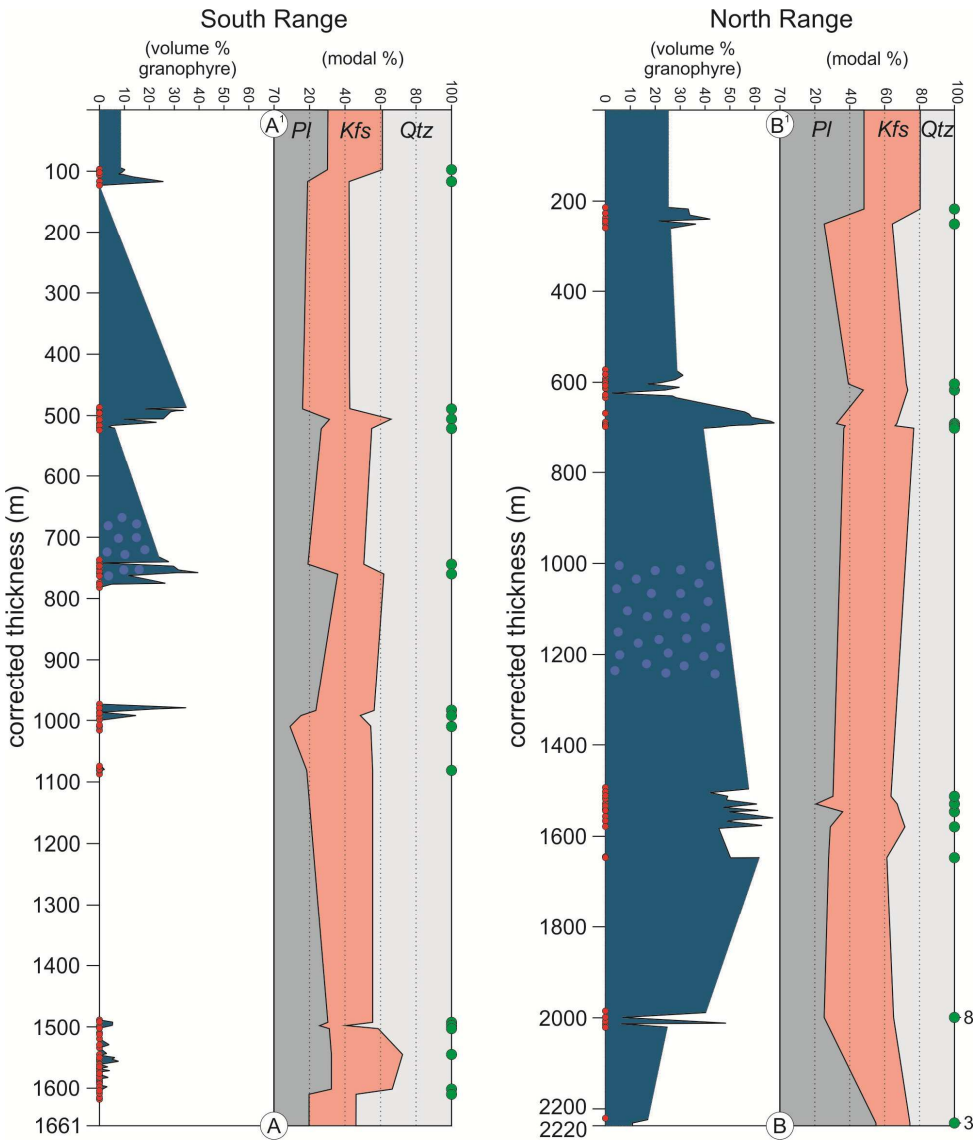

Figure 2-2. Graphic logs summarizing relative abundance of granophyre (left, in blue) and modal mineralogy (right) of samples from the traverses shown in Figure 1. Samples are arranged from top of the granophyre unit to contact with the quartz gabbro (A^1 to A in the South Range; B^1 to B in the North Range). Red dots indicate location of samples used in this study, whereas green dots indicate samples used for modal analyses. The blue dots show approximate area where miarolitic cavities.

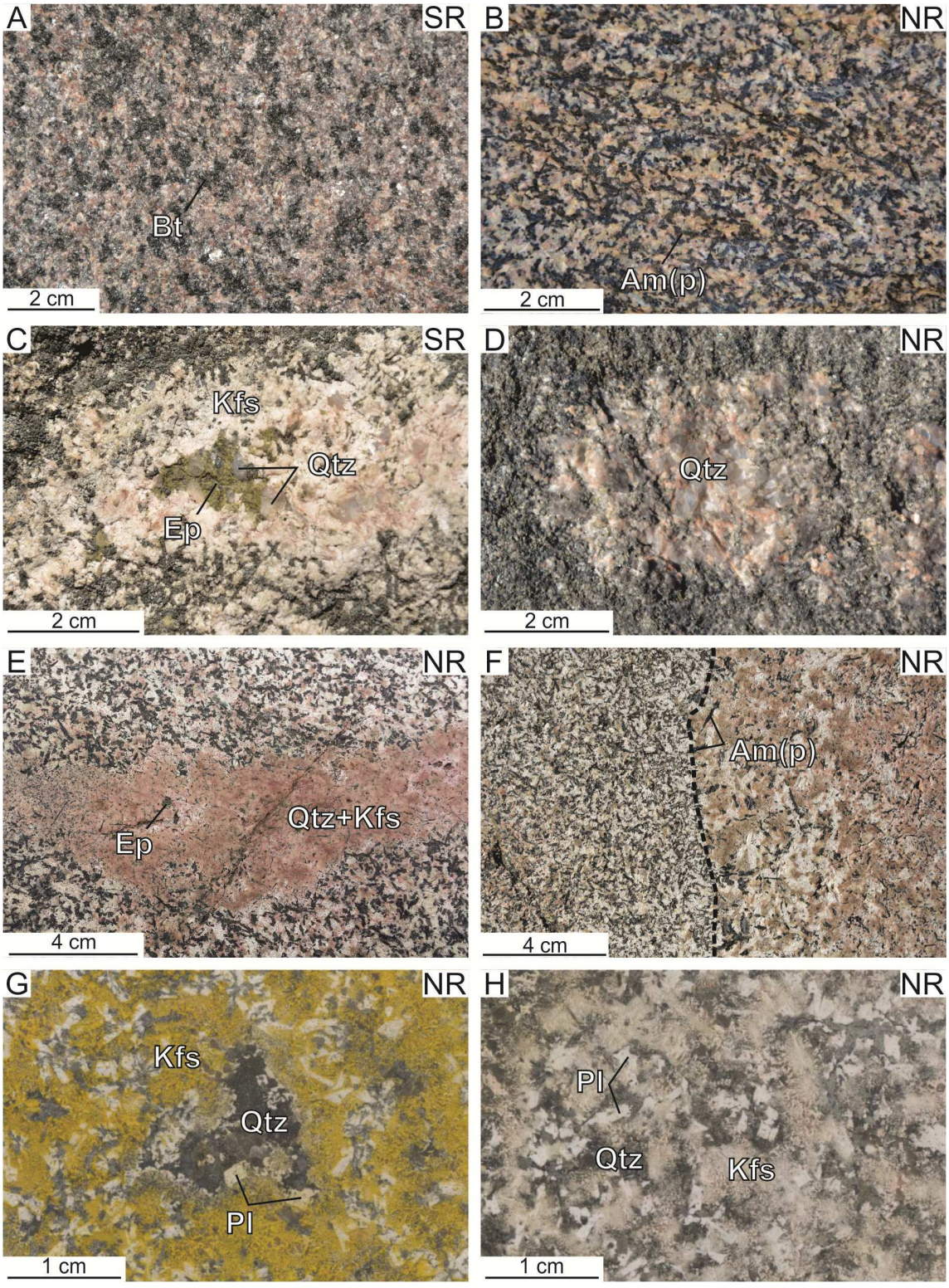
A
SR
Bt
2 cm
B
NR
Am(p)
2 cm
C
SR
Kfs
Qtz
Ep
2 cm
D
NR
Qtz
2 cm
E
NR
Ep
Qtz+Kfs
4 cm
F
NR
Am(p)
4 cm
G
NR
Kfs
Qtz
Pl
1 cm
H
NR
Pl
Qtz
Kfs
1 cm

Figure 2-3. Representative photographs from the granophyre unit in the North Range (NR; B, D, E, F, G, H) and South Range (SR; A, C). (A) Outcrop from SR containing biotite in a quartz-feldspar matrix. (B) Outcrop from the NR containing euhedral primary amphibole in a quartz-feldspar matrix. (C) Outcrop from SR containing an epidote and quartz-filled miarolitic cavity within a coarse-grained quartz-K-feldspar domain. (D) Outcrop from SR containing a quartz-filled miarolitic cavity. (E) Outcrop from NR containing a felsic domain consisting of quartz and K-feldspar with fine-grained primary acicular amphibole. (G) Stained slab (K-feldspar is yellow) from NR (35 volume % granophyre). Notice that the plagioclase did not stain magenta as it is almost pure albite. (H) Stained slab, as in previous photo, from NR (40 volume % granophyre). Notice that the plagioclase did not stain magenta but in this sample K-feldspar also did not stain because of increased porosity.(F) Outcrop from NR containing a coarse-grained K-feldspar-quartz-amphibole felsic domain (right) in contact with a finer-grained acicular amphibole-quartz-feldspar. Abbreviations for all figures: Am (p) - primary amphibole; Bt – biotite; Kfs – K-feldspar; Pl – plagioclase; Qtz – quartz.

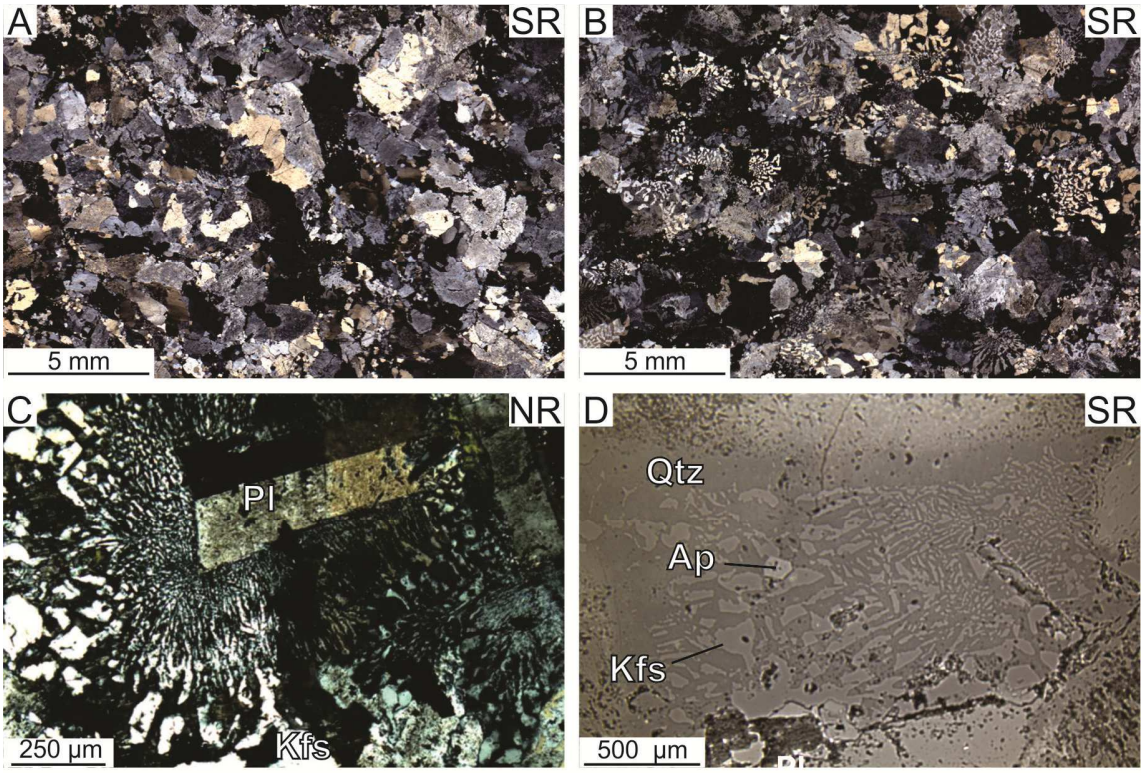

Figure 2-4. Scanned polished thin section images and photomicrographs in plane-polarized (PPL) and reflected (RF) light showing textural characteristics of granophyre in the granophyre unit. (A) Sample with no recognizable granophyre. (B) Sample with 34 volume % granophyre. (C) Example of a plagioclase lath acting as a nucleation point for granophyre. Notice the coarsening of quartz and K-feldspar away from plagioclase. (D) Image in RF showing the well defined nature of the granophyre texture and intergrowth of fine-grained domains. Notice the coarsening away from a plagioclase lath and the termination of granophyre into a domain of quartz. Abbreviations: Ap – apatite; Kfs – K-feldspar; Pl – plagioclase; Qtz – quartz.

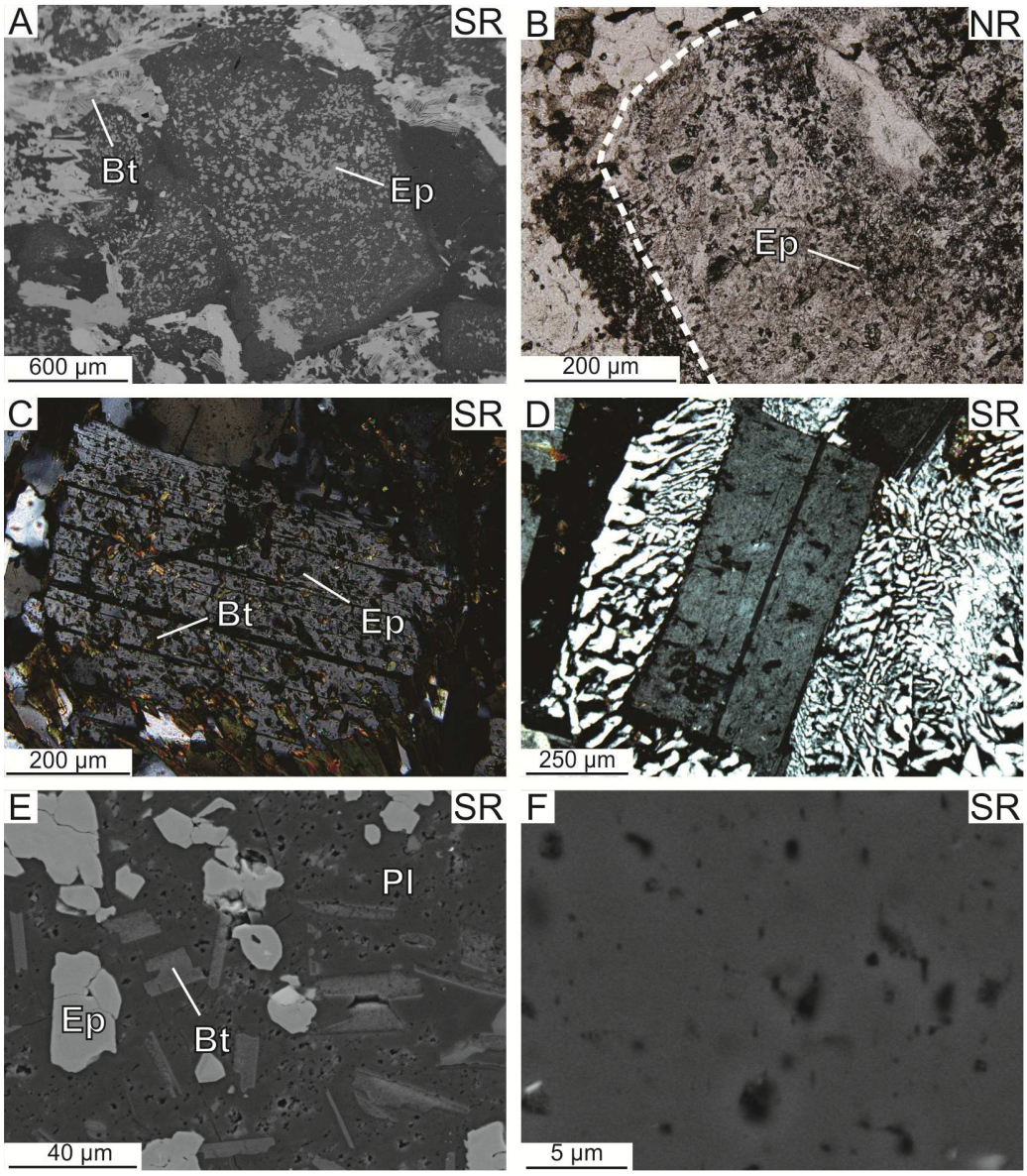
A
SR
Bt
Ep
600 µm
B
NR
Ep
200 µm
C
SR
Bt
Ep
200 µm
D
SR
250 µm
E
SR
Pl
Ep
Bt
40 µm
F
SR
5 µm

Figure 2-5. Backscattered electron (BSE) images (A, E, F) and photomicrographs in plane polarized (B) and cross-polarized (C, D) light summarizing plagioclase alteration textures in the granophyre unit from the North Range (NR) and South Range (SR). (A) Plagioclase grain exhibiting pit texture where epidote has precipitated in the pits. Notice biotite alteration in groundmass and along grain boundaries. (B) Example of re-equilibrated plagioclase. The white dashed line represents the contact between the plagioclase grain and surrounding groundmass which is also indicated by the termination of pervasive epidote alteration. (C) Euhedral plagioclase grain exhibiting albite twinning. The grain is strongly altered and contains pervasive pit texture which is lined by biotite, which is also commonly observed in plagioclase-hosted pits in the NR. (D) Euhedral plagioclase lath acting as a nucleus for granophyre. The plagioclase grain exhibits albite twinning and is weakly equilibrated with minor pit texture and notable absence of secondary phases within pits.(E) High magnification image of re-equilibrated plagioclase. Notice the abundant pits in the host plagioclase and the secondary biotite and epidote occurring within the altered grain, a common alteration assemblage in the SR. (F) High magnification image of plagioclase. Image shows pits which are often void of any secondary phase but varies between samples. Abbreviations: Bt – biotite; Ep – epidote; Pl – plagioclase.

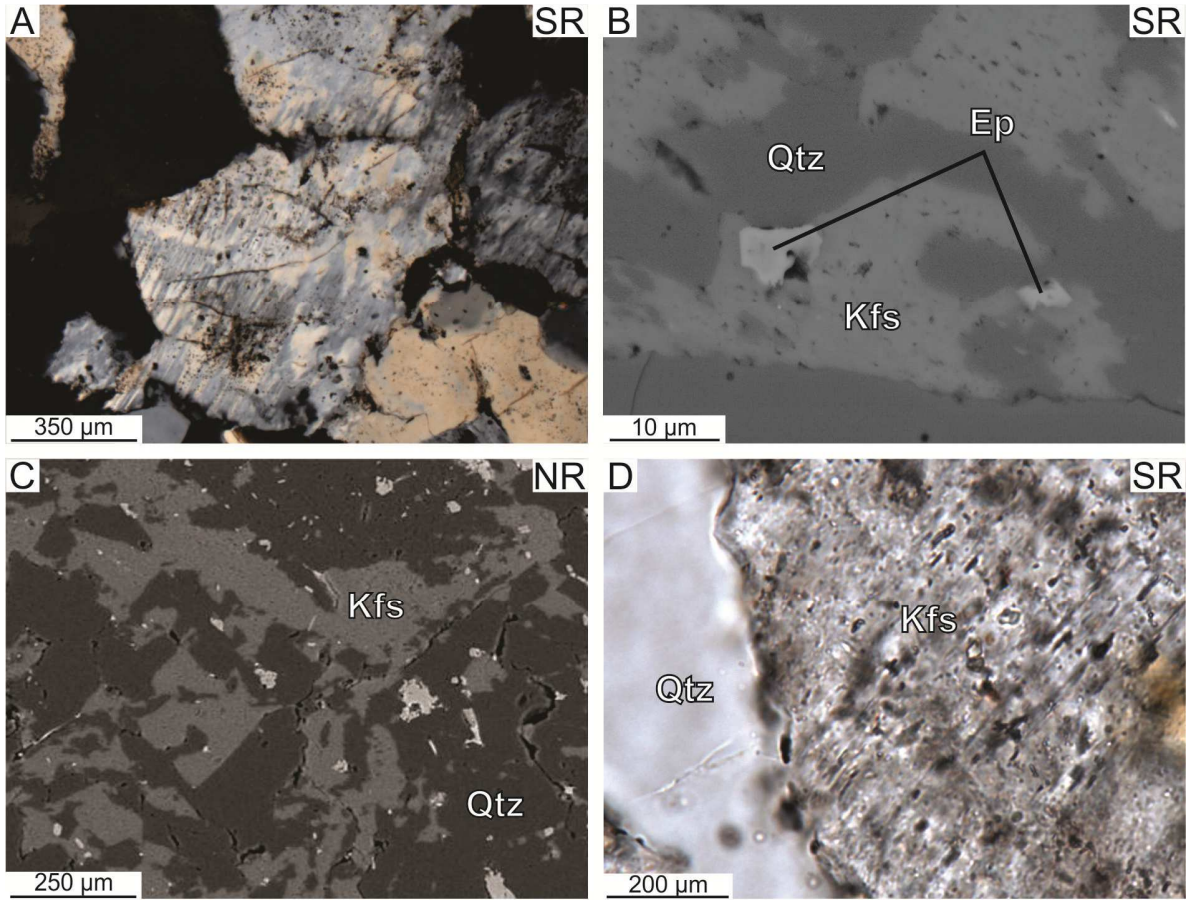

Figure 2-6. Photomicrographs in cross-polarized (A) and plane-polarized (D) light and back-scattered electron (BSE) images (B, D) showing characteristics of K-feldspar in the granophyre unit (GR) from the North Range (NR) and South Range (SR). (A) Perthitic texture in K-feldspar and subhedral quartz. Note that it is very rare to observe perthitic texture in samples of the GR. (B) High magnification showing granophyre. (C) K-feldspar and quartz hosted in granophyre. (D) K-feldspar and quartz within granophyre. Notice the abundant fluid inclusions hosted in K-feldspar. Abbreviations: Ep – epidote; Kfs – K-feldspar; Qtz – quartz.

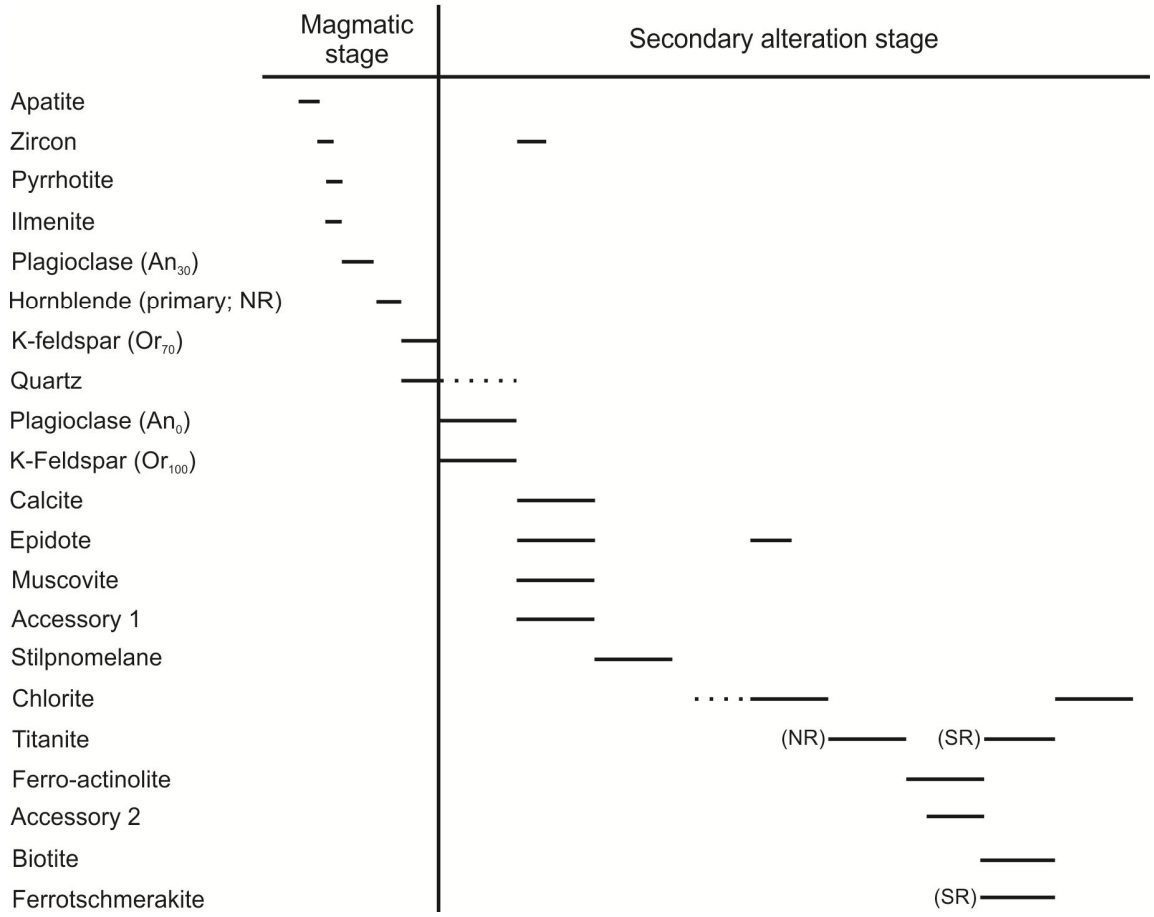

Figure 2-7. Inferred paragenesis for the GR, subdivided into primary phases (related to the magmatic stage) and secondary phases (related to later alteration). Accessory 1 represents zircon altering to baddeleyite, galena, thorite and uraninite. Accessory 2 represents ilmenite altering to hematite and rutile.

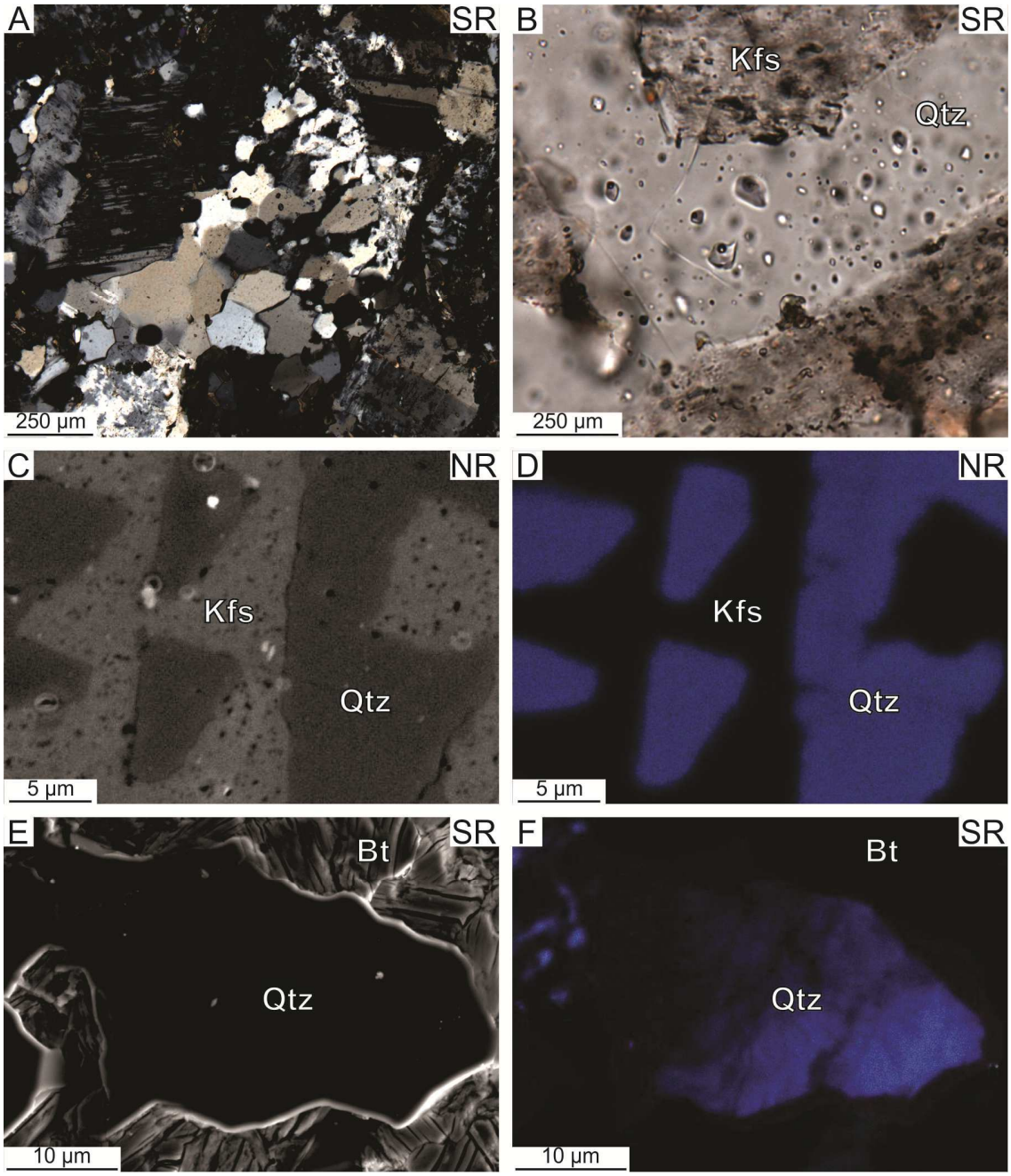
A
SR
250 µm
B
SR
Kfs
Qtz
250 µm
C
NR
Kfs
Qtz
5 µm
D
NR
Kfs
Qtz
5 µm
E
SR
Bt
Qtz
10 µm
F
SR
Bt
Qtz
10 µm

Figure 2-8. Photomicrographs in cross-polarized (A) and plane-polarized (B) light, back-scattered electron (BSE; C, E) and cathodoluminescence (CL; D, F) images summarizing characteristics of quartz in the granophyre unit (GR) from the North Range (NR) and South Range (SR). (A) Recrystallized quartz domain with development of subgrains in a moderately altered sample. (B) Granophyre showing abundant quartz-hosted fluid inclusions. (C) Pitted K-feldspar caused by re-equilibration with a fluid but note the apparent lack of pitted texture in quartz. (D) CL image of image D showing uniform blue colour of quartz which indicates it has not been modified due to interaction with a fluid. (E) Quartz surrounded by secondary biotite. (F) CL images of image E. The irregular blue colouration in the quartz indicates the grain has re-equilibrated with a fluid. Abbreviations: Bt – biotite; Kfs – K-feldspar; Qtz – quartz.

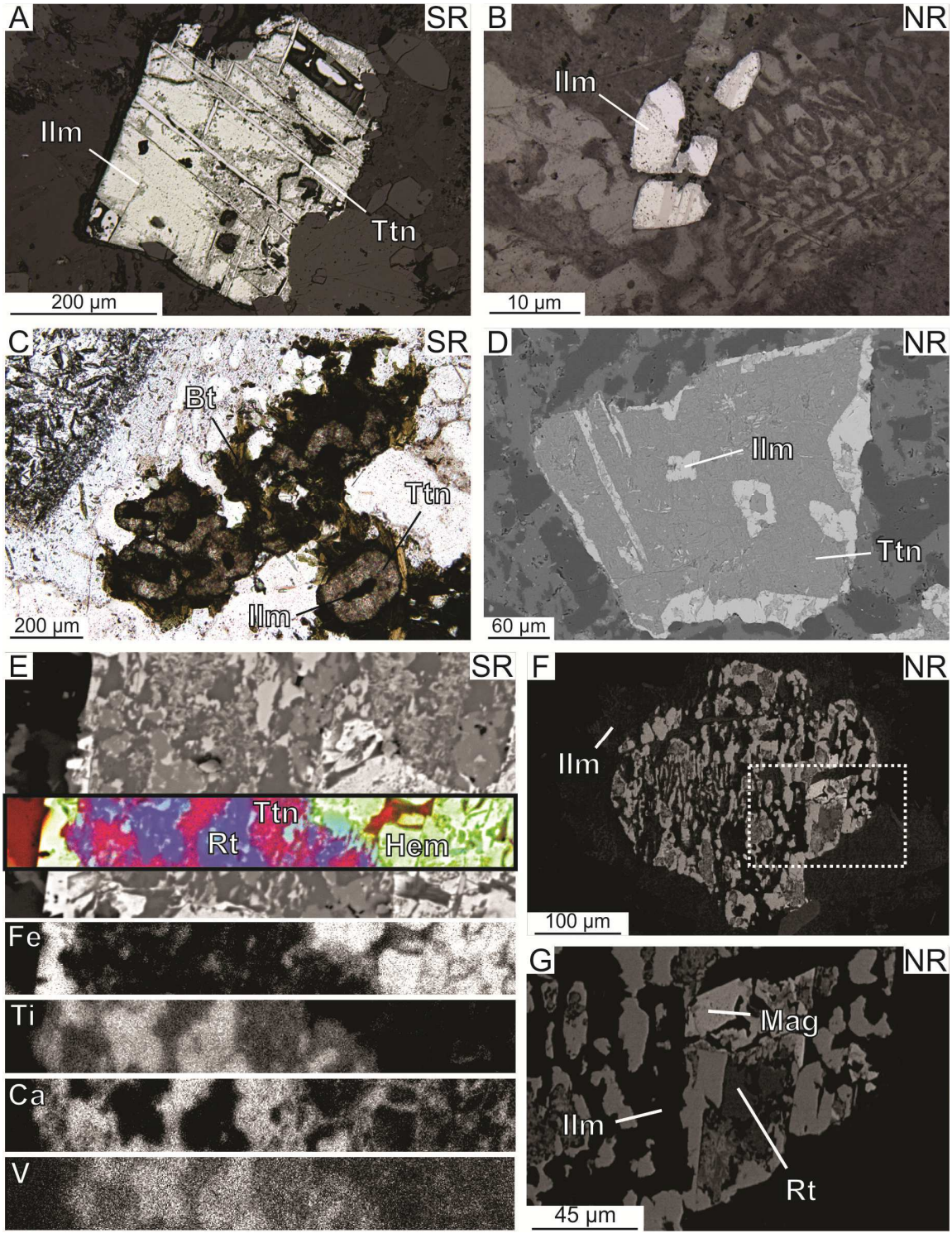
A
SR
Ilm
Ttn
200 µm
B
NR
Ilm
10 µm
C
SR
Bt
Ttn
Ilm
200 µm
D
NR
Ilm
Ttn
60 µm
E
SR
Ttn
Rt
Hem
Fe
Ti
Ca
V
F
NR
Ilm
100 µm
G
NR
Mag
Ilm
Rt
45 µm

Figure 2-9. Photomicrographs in reflected light (A, B) and plane-polarized light (C), back-scattered electron (BSE; D, E, F, G) and X-ray (E) images summarizing the characteristics of oxides and related alteration phases in the granophyre unit (GR) from the North Range (NR) and South Range (SR). (A) Primary ilmenite being replaced by titanite. (B) Primary ilmenite showing its textural relationship with granophyre. (C) Ilmenite (core) being partially replaced by titanite (rim) with biotite. This style of replacement common in the SR. (D) Titanite replacing ilmenite with an original primary amphibole. This style of replacement is unique to the NR. (E) BSE image and accompanying X-ray maps (Fe, Ti, Ca, V) of a complex replacement reaction of ilmenite being altered to rutile, hematite, and titanite. (F) Complex replacement reaction of ilmenite to magnetite and rutile. (G) BSE image of white box inset from F. This image better shows the replacement of ilmenite by magnetite and ilmenite. Abbreviations: Bt – biotite; Hem – hematite; Ilm – ilmenite; Mag – magnetite; Rt – rutile; Ttn – titanite.

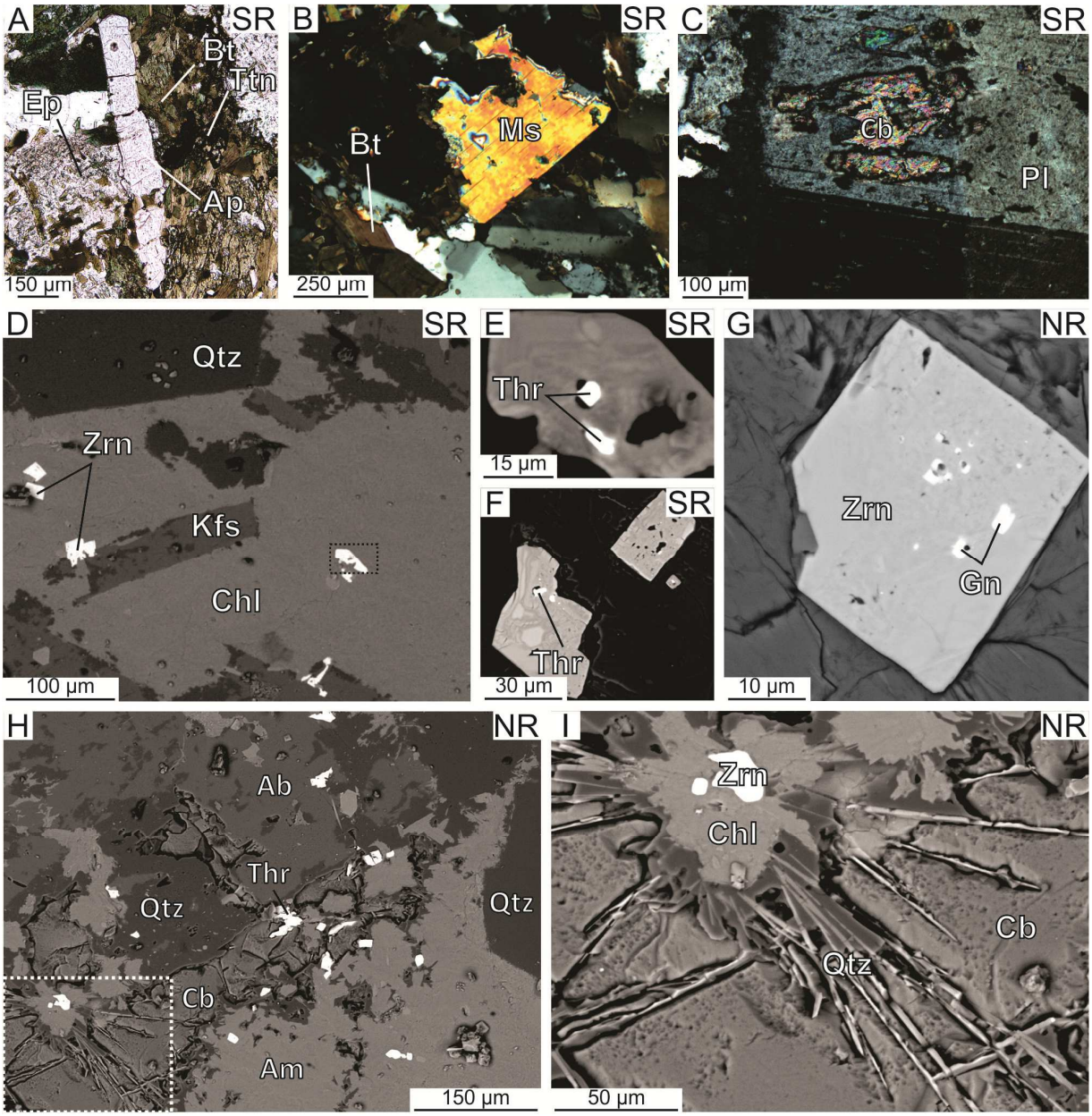
A
SR
Bt
Ttn
Ep
Ap
150 µm
B
SR
Ms
Bt
250 µm
C
SR
Cb
Pl
100 µm
D
SR
Qtz
Zrn
Kfs
Chl
100 µm
E
SR
Thr
15 µm
F
SR
Thr
30 µm
G
NR
Zrn
Gn
10 µm
H
NR
Ab
Thr
Qtz
Qtz
Cb
Am
150 µm
I
NR
Zrn
Chl
Cb
Qtz
50 µm

Figure 2-10. Photomicrographs in plane-polarized light (A) and cross-polarized light (B, C) and back-scattered electron (BSE; D, E, F, G, H, I) images summarizing the textures and characteristics of accessory phases in the granophyre unit (GR) from the North Range (NR) and South Range (SR). (A) Apatite surrounded by a biotite-epidote- titanite alteration assemblage. (B) Subhedral muscovite and fine-grained biotite in a quartz-K-feldspar domain. (C) Altered plagioclase grain with albite twinning and containing moderate pitted texture with carbonate. (D) Chlorite after biotite in a quartz-K-feldspar matrix. The bright phase in the large domain of chlorite is zircon. (E) BSE image of dashed black box in D showing a zoned zircon exhibiting pitted texture. The bright white phase is thorite. Notice the change in grey scale within the zircon indicating zoning. (F) Zircon exhibiting secondary alteration texture and pitted texture with thorite. (G) Zircon exhibiting weak pitted texture and galena inclusions. (H) An example of a complex alteration assemblage in the NR containing secondary amphibole and carbonate with minor thorite in a quartz-albite matrix. (I) BSE image of white dashed line box from H. The section contains hydrothermal zircon rimmed by chlorite and fibrous quartz in carbonate. Abbreviations: Ab – albite; Am – amphibole; Ap – apatite; Bt – biotite; Cb – carbonate; Chl – chlorite; Ep – epidote; Gn – galena; Kfs – K-feldspar; Ms – muscovite; Pl – plagioclase; Qtz – quartz; Thr – thorite; Zrn– zircon.

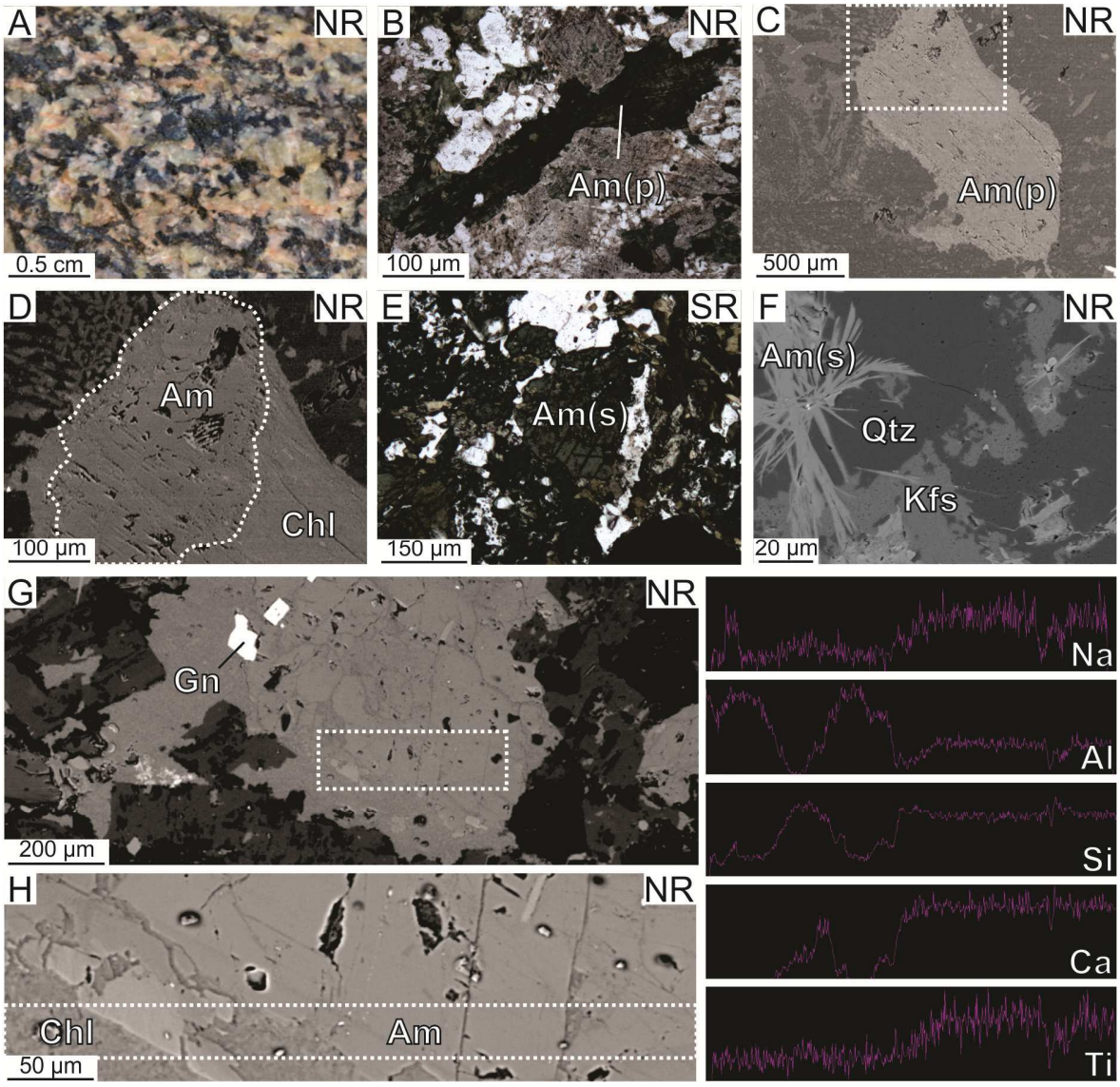
A
NR
0.5 cm
B
NR
Am(p)
100 µm
C
NR
Am(p)
500 µm
D
NR
Am
Chl
100 µm
E
SR
Am(s)
150 µm
F
NR
Am(s)
Qtz
Kfs
20 µm
G
NR
Gn
200 µm
H
NR
Chl
Am
50 µm
Na
Al
Si
Ca
Ti

Figure 2-11. Photographs of outcrop (A), photomicrographs in plane-polarized light (B) and cross-polarized light (E), back-scattered electron (BSE; C, D, F, G, H) images and X-ray maps characterizing different styles of amphibole in the granophyre unit (GR) from the North Range (NR) and South Range (SR). (A) GR outcrop containing primary amphibole. (B) Altered primary amphibole in a quartz-K-feldspar matrix. (C) Primary amphibole in a quartz-K-feldspar matrix that has experienced partial re-equilibration producing pit texture (top and bottom of grain) and replacement (middle of grain). (D) BSE image of white dashed box from C. The image shows the pitted texture in greater detail of the primary amphibole domain that is now chemically secondary amphibole. The lower portion of the grain has been replaced by chlorite. (E) Secondary acicular amphibole as a mafic patch. (F) Secondary, acicular amphibole showing its relationship to primary features of the GR. (G) Primary amphibole that has re-equilibrated to form secondary amphibole. Notice the grey-scale change in the white dashed box showing domains of primary and re-equilibrated amphibole. (H) BSE image of the area in G showing alteration of a primary amphibole and its replacement to secondary amphibole. The dashed white box indicates the area that is correlated with the X-ray traverses to the right. Domains of primary amphibole correspond with higher content of Na, Si, Ca and Ti lower content of Al. Abbreviations: Am – amphibole; Am (p) - primary amphibole; Am (s) - secondary amphibole; Chl – chlorite; Gn – galena; Kfs – K-feldspar; Qtz – quartz.

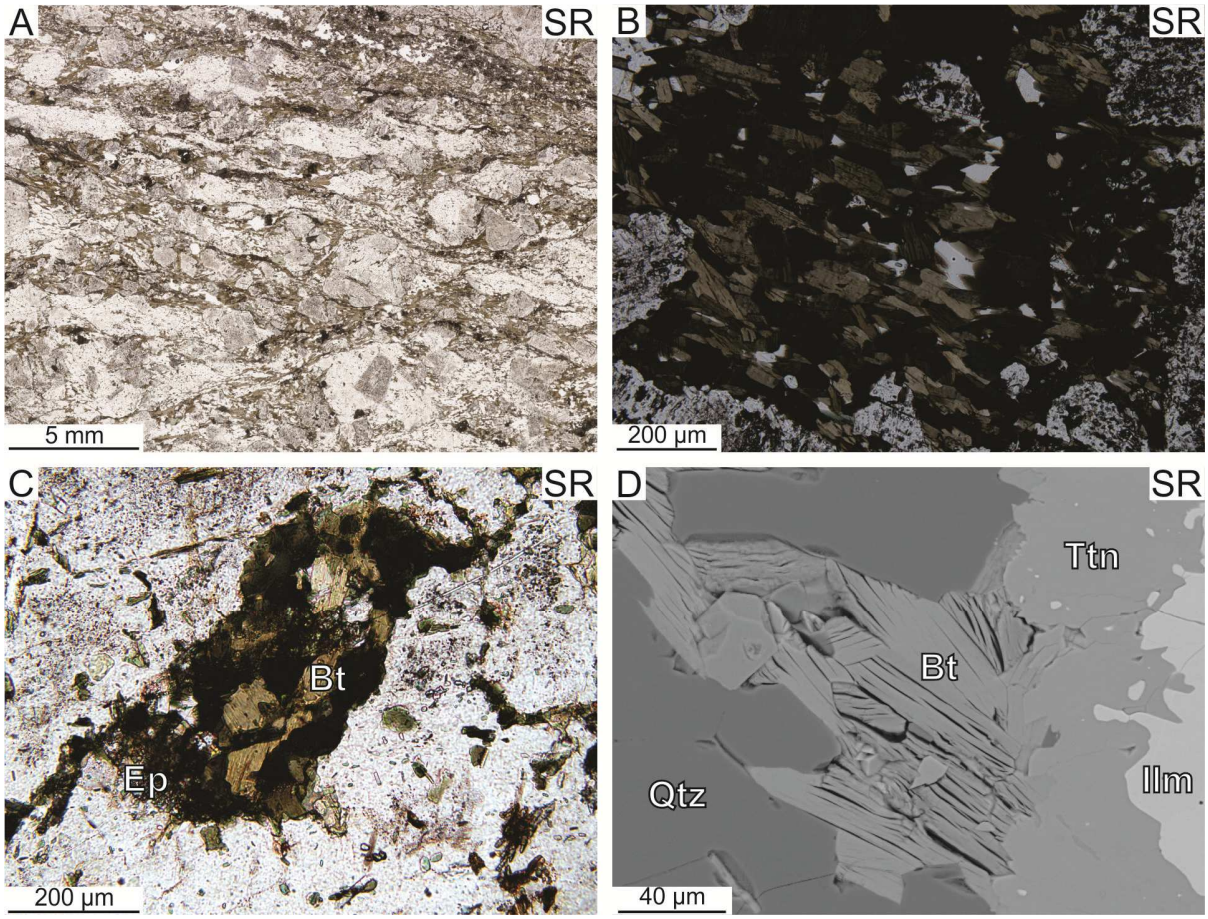

Figure 2-12. Photomicrographs in plane-polarized light (A, B, C) and back-scattered electron (BSE) images (D) summarizing the characteristics of biotite in the GR from the North Range (NR) and South Range (SR). (A) Pervasive secondary biotite exhibiting a moderate fabric.(B) A mafic patch containing biotite. (C) A mafic patch containing biotite and epidote. (D) An alteration assemblage in the SR consisting of ilmenite with a titanite rim with biotite in quartz. Abbreviations: Bt – biotite; Ep – epidote; Ilm – ilmenite; Qtz – quartz; Ttn – titanite.

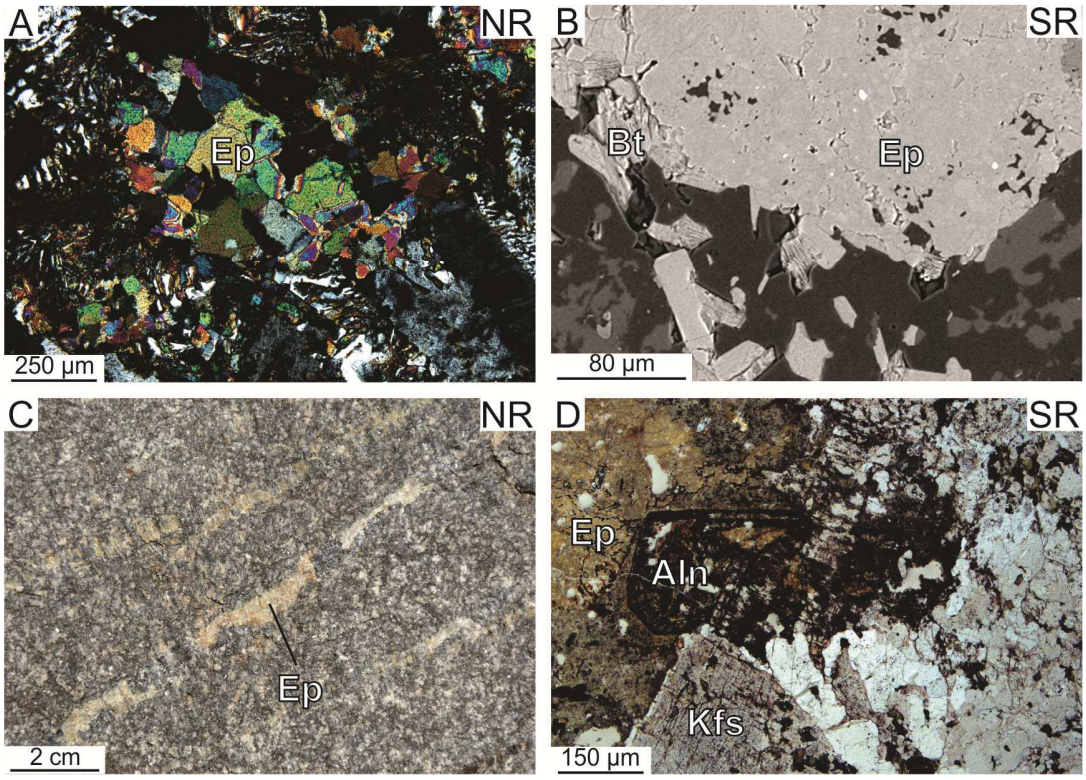

Figure 2-13. Photomicrographs in cross-polarized light (A) and plane-polarized light (D), back-scattered electron (B) image, and photograph of outcrop summarizing the characteristics of epidote in the granophyre unit (GR) from the North Range (NR) and South Range (SR). (A) Medium-grained epidote in fine-grained granophyre matrix. (B) Pervasive epidote with minor biotite. (C) Example of epidote vein present in outcrop. (D) Subhedral allanite grain surrounded by epidote in a K-feldspar and quartz matrix. Allanite is rare but where present is typically rimmed or associated with epidote. Abbreviations: Aln – allanite; Bt – biotite; Ep – epidote; Kfs – K-feldspar.

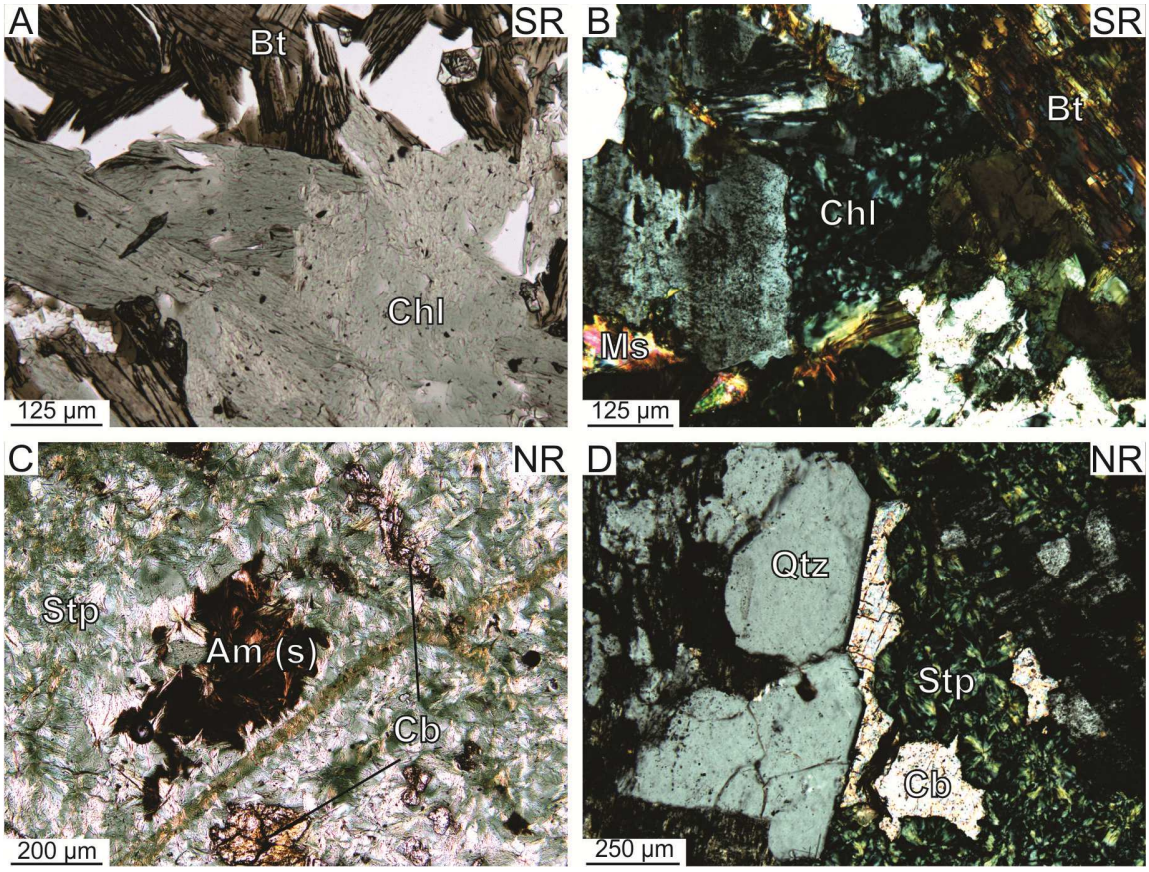

Figure 2-14. Photomicrographs in plane-polarized light (A, C) and cross-polarized light (B, D) summarizing the characteristics of chlorite and stilpnomelane in the granophyre unit (GR) from the North Range (NR) and South Range (SR). (A) Chlorite-biotite assemblage, a common alteration assemblage in the SR. (B) Chlorite and biotite in K-feldspar and quartz. Notice that biotite is partially chloritized. (C) Stilpnomelane and fibrous amphibole assemblage with minor carbonate. (D) Stilpnomelane and carbonate alteration assemblage. Abbreviations: Am(s) – secondary amphibole; Bt – biotite; Cb – carbonate; Chl – chlorite, Ms – muscovite; Qtz – quartz; Stp – stilpnomelane.

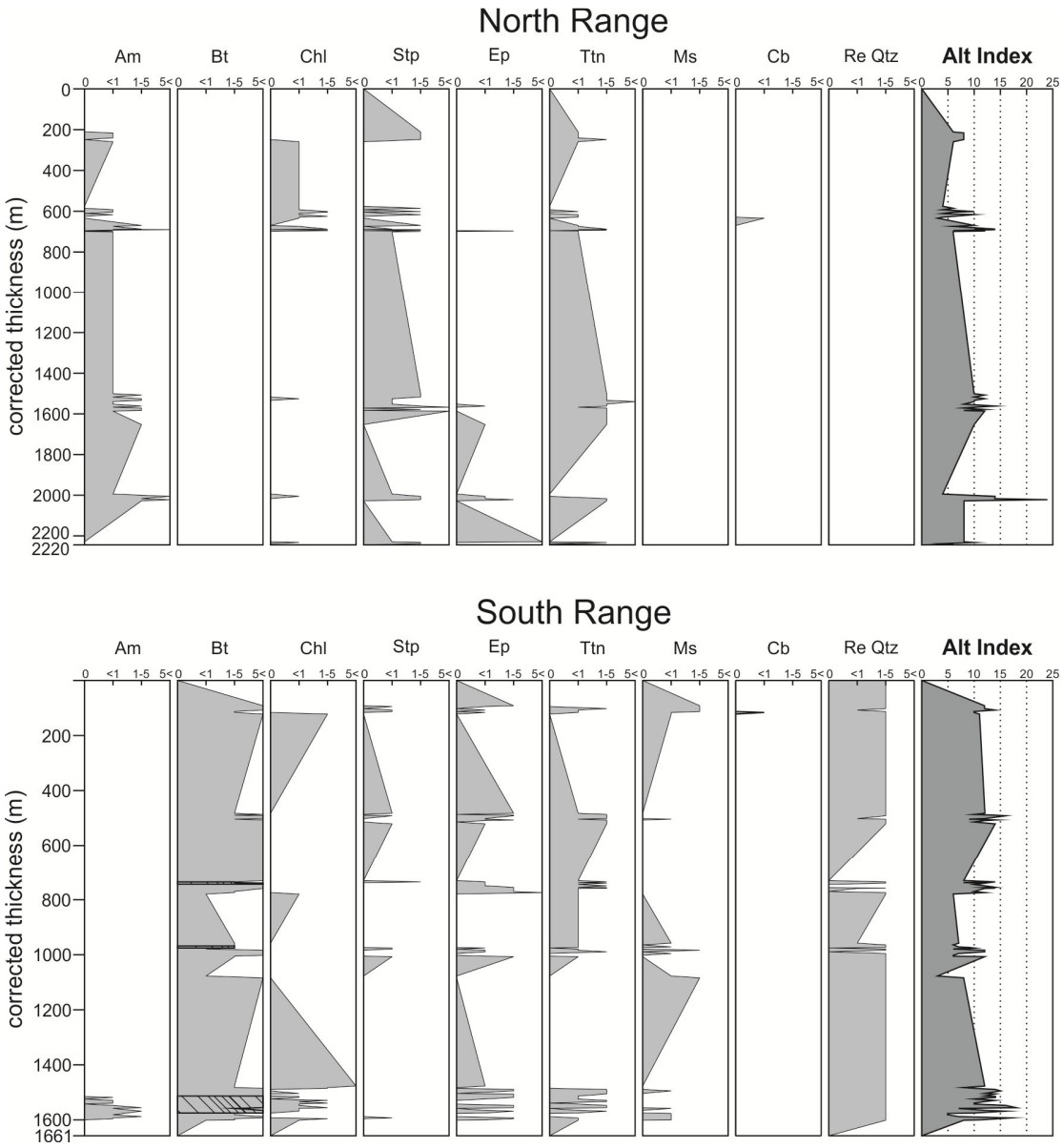

Figure 2-15. A summary of the alteration index (AI) calculated for the granophyre unit (GR) from the North Range (NR) and South Range (SR); see text for discussion of the calculation for the AI.

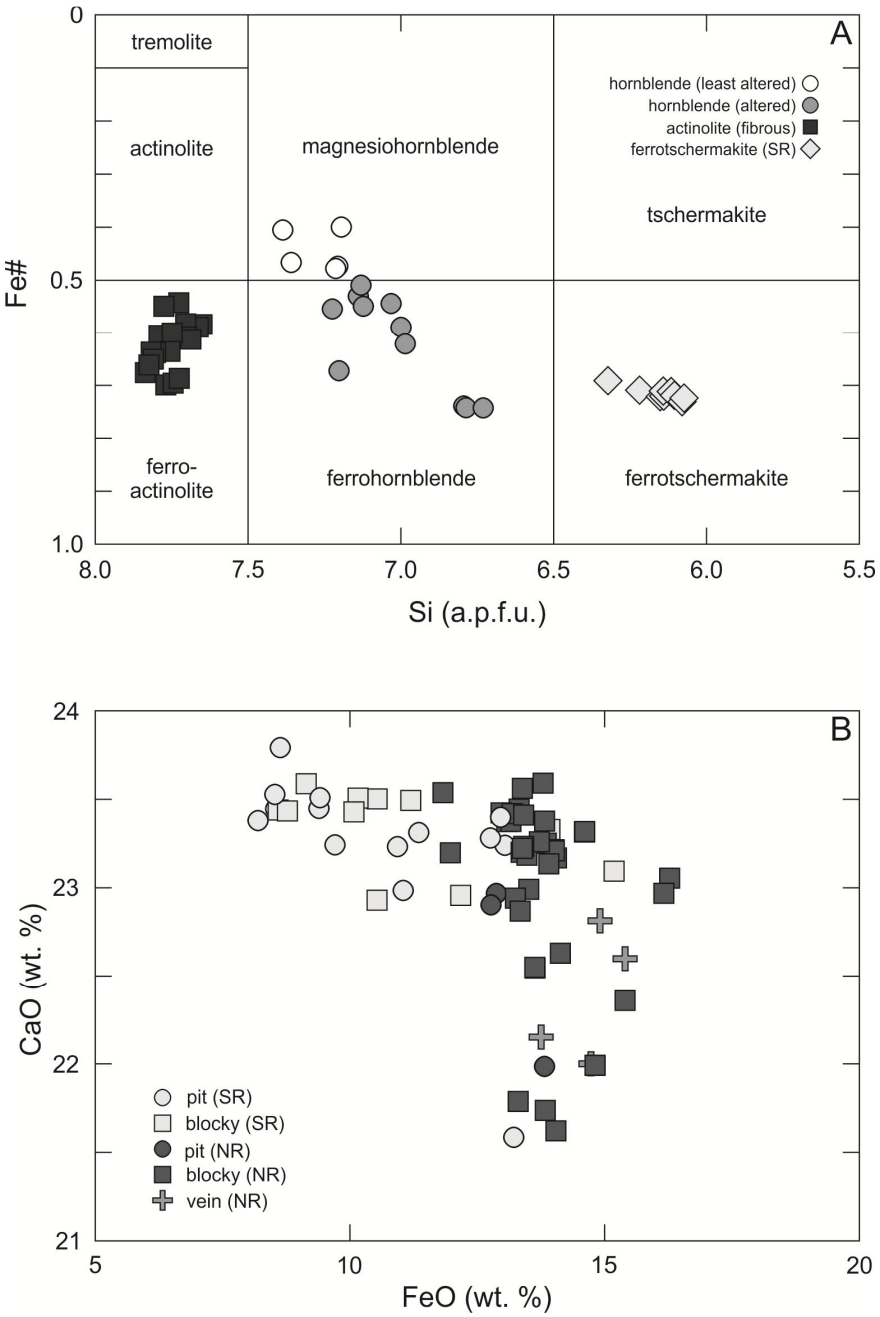

Figure 2-16. Mineral chemistry for samples from the granophyre unit from the North Range (NR) and South Range (SR). (A) Plot of Si (atoms per formula unit) against Fe# (Fe/(Fe+Mg)) for amphibole based on the classification criteria Leake et al. (1997). (B) Plot of FeO (wt. %) against CaO (wt. %) for epidote. Epidote styles include pit-hosted in plagioclase, blocky/pervasive, and one sample from an epidote vein.

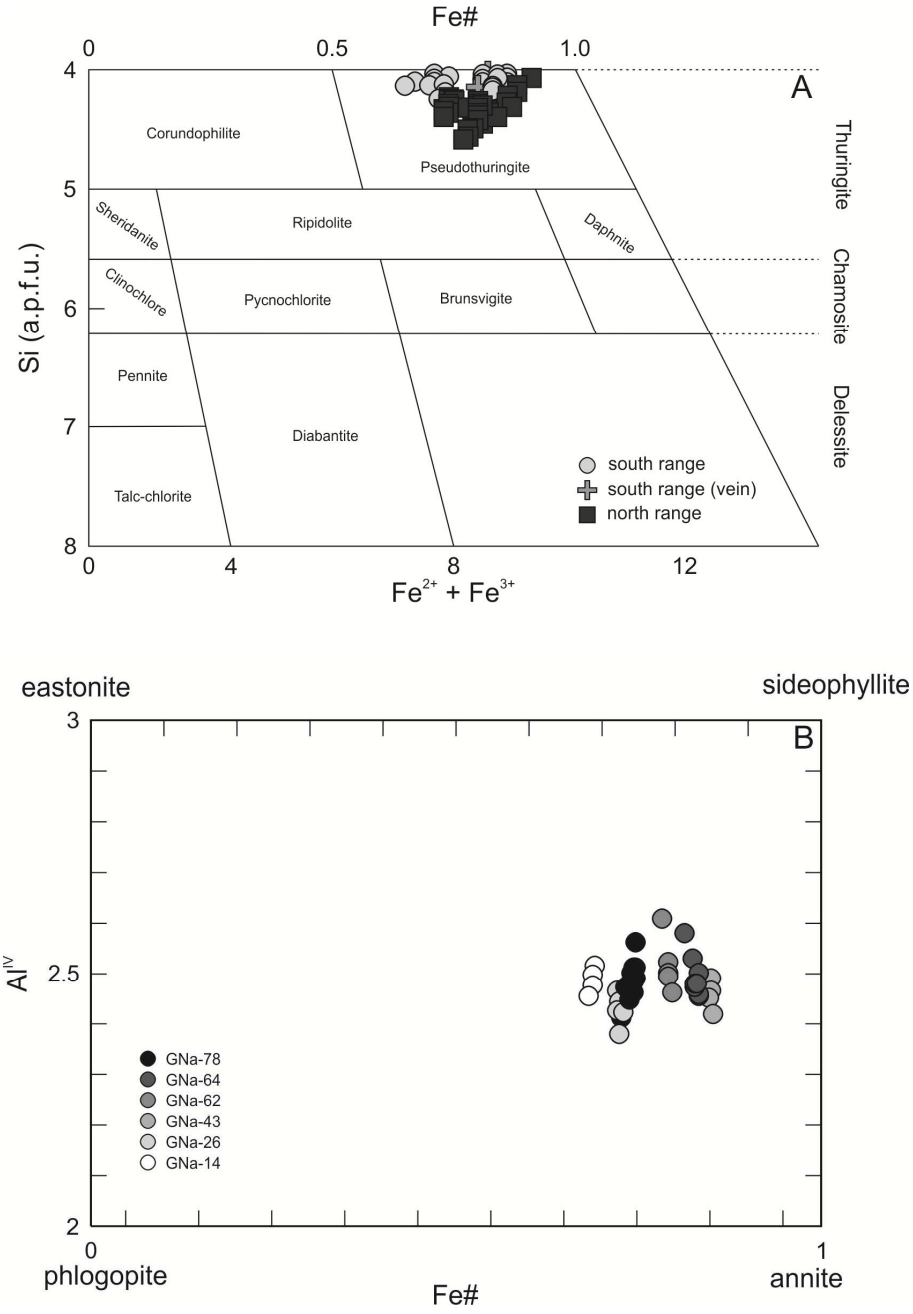

Figure 2-17. Mineral chemistry for samples from the granophyre unit from the North Range (NR) and South Range (SR). (A) Plot of Fe# (Fe/(Fe+Mg)) and total Fe (Fe^{2+}+Fe^{3+}; atoms per formula unit) against Si (atoms per formula unit) for chlorite (after Deer et al. 1966). (B) Plot of Fe# (Fe/(Fe+Mg)) against Al^{IV} for biotite data (after Bailey 1984).

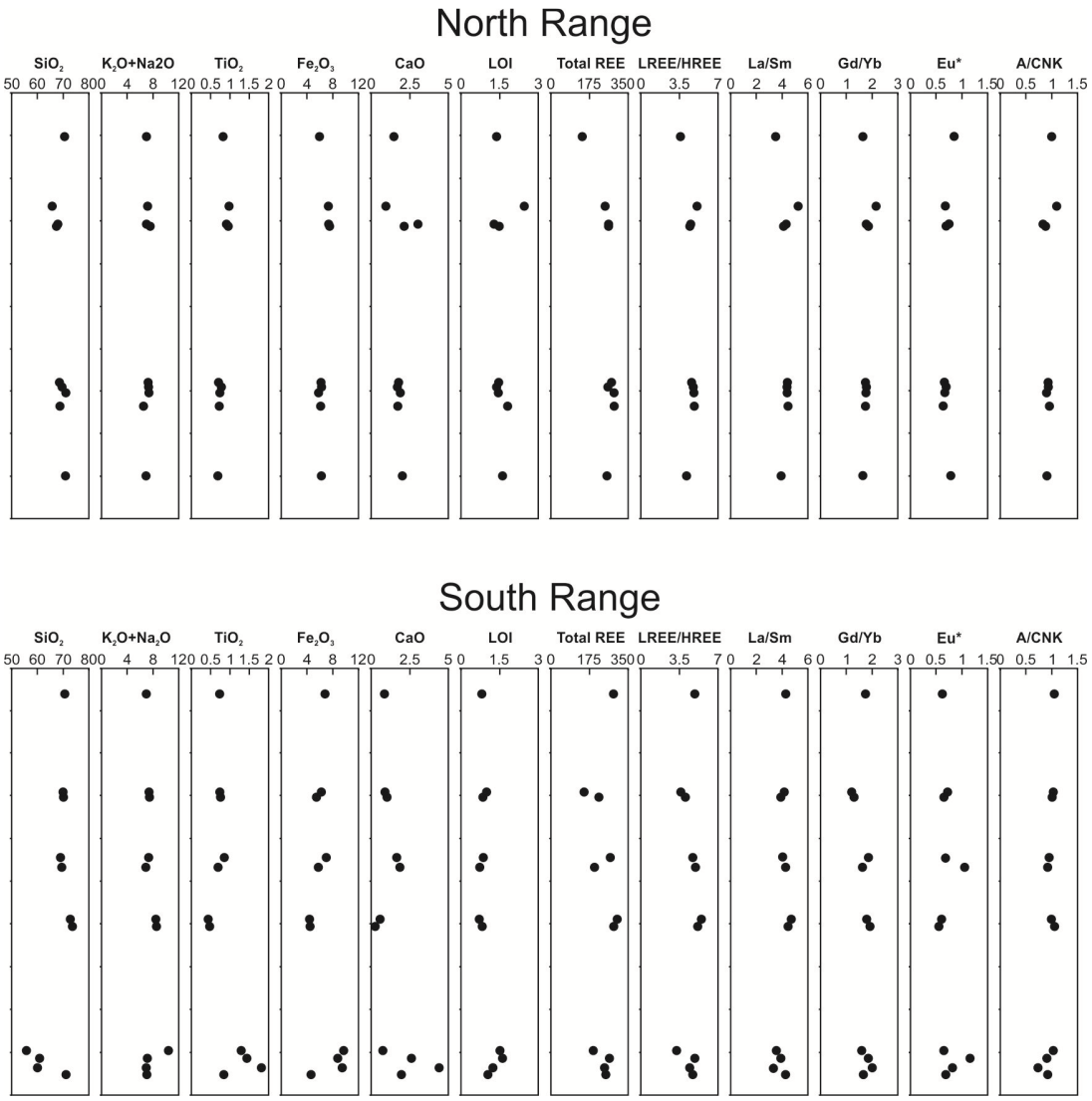

Figure 2-18. Summary of major-oxide and selected trace element profiles for whole rock data of the granophyre unit in the North and South Ranges arranged from stratigraphic top to bottom. Tick marks on left side indicate sample locations. Note that the data are shown in wt. % for major elements and ppm for the rare earth elements (REE). The term Eu* is the Eu anomaly and A/CNK is a measure of peraluminosity.

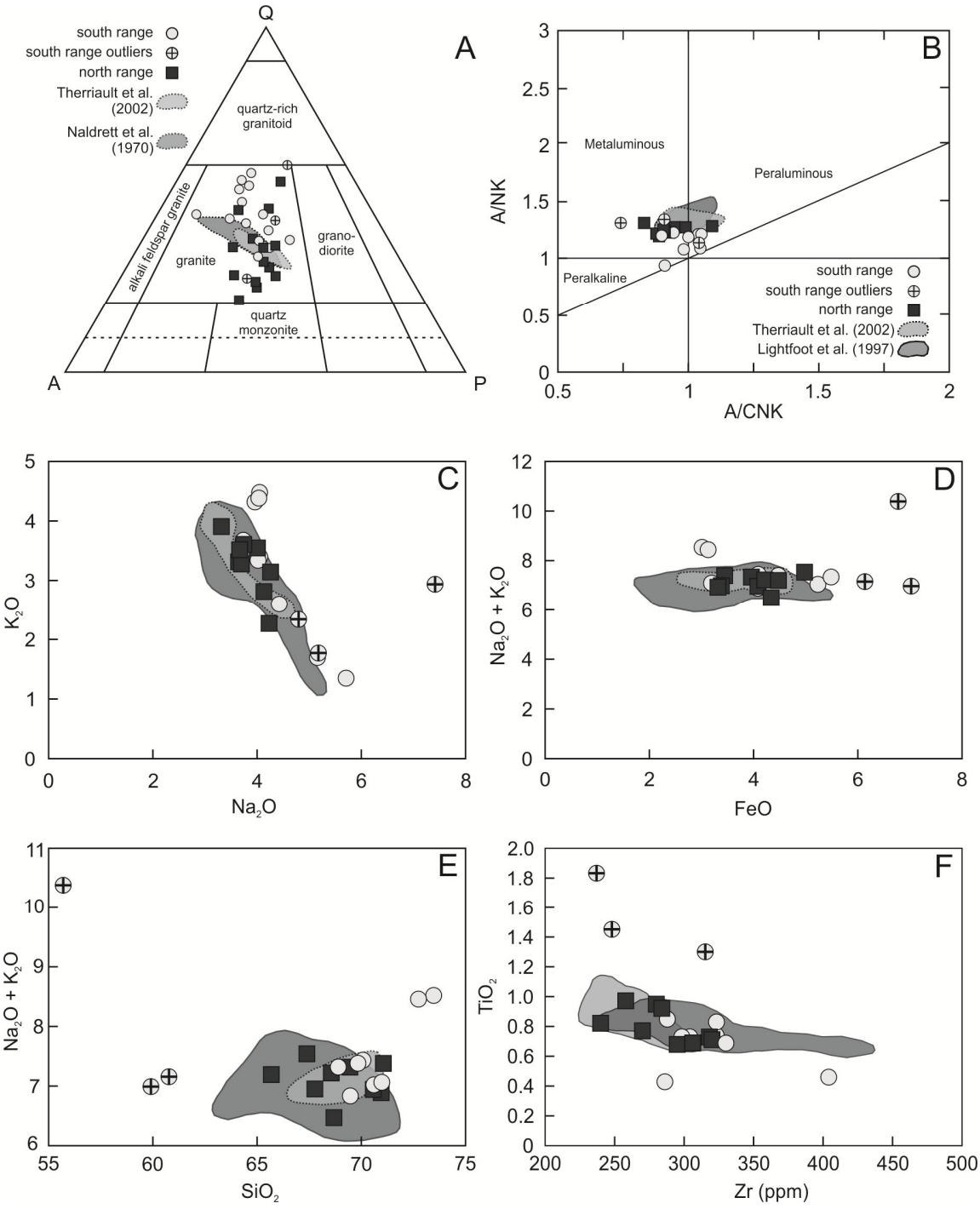
A
Q
A
P
south range
south range outliers
north range
Therriault et al. (2002)
Naldrett et al. (1970)
quartz-rich granitoid
alkali feldspar granite
granite
grano-diorite
quartz monzonite
B
A/NK
A/CNK
Metaluminous
Peraluminous
Peralkaline
south range
south range outliers
north range
Therriault et al. (2002)
Lightfoot et al. (1997)
C
K2O
Na2O
D
Na2O + K2O
FeO
E
Na2O + K2O
SiO2
F
TiO2
Zr (ppm)

Figure 2-19. Figures summarizing the whole rock geochemistry of the NR and SR GR. (A) A QAP (quartz, K-feldspar, plagioclase) ternary plot (after Steckeisen 1974) used to classify samples from this study based on point counting (see text for discussion). Note samples from this study are plotted as points (light grey circle =SR; dark grey square =NR) whereas the fields (grey shades) are normative percentages based on point counting from other studies (Therriault et al. 2002). (B) Plot of A/NK versus A/CNK showing that the samples are metaluminous to peraluminous. These symbols are used for remaining four diagrams. (C-F) Binary plots (in wt. %) for the whole rock geochemistry of the GR.

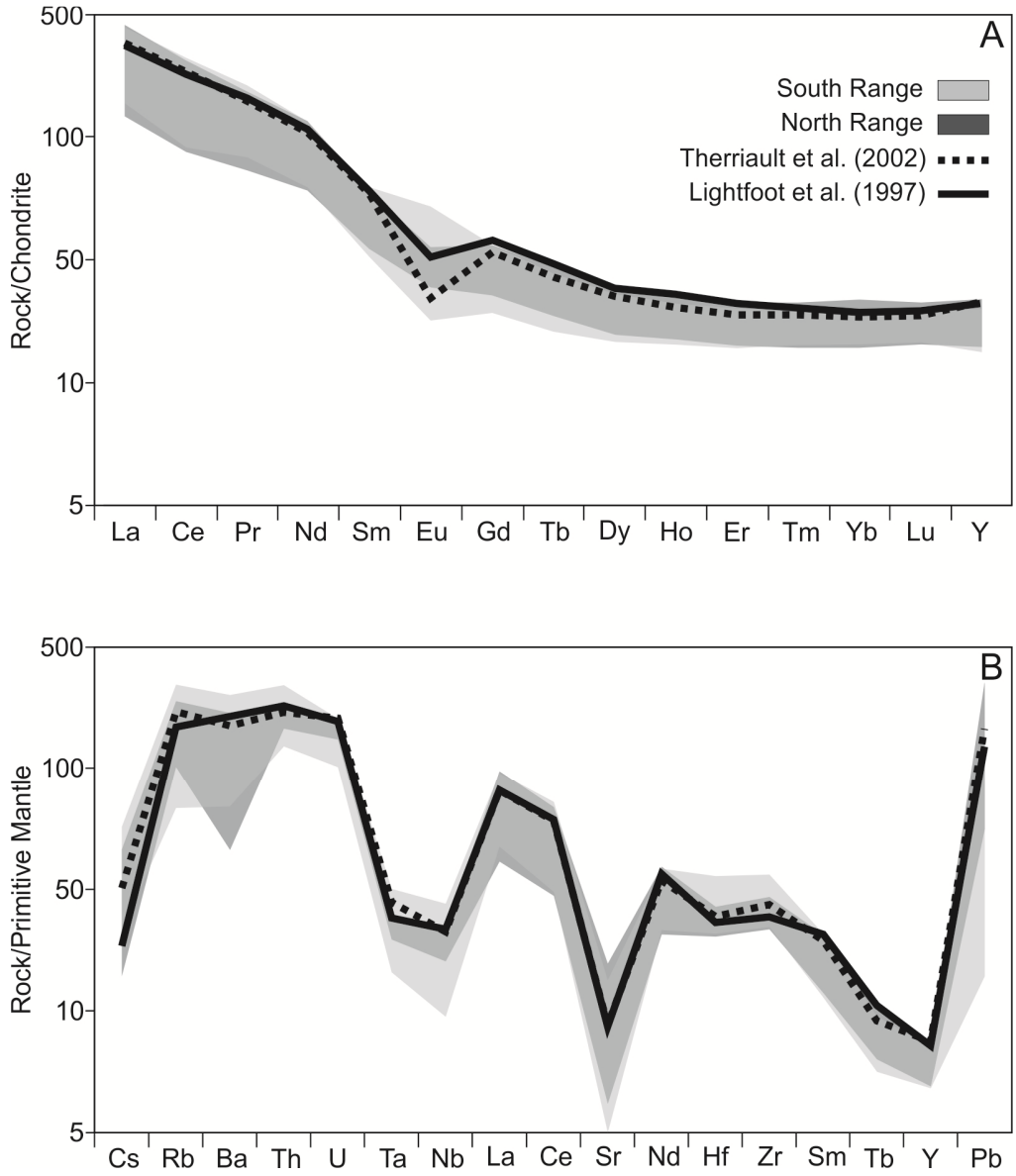

Figure 2-20.Chondrite- and primitive mantle-normalized spidergrams comparing trace element for samples of this study and previous work. a) Rare-earth elements. b) Extended spidergram. Data normalized to chondrite and primitive mantle values (McDonough and Sun 1995).

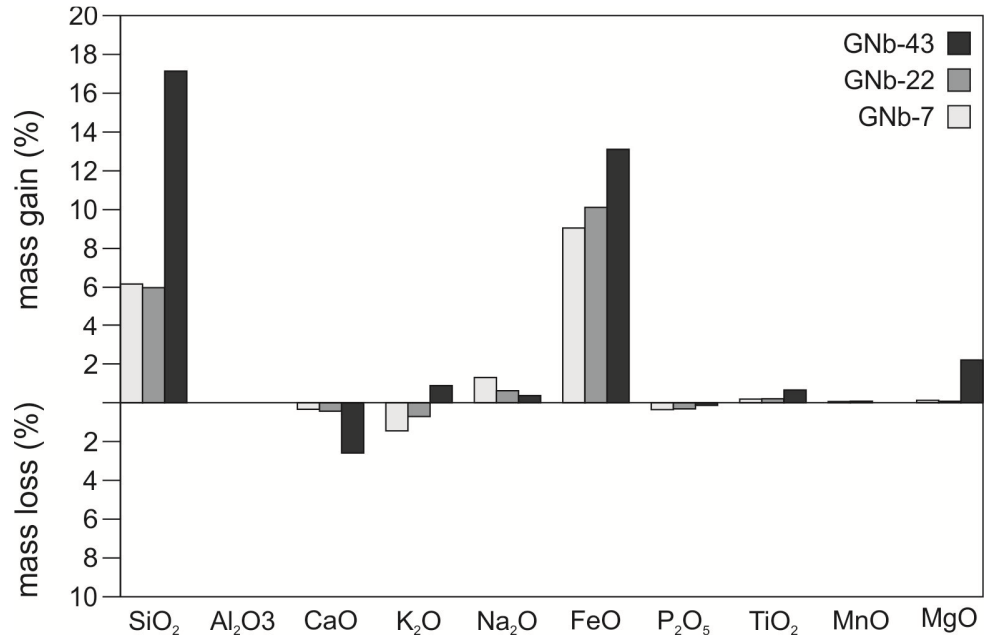

Figure 2-21. Plot summarizing the gains and losses for whole rock major element concentrations. See text for explanation.

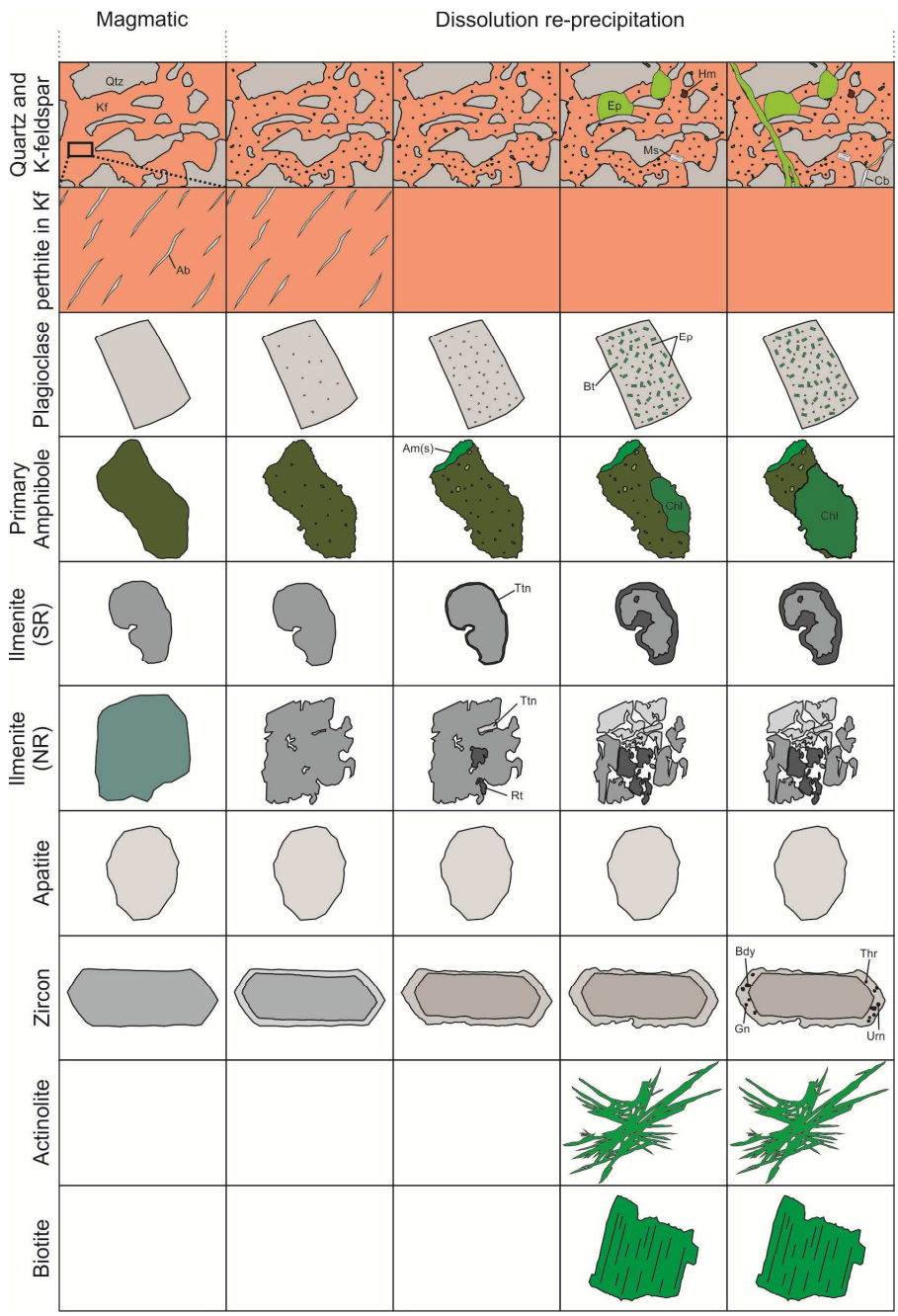

Figure 2-22.Schematic diagram summarizing the evolution of the mineral textures in the GR. The figure shows the transition for each primary phase and the two main secondary phases from the NR (ferro-actinolite) and SR (biotite) from their original habit through the alteration via coupled dissolution-precipitation. Note that this figure does not incorporate every alteration phase.

Table 2-1. Summary of petrographic observations of alteration mineralogy from GR samples.

Mineral	Location	Size (mm)	Shape	Habit	Comments
quartz	SR, NR	0.1 - 5	equant	s, a	Present asrecrystallized aggregates; more abundant in the SR in shear zones; hosts abvundant secondary fluid inclusions.
plagioclase (albite)	SR, NR	0.15 - 4	tabular to lath-like	e, s	Rare albite twinning at bottom of SR maintain albite twinning; Ab_{100} composition; has pitted texture that are filled with epidote and biotite; laths often rimmed by epidote ± biotite ± actinolite.
alkali feldspar (Kf)	SR, NR	0.1 - 3	tabular	s, a	Contains <2 wt. % Ba; Or_{100} composition; ;ften exhibits "pitted" texture but to a lesser degree than plagioclase. Pits are often filled with secondary phases.
ferroactinolite	NR	0.05 - 0.4	fibrous, bladed	e, s, a	Coarser grained at bottom of SR, radial,needle-like habit very common, also occurs as replacement of primary amphibole. Can be intergrown with oxide phases
hornblende	SR, NR	0.05 - 0.7	subhedral to euhedral, lath-like	e, s	later altered to biotite, chlorite
ferrotschermakite	SR	0.1 - 0.4	subhedral to euhedral	e, s	Occurs near the bottom of the SR
epidote	SR, NR	0.05 - 0.3	rounded, equant	e, s, a	Usually occurs as small grains in large clotted zones and as inclusions in plagioclase. Can also be pervasive. Also most abundant phase as inclusion in plagioclase. Also present along grain boundaries.
biotite	SR	0.05 - 0.5	tabular, lath-like, aggregates	e	can be present as inclusions in alkali feldspar, commonly poorly to moderately foliated, can contain radiation halos from zircon, allanite inclusions, present along primary grain boundaries, infilling fractures. Green colour caused by Fe content. Usually exhibits a foliation.
chlorite	SR, NR	0.1 - 1	platey, radial	e, s, a	Occurs as inidividual grains and as aggregations, also as late veins. Often associated with biotite and/or epidote. Can be replacing biotite and secondary amphibole. More abundant in top half of the unit.
muscovite	SR, NR	0.05 - 0.5	tabular, lath-like, rarely equant	e, s, a	rare throughout most of unit but a few samples contain up to ~3 modal %
stilpnomelane	SR, NR	0.01 - 0.04	platey, radial, plumose	e, s	commonly exhibits radial texture
calcite	SR, NR	corona: 0.1-0.4; euhedral: 0.25-2	equant, aggregates	s, a	occurs as individual grains and as coronas around ilmenite (SR only)
titanite	SR, NR	0.01 - 0.1	diamond-shaped or rounded, irregular	e, s	most common alteration product from ilmenite, can occur as lamellar exsolution from ilmenite
hematite	SR, NR	0.01 - 0.03	aggregate, ~equant	s	occurs as alteration product of ilmenite
rutile	SR, NR	0.01 - 0.03	aggregate, rounded	a	occurs as an alteration product of ilmenite (alteration corona)
baddeleyite	SR, NR	~0.025 - 0.01	equant	s	can occur as inclusions in alkali feldspar, associated with zircon
uraninite	SR, NR	~0.025 - 0.01	equant	s	occurs only as inclusions in alkali feldspar
galena	SR, NR	0.01	equant	s	occurs only as inclusions in alkali feldspar
allanite	SR, NR	0.02 - 0.1	equant, aggregate	s	commonly associated with epidote, either as rim or as core rimmed by epidote
zircon	SR, NR	0.01-0.05	equant, rounded	e,s	commonly associated with epidote

Table 2-2. Average EMPA data for amphibole grains from the GR.

	GNb-36 n=5 hornblende (least alt.)		GNb-36 n=6 hornblende (alt.)		GNb-33 n=7 hornblende (alt.)		GNb-36 n=8 actinolite		GNb-41 n=10 actinolite		GNa-14-11 n=9 tschermakite	
	avg.	σ	avg.	σ	avg.	σ	avg.	σ	avg.	σ	avg.	σ
SiO_2	48.51	0.82	46.18	0.79	43.83	1.93	50.52	0.53	50.41	0.46	39.98	0.53
TiO2	0.66	0.33	1.05	0.22	1.20	0.41	0.38	0.14	0.42	0.15	0.30	0.05
$Al2O_3$	4.21	0.58	5.10	0.36	5.71	1.15	1.49	0.28	1.45	0.30	14.61	0.67
FeO	20.71	1.53	24.40	1.07	28.44	1.35	28.05	1.93	27.20	1.08	24.35	0.23
Cr_2O_3	0.00	0.00	0.00	0.01	0.00	0.00	0.01	0.01	0.00	0.00	0.00	0.00
MnO	0.34	0.04	0.36	0.04	0.38	0.07	0.36	0.09	0.28	0.07	0.44	0.02
MgO	10.97	0.91	8.40	0.82	5.47	1.37	6.96	1.03	7.14	0.54	4.49	0.26
CaO	10.11	0.46	9.69	0.39	9.71	0.27	8.25	1.81	9.26	0.71	11.51	0.12
Na_2O	1.76	0.11	1.98	0.09	2.00	0.16	1.34	0.42	1.21	0.15	1.35	0.07
K_2O	0.55	0.10	0.70	0.08	0.86	0.18	0.20	0.08	0.28	0.06	0.87	0.07
F	1.03	0.20	1.01	0.32	1.34	0.27	0.09	0.05	0.27	0.10	0.02	0.05
Cl	0.26	0.06	0.35	0.09	0.38	0.16	0.18	0.03	0.15	0.04	0.20	0.03
Subtotal	99.11	0.30	99.22	0.41	99.33	0.40	97.81	0.49	98.07	0.32	98.12	0.31
O = Cl, F	0.49	0.07	0.50	0.13	0.65	0.12	0.08	0.02	0.15	0.04	0.05	0.02
Total	98.62	0.32	98.71	0.36	98.68	0.32	97.73	0.48	97.93	0.31	98.06	0.33
Si (p.f.u.)	7.27	0.09	7.07	0.07	6.89	0.22	7.75	0.05	7.75	0.06	6.15	0.08
Al	0.68	0.10	0.87	0.07	1.03	0.23	0.17	0.05	0.19	0.05	1.85	0.08
Fe^{3+}	0.05	0.02	0.07	0.02	0.08	0.02	0.08	0.06	0.06	0.03	0.00	0.00
Ti	0.00	0.00	0.00	0.00	0.00	0.00	0.00	0.00	0.00	0.00	0.00	0.00
T sites	8.00	0.00	8.00	0.00	8.00	0.00	8.01	0.03	8.00	0.00	8.00	0.00
Al	0.06	0.01	0.05	0.01	0.03	0.01	0.09	0.02	0.07	0.01	0.80	0.05
Cr	0.00	0.00	0.00	0.00	0.00	0.00	0.00	0.00	0.00	0.00	0.00	0.00
Fe^{3+}	0.43	0.09	0.48	0.11	0.45	0.08	0.63	0.31	0.44	0.16	0.52	0.03
Ti	0.07	0.04	0.12	0.03	0.14	0.05	0.04	0.02	0.05	0.02	0.03	0.01
Mg	2.45	0.18	1.92	0.17	1.28	0.30	1.59	0.22	1.64	0.12	1.03	0.06
Fe^{2+}	1.96	0.17	2.41	0.20	3.07	0.33	2.62	0.43	2.79	0.22	2.59	0.03
Mn	0.02	0.00	0.02	0.00	0.02	0.00	0.02	0.01	0.02	0.00	0.03	0.00
Ca	0.00	0.00	0.00	0.00	0.00	0.00	0.00	0.00	0.00	0.00	0.00	0.00
C sites	5.00	0.00	5.00	0.00	5.00	0.00	5.00	0.00	5.00	0.00	5.00	0.00
Mg	0.00	0.00	0.00	0.00	0.00	0.00	0.00	0.00	0.00	0.00	0.00	0.00
Fe^{2+}	0.16	0.03	0.17	0.03	0.15	0.03	0.27	0.12	0.21	0.05	0.02	0.01
Mn	0.02	0.00	0.02	0.00	0.03	0.00	0.02	0.01	0.02	0.00	0.03	0.00
Ca	1.62	0.07	1.59	0.07	1.64	0.06	1.36	0.30	1.53	0.12	1.90	0.02
Na	0.20	0.04	0.22	0.04	0.19	0.03	0.20	0.08	0.18	0.02	0.06	0.01
B sites	2.00	0.00	2.00	0.00	2.00	0.00	1.86	0.11	1.93	0.06	2.00	0.00
Ca	0.00	0.00	0.00	0.00	0.00	0.00	0.00	0.00	0.00	0.00	0.00	0.00
Na	0.31	0.04	0.37	0.06	0.42	0.08	0.19	0.05	0.18	0.02	0.35	0.02
K	0.11	0.02	0.14	0.02	0.17	0.04	0.04	0.02	0.05	0.01	0.17	0.01
A sites	0.42	0.04	0.51	0.07	0.59	0.12	0.23	0.03	0.24	0.03	0.52	0.02
cations	15.42	0.04	15.51	0.07	15.59	0.12	15.10	0.08	15.17	0.07	15.52	0.02
Cl	0.07	0.02	0.09	0.02	0.10	0.04	0.05	0.01	0.04	0.01	0.05	0.01
F	0.49	0.09	0.49	0.16	0.67	0.13	0.05	0.02	0.13	0.05	0.01	0.02
oxygen	23.07	0.02	23.06	0.02	23.03	0.02	23.17	0.07	23.14	0.01	23.00	0.00
Mg#	0.56	0.04	0.44	0.04	0.29	0.07	0.38	0.06	0.37	0.03	0.28	0.01
Fe#	0.44	0.04	0.56	0.04	0.71	0.07	0.62	0.06	0.63	0.03	0.72	0.01

Cations calculated on the basis of 23 (O, F, Cl) p.f.u. and the average ferric iron constraint (values obtained from the average 15eNK and 13eCNK)

Table 2-3. Average EMPA data for epidote grains from the GR.

	GNa-26 n=4 blocky		GNa-43 n=3 blocky		GNa-64 n=3 blocky		GNb-06 n=6 blocky		GNb-12 n=7 blocky		GNb-33 n=2 blocky		GNb-41 n=4 blocky	
	avg.	σ	avg.	σ	avg.	σ	avg.	σ	avg.	σ	avg.	σ	avg.	σ
SiO_2	38.00	0.26	37.27	0.28	37.89	0.24	37.27	0.22	37.28	0.24	37.34	0.08	36.97	0.46
Al_2O_3	26.13	0.81	22.14	1.60	25.79	0.30	21.74	1.45	23.38	0.74	23.24	0.59	21.35	0.63
FeO	9.27	0.88	13.76	1.51	10.26	0.25	14.83	1.27	13.19	0.92	13.57	0.30	14.26	0.54
Fe_2O_3	0.00	0.00	0.00	0.00	0.00	0.00	0.00	0.00	0.00	0.00	0.00	0.00	0.00	0.00
MgO	0.01	0.01	0.02	0.03	0.00	0.00	0.02	0.03	0.02	0.02	0.02	0.02	0.00	0.00
CaO	23.35	0.29	23.13	0.19	23.48	0.04	22.25	0.64	23.31	0.14	23.39	0.28	22.76	0.62
Total	96.74	0.44	96.32	0.26	97.42	0.24	96.11	0.40	97.17	0.19	97.56	0.12	95.35	1.58
Si	2.99	0.01	2.99	0.01	2.97	0.01	3.00	0.01	2.96	0.01	2.96	0.00	3.00	0.01
Al	2.42	0.06	2.09	0.13	2.38	0.02	2.06	0.13	2.19	0.06	2.17	0.05	2.04	0.04
Fe^{3+}	0.61	0.06	0.92	0.11	0.67	0.02	1.00	0.09	0.87	0.06	0.90	0.02	0.97	0.04
Mg	0.00	0.00	0.00	0.00	0.00	0.00	0.00	0.00	0.00	0.00	0.00	0.00	0.00	0.00
Ca	1.97	0.02	1.99	0.03	1.97	0.01	1.92	0.06	1.98	0.01	1.98	0.03	1.98	0.03
cations	7.99	0.01	8.00	0.01	8.00	0.01	7.97	0.02	8.01	0.01	8.01	0.01	7.99	0.01
O	12.50	0.00	12.50	0.00	12.50	0.00	12.50	0.00	12.50	0.00	12.50	0.00	12.50	0.00
Ps	0.20	0.00	0.30	0.00	0.20	0.00	0.33	0.05	0.30	0.00	0.30	0.00	0.30	0.00

	GNb-51 n=16 blocky		GNa-14 n=3 pit		GNa-26 n=5 pit		GNa-43 n=2 pit		GNa-62 n=5 pit		GNb-41 n=3 pit		GNb-06 n=4 vein	
	avg.	σ	avg.	σ	avg.	σ	avg.	σ	avg.	σ	avg.	σ	avg.	σ
SiO_2	37.71	0.47	37.83	0.18	37.62	0.53	37.46	0.36	38.21	0.21	37.55	0.21	37.02	0.14
Al_2O_3	23.08	0.60	25.77	1.27	24.36	1.32	22.74	0.02	26.67	0.62	22.65	0.14	22.02	0.85
FeO	13.40	0.30	10.39	1.53	11.47	1.54	12.99	0.06	8.88	0.64	13.15	0.58	14.70	0.69
Fe_2O_3	0.00	0.00	0.00	0.00	0.00	0.00	0.00	0.00	0.00	0.00	0.00	0.00	0.00	0.00
MgO	0.01	0.02	0.01	0.01	0.02	0.02	0.01	0.01	0.00	0.00	0.13	0.21	0.03	0.02
CaO	23.20	0.24	23.53	0.24	22.90	0.76	23.32	0.11	23.42	0.11	22.62	0.55	22.39	0.38
Total	97.40	0.26	97.53	0.14	96.37	1.06	96.52	0.32	97.18	0.31	96.10	0.14	96.15	0.17
Si	2.99	0.04	2.97	0.01	2.99	0.00	2.99	0.02	2.99	0.01	3.01	0.01	2.98	0.01
Al	2.15	0.05	2.38	0.11	2.28	0.10	2.14	0.01	2.46	0.05	2.14	0.01	2.09	0.07
Fe^{3+}	0.89	0.02	0.68	0.10	0.76	0.11	0.87	0.00	0.58	0.04	0.88	0.04	0.99	0.05
Mg	0.00	0.00	0.00	0.00	0.00	0.00	0.00	0.00	0.00	0.00	0.02	0.02	0.00	0.00
Ca	1.97	0.02	1.98	0.01	1.95	0.04	2.00	0.02	1.96	0.01	1.94	0.04	1.93	0.04
cations	7.99	0.02	8.00	0.01	7.98	0.01	8.00	0.01	7.99	0.00	7.98	0.00	7.98	0.01
O	12.50	0.00	12.50	0.00	12.50	0.00	12.50	0.00	12.50	0.00	12.50	0.00	12.50	0.00
Ps	0.30	0.00	0.20	0.00	0.24	0.05	0.30	0.00	0.20	0.00	0.30	0.00	0.30	0.00

Mineral formula based on 12.5 oxygens

Table 2-4. Average EMPA data for chlorite grains from the GR.

	GNa-14 n=2		GNa-26 n=4		GNa-43 n=5		GNa-62 n=6		GNa-62-9 (vein) n=3		GNa-64 n=6	
Sample	avg.	σ	avg.	σ	avg.	σ	avg.	σ	avg.	σ	avg.	σ
SiO_2	24.23	0.20	24.06	0.19	23.21	0.27	24.12	0.64	23.47	0.27	23.34	0.25
TiO_2	0.04	0.03	0.06	0.02	0.04	0.04	0.07	0.05	0.04	0.01	0.05	0.02
Al_2O_3	21.51	0.14	20.77	0.14	20.34	0.58	19.81	0.59	19.89	0.33	20.18	0.42
Fe_2O_3	0.00	0.00	0.00	0.00	0.00	0.00	0.00	0.00	0.00	0.00	0.00	0.00
FeO	33.48	0.45	34.88	0.18	39.93	1.82	38.66	0.46	38.98	0.47	40.57	0.22
MnO	0.55	0.05	0.74	0.02	0.72	0.04	0.75	0.01	0.75	0.03	0.84	0.02
MgO	9.59	0.42	8.07	0.14	3.80	0.30	5.27	0.12	5.15	0.26	4.54	0.15
CaO	0.00	0.00	0.01	0.01	0.01	0.03	0.02	0.02	0.01	0.01	0.00	0.01
Na_2O	0.00	0.00	0.00	0.00	0.00	0.00	0.00	0.00	0.00	0.00	0.02	0.05
K_2O	0.01	0.01	0.01	0.02	0.02	0.03	0.26	0.38	0.00	0.00	0.01	0.02
H_2O	10.56	0.05	11.38	0.27	11.89	1.47	11.02	0.69	11.71	0.99	10.41	0.29
Total	99.98	0.01	99.98	0.03	99.96	0.06	99.98	0.02	99.99	0.01	99.97	0.04
Si	4.12	0.02	4.09	0.04	4.02	0.08	4.19	0.13	4.05	0.09	4.12	0.05
Al^{IV}	3.88	0.02	3.91	0.04	3.96	0.06	3.81	0.13	3.92	0.06	3.88	0.05
T sites	8.00	0.00	8.00	0.00	7.97	0.06	8.00	0.00	7.97	0.05	8.00	0.00
Al^{VI}	0.43	0.02	0.25	0.05	0.19	0.20	0.24	0.16	0.13	0.16	0.31	0.08
Ti	0.01	0.00	0.01	0.00	0.01	0.01	0.01	0.01	0.01	0.00	0.01	0.00
Fe^{3+}	0.00	0.00	0.00	0.00	0.00	0.00	0.00	0.00	0.00	0.00	0.00	0.00
Fe^{2+}	4.76	0.08	4.96	0.04	5.78	0.38	5.62	0.08	5.63	0.12	5.99	0.05
Mn	0.08	0.01	0.11	0.00	0.11	0.01	0.11	0.00	0.11	0.00	0.13	0.00
Mg	2.43	0.10	2.04	0.04	0.98	0.06	1.37	0.04	1.32	0.07	1.20	0.04
Ca	0.00	0.00	0.00	0.00	0.00	0.01	0.00	0.00	0.00	0.00	0.00	0.00
Na	0.00	0.00	0.00	0.00	0.00	0.00	0.00	0.00	0.00	0.00	0.01	0.02
K	0.00	0.00	0.00	0.00	0.00	0.01	0.06	0.08	0.00	0.00	0.00	0.00
cations	15.71	0.01	15.37	0.09	15.04	0.53	15.41	0.24	15.17	0.35	15.64	0.10
F	0.00	0.00	0.01	0.01	0.03	0.03	0.01	0.01	0.00	0.01	0.00	0.00
Cl	0.02	0.01	0.02	0.01	0.05	0.06	0.03	0.02	0.03	0.02	0.01	0.01
OH	12.00	0.03	12.91	0.27	13.71	1.36	12.78	0.71	13.49	0.99	12.27	0.30
O	36.00	0.00	36.00	0.00	36.00	0.00	36.00	0.00	36.00	0.00	36.00	0.00
Fe#	0.66	0.01	0.71	0.01	0.85	0.01	0.81	0.01	0.81	0.01	0.83	0.01
Mg#	0.34	0.01	0.29	0.01	0.15	0.01	0.20	0.01	0.19	0.01	0.17	0.01

Cations calculated on the basis of 24 (O, OH, F, Cl)

Table 2-4 (cont'd). Average EMPA data for chlorite grains from the GR.

	GNa-78 n=6		GNb-06 n=6		GNb-12 n=13		GNb-33 n=12		GNb-51 n=11	
Sample	avg.	σ	avg.	σ	avg.	σ	avg.	σ	avg.	σ
SiO_2	24.08	0.53	23.94	0.51	24.66	0.25	24.83	0.31	25.13	0.57
TiO_2	0.09	0.05	0.02	0.02	0.01	0.03	0.00	0.01	0.07	0.09
Al_2O_3	20.56	0.29	18.94	0.82	18.36	0.56	18.39	0.41	17.55	0.69
Fe_2O_3	0.00	0.00	0.00	0.00	0.00	0.00	0.00	0.00	0.00	0.00
FeO	36.34	0.24	42.12	0.33	40.35	0.60	37.96	0.34	40.31	0.24
MnO	0.57	0.02	0.30	0.02	0.42	0.03	0.30	0.02	0.45	0.03
MgO	7.48	0.21	3.34	0.59	5.55	0.33	7.49	0.30	5.87	0.43
CaO	0.05	0.07	0.04	0.03	0.05	0.03	0.05	0.02	0.10	0.04
Na_2O	0.08	0.11	0.00	0.00	0.04	0.05	0.04	0.05	0.02	0.04
K_2O	0.14	0.22	0.01	0.01	0.02	0.03	0.02	0.01	0.01	0.02
H_2O	10.59	0.79	11.29	0.27	10.51	0.27	10.88	0.37	10.46	0.36
Total	99.98	0.02	100.00	0.02	99.97	0.02	99.97	0.02	99.97	0.03
Si	4.16	0.12	4.20	0.09	4.33	0.06	4.30	0.06	4.42	0.10
Al^{IV}	3.84	0.12	3.79	0.09	3.66	0.06	3.68	0.06	3.56	0.12
T sites	8.00	0.00	7.99	0.02	8.00	0.01	7.98	0.03	7.98	0.03
Al^{VI}	0.34	0.19	0.12	0.10	0.13	0.08	0.07	0.06	0.07	0.07
Ti	0.01	0.01	0.00	0.00	0.00	0.00	0.00	0.00	0.01	0.01
Fe^{3+}	0.00	0.00	0.00	0.00	0.00	0.00	0.00	0.00	0.00	0.00
Fe^{2+}	5.24	0.01	6.18	0.06	5.93	0.11	5.49	0.07	5.93	0.04
Mn	0.08	0.00	0.05	0.00	0.06	0.00	0.04	0.00	0.07	0.00
Mg	1.92	0.06	0.87	0.15	1.45	0.08	1.93	0.07	1.54	0.11
Ca	0.01	0.01	0.01	0.01	0.01	0.00	0.01	0.00	0.02	0.01
Na	0.03	0.04	0.00	0.00	0.01	0.02	0.01	0.02	0.01	0.01
K	0.03	0.05	0.00	0.00	0.00	0.01	0.00	0.00	0.00	0.00
cations	15.66	0.26	15.23	0.09	15.60	0.09	15.54	0.13	15.62	0.13
F	0.00	0.00	0.00	0.00	0.01	0.02	0.01	0.02	0.00	0.01
Cl	0.02	0.01	0.01	0.01	0.01	0.01	0.01	0.02	0.02	0.02
OH	12.20	0.83	13.22	0.28	12.33	0.28	12.57	0.38	12.27	0.39
O	36.00	0.00	36.00	0.00	36.00	0.00	36.00	0.00	36.00	0.00
Fe#	0.73	0.01	0.88	0.02	0.80	0.01	0.74	0.01	0.79	0.01
Mg#	0.27	0.01	0.12	0.02	0.20	0.01	0.26	0.01	0.21	0.01

Cations calculated on the basis of 24 (O, OH, F, Cl)

Table 2-5. Average EMPA data for stilpnomelane grains from the GR.

	GNb-6 n = 7		GNb-6 (vein) n = 4		GNb-12 n = 9		GNb-33 n = 3		GNb-51 n = 2	
	avg.	σ	avg.	σ	avg.	σ	avg.	σ	avg.	σ
SiO2	45.05	0.20	44.74	0.27	45.31	0.53	45.39	0.57	44.95	0.43
TiO2	0.01	0.01	0.00	0.00	0.03	0.05	0.02	0.03	0.00	0.00
Al2O3	6.55	0.13	6.39	0.20	6.60	0.32	6.29	0.37	7.02	0.01
Cr2O3	0.00	0.00	0.01	0.01	0.00	0.00	0.00	0.00	0.00	0.00
FeO	34.28	0.20	33.91	0.32	33.18	0.28	31.87	0.21	34.50	0.03
MnO	0.70	0.03	0.66	0.01	1.02	0.03	0.72	0.02	1.18	0.01
MgO	2.00	0.06	2.07	0.05	3.22	0.13	4.53	0.17	2.87	0.03
CaO	0.25	0.05	0.24	0.03	0.27	0.07	0.24	0.11	0.09	0.03
Na2O	0.35	0.09	0.15	0.03	0.67	0.10	0.59	0.11	0.79	0.14
K2O	1.83	0.10	1.86	0.09	1.83	0.17	1.50	0.05	1.56	0.43
F	0.01	0.01	0.02	0.03	0.00	0.00	0.00	0.00	0.00	0.00
Cl	0.02	0.00	0.02	0.00	0.01	0.01	0.01	0.01	0.02	0.00
Total	91.05	0.88	90.07	1.04	92.13	1.70	91.16	1.65	92.99	1.12
Si	7.902	0.027	7.922	0.054	7.826	0.075	7.847	0.076	7.738	0.004
Ti	0.001	0.001	0.000	0.000	0.004	0.006	0.002	0.004	0.000	0.000
Al	1.354	0.025	1.333	0.035	1.344	0.066	1.282	0.076	1.424	0.013
Fe	5.029	0.025	5.022	0.036	4.794	0.035	4.608	0.017	4.967	0.046
Mn	0.104	0.004	0.098	0.002	0.149	0.005	0.105	0.002	0.172	0.003
Mg	0.522	0.015	0.546	0.014	0.828	0.035	1.168	0.044	0.736	0.002
Ca	0.048	0.008	0.046	0.006	0.049	0.013	0.044	0.020	0.017	0.006
Na	0.119	0.031	0.053	0.011	0.224	0.034	0.199	0.035	0.265	0.046
K	0.409	0.023	0.421	0.019	0.403	0.035	0.330	0.009	0.343	0.091
F	0.003	0.008	0.012	0.018	0.000	0.000	0.000	0.000	0.000	0.000
Cl	0.005	0.001	0.006	0.001	0.004	0.003	0.004	0.004	0.006	0.001
Total	15.497	0.033	15.460	0.053	15.625	0.068	15.588	0.050	15.667	0.078

Cations calculated based on 15 octahedral and tetrahedral p.f.u. and 27 (O,OH,F,Cl)

Table 2-6. Average EMPA data for titanite grains from the GR.

	GNa-26 n = 6		GNa-62 n = 5		GNa-64 n = 1		GNb-36 n = 2		GNb-41 n = 8		GNb-51 n = 2	
	avg	stdev	avg	stdev	avg	stdev	avg	stdev	avg	stdev	avg	stdev
SiO2	30.42	0.10	30.40	0.30	30.60	n/a	30.57	0.39	30.75	0.36	31.14	0.08
TiO2	36.65	0.38	36.76	0.35	36.16	n/a	30.30	0.68	32.97	1.89	26.41	0.07
Al2O3	2.27	0.17	2.38	0.22	2.76	n/a	5.40	0.17	3.65	0.98	5.50	0.16
FeO	0.55	0.07	0.57	0.07	0.61	n/a	2.12	0.73	1.83	0.48	4.81	0.21
MnO	0.06	0.01	0.03	0.01	0.04	n/a	0.02	0.00	0.01	0.01	0.02	0.03
CaO	28.60	0.17	28.54	0.30	29.26	n/a	27.97	0.04	28.40	0.28	28.20	0.18
F	0.42	0.10	0.55	0.13	0.61	n/a	1.47	0.35	0.85	0.32	1.16	0.34
Total	98.97	0.37	99.23	0.88	100.02	n/a	97.85	0.12	98.46	0.46	97.24	0.59
Si	0.997	0.004	0.992	0.006	0.992	n/a	1.001	0.010	1.010	0.011	1.040	0.009
Ti	0.904	0.009	0.903	0.011	0.881	n/a	0.746	0.015	0.814	0.049	0.663	0.005
Al	0.088	0.007	0.091	0.008	0.105	n/a	0.208	0.006	0.141	0.037	0.216	0.004
Fe	0.015	0.002	0.016	0.002	0.016	n/a	0.058	0.020	0.050	0.013	0.134	0.007
Ca	1.005	0.005	0.998	0.003	1.016	n/a	0.981	0.004	0.999	0.007	1.009	0.005
F	0.044	0.011	0.057	0.013	0.062	n/a	0.152	0.036	0.089	0.033	0.122	0.034
Cation total	3.052	0.006	3.057	0.008	3.073	n/a	3.146	0.029	3.103	0.029	3.185	0.013

Mineral formula based on 5 oxygens
Cl was below detection limit

Table 2-7. Average EMPA data for biotite grains from the GR.

	GNa-14		GNa-26		GNa-43		GNa-62		GNa-64		GNa-78	
	n=4		n=5		n=5		n=5		n=8		n=13	
	avg.	σ	avg.	σ	avg.	σ	avg.	σ	avg.	σ	avg.	σ
SiO_2	34.68	0.31	34.49	0.40	33.54	0.16	33.47	0.55	33.87	0.29	34.34	0.38
TiO_2	1.84	0.17	1.91	0.20	1.49	0.11	1.23	0.10	1.74	0.19	2.13	0.11
Al_2O_3	16.67	0.13	16.77	0.18	16.22	0.08	15.79	0.21	16.47	0.23	16.43	0.29
Cr_2O_3	0.00	0.00	0.01	0.01	0.02	0.01	0.01	0.00	0.01	0.02	0.01	0.02
FeO	26.37	0.14	26.56	0.21	31.25	0.18	30.39	0.39	30.86	0.37	28.00	0.20
MnO	0.29	0.01	0.36	0.02	0.33	0.01	0.37	0.03	0.40	0.01	0.28	0.01
MgO	6.75	0.08	5.69	0.06	3.11	0.06	4.53	0.16	3.62	0.20	5.51	0.15
BaO	ND	ND	ND	ND	ND	ND	ND	ND	ND	ND	ND	ND
CaO	0.01	0.01	0.03	0.03	0.02	0.02	0.08	0.07	0.18	0.15	0.04	0.05
Na_2O	0.01	0.01	0.02	0.02	0.01	0.02	0.03	0.03	0.07	0.08	0.08	0.09
K_2O	9.64	0.08	9.33	0.30	9.32	0.10	8.57	0.76	8.84	0.39	9.56	0.21
F	0.14	0.04	0.20	0.03	0.25	0.05	0.27	0.06	0.25	0.07	0.27	0.04
Cl	0.18	0.02	0.20	0.01	0.32	0.01	0.27	0.02	0.16	0.01	0.09	0.01
H_2O	3.40	0.29	4.44	0.70	4.13	0.15	5.01	1.15	3.53	0.42	3.26	0.58
Subtotal	100	0	100	0	100	0	100	0	100	0	100	0
O = F, Cl	0.10	0.01	0.13	0.01	0.18	0.02	0.18	0.02	0.14	0.03	0.13	0.02
Total	99.90	0.01	99.87	0.01	99.82	0.02	99.82	0.02	99.86	0.03	99.87	0.02
Si	5.51	0.03	5.57	0.03	5.54	0.03	5.48	0.06	5.51	0.04	5.52	0.04
Al^{IV}	2.49	0.03	2.43	0.03	2.46	0.03	2.52	0.06	2.49	0.04	2.48	0.04
Al^{VI}	0.63	0.04	0.76	0.03	0.69	0.02	0.53	0.06	0.66	0.07	0.62	0.04
Ti	0.22	0.02	0.23	0.02	0.18	0.01	0.15	0.01	0.21	0.02	0.26	0.01
Fe^{2+}	3.51	0.03	3.59	0.03	4.31	0.02	4.16	0.03	4.20	0.04	3.76	0.04
Cr	0.00	0.00	0.00	0.00	0.00	0.00	0.00	0.00	0.00	0.00	0.00	0.00
Mn	0.04	0.00	0.05	0.00	0.05	0.00	0.05	0.00	0.06	0.00	0.04	0.00
Mg	1.60	0.01	1.37	0.02	0.77	0.01	1.11	0.04	0.88	0.05	1.32	0.03
Ba	0.00	0.00	0.00	0.00	0.00	0.00	0.00	0.00	0.00	0.00	0.00	0.00
Ca	0.00	0.00	0.01	0.01	0.00	0.00	0.01	0.01	0.03	0.03	0.01	0.01
Na	0.00	0.00	0.01	0.01	0.00	0.01	0.01	0.01	0.02	0.02	0.03	0.03
K	1.96	0.02	1.92	0.06	1.96	0.02	1.79	0.16	1.83	0.09	1.96	0.05
cations	15.96	0.02	15.93	0.05	15.97	0.02	15.81	0.14	15.89	0.07	15.99	0.04
F	0.07	0.02	0.10	0.01	0.13	0.03	0.14	0.03	0.13	0.03	0.14	0.02
Cl	0.05	0.01	0.05	0.00	0.09	0.00	0.08	0.01	0.04	0.00	0.03	0.00
OH	3.61	0.32	4.79	0.80	4.55	0.17	5.49	1.31	3.83	0.46	3.50	0.65
Fe#	0.69	0.01	0.72	0.00	0.85	0.00	0.79	0.01	0.83	0.01	0.74	0.01
Mg#	0.31	0.01	0.28	0.00	0.15	0.00	0.21	0.01	0.17	0.01	0.26	0.01

Cations calculated on the basis of 24 (O, OH, F, Cl)

Table 2-8. Analysis for whole rock major and trace elements from the GR.

Sample	GNa-7	Gna-13	GNa-21	GNa-28	GNa-38	GNa-44	GNa-52	GNa-62	GNa-69	GNa-74	GNa-80
SiO_2 (wt. %)	71	59.9	60.8	55.7	73.5	72.8	69.5	68.9	70.1	69.9	70.6
TiO_2	0.83	1.83	1.45	1.3	0.46	0.43	0.69	0.85	0.74	0.73	0.73
Al_2O_3	13.05	13.6	13.85	17.4	12.45	12.2	12.4	12.4	12.15	12.1	12.15
Fe_2O_3	1.01	1.87	2.01	2.17	1.04	0.84	1.15	0.86	0.86	1.20	0.86
FeO	3.19	7.03	6.14	6.78	3.01	3.13	4.09	5.49	4.09	4.48	5.24
MnO	0.05	0.14	0.11	0.07	0.05	0.05	0.07	0.09	0.07	0.08	0.08
MgO	0.73	2.07	1.86	2.27	0.53	0.27	1.09	0.9	0.49	0.97	0.88
CaO	1.92	4.35	2.63	0.72	0.23	0.55	1.82	1.59	1	0.87	0.85
Na_2O	5.72	5.19	4.81	7.44	4.05	4.04	5.16	4.01	4.05	3.73	4.43
K_2O	1.34	1.76	2.32	2.92	4.46	4.39	1.68	3.31	3.38	3.65	2.59
P_2O_5	0.14	0.6	0.31	0.27	0.06	0.05	0.19	0.19	0.14	0.14	0.14
BaO	0.06	0.07	0.09	0.09	0.14	0.16	0.06	0.12	0.12	0.14	0.1
C	0.03	0.04	0.02	0.01	0.03	0.02	0.01	0.06	0.01	0.01	0.01
Cl (ppm)	330	650	500	500	330	420	370	490	250	220	230
F (ppm)	490	950	840	1010	300	290	530	810	600	710	750
LOI	1.03	1.24	1.63	1.52	0.82	0.69	0.74	0.87	0.84	0.99	0.81
$\delta^{18}O$ ‰	-	6.2	-	-	7.5	7.4	-	-	-	-	7.0
Fe#	0.85	0.81	0.81	0.79	0.88	0.94	0.83	0.88	0.91	0.85	0.88
Rb (ppm)	45	46	78	79	137	127	55	99	96	139	93
Sr	285	273	264	63.3	92.5	117	238	196	130.5	127.5	120
Ba	494	604	828	797	1245	1400	484	1010	1090	1220	912
Cs	0.5	0.5	0.9	1.3	1.1	1.3	1.0	1.3	0.6	0.9	0.9
Ga	18.7	19.7	21.5	25.5	18.6	18.2	18.2	18.8	17.7	18.6	18.4
As	0.8	0.5	0.4	0.6	0.7	0.9	3.3	1.7	0.4	0.4	0.7
Nb	15	14.1	15.1	19.7	16.1	14.6	6.8	14.4	15.3	15.3	15.4
Cu	3	1	1	19	<1	3	<1	1	1	<1	1
Zn	30	59	53	53	36	37	47	71	49	56	42
Pb	<2	3	<2	5	3	5	3	7	3	5	3
Th	16.9	10.5	12.9	16.4	18.4	18.1	18.4	13.3	15.1	14.6	15.0
U	3.38	2.22	2.53	3.3	2.97	2.66	3.41	2.75	2.9	2.75	3.03
Zr	323	237	248	315	404	286	330	288	323	298	304
Y	30	30.9	31.1	31.2	29.7	29.8	21.7	32	27.3	22.1	32.4
Hf	8.7	6.4	6.8	8.5	11.2	8.1	9	7.4	8.2	7.6	7.9
Nb	15	14.1	15.1	19.7	16.1	14.6	6.8	14.4	15.3	15.3	15.4
Sc	10	22	21	16	8	8	12	14	11	10	10
V	58	65	104	100	8	6	55	9	15	16	22
Cr	20	10	20	20	20	20	10	20	10	10	20
Co	7	16	13	19	2	2	7	7	5	6	8
La	56	47	58	41	68	68	43	57	42	34	61
Ce	110	101	110	73	113	133	91	116	102	58	125
Pr	12.6	12.0	13.4	9.6	15.5	14.8	9.5	13.3	10.3	8.0	14.0
Nd	44.7	46.2	48.8	35.8	54.2	51.9	33.8	50.2	38.1	29.6	51.2
Sm	8.07	8.83	9.17	7.19	9.5	8.96	6.22	8.73	6.73	5.05	8.95
Eu	1.6	2.15	3.05	1.5	1.52	1.52	1.89	1.74	1.25	1.06	1.61
Gd	6.2	7.26	7.21	6.71	7.49	6.6	4.75	7	5.07	3.99	6.92
Tb	0.9	1.01	1.02	1.02	1.03	0.97	0.68	1.01	0.8	0.61	1.02
Dy	5.13	5.5	5.66	6.01	5.59	5.47	3.87	5.82	4.76	3.76	5.74
Ho	1.08	1.15	1.16	1.22	1.16	1.09	0.81	1.18	1.04	0.82	1.18
Er	3.13	3.15	3.2	3.42	3.22	3.01	2.35	3.17	2.93	2.43	3.27
Tm	0.47	0.45	0.48	0.51	0.5	0.46	0.36	0.48	0.47	0.39	0.49
Yb	3.06	2.91	3.13	3.36	3.14	2.99	2.36	3.07	3.18	2.7	3.2
Lu	0.48	0.44	0.47	0.51	0.49	0.45	0.37	0.47	0.5	0.42	0.49

Table 2-8 (cont'd). Analysis for whole rock major and trace elements from the GR.

Sample	GNb-7	GNb-11	GNb-14	GNb-19	GNb-22	GNb-28	GNb-35	GNb-43	GNb-50
SiO_2 (wt. %)	70.9	68.7	71.1	69.5	68.6	67.8	67.4	65.7	70.6
TiO_2	0.68	0.71	0.73	0.77	0.69	0.92	0.95	0.97	0.82
Al_2O_3	12.15	11.85	12.3	12.1	11.95	12.5	12.5	12.55	12.1
Fe_2O_3	2.51	1.26	1.92	1.84	1.48	3.62	1.95	2.27	1.33
FeO	3.32	4.34	3.45	3.96	4.22	3.38	4.98	4.48	4.09
MnO	0.07	0.09	0.09	0.09	0.08	0.1	0.1	0.06	0.07
MgO	0.48	0.57	0.55	0.55	0.54	0.72	0.91	2.21	0.73
CaO	2	1.7	1.87	1.69	1.77	3	2.11	0.92	1.46
Na_2O	4.12	4.22	4.25	3.73	3.32	3.69	4.01	3.67	3.65
K_2O	2.78	2.25	3.13	3.58	3.89	3.27	3.51	3.51	3.3
P_2O_5	0.12	0.14	0.16	0.15	0.14	0.25	0.27	0.26	0.18
BaO	0.06	0.11	0.12	0.13	0.13	0.12	0.11	0.04	0.12
C	0.01	0.09	0.04	0.01	0.01	0.01	0.01	0.01	0.03
Cl (ppm)	390	470	570	590	590	450	630	510	440
F (ppm)	430	690	840	790	830	570	900	680	400
LOI	1.6	1.81	1.44	1.38	1.45	1.27	1.47	2.45	1.38
$\delta^{18}O$ ‰	-	8.2	-	9.0	-	-	-	8.9	7.1
Fe#	0.91	0.91	0.90	0.91	0.91	0.89	0.88	0.74	0.88
Rb (ppm)	68	65	89	96	119	96	101	99	114
Sr	329	195	213	167.5	162	163	182.5	87.5	175.5
Ba	503	935	1075	1050	1170	1005	986	318	1080
Cs	0.3	0.3	0.4	0.5	0.5	0.4	0.7	1.1	0.4
Ga	19.5	18.8	19.4	17.8	19.2	20.2	19.4	18.6	17.5
As	0.3	0.5	0.4	1	0.6	1.4	1.3	0.5	0.9
Nb	15.2	14.8	15.3	14.3	14.9	13.5	13.7	12.7	11.3
Cu	14	3	2	2	3	7	3	<1	1
Zn	30	163	53	67	57	50	73	39	23
Pb	6	5	14	7	16	7	7	6	4
Th	13.9	15.4	15.2	12.9	15.0	13.5	13.2	12.4	12.3
U	3.32	3.14	3.31	2.9	3.32	3.01	3	2.8	3.31
Zr	295	320	318	270	306	284	280	258	240
Y	34.4	32.9	33.7	30.1	32.7	31.5	31.9	30.7	22.3
Hf	7.8	8	8.2	6.9	7.9	7.3	7.2	6.6	6.2
Nb	15.2	14.8	15.3	14.3	14.9	13.5	13.7	12.7	11.3
Sc	14	11	11	11	11	14	14	15	12
V	6	17	19	17	17	103	98	182	100
Cr	20	10	20	10	10	20	20	10	20
Co	5	6	6	6	6	13	13	13	10
La	53	64	62	55	60	56	55	69	29
Ce	107	122	125	113	120	112	112	85	54
Pr	12.7	14.3	14.1	12.6	13.3	12.8	12.7	13.2	7.0
Nd	47.3	52.7	51	46.1	49	47.1	47.8	48.4	28.1
Sm	8.47	8.92	8.83	7.92	8.47	8.19	8.32	8.23	5.27
Eu	2	1.67	1.72	1.62	1.67	1.84	1.75	1.68	1.38
Gd	7.05	7.12	7	6.44	7.07	6.83	7.14	6.95	4.6
Tb	1.06	1.06	1.04	0.95	1.05	1.01	1.07	0.97	0.68
Dy	6.18	6.01	5.93	5.42	5.97	5.78	5.9	5.39	3.88
Ho	1.27	1.22	1.24	1.13	1.23	1.2	1.21	1.11	0.82
Er	3.43	3.34	3.4	3.05	3.38	3.24	3.23	2.92	2.26
Tm	0.52	0.49	0.51	0.46	0.52	0.49	0.5	0.43	0.35
Yb	3.5	3.31	3.24	2.93	3.28	3.13	3.12	2.62	2.27
Lu	0.53	0.49	0.49	0.45	0.49	0.49	0.48	0.4	0.35

Table 2-9. Summary of mass balance calculations for representative samples from the NR GR.

Least Altered - Calculated	GNb-07	GNb-22	GNb-35	GNb-43	GNb-50
SiO_2	73.5562	72.8237	69.098	68.68	67.1129
Al_2O_3	13.6669	13.7319	16.2183	16.40	17.3879
CaO	2.5129	2.389	3.2526	3.72	3.9685
K_2O	4.5015	5.0981	4.5086	3.69	3.6904
Na_2O	3.319	3.1843	4.1495	4.41	4.7378
FeO	0.9318	1.083	1.083	1.23	1.2342
P_2O_5	0.4121	0.4121	0.4121	0.41	0.4121
TiO_2	0.5691	0.5833	0.5833	0.60	0.5975
MnO	0.0115	0.0151	0.0151	0.02	0.0187
MgO	0.4008	0.5343	0.5343	0.67	0.6678
Altered - Measured	**GNb-07**	**GNb-22**	**GNb-35**	**GNb-43**	**GNb-50**
SiO_2	70.9	68.6	67.4	65.7	70.6
Al_2O_3	12.15	11.95	12.5	12.55	12.1
CaO	2	1.77	2.11	0.92	1.46
K_2O	2.78	3.89	3.51	3.51	3.3
Na_2O	4.12	3.32	4.01	3.67	3.65
FeO	8.9	9.77	11.71	11	9.38
P_2O_5	0.12	0.14	0.27	0.26	0.18
TiO_2	0.68	0.69	0.95	0.97	0.82
MnO	0.07	0.08	0.1	0.06	0.07
MgO	0.48	0.54	0.91	2.21	0.73
GNb-07	**Least Alt**	**Altered**	**Mass Factor**	**Recon Comp**	**Mass Change**
SiO_2	73.56	70.90	1.12	79.75	6.20
Al_2O_3	13.67	12.15	1.12	13.67	0.00
CaO	2.51	2.00	1.12	2.25	-0.26
K_2O	4.50	2.78	1.12	3.13	-1.37
Na_2O	3.32	4.12	1.12	4.63	1.32
FeO	0.93	8.90	1.12	10.01	9.08
P_2O_5	0.41	0.12	1.12	0.13	-0.28
TiO_2	0.57	0.68	1.12	0.76	0.20
MnO	0.01	0.07	1.12	0.08	0.07
MgO	0.40	0.48	1.12	0.54	0.14
GNb-22	**Least Alt**	**Altered**	**Mass Factor**	**Recon Comp**	**Mass Change**
SiO_2	72.82	68.6	1.15	78.83	6.01
Al_2O_3	13.73	11.95	1.15	13.73	0.00
CaO	2.39	1.77	1.15	2.03	-0.36
K_2O	5.10	3.89	1.15	4.47	-0.63
Na_2O	3.18	3.32	1.15	3.82	0.63
FeO	1.08	9.77	1.15	11.23	10.14
P_2O_5	0.41	0.14	1.15	0.16	-0.25
TiO_2	0.58	0.69	1.15	0.79	0.21
MnO	0.02	0.08	1.15	0.09	0.08
MgO	0.53	0.54	1.15	0.62	0.09
GNb-43	**Least Alt**	**Altered**	**Mass Factor**	**Recon Comp**	**Mass Change**
SiO_2	68.68	65.7	1.31	85.83	17.15
Al_2O_3	16.40	12.55	1.31	16.40	0.00
CaO	3.72	0.92	1.31	1.20	-2.51
K_2O	3.69	3.51	1.31	4.59	0.90
Na_2O	4.41	3.67	1.31	4.79	0.38
FeO	1.23	11	1.31	14.37	13.14
P_2O_5	0.41	0.26	1.31	0.34	-0.07
TiO_2	0.60	0.97	1.31	1.27	0.67
MnO	0.02	0.06	1.31	0.08	0.06
MgO	0.67	2.21	1.31	2.89	2.22

Chapter 3

Evidence for generation and collapse of a large-scale hydrothermal system in a cooling impact melt sheet: The granophyre unit of the Sudbury Igneous Complex, Ontario, Canada

3.1 Abstract

The granophyre unit (GR) is the upper (1.5 km) portion of the ca. 2.5 km-thick Sudbury Igneous Complex (SIC) and contains geochemical and textural evidence for pervasive hydrothermal circulation and alteration. This alteration is preserved as heterogeneous assemblages of epidote, chlorite, stilpnomelane, titanite, biotite (South Range; SR), ferro-actinolite (North Range; NR) with lesser muscovite, ferrotschermakite (SR) and carbonate. Quartz-hosted fluid inclusion petrography and microthermometry of select GR samples reveal three fluid inclusion assemblages (FIA) at 20°C: (1) L + V aqueous inclusions with 30 vol. % vapour; (2) liquid (L) + vapour (V) aqueous inclusions with 10 vol. % vapour; and (3) L + V + H (halite) aqueous inclusions with 10 vol.% V. Type 1 inclusions are rare (approximately 5% of inclusions) and record total homogenization temperatures (Th) ranging from 310° to 345°C with salinities of 20.2 to 23.5 wt. % equiv. NaCl. Type 2 inclusions are the most abundant (present in all samples) and yield Th values from 109° to 168°C with salinities of 20.1 to 24.0 wt. % equiv. NaCl. Type 3 inclusions are less abundant (present in approximately 30 % of samples) and yield vapour homogenization temperatures ranging from 108° to 155°C, Th values from 153° to 227°C, and salinities from 30.3 to 33.9 wt. % equiv. NaCl. Evaporate mounds are most representative of type 2 fluid inclusions and shows average cation contents (normalized to 100 wt. %) of Cl (52), Na

(40), Ca (6), K (1), and Fe (1) for the North Range and Cl (52), Na (39), Ca (6), K (3), Fe (2) from the South Range.

Whole rock oxygen isotope data show the SR has a lower average $\delta^{18}O$ value (+7.0 ± 0.6‰) than the NR (+8.3 ± 0.9‰), although the $\delta^{18}O$ ranges overlap (+6.2 to +7.5‰ and +7.1 to 9.0‰, respectively). In situ SIMS $\delta^{18}O$ data for quartz vary over a wider range (+6.9 to +14.8‰) but are, on average, lower in the NR (+9.9 ± 2.1‰) than in the SR (+12.1 ± 2.0‰).

The combined results of this study reflect a complex and protracted hydrothermal history for the GR. An early magmatic fluid exsolved from the crystallizing GR reacted with plagioclase (i.e., saussuritization) and formed early epidote and muscovite in plagioclase, K-feldspar, and void spaces. The system was then overprinted by evolved seawater sourced from the shallow continental sea above the Sudbury Structure. This fluid circulated within the overlying Onaping Formation prior to its incorporation in the GR hydrothermal system and was trapped at high temperature (type 1 fluid inclusions) and at lower temperatures (type 2 and 3 fluid inclusions). End-member orthomagmatic fluid was not preserved in the fluid inclusion record but any amount of this fluid present at the time of seawater incursion is expected to have mixed with the modified seawater fluid. Results of this study indicate the hydrothermal system previously identified in the Onaping Formation was related to a convecting hydrothermal cell in the GR that has not previously been documented.

3.2 Introduction

Hydrothermal systems are common in where high geothermal gradients occur in crustal settings and they are often associated with ore deposits. These hydrothermal systems have the ability to alter, both texturally and chemically, large volumes of rock (Pirajno 2009; Plumper and Putnis 2009). They also involve the transfer of both heat and mass, in some cases involving the heating of ambient water to very high temperatures (e.g., >350°C in VMS settings). Three essential components are needed to generate a hydrothermal system: (i) a source of sustained heat; (ii) a fluid phase, typically aqueous solutions of variable dissolved solute content; and (iii) a rock to host the system (Kesler 2005; Pirajno 2009). In addition, the fluid flow, hence the redistribution of both heat and mass, in hydrothermal systems is controlled by certain rock properties, in particular porosity, permeability, and large scale plumbing structures (e.g., faults, fractures). The latter is of particular importance as it provides the means of focusing solutions, which is critical in the case of ore deposit formation (Pirajno 2009).

Hydrothermal systems are particularly important for generation of ore deposits, including porphyry (e.g., Dilles and Einaudi 1992; Seedorf et al. 2005; Rusk et al. 2008), epithermal (e.g., Hedenquist et al. 1998; Simmons et al. 2005; Lee et al. 2014), seafloor massive sulfide or volcanogenic massive sulfide (VMS; e.g., Franklin et al. 2005; van Ruitenbeek et al. 2012), and both orogenic and Carlin gold (e.g., Mikucki 1998; Hickey et al. 2014). These systems can be long lived and in most cases involve the leaching, mobilization and deposition of metals via fluid-rock interaction within and along aquifers. Studies carried out in such settings provide insight into how fluids react with their host and also the source and contributions of different fluids (Audétat and Pettke 2003; Holk and Taylor 2007; Lowenstern et al. 2012). These systems

have been characterized using a variety of methods, commonly involving detailed mineralogical (e.g., petrography, SEM-EDS, XRD), mineral chemical and isotopic studies, and fluid inclusion analysis (Holk et al. 2008; Thorne et al. 2009; Hensler et al. 2014; Zou et al. 2016).

Meteoritic impact structures are also favourable locations where hydrothermal systems develop because they provide a heat source (i.e., impact melt) that can drive fluids sourced from either the melt sheet, surficial fluids, or metamorphic fluids (e.g., Osinski et al. 2005). The potential for fluid flow in this setting is enhanced due to structural plumbing via zones of fracturing and brecciation related to impact. The duration of such hydrothermal systems is poorly understood; however, their longevity is assumed to increase with crater size (Osinski et al. 2013). Impact-generated hydrothermal systems, either directly or indirectly, have been studied at various sites, including Ries, Germany (Newsom et al. 1986; Muttik et al. 2010), Puchezh-Katunki, Russia (Naumov 1993), Manson, USA (McCarville and Crossey 1996), Vredefort, South Africa (Reimold et al. 1999; Grieve and Therriault 2000), Kardla, Estonia (Puura et al. 2000, 2002; Versh et al. 2008), Sudbury and Haughton, Canada (Ames et al. 1998; Molnár et al. 2001; Osinski et al. 2001; Osinski et al. 2005), and Vargeao, Brazil (Yokoyama et al. 2015). This work has shown that hydrothermal circulation can extend to depths up to several km (Komor et al. 1988; Zurcher and Kring 2004). Also relevant is that the effects of fluid flow are enhanced, as might be expected, if the impact occurs in a subaqueous (e.g., marine) setting (Goto et al. 2004; Pirajno 2005).

The granophyre unit (GR) of the 1.85 Ga Sudbury Igneous Complex (SIC) represents the upper crystallized layer of an impact generated melt sheet. Post-impact hydrothermal circulation was in

this setting has been shown to have been protracted and widespread with multiple events recorded, as documented through detailed mineral-chemical, isotopic and fluid inclusion studies (Li and Naldrett 1993; Ames et al. 1998; Marshall et al. 1999; Molnár et al. 2001; Hanley and Bray 2009; Campos-Alvarez et al. 2010; Stewart et al. 2014; Tuba et al. 2014). This setting provides an ideal site to study hydrothermal processes because the GR itself lacks mineralization despite being extensively altered and both underlain and overlain by varied ore systems. The latter is for example represented by footwall Ni-Cu-PGE sulfide ore deposits and Zn-Pb-Cu SEDEX mineralization, respectively (Ames et al. 2008 and references therein).

This study presents the second part of an integrated study on documenting the nature of fluid-rock interaction in the GR and how this relates to the post-impact cooling history of the Sudbury environment. In a companion study (see Chapter 2) the mineral-chemical evidence for widespread pervasive alteration is presented. Here the results of a fluid inclusion study are integrated with $\delta^{18}O$ from both conventional whole rock analysis and in situ SIMS data for quartz. These latter data are used to address the potential source of fluids implicated in the alteration and with the fluid inclusion results are discussed in the context of the hydrothermal history of the SIC.

3.3 Geological Background

3.3.1 Geological Setting

The SIC is part of the Sudbury Structure (SS) which is located at the boundary between the Superior and Southern Provinces of the Canadian Shield. The SS is defined (Dressler 1984) as containing the SIC proper (Fig. 1A), the Whitewater Group, which is the crater-fill sequence

above the SIC, and brecciated footwall rocks which underlie the SIC. The basement rocks to the SIC are divided into: (i) the North Range (NR) which consists of Archean para- and orthogneisses and 2.6 Ga granites (Lafrance et al. 2008), and (ii) the South Range (SR) which consists of metavolcanics and metasedimentary rocks of the Paleoproterozoic Huronian Supergroup (Dressler 1984).

The complex geology of the Sudbury area relates to a combination of a meteorite impact event at 1850 Ma and associated post-impact deformation. Based on available evidence, it is now widely accepted that the SS is the result of an impact event (Dietz 1964) at 1.85 Ga (Krough et al. 1984) and that the SIC is the product of differentiation and crystallization of the impact-generated melt sheet (e.g., Golightly 1994; Mungall et al. 2004). The SIC contains several units which are from bottom to top: (i) the sublayer and associated quartz dioritic offset dikes, (ii) norite (both mafic and overlying felsic), (iii) quartz gabbro, and (iv) the GR (Naldrett et al. 1970; Coats and Snajdr 1984; Lightfoot et al. 1997). Overlying the GR and at the base of the Onaping Formation is a semi-conformable, clast-rich intrusive body called the Basal Onaping Intrusion that is interpreted be part of the impact melt sheet (Ames et al. 2005; Anders et al. 2015). The overlying Whitewater Group contains the Onaping, Onwatin, and Chelmsford formations. The Onaping Formation is interpreted as a fallback breccia (French 1967) whereas the Onwatin and Chelmsford formations are composed of post-impact clastic sediments (Coleman 1905; Rousell 1984). The SS has been affected by several pre-, syn-, and post-impact deformation events (Brocoum and Dalziel 1974; Rousell 1984a; Bailey et al. 2004; Riller et al. 1999; Raharimahefa et al. 2014). Post-impact deformation was particularly strong in the SR where units are

overturned and thrusting is more abundant (Peredery and Morrison 1984; Mukwakwami et al. 2012).

The crystallization of the SIC is related to the formation of magmatic Ni-Cu-PGE sulfide deposits, of which there are three types: (i) contact; (ii) offset, and (iii) footwall. Contact deposits occur in depressions or embayment structures at or near the SIC contact with the basement rocks and are composed of pyrrhotite, pentlandite, chalcopyrite, and minor pyrite and magnetite (Naldrett 1984; Ames and Farrow 2007). Offset deposits are hosted in radial and concentric quartz diorite dikes in the SS and mineralization is composed of pyrrhotite, pentlandite, and chalcopyrite (Farrow and Lightfoot 2002). The footwall deposits are divided into two sub-types: (a) sharp-walled veins, which are typically sharp planar surfaces with variable modal proportions of sulfides with PGE mineralization; and (b) low-sulfide (<5 modal %) PGE-rich (i.e., Pt + Pd + Au > 5 g/t) deposits with disseminated sulfides (Ames and Farrow 2007).

In contrast to the magmatic ores, syn-genetic massive sulfide ore (Zn-Cu-Pb) formed at the top of the Onaping Formation where it replaces carbonate of the Vermillion Formation (Ames et al. 1998). Also noted and of particular relevance to this study is the presence of widespread hydrothermal alteration, which has been well-documented in the basin fill sequence but rarely in the SIC proper. The extent of this system is discussed in detail below.

3.3.2 Characteristics of hydrothermal domains in the Sudbury Structure

Previous research pertaining to hydrothermal activity related to the SS has focussed primarily on processes related to mineralization in footwall settings (e.g., Farrow and Watkinson 1992; Li and

Naldrett 1993; Jago et al. 1994; Molnár et al. 1997, 1999, 2001; Marshall et al. 1999; Molnár and Watkinson 2001; Péntek et al. 2008, 2013; Campos-Alvarez et al. 2010; Tuba et al. 2010, 2014). In contrast, comparatively less work has been done on fluid mediated alteration in the hanging wall hydrothermal system. This limited work has shown that the hanging wall system is distinct from the footwall system, but the relationship between these two systems is unclear (e.g., Ames et al. 1998, 2006; Farrow and Watkinson 1999; Campos-Alvarez 2010).

The hanging wall hydrothermal system, which records fluid temperatures up to 250° to 300°C (Ames et al. 2006), is represented by the presence of vertically stacked basin-wide, semi-conformable alteration zones in the Onaping Formation that are defined by an upper calcite-chlorite zone, transition zone, ferro-actinolite-chlorite zone, albite zone, and lower silicified zone (Ames and Gibson 1995; Ames et al. 1998; Ames 1999). This hydrothermal system is considered to be responsible for the Errington and Vermillion Zn-Pb-Cu massive sulphide deposits (Ames 1999).

Alteration within the lower hydrothermal system (footwall) has been shown to be related in part to Cu(-Ni)-PGE mineralization in Sudbury breccia or other impact-related breccias. The alteration is present as cm-scale zones which border the sulfide bodies and contain varying amounts of amphibole, biotite, epidote, albite, quartz, scapolite, magnetite, biotite, alkali feldspar and titanite (Farrow and Watkinson 1992; Molnár et al. 1997, 1999, 2001; Ames et al. 2006).

Fluid inclusion and stable isotopic studies provide evidence for multiple fluid events which are interpreted to result from cooling of the SIC and later tectonic events (e.g., Farrow 1994; Molnár

et al. 2001; Marshall et al. 1999; Ames et al. 2006; Tuba et al. 2010; Tuba et al. 2014). Hanley and Mungall (2003) describe hydrothermal alteration related to Cu-Ni-PGE footwall deposits as manifested by zone enrichment in hydrosilicates (e.g., chlorite, amphibole) and large (200 m) halogen-rich halos surrounding ore deposits.

The results of several fluid inclusion studies conducted on the SIC and its footwall and are summarized in Table 1. These studies indicate that there are several possible fluid sources contributing to the hydrothermal systems, including: (i) Paleoproterozoic seawater or its evolved equivalent; (ii) formational brines and regional groundwater sourced in the basement; (iii) orthomagmatic fluids from the SIC; (iv) high-salinity fluids exsolved from crystallized sulfide melts; and (v) fluids exsolved from footwall granophyres. Furthermore, fluids generated from the Penokean Orogeny might also have contributed to the hydrothermal fluid budget of the SS; however, these fluids would have likely have been localized to the SR (Molnár and Watkinson 2001).

3.4 Analytical Methods

3.4.1 Sample Collection

This study uses a subset of samples from a more complete suite of 134 samples collected from the GR - 82 in the SR (GNa; Fig. 1B) and 52 in the NR (GNb; Fig. 1B) - along highway #144 that were used for a detailed petrological study, as summarized in Chapter 2. Based on this latter work, samples were selected in order to characterize quartz-hosted fluid inclusions in the GR and the $\delta^{18}O$ values of both wholes and quartz.

3.4.2 Fluid Inclusion Petrography and Thermometry

A detailed study of 47 (NR = 21; SR = 26) polished thin sections containing fluid inclusions followed standard protocol in order to determine the types and abundances of fluid inclusions present. This study followed the protocol and application of the fluid inclusion assemblage (FIA) concept of Goldstein and Reynolds (1994) and Goldstein (2003). A subset of these samples (n = 12) was used for microthermometric study to ensure representative coverage of each range. Microthermometry was conducted on 100 μm thick, double-polished sections in the Fluid Inclusion Laboratory at Laurentian University, using a Linkham THMSG600 heating-freezing stage with an automated controller unit and Olympus BX-51 microscope equipped with a Q-imaging digital capture system. Calibration of the system was done using synthetic fluid inclusion standards, including CO_2 (-56.5°C), H_2O (0°C), and the critical point of H_2O (374.1°C). Uncertainties are estimated to be ± 0.1°C for low-temperature phase changes (i.e., ice melting) and ± 2°C for high-temperature phase changes (i.e., L-V homogenization). Salinities were calculated using the final melting temperature of ice (Tm(ice)) for aqueous inclusions using the expression of Bodnar (1994) and for halite-bearing inclusions using the melting temperature of halite (Tm(halite); Sterner et al. 1988). The data reported in all tables and figures are for FIA.

3.4.3 Evaporate Mound Analyses

After completion of microthermometry, samples were prepared for evaporate mound analyses following the procedures outlined in Kontak (2004). Quartz chips were heated at a rate of 50°C/minute to between 480° and 530°C to induce decrepitation followed by cooling at the same rate to room temperature. The chips were then mounted on glass slides with double-sided carbon tape and subsequently carbon coated. Mound analysis were done at the Central Analytical

Facility (CAF) Laurentian University using an Oxford S-Sight energy dispersive spectrometer (EDS) mounted on a JEOL 6400 scanning electron microscope (SEM). The operating conditions were a 10 to 20 second count time using a 15 kV accelerating voltage, a 1.005 nA beam current, beam size of a 1 to 2 microns, and a working distance of 15 mm. Detection limit was approximately 0.2 wt. %. The data were processed using INCA software.

During SEM-EDS data collection, the chemistry of the mounds was obtained by operating in raster mode in order to obtain average compositions and to preclude the effects of elemental fractionation on the analyses (e.g., Haynes et al. 1988; Kontak 2004, 2014); a representative X-ray map of a mound is shown in Figure 2. From the later image, it is apparent that point rather than raster analysis would not provide representative mound analysis and affect the calculated K:Na and K:Ca ratios. Furthermore, in order to ensure that data collected were representative of a group of inclusions, using a similar approach to FIAs as in microthermometry, several mounds from a "mound field" were analyzed (see Kontak (2014) for discussion). The evaporate mound compositions were normalized to 100% and are presented in ternary plots because the actual total solute contents (i.e., salinities) of the fluid inclusions from which the mounds originated are not known. However, as is discussed below, since the dominant fluid type in the studied samples has a uniform salinity it is possible to infer semi-quantitatively the abundance of elements (e.g., Pandur et al. 2014).

3.4.4 Cathodoluminescence (CL) Imaging

Cathodoluminescence (CL) measurements of quartz were performed on carbon-coated polished thin sections at the CAF laboratory of Laurentian University. The CL system has an HKL

Backscatter Diffraction unit and a GatanChromaCL mirror-type cathodoluminescence (CL) detector and a linear array photomultiplier tube with 16 separate photocathodes.

3.4.5 Oxygen Isotopes

Stable isotope ratios for oxygen ($^{18}O/^{16}O$) were obtained for both whole rock and quartz; the latter using the SIMS method. The data for stable isotopic analyses are reported using the following notation:

$$\Delta = \frac{(R_{sample} - R_{SMOW})}{R_{SMOW}} \times 10^3 \quad (1)$$

where delta refers to the $\delta^{18}O$ and R represents the $^{18}O/^{16}O$ ratio in either the sample or the standard, which in the case of oxygen isotopes is standard mean ocean water (SMOW). The data are also reported in the convention of per mil (‰).

3.4.6 Whole Rock oxygen isotope analysis

Powders of whole rock material previously used for geochemical analyses (see Chapter 2) were submitted for $\delta^{18}O$ analyses at the Queen's University Facility for Isotope Research (QFIR), Kingston, Ontario, Canada. Oxygen was extracted from silicate minerals using the BrF_2 method (Clayton and Mayeda 1963). The stable isotopic measurements were done using a Finnigan MAT 252 mass spectrometer. The data are reported using the standard nomenclature of $\delta^{18}O$ and reference to Standard Mean Ocean Water (SMOW). Repeated measurements of standards indicate that values are reproducible to ±0.2‰.

3.4.7 Quartz oxygen isotope analysis by secondary ion mass spectrometry (SIMS)

Six samples (three from NR and three from SR) were selected for in situ measurement of $\delta^{18}O$ in quartz using SIMS at the Secondary Ion Mass Spectrometry Laboratory, University of Manitoba, Canada. Samples from the GR were selected based on the quality of quartz response to CL and also to ensure representative stratigraphic coverage. Detailed analytical protocol is described by Sharpe and Fayek (2011). Prior to analysis, each sample was cleaned using water and then soap in an ultrasonic bath followed by immersion in an ultrasonic bath using deionized water and finally ethanol. After cleaning, a gold coating was sputtered onto the sample surface to provide conductivity. Each sample was analyzed 8 to 12 times to ensure representative analyses and coverage. A ~7 nA primary ion beam of Cs^+, accelerated at 10 keV, was focused to a ~30 μm spot size. The entrance and exit slits were narrowed to obtain flat-top peaks. Ions were detected using a Balzers SEV 1217 electron multiplier coupled with an ion-counting system using a deadtime of ~52 seconds. Isotopes detected include ^{18}O and ^{16}O. Each analysis typically lasted ~10 minutes and comprised of 70 cycles. Counts were ~$1x10^6$ for ^{16}O. Standard deviations of reproducibility for quartz were ±0.7‰. Additional discussion on this technique is described by Riciputi et al. (1998).

3.5 Results

3.5.1 The granophyre unit of the SIC

A detailed study of the petrography and whole rock and mineral chemistry of the GR is provided in Chapter 2 and only a summary is provided here; representative images of the unit are show in Figure 3. The GR consists of two-feldspar monzogranite characterized by variably developed (0 to 65 vol. %; Fig. 3A, B) granophyric intergrowth of quartz and K-feldspar nucleating from

plagioclase laths. The primary mineralogy of the GR (Fig. 3C, D) is dominated by quartz, alkali feldspar and plagioclase with lesser amphibole (NR only), apatite, ilmenite, and titanite, and zircon. Primary amphibole is only present in the NR where it is more abundant in the lower portion and has an acicular habit (Fig. 3E, F). Miarolitic cavities lined with quartz, K-feldspar and epidote are present in both the SR and NR (Figs. 3G, H) and are concentrated in the middle of the GR and indicate the melt was saturated in volatiles during its terminal stage of crystallization (Zieg and Marsh 2005). Coarse-grained felsic domains occur in the lower portion (bottom ~300 m) of the NR (Fig. 3I). Importantly, the degree of textural preservation of the unit is greater than in the NR whereas local shear-related deformation has destroyed much of the primary texture in the SR.

The mineral textures and chemistry in the GR reflect pervasive alteration due to fluid-rock interaction during its subsolidus history; representative images of these textures are provided in Figure 4. Significant differences in alteration style and mineral assemblages were noted between the NR and SR. The SR alteration assemblage consists of biotite-epidote-titanite with lesser muscovite-stilpnomelane-chlorite (Fig. 4A-F), whereas the NR alteration assemblage consists of epidote- ferro-actinolite-stilpnomelane with varying amounts of chlorite (Fig. 4G-L). Evidence for alteration includes replacement of primary feldspars by near end-member albite ($An_{0-5}Ab_{95-100}$) and orthoclase ($Or_{95-100}Ab_{5-0}$), presence of pervasive epidote, saussuritization of plagioclase, pitted silicate phases (e.g., Engvik et al. 2008), replacement of ilmenite by titanite, rutile, and hematite (Fig. 4M, N), and replacement of primary amphibole by secondary Fe-rich (Fe# (Fe/Fe+Mg) = 0.40 to 0.48 and 0.51 to 0.74, respectively) amphibole phases (e.g., ferro-actinolite).

3.5.2 Cathodoluminescence of granophyric quartz

Representative CL images of quartz in GR samples provide observations for the least altered (Fig. 5A-F), through moderately altered (Figs. 5G, H) and most altered (Figs. 5I, J) areas, as inferred based on the nature of the CL response. In general, the CL images show two styles of response: (i) a strong signal represented by a bright blue response which reflects least-altered quartz, and (ii) a weak signal, as represented by a dark blue response that relates to altered quartz. The latter quartz often exhibits moderate to strong patterns of internal fracturing that is not visible optically as viewed under either plane polarized light or in cross nicols.

3.5.3 Quartz-hosted Fluid Inclusions

3.5.3.1 Petrography and fluid inclusions

Fluids inclusions are present along healed micro-fractures in both singular grains of sub- to euhedral quartz and in areas of granophyre-hosted quartz. In both cases fluid inclusions are abundant (Figs. 6A, B). They are also present, but to a lesser extent, in adjacent feldspar phases, both albite and K-feldspar, throughout the NR and SR. Fluid inclusions vary considerably in size (i.e., 3 to 20 μm) and are generally equant to elliptical in shape, but also include negative shapes. As the inclusions are aqueous in nature, the terminology used reflects this, thus L_{H2O}-V_{H2O} is simply referred to as L-V types.

Based on petrographic study of 47 samples, three fluid inclusion types were recognized: (1) L-V with about 20-30% V (Fig. 6C); (2) L-V with about 10% V (Fig. 6D); and (3) L-V-solids with about 10% V, with halite as the most common solid phase (Fig. 6E). In rare cases inclusions

were noted to contain small irregularly shaped trapped solids that were not identified. Type 2 fluid inclusions are also present in K-feldspar within GR (Fig. 6F).

3.5.3.2 Microthermometry

Fluid inclusion microthermometric data were collected on FIAs from a total of 12 samples, six from each range, in order to characterize their homogenization temperature and chemistry. The data collected include: (i) temperature of freezing (Tf), as this is a general indication of the abundance of divalent cations in the inclusions (e.g., Ca; see Wilksinson 2017) for discussion); (ii) first appearance of a liquid phase, otherwise referred to as the eutectic temperature (Te), which in helps define the bulk composition of the system (i.e., cations present in addition to Na; Davis et al. 1990); (iii) the temperature at which the last solid phase melts in the L-V inclusions, which in these inclusions was always ice (Tm(ice)); (iv) the melting point of halite (Tm(halite)); and (v) the total homogenization temperature (Th), this being the point where the inclusions become a single homogeneous inclusion either by disappearance of the V phase or halite. Hydrohalite melting temperatures were not collected due to the small size of fluid inclusions. A summary of the microthermometric data is presented in Table 2 and in Figures 7 and 8, with the latter figure summarizing data for individual FIAs in histograms (Fig. 8A-C) and in temperature-salinity space (Fig. 8D).

Type 1 L-V

Type 1 inclusions (Fig. 6C) are present in approximately 5% of samples and have Tf values from -95° to -64°C, Te from -25º to -20.5°C, Tm(ice) from -21° to -17°C, and Th from 310° to 345°C. Data indicate salinity between 20.2 and 23.5 wt. % equiv. NaCl. The fluid inclusions are

identified in both ranges, but FIAs appropriate for microthermometry were only identified therefore measured in the NR.

Type 2 L-V

Type 2 inclusions (Fig. 6D) are the most abundant type and are present in every sample. They are associated with monophase L-type inclusions which become L-V upon cooling; hence they are considered to be metastable at room temperature. The Tf for these inclusions ranges from -90° to -59°C. Ice was observed to melt during heating runs, but due to their small size it was not possible to also observe hydrohalite melting. The Tm(ice) was -25° to -17.2°C in the SR and -22.5° to -16.8°C in the NR. Importantly, within an FIA the ranges were only a few degrees. Fluid salinities range between 20.4 and 23.7 wt. % equiv. NaCl. in the SR and 20.1 to 24 wt. % equiv. NaCl. in the NR. The Th values for FIA ranged between 109° to 168°C in the SR and 123° to 150°C in the NR, but for any FIA the range was only a few degrees (i.e., <6°C).

Type 3 L-V-Halite (±solids)

Type 3 inclusions (Fig. 6E) are present in approximately 30% of samples. Fluid inclusion assemblages with uniform phase proportions were present however in only three samples (GNa-5; GNb-7; GNb-50). The Tf ranged between -78° to -64°C, Te was between -25.1° to -23.1°C, Tm(ice) was between -22° and -17.1°C and Tm(halite) between 153° and 227°C. It was not possible to observe melting of hydrohalite in these inclusions due to their small size. The Th values of between 108° and 156°C are very similar to those in type 2 inclusions in both the SR and NR. Salinities for these inclusions range from 30.3 to 33.9 wt. % equiv. NaCl. were calculated by using the dissolution temperature for halite and the equation by Bodnar (2003).

3.5.4 Evaporate mound chemistry of decrepitated quartz-hosted inclusions

Twenty sections used for fluid inclusion microthermometry were also used for evaporate mound analysis, representative images of which are shown in Figures 2 and 9. The distribution of samples through the GR that were analysed is summarized in Figure 10. In addition, the following points are noted in regards to the chemical data discussed below: (i) when chemistry is referred to, it is for data normalized to 100 wt. %; (ii) as the method uses ratios rather than absolute elemental concentrations, the data for are shown on ternary plots for elements of high concentration (Na, Ca, K) and in a log section through the SIC for other elements (Fe, Mg, S); and (iii) as most of the fluid inclusions observed petrographically are type 2, it is considered that these inclusions dominate the mounds analysed. Furthermore, most of the quartz-hosted fluid inclusions used for mound analyses were contained within granophyre textured domains of the samples.

Evaporate mounds occur in either mound fields (Fig. 9A) or in smaller groups (Fig. 9B-D). Relevant to the chemistry of the mounds are their shapes, as this reflects a chemical control (e.g., Kontak 2004; Kontak and Kyser 2011). For the representative mounds shown in Figures 2 and 9 there is a correlation seen between chemistry and shape such that Na equates to the cubic habit typical of halite (e.g., Fig. 9D). In contrast, more irregular shapes characterize areas dominated by Ca, which can be seen in Figures 9E and F where cubes of halite are surrounded by the more amorphous looking material enriched in Ca. The chemistry collected for the mounds generally reflects these morphological observations.

The chemistry summarized in Figure 10 and Table 3 reflects the decreasing elemental concentrations of Na, Ca, K, Fe, S, and Mg. The ternary plots also show there are subtle trends of changing K such that for the SR K increased down section, whereas for the NR K is more variable, but in both cases the amount of K clearly changes. For the other elements summarized in Figure 10, Fe shows the most consistent enrichment and is more enriched in the SR. Magnesium, while present in only the SR is only at low levels in two samples (≤0.7 wt. %). Manganese is present in the SR in low levels (≤0.6 wt. %). In one sample (GNa-58) relatively high S (2.5 wt. %) was noted, whereas for others, where detected, it is less than 0.5 wt. %. Fluorine is present in ~50% of samples at levels up to 3.7 wt. % and includes samples from both the bottom and top of each range.

Examining the data specifically for each range, the average elemental contents normalized to 100 wt. % for the SR, are: Cl (52), Na (39), Ca (6), K (3), Fe (2). In comparison the averages for the NR are: Cl (52), Na (40), Ca (6), K (1), and Fe (1). If the average fluid composition of 23 wt. % equiv. NaCl, as determined from microthermometry, is considered as representing the total salinity of the fluids and thereby the mounds, then it is possible to semi-quantitatively calculate the solute contents of the fluids (e.g., Pandur et al. 2014). Using this approach yields the following estimated composition for the SR fluid: 88 800 ppm Na, 12 700 ppm Ca, 5800 ppm K, and 3600 ppm Fe. For the NR fluid the values are: of 91 900 ppm Na, 13 600 ppm Ca, 3400 ppm K, and 1600 ppm Fe. The dominant anion in all samples is Cl with minor amounts of F in both the SR and NR samples.

3.5.5 Oxygen Isotopes

Eight samples, four from the SR (GNa-13, GNa-38, GNa-44, GNa-80) and four from the NR (GNb-11, GNb-19, GNb-43, GNb-50), were selected for whole rock oxygen isotopic analysis. These samples were selected in order to achieve complete coverage of the GR, with one sample analyzed from each of the top and bottom, and two samples analyzed from the middle of both the NR and SR. Of these samples, three from each of the SR (GNa-13, GNa-44, GNa-80) and NR (GNb-11, GNb-19, GNb-50) were analyzed in situ for $\delta^{18}O_{quartz}$ values using SIMS. Sites for analysis in quartz were selected based on the CL response of the quartz to locate quartz that was least altered (uniform bright signal) and altered quartz (variable bight to dark signal). Samples selected for whole rock $\delta^{18}O$ analyses were also the most leucocratic as this facilitated doing fluid/rock modeling. The whole rock and quartz $\delta^{18}O$ results are presented in Tables 4 and 5 and summarized in Figures 11 and 12.

In the SR, the four whole rock samples have an average $\delta^{18}O$ value of +7.0±0.6‰ (range from +6.2 to +7.5‰). The two samples from the middle of the SR have the highest $\delta^{18}O$ values of +7.4 and +7.5‰, whereas the lower and uppermost samples have values of +6.2 and +7.0‰, respectively. In the NR GR, the four samples analyzed have an average $\delta^{18}O$ value of +8.3±0.9‰, (range from +7.1 to +9.0‰). Similar to the SR, the two samples from the middle of the NR GR have the highest whole rock $\delta^{18}O$ values (+9.0 and +8.9‰), whereas the lower and uppermost samples have values of +8.2 and +7.1‰, respectively.

The measured $\delta^{18}O_{quartz}$ values for the six samples analyzed vary significantly within and between the ranges (Fig. 11). In the SR, the three samples analyzed have an average $\delta^{18}O_{quartz}$

value of +12.1‰, ranging from +9.3 to +14.8‰ for a total variation of 5.4‰. In the NR, the three samples analyzed have an average $\delta^{18}O_{quartz}$ value of +9.9‰, ranging from +6.9 to +12.8‰ for a total variation of 5.9‰. For both ranges, the $\delta^{18}O_{quartz}$ values also vary up to 5‰ between grains within a single sample (e.g., GNb-11) and up to 3.5‰ within a single grain (e.g., GNb-19). Sample GNa-13 is the only sample in which the variation in $\delta^{18}O_{quartz}$ values is minimal, ranging from +9.3 to +10.3‰.

3.6 Discussion

In this section, we unravel the fluid history of the GR by first examining fluid inclusion data to characterize the fluid composition and thermal evolution. The origin of fluids contributing to the hydrothermal fluid system is then discussed along with the reason for the high fluid salinities. We then use oxygen isotope data to further characterize the nature of the fluid and water:rock ratios. Finally, we present a model for the onset, duration, and collapse of the hydrothermal system in the GR by incorporating previous work and new results from this study.

3.6.1 Fluid Inclusion Trapping Temperatures

The fluid inclusion data for both the NR and SR GR reflect two distinct fluid inclusion types. Type 2 and 3 fluid inclusions are the most abundant and have lower Th values (108° to 168°C), whereas type 1 inclusions are much less common and have higher Th values (310° to 345°C). In order to assess the origin of these fluids, the fluid inclusion trapping temperatures (Tt) must be determined. As measured Th values do not equate to the actual Tt values (note the exception of boiling) due to the need for a pressure correction (Roedder 1984; Bodnar 2003), this aspect is first considered. In this context and for the purpose of this study, the lithostatic pressure during

trapping is estimated to be 1.2 to 1.5 kbar based on the inferred thickness of the SIC GR and crater fill sequence (Molnár et al. 1999; Péntek et al. 2008). We note that the upper limit of the range takes into account the differential thickness of the top versus bottom of the GR of ca. 0.6 kbar (average 1.8 km). This pressure estimate, in conjunction with the measured salinity of the fluid inclusions and isochoric diagrams of Bodnar and Vityk (1994; Fig. 13), produces Tt estimates of 405° to 430°C for type 1 fluids and 157° to 218°C for types 2 and 3 fluids inclusions. The implications of these Tt values and the measured fluid salinities are discussed for each fluid inclusion type below.

3.6.2 Nature of type 1 fluid

Type 1 fluid inclusions are rare in both the NR and SR, and only three samples (five FIAs in total) have FIAs appropriate for microthermometry. The Te and Tm(ice) values recorded for these samples are similar, and overall these inclusions have an average salinity of 21 wt. % equiv. NaCl. Given that the Te values are around -23°C rather than -21.1°C, as expected for the pure NaCl-H_2O binary system, a small amount of a divalent cation must be present in addition to Na as the main cation.

In order to assess the source of this fluid inclusion type, it is important to understand its entrapment relative to types 2 and 3 fluid inclusions. All three inclusions are secondary and cross cutting relationships are lacking; therefore, the relative timing is argued based on the following reasoning. In order for type 1 fluids to attain the high recorded temperatures of 405° to 430°C, it is most likely that the inclusions reflect entrapment during the post-crystallization cooling history of the SIC, and in this sense would have to pre-date types 2 and 3 fluids. Although such high

temperatures may have been attained during later metamorphism, this has only been documented in the SR (Card and Jackson 1995; Lafrance et al. 2008), whereas these fluids are present in both the NR and SR. Thus, although somewhat tenuous based on lack of data, type 1 fluids are considered to have been trapped during the cooling history of the SIC.

3.6.3 Nature of type 2 and 3 fluids

The microthermometric data collected for type 2 and 3 FIAs (Te, Tm(ice), Th) exhibit only slight variation, indicating that the trapping conditions were similar throughout the GR for these two fluid types. Type 2 and 3 fluid inclusions differ with respect to their abundance – with type 2 inclusions occurring in approximately 85% and type 3 inclusions occurring in approximately 5% of inclusions in the GR – and their salinities, as determined from measured Tm(ice) values and Th(Halite), respectively. Fluid salinities are estimated to range between 20.4 and 23.7 wt. % equiv. NaCl for type 2 fluid inclusions and between 30.3 and 33.9 wt. % equiv. NaCl for type 3 fluid inclusions. Similar to type 1 inclusions, the Te values are lower than expected for pure $NaCl\text{-}H_2O$ fluids for both type 2 (Te ~-26°C) and type 3 (Te ~-24°C) inclusions, indicating that a small amount of a divalent cation must be present in addition to Na. Hydrohalite should also be present in both type 2 and 3 fluid inclusions based on the depressed Tm(ice) values obtained. However, as noted above, the fluid inclusions are too small to observe and measure Tm(HH), thus it was not possible to estimate the wt. % $CaCl_2$ in type 2 and 3 inclusions. For this reason, the calculated salinities for type 2 and 3 fluids are likely higher than the true salinities. The lowest possible salinity for type 3 fluids is 26.3 wt. % equiv. NaCl because this is the minimum salinity required for halite saturation. There are no controls on the true salinity of type 2 fluids; however, the absence of halite suggests that there is an appreciable difference between the true

salinities of type 2 and 3 fluids. The similarities in the microthermometric data for type 2 and 3 inclusions suggest that these inclusions may represent a similar fluid, whereas the differences in salinity suggest otherwise, and this is addressed in detail below.

There are two possible explanations for the presence of type 2 and 3 fluid inclusions: (i) these fluid inclusions represent a single fluid near halite saturation that was trapped both as L+V and L+V+H; or (ii) two separate fluids with different salinities were trapped under similar conditions. Evaporate mound data for the GR reveal a continuum of compositions with respect to Na:Ca ratios. If these data are representative of two discrete fluids trapped at separate time intervals, it is expected that the evaporate mound data would form two compositional clusters. Instead, there is continuum of compositions that likely reflects the heterogeneous character of a single fluid. Therefore, where it is not possible to unequivocally determine which of the two possibilities produced the type 2 and 3 fluid inclusions in the GR, it is more likely that the two fluid inclusion types represent a single but slightly chemically heterogeneous fluid.

The similarity in salinities between type 1 and 2 fluid inclusions must also be considered. Although these fluid inclusion types exhibit significant differences in microthermometric data, the salinity of type 1 inclusions (21 wt. % equiv. NaCl) falls within the range of salinities for type 2 inclusions (20.4 and 23.7 wt. % equiv. NaCl). There are two possible explanations for the similar salinities but different trapping temperatures of these inclusion types: (i) type 1 and 2 inclusions represent two distinct fluids with the same salinities but different temperatures; or (ii) the two inclusion types represent two trapping events of the same fluid at different temperatures.

In order to determine which of these explanations is more probable, the potential fluid sources to the GR must first be considered and this is done below.

3.6.4 Potential fluid sources

In general, two main fluid sources were likely available during the cooling of the SIC, one cognate to the complex and the other exotic. In the first case, the presence of miarolitic cavities and bubble trains (see Chapter 2) clearly indicates volatile saturation of the melt occurred, as would be expected for such a high-level felsic magmatic body. Circulation of exsolved magmatic volatiles is common in low-pressure felsic intrusive settings (e.g., Peretyazhko 2010), and this would also have been the case in the GR. As for exotic fluids, they may have originated from either infiltration of a chemically modified and heated down-welling fluid which originated in the overlying crater (i.e., seawater) or a fluid which originated in the basement to the SIC. The microthermometric and salinity data expected for these potential fluid sources provide an important comparison to the results for type 1, 2, and 3 fluids and this is discussed below.

For the pressures and temperatures appropriate for the GR (1.5 kbar and 700° to 750°C; Darling et al. 2009), fluid inclusions containing exsolved magmatic volatiles are expected to have Th values in excess of 600°C ("A" in Fig. 13) and such inclusions would be easily recognized if preserved (i.e., near critical type with low density and high V:L ratio); such inclusions are lacking. Instead, the highest temperature inclusions, type 1, would require a pressure correction to ca, 3.5-4 kbar if they represented orthomagmatic fluids ("B" in Fig. 13), which is not consistent with geological constraints for the SIC. Furthermore, experimental studies show that partitioning of Cl into an exsolved magmatic fluid is strongly dependent on pressure, and for <2

kbar (Webster 1992), which is relevant for the SIC, fluids having <5 wt. % equiv. NaCl are expected, which contrasts with the 20 to 24 wt. % equiv. NaCl of type 1 fluids. This is further supported by fluid inclusion studies done in porphyry-epithermal systems, where the salinities for bulk aqueous fluids exsolved from felsic magmas at <1.3 kbar generally range from 2 to 10 wt. % equiv. NaCl and typically ca. 6 wt. % equiv. NaCl (Hedenquist et al. 1998). Where high-salinity fluids are reported for low-pressure magmatic-hydrothermal ore systems (e.g., porphyry and Sn-W deposits; 0 to 70 wt. % equiv. NaCl; Wilkinson 2001), the salinities are much higher than those measured in the GR (i.e., >35 wt. % equiv. NaCl) and are attributed to fluid unmixing (e.g., Hedenquist and Lowenstern 1994). Again, evidence supporting fluid unmixing in the GR is lacking due to the absence of the expected low-density complementary fluid inclusions (e.g., Bodnar 2003), and these high salinities are therefore not expected for the exsolved magmatic fluids in the GR. Thus, type 1 fluid cannot represent an unmodified orthomagmatic fluid.

Other possible sources fluids to the GR are those sourced from the basement to the SIC or modified seawater, hence exotic to the SIC. In this regard, the presence of high temperature, high-salinity fluids in basement granophyres genetically linked to formation of the SIC is noted (Farrow and Watkinson 1992; Molnár et al. 2001; Hanley et al. 2011). These fluids have Th values of 502° ± 44°C and an average salinity of 60 ± 6 wt. % equiv. NaCl (Hanley et al. 2011). Limited thermometric data exists for chemically modified and heated seawater originating from the overlying crater, but Th values of 86° to 172°C are reported by Davies et al. (1990). Salinities for this fluid have not been reported in the literature.

Based on the above, the expected orthomagmatic fluid temperatures are too high for all fluid inclusion types observed assuming such fluids were trapped shortly after their exsolution ("A"; Fig. 13). Alternatively, the orthomagmatic fluids may have cooled isobarically and been subsequently trapped at ca. 405° to 430°C, and this may be a possible source for type 1 fluid inclusions ("C"; Fig. 13); however, the expected salinities for such exsolved magmatic fluids (see above) from the GR are significantly lower than those reported for type 1 inclusions. Cooled basement fluids may also be the source of type 1 inclusions; however the salinities of these fluids are significantly higher than these inclusions. Therefore, type 1 inclusions neither represent end-member orthomagmatic nor basement fluids. It is possible that the salinity of orthomagmatic fluids increased prior to trapping by fluid-rock interaction. This process could increase fluid salinity by formation of hydrous minerals through alteration of primary silicates (e.g., epidote after plagioclase), resulting in dehydration of the fluid. However, an increase in fluid salinity from 5 to >20 wt. % equiv. NaCl requires that the original fluid lose approximately 75% of its original H_2O component, which is considered unlikely and is difficult to evaluate. Alternatively, mixing with higher salinity fluids, such as the basement fluids, may have led to an increase in salinity of the orthomagmatic fluid. If this were the case, it is highly unlikely that the resulting salinity would be consistent throughout the GR and fall exactly within the range of salinities for type 2 inclusions (i.e., uniform mixing). Furthermore, there is no evidence to suggest that basement fluids have infiltrated the GR. Given that type 2 and 3 inclusions are also not the appropriate temperatures or salinities to represent end-member orthomagmatic or basement fluids, it is suggested that types 2 and 3 inclusions represent a lower temperature trapping event of the same fluid represented by type 1 inclusions. The most likely source for this fluid is

chemically modified and heated seawater with a variable magmatic fluid component, and this is further considered below.

3.6.5 Seawater infiltration of the granophyre unit

Chemically modified and heated seawater is considered an appropriate fluid source for the GR given the salinity and temperature recorded by the fluid inclusions. Previous workers have attributed the laterally extensive alteration present throughout the crater fill Onaping Formation to circulation of a hydrothermal fluid consisting dominantly of seawater with a contribution of magmatic fluid derived from the SIC (Ames 1999; Ames et al. 2006). This fluid penetrated the Sudbury basin through faults that have been well documented in the Onaping Formation (Ames 1999). Early saussuritization of feldspar enhanced the permeability and porosity of the GR (see Chapter 2), and this may have facilitated fluid infiltration and circulation into the unit. Furthermore, Osinski et al. (2013) note that the degree of alteration in impact sites is a product of the availability of fluid in the overlying crater. A continual source of fluids from an overlying crater lake or, in the case of Sudbury, shallow sea results in more intensive impact-generated hydrothermal alteration (Osinski et al. 2013). It follows that the fluids responsible for pervasive alteration in the rocks directly overlying the GR were also involved in the hydrothermal system in the GR itself.

The composition of Paleoproterozoic seawater is interpreted to be similar to modern seawater with respect to its temperature, salinity, and dissolved cation concentrations (e.g., Holland 1984; Grotzinger and Kasting 1993). Modern ambient seawater is 2°C, has an average salinity of 3.5 wt. % equiv. NaCl, a Na^{2+} concentration of approximately 470 mmol/kg (~10,800 ppm) and a

Ca^{2+}concentration of approximately 10 mmol/kg (~400 ppm; Millero 2003). The temperature and salinity of modern seawater is significantly lower than all three fluid inclusion types in the GR and the Na:Ca ratio is significantly higher than the average ratio reported for evaporate mounds in the GR (~7:1), and these discrepancies are accounted for below.

Source of heat: As mentioned previously, there is limited microthermometric data for the modified seawater fluid in the Onaping Formation. The data available indicate that within ~200 m of the top of the Onaping Formation the fluid temperatures were at least 170°C and that the temperature of fluids recorded by fluid inclusions in the Whitewater Group increase with increasing depth (Davies et al. 1990). There is no fluid inclusion data for the lower portion of the Onaping Formation, but Ames et al. (2006) note that the temperatures in the Sudbury basin reached up to 250° to 300°C based on the hydrothermal alteration assemblages present. Circulation of high temperature fluids (>340°C) at the base of the Onaping Formation has also been inferred from the presence of pervasive to patchy silicification (Ames 1999; Ames et al. 2002; Ames et al. 2005). It is therefore highly likely that the temperature of modified seawater in the GR would be in excess of 300°C, and it is not unreasonable that it would have achieved temperatures reflected by the type 1 fluid inclusions. These temperatures are recorded for fluids in active VMS settings where seawater infiltrates the seafloor and is heated by a high-level heat source (e.g., Franklin et al. 2005). In VMS systems, lower temperature hydrothermal fluids commonly overprint the high-level heat source due to collapse of the overlying hydrothermal system during cooling (Galley 2003). This is interpreted to have occurred in the GR as well, as reflected by overprinting textures of hydrothermal alteration (see Chapter 2) and the lower temperatures recorded by type 2 and 3 fluid inclusions.

Source of salinity: Given that end-member seawater has an average salinity of 3.5 wt. % equiv. NaCl, which is significantly lower than the salinities of types 1, 2, and 3 fluid inclusions, a mechanism for increasing fluid salinity in the GR is required. This may be achieved either through modification of the fluid by fluid-rock interaction in the GR, or the seawater salinity may have been increased prior to its incorporation into the GR hydrothermal system. We discuss the latter model first below.

The Sudbury impact occurred in a shallow continental sea, foreland to the Penokean orogeny (Ames et al. 1998). The Onaping Formation overlying the GR is documented to have formed in a shallow marine to locally subaerial setting (Ames 1999) over a prolonged period of time (Gibbins 1997). The Onwatin Formation of the Whitewater Group overlies the Onaping Formation and is interpreted to have formed in a deep, restricted basin where the bottom waters were stagnant and anoxic (Rousell 1984a). Opening of this basin is represented by the overlying Chelmsford Formation, which consists of greywacke and minor siltstone interpreted to be a proximal turbidite succession (Rousell 1984a). A whole rock Rb/Sr age for the Chelmsford Formation of 1740 Ma (Fairbairn et al. 1968) suggests that this basin remained restricted for approximately 100 Ma after impact, significantly later than cessation of the SIC-driven hydrothermal system, which is interpreted to have lasted for approximately 1 Ma (Ames et al. 1998). Therefore, we suggest that the restricted nature of the basin may have contributed to an increase in fluid salinity through evaporation of seawater. This setting shares similarities with the environment of formation for sedimentary exhalative deposits (SEDEX), where hydrothermal fluids are sourced from brines formed by seawater evaporation that have gravitationally settled to the bottom of the basin (Leach et al. 2005; Goodfellow 2007). These brines then penetrate the

basin floor due to the permeability and porosity of the sediments and solubilize and transport metals (Leach et al. 2005). Although no mineralization is observed in the GR, SEDEX-type deposits have been documented in the Errington-Vermillion Formation overlying the Onaping Formation (Rousell 1984b). Furthermore, the fluid salinities in SEDEX deposits recorded by fluid inclusion data (Leach et al. 2005) are very similar to the salinities for type 1 and 2 fluid inclusions in the GR.

In order to test the plausibility of this hypothesis, the paleolatitude for the SS must be considered. Seawater evaporation to produce saline brines typically requires latitudes of 25° ±10°, where evaporation exceeds precipitation (Warren 2006). Paleomagnetic data for Laurentia is available at 1.88 and 1.83 Ga but not for 1.85 Ga when the Sudbury impact occurred, and the paleolatitude must therefore be approximated. The available data is variable and some of it is controversial (Pesonen et al. 2003); however, modeling of these data in conjunction with continental reconstructions in the Paleoproterozoic indicates that the SS likely remained at moderate latitudes of ~30° during the time of impact and subsequent cooling of the SIC (Pesonen et al. 2003; Zhao et al. 2004), which is appropriate for seawater evaporation. Notably lacking from the rock record are evaporites indicative of seawater evaporation. Fluid inclusion data for SEDEX deposits formed from brines produced through seawater evaporation indicates that the seawater was near halite saturation (e.g., Leach et al. 2005). It is therefore possible that evaporation increased the seawater salinity without reaching halite saturation, and thus an evaporite record is absent.

Salinity increase by fluid-rock interaction has been well studied in VMS systems, where hydrothermal fluids produced by heating and chemical modification of seawater typically have higher salinities than end-member seawater. This increase in salinity is achieved by fluid-rock interaction and precipitation of hydrous minerals, resulting in a dehydration of the initial fluid. However, the resulting salinities of these hydrothermal fluids do not typically exceed 2x the salinity of seawater (i.e., an increase from 3.5 to 7 wt. % equiv. NaCl), because doubling the salinity of a fluid by dehydration requires that this process consume 50% of the original H_2O component of the fluid (Delaney et al. 1987; Ioannou et al. 2007). It is therefore unlikely that modified seawater in the GR hydrothermal system achieved a salinity of >20 wt. % equiv. NaCl through fluid-rock interaction alone. Therefore, we suggest that the high salinities documented for the fluid inclusions in the GR are the product of some combination of seawater evaporation in a restricted basin prior to incorporation of the fluid into the GR hydrothermal system and water-rock interaction to dehydrate this fluid.

Source of calcium: Evaporate mound data for fluid inclusions in the GR indicates that the ratio of Na:Ca was approximately 7:1, whereas the ratio of these cations in end-member seawater is typically around 27:1 (Millero 2003). The modified seawater fluid therefore requires a source of Ca. Mass balance calculations for the GR (see Chapter 2) indicate that the altered rocks contain slightly less Ca than the least altered rocks, and it is possible that this alteration provided some of the Ca to the fluid. Additionally, extensive albitization is reported in the lower portion of the Onaping Formation (Ames et al. 2006), and the cation exchange reaction resulting in the alteration of plagioclase to end-member albite can significantly increase the Ca content of a fluid (e.g., Tivey 2007). In VMS vent fluids where albitization has contributed to an increase in the Ca

concentration of the fluid, Na:Ca ratios are in the range of 9:1 (e.g., Butterfield et al. 1994), and this process is therefore proposed as the source of Ca for the fluids in the GR hydrothermal system. Furthermore, the mass balance calculations for the GR (see Chapter 2) indicate that the altered rocks experienced a slight gain in Na, and this may have also contributed to a decrease in the Na:Ca ratio of the fluid. Furthermore, the large vitric component of the Onaping Formation (Ames et al. 2002; O'Sullivan et al. 2016) contributed to its highly reactive nature, facilitating alteration and cation exchange with the fluid.

Magmatic component: As mentioned previously, the modified seawater fluid responsible for hydrothermal alteration in the overlying Onaping Formation is interpreted to have included a variable component of magmatic fluid from the SIC (Ames 1999; Ames et al. 2006). An orthomagmatic fluid was also clearly present throughout the GR as reflected by the presence of miarolitic cavities and bubble trains and extensive saussuritization of feldspar (Chapter 2). Lining of pits and void spaces by early epidote and muscovite is also interpreted to be the product of a dominantly orthomagmatic fluid, as this type of alteration is similar to the magmatic-hydrothermal alteration observed in high-level synvolcanic intrusions in VMS settings (Galley 2003). However, the distribution of miarolitic cavities in the GR is limited, suggesting that the volume of this exsolved fluid was minimal and it therefore cannot account for the entirety of the alteration observed throughout the GR. Furthermore, as outlined above, the fluid inclusion microthermometric and salinity data is inconsistent with an end-member orthomagmatic fluid. Therefore, the effects of an early orthomagmatic fluid are observed in the alteration assemblages in the GR but this fluid is not preserved in the fluid inclusion record. It is not possible to quantify the proportion of this fluid that may have been incorporated into the

seawater-dominant hydrothermal fluid trapped as fluid inclusions in the GR; however, it is expected that, if any amount of this orthomagmatic fluid were present at the time of seawater infiltration, mixing between the two fluids would have occurred.

3.6.6 Oxygen Isotopes

In this section the results of both whole rock and mineral (i.e., quartz) oxygen isotopic analyses are used to address the original $\delta^{18}O$ value of the GR melt, providing the basis for assessing the nature and extent of fluid-rock interaction recorded by the alteration in the GR (see Chapter 2). The application of water:rock (W/R) modeling is also applied in the context of how much fluid was involved in modification of the $\delta^{18}O$ signature of the GR. This work follows on the application of experimental and theoretical analysis of $\delta^{18}O$ to natural settings which has improved our understanding of oxygen isotope systematics in igneous rocks and fluid-rock interaction (e.g., Chacko et al. 2001; Jourdan et al. 2009). Also relevant here is that several studies on high-temperature (>400°C) fluid-rock interaction have been done for similar rock types (O'Neil and Taylor 1967; Clayton et al. 1972; Matsuhisa et al. 1979; Clayton et al. 1989), whereas fewer have been done on low-temperature settings (Matthews and Beckinsale 1979; Kita et al. 1985; Clayton et al. 1989).

3.6.6.1 Interpretation of whole rock oxygen isotope data

The whole rock $\delta^{18}O$ results for the GR are variable within and between the NR and SR (Table 3). The $\delta^{18}O$ values for representative samples from each range reveal the NR has a higher average value (+8.3±0.9‰ versus+7.0±0.6‰) and a slightly larger variation (+7.1 to +9.0‰

versus +6.2 to +7.5‰) than the SR. Additionally, the whole rock $\delta^{18}O$ values for the both the NR and SR are higher towards the centre of the units than near the upper and lower contacts.

The first reported whole rock $\delta^{18}O$ analysis for the GR yielded a value of +7.8‰ (Taylor 1968). Subsequently Ding and Schwarcz (1984), as part of a study of the SIC and its surroundings, determined the $\delta^{18}O$ for the GR ranged from +5.3 to +9‰ with values of +6.0 to +9.1‰ for the NR and +7.1 to +7.5‰ for SR. These values are very similar to those recorded in the present study, with the exception of the value of +6.2‰ recorded in the SR, which is much lower than the results of Ding and Schwarcz (1984). It is noted, however, that this value was only measured in one sample and this sample was taken much closer to the contact between the GR and the quartz gabbro than any of the samples analyzed by Ding and Schwarcz (1984). It is also noted that the NR traverse completed in the present study is identical to the northwest traverse of Ding and Schwarcz (1984).

In order to assess the $\delta^{18}O$ values recorded for the GR, these values must be compared with analogous systems where least altered rocks have been analyzed. The generally accepted $\delta^{18}O$ values for least altered igneous rocks range from +6 to +10‰, with the higher values recorded for more felsic rocks (Taylor 1968). A system analogous to the GR is a high level felsic intrusion, and typical $\delta^{18}O$ values for rocks in these systems fall in the range of +9 to +10‰ (e.g., Rashoop granophyre of the Bushveld Complex, Arch Rock granodiorite in Yosemite, Podlesi granite; Pollard et al. 1991; Taylor 1968; Zak et al. 2005). In contrast and for comparison, high-level mafic intrusions typically exhibit $\delta^{18}O$ values between +6 and +7‰ (e.g., +6.9‰ for mafic granodiorite, Duluth Complex, Taylor 1968; +5.0 to +7.0‰ for Dufek

Intrusion, Antarctica, Kistler et al. 2000). The values reported for the GR in the current study and by Ding and Schwarcz (1984) are therefore much lower than expected for such an evolved felsic melt produced through fractional crystallization. There are several factors that can significantly influence $\delta^{18}O$ values, including changes to the source magma during fractional crystallization by assimilation of host rock, degassing, and subsolidus exchange (Taylor and Sheppard 1986). The degree of fractional crystallization is also a significant control on the $\delta^{18}O$ value but the maximum range in $\delta^{18}O$ for a rock where its genesis was controlled by only fractional crystallization is ±1‰ (Taylor 1968). Assimilation of host rocks has not been recorded for the GR, and the low concentration of localized miarolitic cavities (Chapter 2) suggests that voluminous, homogenous degassing did not occur. Evidence for pervasive alteration of the GR has been documented in Chapter 2 of this volume and in this study, and it is therefore likely that the lower than expected whole rock $\delta^{18}O$ values for the GR reflect the effects of sub-solidus re-equilibration and are not representative of primary whole rock $\delta^{18}O$ values.

Water-isotope exchange can either increase or decrease the $\delta^{18}O$ value of the whole rock depending on the fluid temperature, the W/R ratio, and the isotopic composition of the fluid. Low fluid temperatures (<250°C), low W/R ratios (<0.1), and fluid $\delta^{18}O$ values >0‰ will all contribute to either an increase or a minimal change in the whole rock $\delta^{18}O$ values. Conversely, high fluid temperatures (>250°C), high W/R ratios (>0.1), and magmatic fluid isotopic signatures ($\delta^{18}O$ <0‰) will decrease whole rock $\delta^{18}O$ values. The high modal abundance of feldspar relative to quartz in the GR is also important because feldspar-H_2O exchange can dominate the whole rock signature provided that fluid/rock ratios are appropriate (e.g., Smith et al. 1998; Allan et al. 2007). Because the $\delta^{18}O$ values recorded for the GR are significantly lower than expected

for a typical evolved felsic melt, it follows that the fluid(s) responsible for these values are high temperature and/or have a magmatic isotopic signature and the W/R ratios were relatively high. Given the variability in $\delta^{18}O$ values for the GR, the intensity of alteration should therefore correlate with the $\delta^{18}O$ values. The majority of the samples analyzed in the study by Ding and Schwarcz (1984) were highly altered based on their alteration index, and this provides a useful comparison to the current study, where the samples with the lowest possible degree of alteration were analyzed. Ding and Schwarz (1984) noted that there is no significant correlation between $\delta^{18}O$ and the degree of alteration, where alteration intensity was determined based on the degree of sericitization and epidote replacement of plagioclase (i.e., saussuritization). This measure of alteration is not as comprehensive as the method applied for the current GR study in Chapter 2 of this volume, where the calculated alteration index (AI) incorporates the modal percent of all alteration mineral phases in the GR in order to assess the alteration intensity of each sample (AI = 3 is least altered; AI = 24 is most altered). When this AI is compared with the $\delta^{18}O$ values measured in the present study for the NR, there is also no clear correlation, with the two highest $\delta^{18}O$ values, +9.0‰ and +8.9‰, corresponding to both the highest (9) and lowest (4) AI coefficients, respectively. In the SR, there is a better correlation between alteration intensity and $\delta^{18}O$, and the sample with the highest $\delta^{18}O$value (+7.5‰) has the lowest AI coefficient (6), whereas the sample with the lowest $\delta^{18}O$value (+6.2‰) has the highest AI coefficient (17).

Therefore, a relationship between the degree of alteration and $\delta^{18}O$ value per sample in the SR exists but is inconsistent. Where the alteration intensity correlates well with the $\delta^{18}O$ values, variations in the degree of alteration may explain the heterogeneity observed in measured $\delta^{18}O$

values; however, this cannot account for anomalous samples that exhibit no clear relationship between alteration intensity and $\delta^{18}O$ values.

3.6.6.2 $\delta^{18}O_{quartz}$ and CL Data

Quartz is generally considered as a reliable indicator of primary $\delta^{18}O$ values for igneous rocks (Taylor 1968; King et al. 1997). In addition, it is typically robust to isotope exchange when compared to the other minerals in granitic rock, such as the feldspars (Taylor 1968). It is, however, possible that in hydrothermal systems quartz is also susceptible to sub-solidus oxygen isotope exchange during fluid interaction (Valley and Graham 1996; Gilliam and Valley 1996).

The results of in situ measured $\delta^{18}O_{quartz}$ values in the GR are separated into three groups (Fig. 12): (i) low values of ~+5 to +8‰; (ii) inferred primary intermediary values of~+8 to +10‰ which are inferred to be magmatic; and (iii) high values of +10 to +15‰. This variability is considered to be significant and implies there has been a heterogeneous re-equilibration of the oxygen isotopic signature for quartz. The $\delta^{18}O_{quartz}$ values vary not only among samples, but also up to 5‰ between grains in the same sample (e.g., GNb-11) and up to 3.5‰ within a single grain (e.g., GNb-19). Such variability within samples and individual grains can be interpreted in different ways: (i) quartz crystallized in an isotopically heterogeneous reservoir; (ii) some quartz might be xenocrystic; and (iii) there has isotopic exchange with a fluid of either different $\delta^{18}O$ values or over variable temperatures. With such processes in mind, the variability in GR quartz, specifically within single grains, is further explored.

The first case requires magma mixing of reservoirs and in this case would require magmas of varying $\delta^{18}O$ values, including both low and high $\delta^{18}O$ types, that coexisted with the median value melt. The generally uniform chemistry of the GR (e.g., Lightfoot et al. 1997) and lack of supporting evidence of mixing, such as comingling textures in outcrop or petrographic features (e.g., sieve plagioclase), argue against this model. As for the presence of quartz xenocrysts, the very high inferred temperatures for the melt sheet (i.e., >2000°C; Grieve et al. 1977) is consistent with the lack of any reported xenocrystic material in the GR. For this reason, the explanation of entraining residual quartz of appropriate $\delta^{18}O$ values is considered unlikely. The third possibility is that fluid interaction has modified the quartz and hence its $\delta^{18}O$ values. In order to assess the latter, CL imaging of the quartz is discussed in the context of the measured $\delta^{18}O$ values.

Cathodoluminescence (CL) imaging is an effective complimentary method to in situ analysis of $\delta^{18}O$ because it has the potential to reveal primary versus modified zones within quartz that would otherwise not be visible by other techniques (e.g., optical microscopy, SEM-BSE imaging). Variations in CL intensity are attributed to either structural defects or chemical impurities (e.g., Ti, Fe) in minerals (e.g., Marshall 1988; Allan et al. 2007; Rusk et al. 2006) which can be generated by: (i) varying conditions during crystal growth such as temperature or chemistry; and (ii) sub-solidus fluid interaction. The zonation in quartz revealed by CL is often considered to be a primary feature and, if matched by variable $\delta^{18}O_{quartz}$, would reflect a heterogeneous reservoir during its growth, such as in a porphyry deposit setting (Allan et al. 2007; Rottier et al. 2016). As noted, variation may also be due to variable temperature, as the previous authors also discuss.

The CL images are useful for the identification of micro-fractures which act as fluid conduits and increase the surface area, thereby enhancing re-equilibration (King et al. 2008). For this reason, CL imaging of quartz was done prior to the in situ $\delta^{18}O_{quartz}$ data collection. Thus in this regard the three groups of $\delta^{18}O_{quartz}$ data described above correlate relatively well with the CL data with the low and high values present in quartz showing alteration features, both in terms of CL signal strength and the abundance of microfractures (Fig. 5J), whereas the quartz having intermediary values (i.e., primary $\delta^{18}O_{quartz}$) shows a magmatic CL signal (Fig. 5E).

Quartz exhibiting microfractures can have a wide range of $\delta^{18}O$ values depending on the degree of fracturing. It is therefore possible for a single quartz grain to yield both magmatic and altered $\delta^{18}O$ values and for this study two samples, these being GNb-11 and GNb-19, exhibited such variation. The primary and modified $\delta^{18}O_{quartz}$ values correlate well with CL images for these two samples (Fig. 5) with the bright CL signal indicative of primary quartz and corresponds with a magmatic $\delta^{18}O$ value (+9.0‰) whereas the darker signal is indicative of alteration along micro-fractures and has a modified $\delta^{18}O$ value (+12.5‰). These results also indicate that $\delta^{18}O_{quartz}$ values around +9‰ are representative of least altered GR.

The modified $\delta^{18}O_{quartz}$ values reflect fluid-rock interaction with both the temperature of reaction and isotopic value of the fluid relevant. At high temperatures (>500°C) there is minimal fractionation and the mineral will approach the value of the fluid if interaction is prolonged, whereas at lower temperatures (<300°C) fractionation is large (Wenner and Taylor 1976). As stated, the $\delta^{18}O$ value of the ingressing fluid is also important as this will be inherited, depending on temperature, by the reacting phase. Thus with these factors considered, the $\delta^{18}O_{quartz}$ values

can be explained using both variation in temperature and $\delta^{18}O$ value of the fluid as follows: (i) the high $\delta^{18}O_{quartz}$ values may reflect either a cooling magmatic fluid (e.g., +8‰) reacting with quartz at >400°C or a ^{18}O-depleted fluid infiltrating and reacting with the quartz at a much lower temperature (<200°C); and (ii) for the low $\delta^{18}O_{quartz}$ values, high temperature interaction (i.e., 400° to 500°C) with a low ^{18}O fluid is required. In the case of the high $\delta^{18}O_{quartz}$ values, the lack of data, such as trace element chemistry on quartz (e.g., Allan and Yardley 2008; Rottier et al. 2016) precludes being more definitive as to which of these models is preferred.

A similar wide range in oxygen isotope values within a single grain was documented in the Proterozoic granitoid rocks of the St. Francois Mountains, Missouri (King et al. 2008). Quartz in these felsic volcanic units has $\delta^{18}O$ values of +8.7 to +16.7‰, thus much like the GR in terms of the overall range. Healed micro-fractures were identified using CL and it was determined that the high $\delta^{18}O$ values were a result of a low-temperature hydrothermal event involving low $\delta^{18}O$ fluids shortly after eruption.

In order to address the nature of the fluid(s) which modified the quartz, we revisit the fluid inclusions discussed earlier. The thermometric data indicates that a high temperature fluid (i.e., ~400°C) interacted with the GR. Such a fluid, if of orthomagmatic origin (i.e., $\delta^{18}O_{H2O}$ = +8‰), could be responsible for the high $\delta^{18}O$ quartz values (i.e., $\Delta_{quartz\text{-}H2O}$ @ 400°C = 4‰). In addition, a much more abundant lower temperature fluid (ca. 200°C) was noted. For this fluid to have been responsible for the high $\delta^{18}O$ quartz values it would need to have had a $\delta^{18}O_{H2O}$ value of ~0 to +3‰, thus modified seawater which fits with what was discussed above. As for the low $\delta^{18}O$ quartz values, this would have to involve a similar fluid to the latter, but at much higher

temperature. The former fluid inclusions may in fact represent some of this fluid, but if it cannot be characterized as such.

3.6.6.3 Comparison of whole rock and quartz $\delta^{18}O$ data

The data presented above indicate discrepancies when considering both the whole rock $\delta^{18}O$ data in conjunction with the $\delta^{18}O$ data. In a simple system where fluid interaction results in low $\delta^{18}O_{quartz}$ values, whole rock values will be similar as all of the reactive mineral phases present should re-equilibrate with the fluid. By corollary, where such a fluid produces high $\delta^{18}O_{quartz}$ values, whole rock values should be similar. This relationship is maintained for all of the samples in the NR and for the majority of samples in the SR, but there are several SR samples in which the whole rock $\delta^{18}O$ values are the same as other samples in the NR and SR, but the $\delta^{18}O$ quartz values are notably higher (e.g., sample GNa-80 has a whole rock $\delta^{18}O$ of +7.0‰ and $\delta^{18}O_{quartz}$ of +13.1 to +14.7‰). This result indicates that there is a process by which the $\delta^{18}O_{quartz}$ value is increased while the whole rock $\delta^{18}O$ is unchanged. A simple explanation for this discrepancy could be due to the sampling procedures. The $\delta^{18}O_{quartz}$ data collected using SIMS may not be representative of the majority of the quartz in a given sample. As documented above, it is clear that $\delta^{18}O_{quartz}$ values are heterogeneous from the outcrop scale down to the quartz grain scale. A maximum of two analyses per grain were acquired for up to five grains per sample and this relatively small data set may not be representative of all quartz in the GR. It is therefore suggested that this discrepancy in $\delta^{18}O_{quartz}$ values may reflect the anomaly rather than the mode. Alternatively, quartz:feldspar ratios may be significantly lower in samples with the anomalously high $\delta^{18}O_{quartz}$ values. As feldspar is more reactive than quartz, it may reflect a different alteration than quartz and if it constitutes a larger volume of the rock this would result in the

noted discrepancy between the $\delta^{18}O$ values. However, for all the samples used, the quartz:feldspar ratios were similar thus this is unlikely to be the case.

3.6.6.4 Implications for primary whole rock oxygen isotope values

Before conducting calculations for whole rock oxygen isotope values of the original GR ($\delta^{18}O^{i}$), the effects of post-crystallization isotope exchange and re-equilibration processes must be understood to determine the reliability of calculated whole rock $\delta^{18}O^{i}$ data. Such processes include diffusion during cooling, temperatures of fluid-rock exchange, and the possibility of multiple fluid generations (e.g., Giletti 1986; Fourie and Harris 2011). Due to evidence for geochemical re-equilibration of the GR presented in Chapter 2, caution must be exercised when using $\delta^{18}O$ data, both whole rock and quartz, to determine which are reliable to use as a proxy for the $\delta^{18}O^{i}$. The $\delta^{18}O^{i}$ whole rock value, and thus the $\delta^{18}O$ magma value ($\delta^{18}O_{magma}$), can be calculated using the measured least altered mineral and whole rock $\delta^{18}O$ data, mineral and whole rock $\delta^{18}O$ data derived from experiments and equations, modal proportions of primary phases, and estimated temperatures of crystallization. All of these data were acquired or derived in this study except an exact estimate on crystallization temperature. An attempt was made to quantify the temperature by using titanite thermometry; however, no primary, unaltered titanite was recognized in the GR. Therefore, we incorporate an estimated temperature of crystallization of the GR into our equations based on Darling et al. (2009) of 700° to 750°C.

This calculation requires that $\delta^{18}O_{quartz}$ values have remained unaffected by sub-solidus re-equilibration and alteration and therefore represent the original, least altered $\delta^{18}O$ quartz values. The rate of diffusion is an important aspect when calculating whole rock $\delta^{18}O^{i}$ since it is

dependent on several factors including grain size, cooling rate, and closure temperatures of oxygen exchange between minerals (i.e., quartz and feldspars; Giletti 1986; Jenkin et al. 1991). For example, the $\Delta_{mineral\text{-}mineral}$ values for igneous minerals from slowly cooled rocks is great than the $\Delta_{mineral\text{-}mineral}$ value for rapidly cooled rocks (Taylor and Sheppard 1986). The GR experienced rapid crystallization due to undercooling of the melt, and is expected to have a small $\Delta_{quartz\text{-}feldspar}$ value (~1‰; Taylor and Sheppard 1986) when compared to a more slowly-cooled granitic rock (~+2‰; Giletti 1986).

Sample GNa-13 was selected for this calculation because its $\delta^{18}O$ quartz values approximate magmatic values and its CL reflects the least-altered quartz. Lackey et al. (2008) showed that the fractionation factor for quartz and alkali feldspar follows:

$$\Delta_{quartz\text{-}feldspar} = 1.00 * 10^6/T^2 \quad (2)$$

where Δ is the equilibrium fractionation constant and T is the temperature (K). Although this value is dependent on feldspar composition, it is inconsequential for variations between K-feldspar and albite (Clayton et al. 1989). Thus for the GR a single calculation equating the two feldspars can be done (i.e., $\Delta_{quartz\text{-}feldspar}$), which is similar to that done by Harris et al. (1997). Using 700°C as the magmatic equilibrium temperature for the GR and an initial $\delta^{18}O_{quartz}$ value of +10‰, the resulting $\delta^{18}O$ value for feldspar is +9‰. Using a quartz:feldspar ratio of 28:72 (note there is 2 modal % primary accessory phases) the $\delta^{18}O$ value of the whole rock is estimated to be +9.3‰. The same calculation done for a NR sample (GNb-50) using $\delta^{18}O$ quartz +9.0‰ and a quartz:feldspar ratio of 47:53 gives whole rock $\delta^{18}O^i$ value of +8.5‰. For

comparison, these data are similar to $\delta^{18}O$ values for the granophyric units in other layered intrusions (i.e., +8.0‰ in Bushveld Complex and +7.6‰ in Skaergaard intrusion; Taylor 1968).

In order to assess the reliability of our initial whole rock $\delta^{18}O$ calculation, we compare this value to the calculated $\delta^{18}O_{magma}$ value. Because the $\Delta_{quartz\text{-}melt}$ value should be ~+1‰ for a rapidly cooled rock, the calculated $\delta^{18}O_{magma}$ value should be within 1‰ of the calculated whole rock $\delta^{18}O^{i}$ value. If we use ~+9‰ as the average initial $\delta^{18}O_{quartz}$ value and a $\Delta_{quartz\text{-}magma}$ of 0.62 from a similar granophyre (Fourie and Harris 2011), the $\delta^{18}O_{magma}$ value is calculated to be +8.4‰ and is well within 1‰ of the calculated initial whole rock $\delta^{18}O$value of +7.6‰ for the GR.

3.6.6.5 Isotopic composition of the altering fluid in the granophyre unit

In order to determine the isotopic composition of the hydrothermal fluid responsible for altering the GR, the calculated $\delta^{18}O$ value of feldspar, derived from the whole rock data, can be used along with its modal abundance, assuming quartz has not been modified and feldspar equilibrated with the fluid. With these assumptions and using the modal abundance of quartz and feldspar along with the $\delta^{18}O$ data for sample GNa-13 (i.e., quartz = 28 modal ‰, whole rock = 6.2‰), the $\delta^{18}O$ value of +4.4‰ is calculated for feldspar in this GR sample. Using this latter value and feldspar-H_2O fractionation equation (O'Neil and Taylor 1967) at 400°C (i.e., average of ~3.0‰), a $\delta^{18}O_{H2O}$ of +1.4‰ is calculated. We note that this calculated value is similar to the inferred $\delta^{18}O$ values of ~-1 to -3‰ for mineralizing fluids which circulated through the Onaping Formation and caused the Errington and Vermillion massive sulfide type mineralization (Whitehead et al. 1990). Mixing of this fluid with any amount of magmatic fluid would have increased the $\delta^{18}O$ value towards our estimated fluid composition.

3.6.6.6 Water:rock modelling

An additional application for $\delta^{18}O$ data is to calculate W/R ratio during fluid interaction and equilibration. Estimated water/rock ratios are based on ^{18}O-^{16}O exchange during isotopic equilibration between quartz, feldspar, and a fluid, and use exchange equations accounting for the mass of O in water and rock (Taylor 1979). Taylor (1977) provides an expression to calculate W/R ratios that incorporates the oxygen isotope mass balance for an open system over the duration of a hydrothermal system:

$$W/R = \ln [(\delta^{18}O^{i}_{fluid} + \Delta - \delta^{18}O^{i}_{rock})/(\delta^{18}O^{i}_{fluid} - (\delta^{18}O^{f}_{rock} - \Delta))] \quad (4)$$

where i represents the initial value, f represents the final value, and Δ is the equilibrium fractionation between fluid and rock at any given temperature. Calculations for the GR use the equilibration of feldspar with the fluid, as is commonly done in such studies as it readily reacts with a fluid compared to quartz (Taylor 1968). To calculate the W/R values, we use data presented above for the GR in addition to temperature estimates based on fluid inclusion thermometry and the chemistry of the feldspars (see above and data in Chapter 2); these two suggest ~400°C.

Using the necessary data (i.e., modal mineralogy, whole rock and quartz $\delta^{18}O$ values) for one sample from each range (GNa-13 in the SR; GNb-50 in the NR), W/R modelling was done and results are presented in Figure 14. Using three different $\delta^{18}O_{H2O}$ values for the reacting fluid (+5, 0 and -2‰), the plots in Figure 13 show: (i) the calculated initial $\delta^{18}O$ feldspar values; (ii) the calculated new $\delta^{18}O$ feldspar values (i.e., black dashed line); and (iii) the modelled W/R

variations at relevant temperatures between 250° and 500°C. For each plot, we note that where the reaction lines and the dashed black line intersect a solution is provided for the calculated $\delta^{18}O$ feldspar and set of conditions used (i.e., W/R ratio, given temperature).

The results of these calculations provide constraints on the isotopic composition of the reacting fluid in the samples modelled based on the conditions noted above. The fluid with a +5‰ value, which would be a slightly modified magmatic fluid that might be produced by mixing with a ^{18}O-depleted fluid, cannot produce the calculated $\delta^{18}O$ feldspar values in either sample regardless of temperature or water/rock ratio. The two other models can produce the necessary $\delta^{18}O$ feldspar values, but at slightly different temperatures and W/R ratios. Given that the mineralizing fluid in the Onaping has a value of -1 to -3‰ (Davies et al. 1990) and we estimated the hybrid hydrothermal fluid to have had a composition of +1.4‰, it is likely that the hybrid fluid was dominantly evolved seawater with a very minor magmatic contribution to account for these values.

The inferred W/R ratios of 5 to 10 are high compared to those in some other hydrothermal systems. For example, at the Qitianling granite, China, where alteration produced skarns and greisens, a W/R ratio near unity was calculated for samples exhibiting chloritic, phyllic, and potassic (i.e., K-feldspar) alteration (Zhao et al. 2011). In a comparable high-level mineralized granite setting at the San Cristobal, Peru, wolframite-base metal mineralization is present in altered rocks which record a W/R ratio of 0.005 to 0.05 (Campbell et al. 1984). These examples are not dissimilar to that suggested for the Rico porphyry molybdenum deposit, Colorado, where data suggest alteration involved a W/R ratio of 1 to 2. The water/rock ratio of the GR is also high

when compared to the alteration found in some VMS systems. For example, at the Lemoine auriferous VMS deposit, Chibougamau Camp, Quebec, the volcanic host rocks experienced a water/rock ratio of 0.2 to 1 (Mercier-Langevin et al. 2014) and for the Noranda area, also in Quebec, the altered volcanic rocks indicate a W/R ratio near unity or slightly more (Beatty and Taylor 1982). In contrast, other settings record much higher water/rock ratios, such as other VMS deposits in the Noranda district, Quebec (McLean and Hoy 1991) and the altered ongonites of Mongolia associated with rare-metal mineralization (Dostal et al. 2015). The latter example is of particular note as it was modelled to involve exchange with a low ^{18}O fluid at 350° to 400°C, then similar to the conditions for the GR. The GR values are also high compared to porphyry deposits. Thus, these comparisons indicate that the results for the GR are not unusual in terms of either W/R ratios or the nature of the fluid, as many systems, in particular the VMS settings, involve exchange with heated and chemically modified low ^{18}O fluids of surficial origin.

3.6.7 Hydrothermal system model

Fluid inclusion thermometric and chemical data have been integrated with oxygen isotopic data in order to characterize the composition and evolution of hydrothermal fluids that affected the GR during its subsolidus cooling. The results of this study are combined with previous work on the hydrothermal history of the SS (e.g., Davies et al. 1990; Ames 1999; Ames et al. 2006) and the paragenesis of hydrothermal alteration mineral assemblages documented in Chapter 2 to provide a complete description of the genesis and development of the hydrothermal system in the GR which is presented below.

A bolide impacted the target rocks at 1.85 Ga which resulted in the generation of a melt sheet that formed the SIC and ejecta that gave rise to the Onaping Formation, now recognized as a complex mixture of fall back material and pyroclastic-like deposits (Peredery 1972; Ames et al. 2006). After the differentiation and crystallization of the SIC, the upper half consisted of the more felsic GR, which formed the basis of this study.

Fluid saturation occurred during the late-stage consolidation of the GR, as recorded by the presence of bubble trains and miarolitic cavities. Pervasive saussuritization of plagioclase, development of albite after primary plagioclase, and precipitation of epidote and muscovite in pits and void spaces (see Chapter 2) are the result of interaction and equilibration between this fluid and the surrounding GR. There is no fluid inclusion record for this end-member fluid, thus microthermometric and salinity data are not obtainable. However, given the pressure conditions for the GR, this fluid is expected to have had a temperature >500° to 600°C (Fig. 13) and a salinity <5 wt. % equiv. NaCl. This fluid likely underwent dehydration through fluid-rock interaction and precipitation of hydrous minerals, resulting in an increase in the salinity of this fluid during its hydrothermal evolution. It is not possible to measure this salinity increase due to the absence of a fluid inclusion record for end-member early orthomagmatic fluid. However, given that a loss of 50% of the original H_2O content of this fluid is required in order to double its salinity, it is unlikely that the resulting salinity of this fluid exceeded 10 wt. % equiv. NaCl.

Similar to hydrothermal systems associated with synvolcanic intrusions in VMS settings (Galley 2003), the magmatic-hydrothermal stage described above was overprinted by a hydrothermal stage as the GR cooled. This stage is reflected by a mineral assemblage characterized by chlorite,

amphibole, biotite, and stilpnomelane that overprints the early epidote and muscovite. Of particular relevance to this study is that the crater fill sequence above the SIC records a subaqueous environment, as preserved in the nature of the Onaping Formation (Ames 1999) and overlying sedimentary rock formations (Ames et al. 2006). Thus, the presence of a long lived igneous body (Ames et al. 1998; Abramov and King 2004) at a high crustal level in proximity to a large volume of water provided the optimum conditions to generate a hydrothermal convection cell. This setting is noted to be analogous to models for ancient and modern VMS settings (e.g., Franklin et al. 1981; Franklin et al. 2005) and thus it is not surprising that similar deposits are noted to have formed above the SIC near the paleo-seafloor (e.g., Erington-Vermillon Zn-Cu-Pb deposits; Ames et al. 2006). This hydrothermal cell promoted the circulation and heating of externally sourced, downward penetrating fluids and their interaction with the strata adjacent and overlying the cooling SIC. The penetration and circulation of such a fluid was likely facilitated by the numerous faults generated as part of the impact event and in part preserved as radial and concentric dikes and breccia zones in the area today (e.g., Ames et al. 2006; Grieve et al. 2010). This fluid is responsible for forming the laterally extensive alteration zones throughout the Onaping Formation (Ames 1999; Ames et al. 2006), and we suggest that the same fluid also penetrated at least the upper part of the SIC as it cooled, this being the GR. It is herein argued that the oxygen isotopic and fluid inclusion data presented above provide further evidence that this fluid interacted with the GR.

Fluid inclusion microthermometric and salinity data for type 1, 2, and 3 fluid inclusions in the GR reflect two trapping events: an early high temperature (405° to 430°C; type 1) and the second lower temperature (157° to 218°C; types 2 and 3). The first event is interpreted to represent the

thermal peak of modified seawater circulation throughout the GR, whereas the second event reflects the waning stages of this hydrothermal event. The salinity data for type 2 and 3 inclusions indicates that the fluid was slightly variable, likely the result of variable fluid-rock interaction throughout the system.

The integration of $\delta^{18}O$ data for quartz and whole rock indicates that the GR interacted with a fluid with a $\delta^{18}O$ value of approximately +1.4‰. This is consistent with seawater (0‰) modified through interaction with felsic igneous rocks (~+9 to +10‰), resulting in an isotopically heavier fluid. It is noted that the hydrothermal fluid documented in the Onaping Formation has a $\delta^{18}O$ value of -1 to -3‰ (Davies et al. 1990), which is within a reasonable range of the $\delta^{18}O$ value calculated for the fluid in the GR. Given the uncertainties associated with these calculations, it is possible that the $\delta^{18}O$ value of the fluid in the GR was as low as -3‰. Quartz $\delta^{18}O$ values also reflect interaction with a fluid having a $\delta^{18}O$ value around 0‰ at both high and low temperatures, resulting in lower (+5 to +8‰) and higher (+10 to +15‰) values, respectively, compared with magmatic quartz $\delta^{18}O$ values (+8 to +10‰).

Water:rock modelling based on the quartz and whole rock $\delta^{18}O$ values in the GR indicate a W/R between 4 and 10. This calculated range for W/R is high but not unreasonable for a system in which there is a continual source of fluid, and similar ratios have been calculated in some VMS settings (e.g., Noranda; McLean and Hoy 1991). The solute chemistry of these saline fluids, as determined using evaporate mounds, is noted to be dominated by Na-Ca-K with minor Fe, S, F and Mn. Lastly it is noted that a seawater origin for the fluids is supported by recent $\delta^{34}S$ values of up to +14.1‰ for secondary sulfides in the GR (Ripley et al. 2015).

The restricted nature of the basin overlying the Sudbury Structure may have provided a means for increasing the salinity of seawater by evaporation. This fluid then gravitationally settled to the bottom of the basin, and these bottom waters are documented to have been stagnant and anoxic (Rousell 1984). This saline fluid then penetrated and interacted with the rocks of the Onaping Formation. The absence of evaporite minerals in the rock record suggests that this process may have not been extensive, and fluid-rock interaction was likely also a key factor in increasing the salinity through fluid dehydration.

The setting for the GR is analogous to a combined SEDEX-VMS system, the former reflecting a restricted basinal setting and the latter an underlying, high level magmatic heat engine. The fluid salinities recorded in the GR are more similar to those in SEDEX settings rather than VMS settings (e.g., Leach et al. 2005; Lydon 1988). The interaction of the down welling and heated seawater derived fluid with crater fill rocks and possibly even basement lithologies would have resulted in modifying substantially the chemistry of this fluid from its original signature likely similar to modern seawater (i.e., Na:Ca = 27; Millero 2003). The large vitric component of the Onaping Formation (Ames et al. 2002; O'Sullivan et al. 2016) contributed to its highly reactive nature, whereas its mafic chemistry (Muir and Peredery 1984) provided a source of Ca and Fe (e.g., O'Sullivan et al. 2016), resulting in a decrease in the Na:Ca of the fluid and Fe-enrichment of the alteration minerals (see Chapter 2), respectively.

A later stage of hydrothermal alteration is not recorded by the fluid inclusion or oxygen isotopic data. It is characterized by a late chloritization of biotite and amphibole documented in Chapter

2. This is interpreted to reflect a retrograde alteration due to progressive cooling that is typically observed in post-impact hydrothermal systems (e.g., Naumov 2005; Osinski et al. 2013).

3.7 Conclusions

The GR of the SIC records geochemical and textural evidence for two main hydrothermal events. The first is an early magmatic-hydrothermal stage resulting from exsolution of an orthomagmatic fluid from the GR itself. All of the fluid inclusions in the GR are secondary and no primary fluid inclusions are preserved, leaving no fluid inclusion record of this primary orthomagmatic fluid. Instead, evidence for this fluid is provided by the end-member albite composition of plagioclase, the pitted texture of plagioclase produced through saussuritization, early epidote and muscovite infilling pits and void spaces, and miarolitic cavities and bubble trains. The second hydrothermal event was dominated by modified seawater derived from the hydrothermal system in the overlying Onaping Formation that was driven by heat from the GR. Progressive cooling of the GR allowed for collapse of this hydrothermal system into the GR, overprinting the earlier magmatic-hydrothermal event. Evidence for this event is recorded by all three fluid inclusion types, which represent two trapping events of this fluid at two different temperatures. Evaporate mound data indicates that this fluid became variably enriched in Ca, likely due to interaction with Ca-bearing mineral phases in the Onaping Formation and GR. The quartz and whole rock oxygen isotopic data also reflect interaction between the GR and a fluid with an isotopic composition consistent with that of modified seawater. The W/R ratio for this early fluid is estimated to have been between 5 and 8, indicating that the system experienced pervasive alteration characteristic of an open system. If any orthomagmatic fluid was still present in the GR

at the time of modified seawater infiltration, it is likely that the two fluids mixed, though it is not possible to document or quantify this process.

Previous work done on hydrothermal processes in the Sudbury Structure has documented hydrothermal systems in the Onaping Formation and in the footwall of the SIC, but no work has been done to investigate the connection, if any, between these systems. A complete understanding of hydrothermal systems in the Sudbury Structure is critical for modelling metal distribution, and the connection between the SIC and the hanging-wall and footwall hydrothermal systems must be established. The results of this study address the connection with the hanging-wall system and clearly show that a connection exists between the ore-forming hydrothermal system in the Onaping Formation and the barren system in the GR.

3.8 References

Abramov, O. and Kring, D. A. (2004): Numerical modeling of an impact-induced hydrothermal system at the Sudbury crater. Journal of Geophysical Research 109, E10007.

Allan, M. M. and Yardley, B. W. D. (2007): Tracking meteoric infiltration into a magmatic-hydrothermal system: A cathodoluminescence, oxygen isotope and trace element study of quartz from Mt. Leyshon, Australia. Chemical Geology 240, 343-360.

Ames D. E., Davidson, A., and Wodicka, N. (2008): Geology of the Giant Sudbury Polymetallic Mining Camp, Ontario, Canada. Economic Geology 103, 1057-1077.

Ames, D. E. (1999): Geology and regional hydrothermal alteration of the crater-fill, Onaping formation: association with Zn-Pb-Cu mineralization, Sudbury Structure, Canada. Unpublished Ph.D. thesis Carleton University, Ottawa, Ontario, 460 p.

Ames, D. E. and Gibson, H. L. (1995): Controls on geological setting of regional hydrothermal alteration within the Onaping Formation, footwall to the Errington and Vermillion base metal deposits, Sudbury Structure, Ontario. Current Research 1995-E. Geological Survey of Canada, 161-173.

Ames, D. E., and Farrow, C. E. G. (2007): Metallogeny of the Sudbury Mining Camp, Ontario, in Goodfellow, W. D., ed., Mineral Deposits of Canada: A Synthesis of Major Deposit-Types, District Metallogeny, the Evolution of Geological Provinces, and Exploration Methods: Geological Association of Canada, Mineral Deposits Division, Special Publication 5, p. 329-350.

Ames, D. E., Davidson, A., Buckle, J., and Card, K. D. (2005): Sudbury bedrock compilation; Geology. Geological Survey of Canada Open File 4570.

Ames, D. E., Golightly, J. P., Lightfoot, P. C., and Gibson, H. L. (2002): Vitric compositions in the Onaping formation and their relationship to the Sudbury Igneous Complex. Economic Geology 97, p. 1541-1562.

Ames, D. E., Jonasson, I. R., Gibson, H. L., and Pope, K. O. (2006): Impact-generated hydrothermal system – constraints from the large Paleoproterozoic Sudbury crater, Canada, in Biological processes associated with impact events, eds. C. Cockell, C. Koeberl, I. Gilmour: Springer.

Ames, D. E., Watkinson, D. H. and Parrish, R. R. (1998): Dating of a regional hydrothermal system induced by the 1850 Ma Sudbury impact event. Geology 26, 447-450.

Anders, D., Osinski, G. R., Grieve, R. A. F., and Brillinger, D. T. M. (2015): The Basal Onaping Intrusion in the North Range: Roof rocks of the Sudbury Igneous Complex. Meteoritics and Planetary Sciences 50, 1577-1594.

Audétat, A. and Pettke, T. (2003): The magmatic-hydrothermal evolution of two barren granites: A melt and fluid inclusion study of the Rito del Medio and Canada Pinabete plutons in northern New Mexico (USA). Geochimica et Cosmochimica Acta 67, 97-121.

Bailey, J., Lafrance, B., McDonald, A. M., Fedorowich, J. S., Kamo, S., and Archibald, D. A. (2004): Mazatzal-Labradorian age (1.7-1.6 Ga) ductile deformation of the South Range Sudbury impact structure at the Thayer Lindsley mine, Ontario. Canadian Journal of Earth Sciences 41, 1491-1505.

Beaty, D. W. and Taylor, H. P. Jr. (1982): Some petrologic and oxygen isotope relationships in the Amulet mine, Noranda, Quebec, and their bearing on the origin of Archean massive sulfide deposits. Economic Geology 77, 95-108.

Bodnar, R. J. (1994): Synthetic fluid inclusions: XII. The system H2O-NaCl. Experimental determination of the halite liquidus and isochores for a 40 wt. % solution. Geochimica et Cosmochimica Acta 58, p. 1053-1063.

Bodnar, R. J. (2003): Introduction to aqueous fluid systems. In Samson, A., Anderson, A., and Marshall, D., eds, Fluid Inclusions L Analysis and Interpretation. Mineralogical Association of Canada Short Course 32, 81-99.

Bodnar, R. J. and Vityk, M. O. (1994): Interpretation of microthermometric data for H2O-NaCl fluid inclusions. In De Viro, B. and Frezzotti, M. L., eds., Fluid Inclusions in Minerals, Methods and Applications. Virginia Tech, Blacksburg, Virginia, 117-130.

Brocoum, S. T., and Dalziel, I. W. D.(1974): The Sudbury Basin, the Southern Province, the Grenville Front and the Penokean Orogen. Geological Society of America Bulletin 85, p. 1571-1580.

Burnham, C. W. (1979): Magmas and hydrothermal fluids. In Barnes, L. H. (ed.) Geochemistry of hydrothermal ore deposits, 2nd edition. John Wiley and Sons, New York, 71-136.

Campbell, A., Rye, D., and Peterson, U. (1984): A hydrogen and oxygen isotope study of the San Cristobal Mine, Peru: Implications of the role of water to rock ratio for the genesis of wolframite deposits. Economic Geology 79, 1818-1832.

Campos-Alvarez, N. (2010): Fluid-rock interaction around mafic to intermediate intrusions: evidence from trace element and isotope geochemistry of minerals. Unpublished Ph.D. thesis University of Windsor, Ontario, p. 250.

Campos-Alvarez, N. O., Samson, I. M., Fryer, B. J., and Ames, D. E. (2010): Fluid sources and hydrothermal architecture of the Sudbury Structure: constraints from femtosecond LA-ICP-MS Sr isotopic analysis of hydrothermal epidote and calcite. Chemical Geology 278, 131-150.

Card, K. D. (1978): Geology of the Sudbury-Manitoulin area, districts of Sudbury and Manitoulin. Ontario Geological Survey Report 166, 238 p.

Chacko, T., Cole, D. R., and Horita, J. (2001): Equilibrium oxygen, hydrogen and carbon isotope fractionation factors applicable to geologic systems. Reviews in Mineralogy and Geochemistry 43, 1-81.

Clayton, R. N., and Mayeda, T. K. (1963): The use of bromine pentafluoride in the extraction of oxygen from oxides and silicates for isotopic analysis. Geochimica et Cosmochimica Acta 27, p. 43-52.

Clayton, R. N., Goldschmidt, J. R., and Mayeda, T. K. (1989): Oxygen isotope fractionation in quartz, albite, anorthite and calcite. Geochimica et Cosmochimica Acta 53, 725-733.

Clayton, R. N., O'Neil, J. R., and Mayeda, T. K. (1972): Oxygen isotope exchange between quartz and water. Journal of Geophysical Research 77, 3057-3067.

Cline, J. S. and Bodnar, R. J. (1991): Can economic porphyry copper mineralization be generated by a "typical" calc-alkaline melt? Journal of Geophysical Research 96, 8113-8126.

Coats, C. J. A., and Snajdr, P.(1984) Ore Deposits of the North Range, Onaping-Levack area, Sudbury, in The Geology and Mineral Deposits of the Sudbury Structure, eds. E. G. Pye, A. J. Naldrett, P. Giblin, Ontario Geological Survey, Special Publication 1, p. 328-346.

Coleman, A. P. (1905): The Sudbury nickel region. Ontario Department of Mines Annual Report 14, 1-188.

Darling, J., Storey, C., and Hawkesworth, C. (2009): Impact melt sheet zircons and their implications for the Hadean crust. Geology 37, 927-930.

Davies, J. F., Leroux, M. V., and Whitehead, R. E. (1990): Oxygen-isotope composition and temperature of fluids involved in the deposition of Proterozoic sedex deposits, Sudbury Basin, Ontario. Canadian Journal of Earth Sciences 27, 1299-1303.

Davis, D. W., Lowenstein, T. K., and Spencer, R. J. (1990): Melting behavior of fluid inclusions in laboratory-grown halite crystals in the systems NaCl-H_2O, NaCl-KCl-H_2O, NaCl+$MgCl_2$-H_2O, and NaCl-$CaCl_2$-H_2O. Geochimica et Cosmochimica Acta 54, 591-601.

Dietz, R. S. (1964): The Sudbury Structure as an astrobleme. Journal of Geology 72, 412-434.

Dilles, J. H. and Einaudi, M. T. (1992): Wall-Rock Alteration and Hydrothermal Flow Paths about the Ann-Mason Porphyry Copper Deposit, Nevada – A 6-Km Vertical Reconstruction. Economic Geology 87, 1963-2001.

Ding, T. P., and Schwarcz, H. P.(1984): Oxygen isotopic and chemical compositions of rocks of the Sudbury Basin, Ontario. Canadian Journal of Earth Sciences 21, p. 305-318.

Dostal, J., Kontak, D. J., Gerel, O., Shellnutt, J. G., and Fayek, M. (2015): Cretaceous ongonites (topaz-bearing albite-rich microleucogranites) from Ongon Khairkhan, Central Mongolia: Products of extreme magmatic fractionation and pervasive metasomatic fluid:rock interaction. Lithos 236-237, 173-189.

Dressler, B. O. (1984): General Geology of the Sudbury Area, in The Geology and Mineral Deposits of the Sudbury Structure, eds. E. G. Pye, A. J. Naldrett, P. Giblin, Ontario Geological Survey, Special Publication 1, 57-82.

Engvik, A. K., Putnis, A., Fitz, J. D., and Austrheim, H. (2008): Albitization of granitic rocks: the mechanism of replacement of oligoclase by albite. The Canadian Mineralogist 46, 1401-1415.

Fairbairn, H. W., Faure, G., Pinson, W. H., and Hurley, P. M. (1968): Rb-Sr whole rock age of the Sudbury Lopolith and basin sediments. Canadian Journal of Earth Sciences 5, 707-714.

Farrow, C. E. G. (1994): Geology, alteration, and the role of fluids in Cu-Ni-PGE mineralization of the footwall rocks to the Sudbury Igneous Complex, Levack and Morgan Townships, Sudbury District, Ontario. Unpublished Ph.D. thesis, Carleton University, Ottawa, Canada. 373 p.

Farrow, C. E. G. and Lightfoot, P. C. (2002): Sudbury PGE revisited: Toward and Integrated model, in Cabri, L. J. ed., The Geology, Geochemistry, Mineralogy and Mineral Beneficiation of Platinum Group Elements, Special Volume 54, Canadian Institute of Mining, Metallurgy and Petroleum, p. 13.

Farrow, C. E. G. and Watkinson, D. H. (1992): Alteration and the role of fluids in Ni, Cu and Platinum-group element deposition, Sudbury Igneous Complex Contact, Onaping-Levack area, Ontario. Mineralogy and Petrology 46, 67-83.

Fourie, D. S. and Harris, C. (2011): O-isotope study of the Bushveld Complex granites and granophyres: constraints on source composition and assimilation. Journal of Petrology 52, 2221-2242.

Franklin, J. M., Gibson, H. L., Jonasson, I. R., and Galley, A. G. (2005): Volcanogenic massive sulfide deposits; in Hedenquist, J. W., Thompson, J. F. H., Goldfarb, R. J., and Richards, J. P., eds., Economic Geology, 100th Anniversary Volume, 523-560.

Franklin, J. M., Lydon, J. W., and Sangster, D. F. (1981): Volcanic-Associated Massive Sulfide Deposits. Economic Geology 75th Anniversary Volume, 485-627.

Frape, S. K. and Fritz, P. (1989): Geochemical trends from ground waters from the Canadian Shield, in: Fritz, P, and Frape, S. K. (eds.) Saline water and gases in crystalline rocks. Geological Association of Canada Special Paper 33, p. 19-38.

Frape, S. K., and Fritz, P.(1982): The chemistry and isotopic composition of saline groundwaters from the Sudbury Basin, Ontario.Canadian Journal of Earth Sciences 19, p. 645-661.

French, B. M. (1967): Sudbury Structure, Ontario: Some Petrographic Evidence for Origin by Meteorite Impact. Science 156, 1094-1098.

Gibbins, S. F. M. (1997): The Sudbury Structure with emphasis on the Whitewater Group. Institute on lake Superior Geology, 43rd Annual Meeting, Sudbury, Field Trip Guide Book 43, pt 4, 53 p.

Giletti, B. J. (1986): Diffusion effects on oxygen isotope temperatures of slowly cooled igneous and metamorphic rocks. Earth and Planetary Science Letters 77, 218-228.

Gilliam, C. E. and Valley, J. W. (1997): Low δ18O magma, Isle of Skye, Scotland. Geochimica et Cosmochimica Acta 61, 4975-4981.

Goldstein, R. (2003): Petrographic analysis of fluid inclusions. In: Samson, I., Anderson, A., and Marshall, D. (eds) Fluid inclusions: analysis and interpretation. Mineralogical Association of Canada Short Course 32:9-54.

Golightly, J. P. (1994): The Sudbury Igneous Complex as an Impact Melt: Evolution and Ore Genesis, in Proceedings of the Sudbury – Noril'sk Symposium, O.G.S. Special Volume 5, p. 105-117.

Goodfellow, W. D., Lydon, J. W., and Turner, R. W. (1993): Geology and genesis of stratiform sediment-hosted (SEDEX) Zn-Pb-Ag sulfide deposits, in Kirkham, R. V., Sinclair, W. D., Thorpe, R. I., and Duke, J. M., eds., Mineral Deposit Modeling, Special Paper 40, Geological Association of Canada, 201-251.

Goto, K., Tada, R., Bralower, T. J., Hasegawa, T., and Matsui, T. (2004): Evidence for ocean water invasion into the Chicxulub crater at the Cretaceous/Tertiary boundary. Meteoritics and Planetary Sciences 39, 1233-1247.

Grieve, R. A. F. and Cintala, M. J. (1992): An analysis of differential impact melt-crater scaling and implications for the terrestrial impact record. Meteoritics 27, 526-539.

Grieve, R. A. F. and Therriault, A. (2000): Vredefort, Sudbury, Chicxulub: Three of a kind?. Annual Review of Earth and Planetary Sciences 28, 305-338.

Grieve, R. A. F., Ames, D. E., Morgan, J. V., and Artemieva, N. (2010): The evolution of the Onaping Formation at the Sudbury impact structure. Meteoritics and Planetary Science 45, 759-782.

Grieve, R. A. F., Dence, M. R., and Robertson, P. B. (1977): Cratering processes: As interpreted from the occurrence of impact melts, in Roddy, D. J., et al. (eds.) Impact and explosion cratering. New York, Pergamon Press, 791-814.

Grotzinger, J.P. and Kasting, J.F. (1993): New Constraints on Precambrian Ocean Composition. The Journal of Geology 101, 100th Anniversary Symposium: Evolution of the Earth's Surface, 235-243.

Hanley, J. J., Ames, D. E., Barnes, J., Sharp, Z., and Guillong, M. (2011): Interaction of magmatic fluids and silicate melt residues with saline groundwater in the footwall of the Sudbury Igneous Complex, Ontario, Canada: new evidence from bulk rock geochemistry, fluid inclusions and stable isotopes. Chemical Geology 281, 1-25.

Hanley, J. J., and Mungall, J. E. (2003): Chlorine enrichment and hydrous alteration of the Sudbury breccia hosting footwall Cu-Ni-PGE mineralization at the Fraser mine, Sudbury, Ontario, Canada. The Canadian Mineralogist 41, 857-881.

Hanley, J. J., Mungall, J. E., Bray, C. J., and Gorton, M. P. (2004): The origin of bulk and water-soluble Cl and Br enrichments in ore-hosting Sudbury breccia in the Fraser Copper zone, Strathcona embayment, Sudbury Ontario, Canada. The Canadian Mineralogist 42, 1777-1798.

Hanley, J. J., Mungall, J. E., Pettke, T., Spooner, E. T. C., and Bray, C. J. (2005): Ore metal redistribution by hydrocarbon-brine and hydrocarbon-halide melt phases, North Range footwall of the Sudbury Igneous Complex, Ontario, Canada. Mineralium Deposita 40, 237-256.

Hanley, J.J. and Bray, C. J. (2009): The trace metal content of amphibole as a proximity indicator for Cu-Ni-PGE mineralization in the footwall of the Sudbury Igneous Complex, Ontario, Canada. Economic Geology 104, 113-125.

Harris, C., Faure, K., Diamond, R. E., and Scheepers, R. (1997): Oxygen and hydrogen isotope geochemistry of S- and I-type granitoids: the Cap Granite suite, South Africa. Chemical Geology 143, 95-114.

Haynes, F. M., Sterner, S. M., and Bodnar, R. J.(1988): Synthetic fluid inclusions in natural quartz. IV. Chemical analyses of fluid inclusions by SEM/EDA: evaluation of method. Geochimica et Cosmochimica Acta 52, 969-977.

Hedenquist, J. W. and Lowenstern, J. B. (1994): The role of magmas in the formation of hydrothermal ore deposits. Nature 370, 519-527.

Hedenquist, J. W., Arribas, A. Jr., and Reynolds, T. J. (1998): Evolution of an Intrusion-Centered Hydrothermal System: Far Southeast-Lepanto Porphyry and Epithermal Cu-Au Deposits, Philippines. Economic Geology 93, 373-404.

Hensler, A.-S., Hagemann, S. G., Brown, P. E., and Rosiere, C. A. (2014): Using isotope chemistry to track hydrothermal processes and fluid sources in itabirite-hosted iron ore deposits in the Quadrilatero Ferrifero, Minas Gerais, Brazil. Mineralium Deposita 49, 293-311.

Hickey, K. A., Barker, S. L. L., Dipple, G. M., Arehart, G. B., and Donelick, R. A. (2014): The Brevity of Hydrothermal Fluid Flow Revealed by Thermal Halos around Giant Gold Deposits: Implications for Calin-Type Gold Systems. Economic Geology 109, 1461-1487.

Holland, H.D. (1984): The Chemical Evolution of the Atmosphere and Oceans. Princeton, Princeton University Press, 582 p.

Holk, G. J. and Taylor, H. P. Jr. (2007): 18O/16O Evidence for Contrasting Hydrothermal Regimes Involving Magmatic and Meteoric-Hydrothermal Waters at the Valhalla Metamorphic Core Complex, British Columbia. Economic Geology 102, 1063-1078.

Holk, G. J., Taylor, B. E., and Galley, A. G. (2008): Oxygen isotope mapping of the Archean Sturgeon Lake caldera complex and VMS-related hydrothermal system, Northwestern Ontario, Canada. Mineralium Deposita 43, 623-640.

Jago, B. C., Morrison, G. G., and Little, T. L. (1994): Metal zonation patterns and microtextural and micromineralogical evidence for alkali- and halogen-rich fluids in the genesis of the Victor Deep and McCreedy East footwall copper orebodies, Sudbury Igneous Complex. Ontario Geological Survey Special Volume 5, 65-75.

Jenkin, G. R. T., Fallick, A. E., Farrow, C. M., and Bowes, G. M. (1991): COOL: A FORTRAN 77 computer program for modelling stable isotopes in cooling closed systems. Computing Geoscience 17, 391-412.

Jourdan, A., Venneman, T., Mullis, J., and Ramseyer, K. (2009): Oxygen isotope sector zoning in natural hydrothermal quartz. Mineralogical Magazine 73, 615-632.

Kesler, S. E. (2005): Ore-Forming Fluids. Elements 1, 13-18.

King, E. M., Barrie, C. T., and Valley, J. W. (1997): Hydrothermal alteration of oxygen isotope ratios in quartz phenocrysts, Kidd Creek mine, Ontario: Magmatic values are preserved in zircon. Geology 25, 1079-1082.

King, E. M., Trzaskus, A. P., and Valley, J. W. (2008): Oxygen isotope evidence for magmatic variability and multiple alteration events in the Proterozoic St. Francois Mountains, Missouri. Precambrian Research 165, 49-60.

Kistler, R. W., White, L. D., and Ford, A. B. (2000): Strontium and Oxygen Isotope Data and Age for the Layered Gabbroic Dufek Intrusion, Antarctica. United States Geological Survey Open File Report 00-133, 29 p.

Kita, I., Taguchi, S., and Matsubaya, O. (1985): Oxygen isotope fractionation between amorphous silica and water at 34-93°C. Nature 314, 83-84.

Komor, S. C., Valley, J. W., and Brown, P. E. (1988): Fluid-inclusion evidence for impact heating at the Siljan Ring, Sweden. Geology 16, 711-715.

Kontak, D. J. (2004): Analysis of evaporate mounds as a complement to fluid-inclusion thermometric data: case studies from granitic environments in Nova Scotia and Peru. The Canadian Mineralogist 42, 1315-1329.

Kontak, D. J. (2014): Using evaporate mound chemistry of fluid inclusions to assess the metal fertility and fluid:rock interaction in a large peraluminous batholith: a case study of the mineralized (Sn-W-U-Cu-Zn-Ag) South Mountain Batholith, Nova Scotia, Canada. Pan-American Current Research on Fluid Inclusions (PACROFI-XII) U.S. Geological Survey and Colorado State University, Abstract Volume.

Kontak, D. J. and Kyser, T. K. (2011): A fluid inclusion and isotopic study of an intrusion-related gold deposit (IRGD) setting in the 380 Ma South Mountain Batholith, Nova Scotia, Canada: evidence for multiple fluid reservoirs. Mineralium Deposita 46, 337-363.

Krough, T. E., Davis, D. W., and Corfu, F.(1984): Precise U-Pb Zircon and Baddeleyite Ages for the Sudbury Area, in The Geology and Mineral Deposits of the Sudbury Structure, eds. E. G. Pye, A. J. Naldrett, P. Giblin, Ontario Geological Survey, Special Publication 1, 431-446.

Lackey, J. S., Valley, J. W., Chen, J. H., and Stockli, D. F. (2008): Dynamic magma systems, crystal recycling, and alteration in the Central Sierra Nevada Batholith: the Oxygen Isotope Record. Journal of Petrology 49, 1387-1426.

Lafrance, B., Legault, D. and Ames, D. E.(2008): The formation of the Sudbury breccia in the North Range of the Sudbury impact structure. Precambrian Research 165, 107-119.

Lee, G., Koh, S.-M., and Pirajno, F. (2014): Evolution of hydrothermal fluids of HS and LS-type epithermal Au-Ag deposits in the Seongsan hydrothermal system of the Cretaceous Haenam volcanic field, South Korea. Ore Geology Reviews 61, 33-51.

Li, C. and Naldrett, A.J. (1993): High chlorine alteration minerals and calcium-rich brines in fluid inclusions from the Strathcona Deep Copper zone, Sudbury, Ontario. Economic Geology 88, 1780–1796.

Lightfoot, P. C., Keays, R., R., Morrison, G. G., Bite, A., and Farrell, K. P.(1997): Geochemical relationships in the Sudbury Igneous Complex: Origin of the Main Mass and Offset Dikes. Economic Geology 92, no. 3, 289-307.

Lowenstern, J. B., Bergfeld, D., Evans, W. C., and Hurwitz, S. (2012): Generation and evolution of hydrothermal fluids at Yellowstone: Insights from the Heart Lake Geyser Basin. Geochemistry, Geophysics, Geosystems 13, Q01017.

Marshall, D. J. (1988): Cathodoluminescence of Geological Materials. Unwin Hyman, Boston. 146 pp.

Marshall, D., Watkinson, D. H., Farrow, C. E. G., Molnár, F., and Fouillac, A.-M. (1999): Multiple fluid generations in the Sudbury Igneous Complex: fluid inclusion, Ar, O, H, Rb and Sr evidence. Chemical Geology 154, 1-19.

Matsuhisa, Y., Goldschmidt, J. R., and Clayton, R. N. (1979): Oxygen isotope fractionation in system quartz-albite-anorthite-water. Geochimica et Cosmochimica Acta 43, 1131-1140.

Matthews, A. and Beckinsale, R. D. (1979): Oxygen isotope equilibration systematics between quartz and water. American Mineralogist 64, 232-240.

McCarville, P. and Crossley, L. J. (1996): Post-impact hydrothermal alteration of the Manson impact structure. Geological Society of America Special Paper 302, 347-376.

McCormick, K. A. and McDonald, A. M. (1999): Chlorine-bearing amphiboles form the Fraser Mine, Sudbury, Ontario, Canada: description and crystal chemistry. The Canadian Mineralogist 37, 1385-1403.

McLean, W. H. and Hoy, L. D. (1991): Geochemistry of hydrothermal altered rocks at the Horne mine, Noranda, Quebec. Economic Geology 86, 506-528.

Mercier-Langevin, P., Lafrance, B., Becu, V., Dube, B., Kjarsgaard, I., and Guha, J. (2014): The Lemoine Auriferous Volcanogenic Massive Sulfide Deposit, Chibougamau Camp, Abitibi Greenstone Belt, Quebec, Canada: Geology and Genesis. Economic Geology 109, 231-269.

Mikucki, E. J. (1998): Hydrothermal transport and depositional processes in Archean lode-gold systems: A review. Ore Geology Reviews 13, 307-321.

Millero, F. J. (2003): Physio-chemical controls of seawater, in Treatise on Geochemistry, Elsevier, Amsterdam, 1-21.

Molnár, F. and Watkinson, D.H. (2001): Fluid-inclusion data for vein type Cu–Ni–PGE footwall ores and their use in establishing an exploration model for hydrothermal PGE-enrichment around mafic ultramafic intrusions. Exploration and Mining Geology 10, 125–141.

Molnár, F., Watkinson, D. H., Jones, P. C., and Gatter, I. (1997): Fluid inclusion evidence for hydrothermal enrichment of magmatic ore at the contact zone of the Ni-Cu-platinum group element 4b deposits, Linsley mine, Sudbury, Canada. Economic Geology 92, 674-685.

Molnár, F., Watkinson, D.H., Everest, J.O. (1999): Fluid–inclusion characteristic of hydrothermal Cu–Ni–PGE veins in granitic and metavolcanic rocks at the contact of the Little Stobie Deposit, Sudbury, Canada. Chemical Geology 154, 279–301.

Molnár, F., Watkinson, D.H., Jones, P.C. (2001): Multiple hydrothermal processes in footwall units of the North Range, Sudbury igneous complex, Canada, and implications for the genesis of vein-type Cu–Ni–PGE deposits. Economic Geology 96, 1645–1670.

Muir, T. L. and Peredery, W. V. (1984): The Onaping Formation: Ontario Geological Survey Special Volume 1, 139-210.

Mukwakwami, J., Lafrance, B., and Lesher, C. M. (2012): Back-thrusting and overturning of the Southern Margin of the 1.85 Ga Sudbury Igneous Complex at the Garson Mine, Sudbury Ontario. Precambrian Research 196-197, 81-105.

Mungall, J. E., Ames, D. E., and Hanley, J. J. (2004): Crustal redistribution in large bolide impacts: geochemical evidence from the Sudbury Structure.Nature 6990, 546-548.

Muttik, N., Kirsimae, K., and Vennemann, T. W. (2010): Stable isotope composition of smectite in suevites at the Ries crater, Germany: Implications for hydrous alteration of impactites. Earth and Planetary Science Reviews 299, 190-195.

Naldrett, A. J. (1984): Mineralogy and composition of the Sudbury ores, in Pye, E. G., Naldrett, A. J., and Giblin, P. E. eds., The Geology and Ore Deposits of the Sudbury Structure. Ontario Geological Survey Special Publication 1, 309-326.

Naldrett, A. J., Bray, J. G., Gasparrini, E. L., Podolsky, T., and Rucklidge, J. C. (1970): Cryptic variation and the petrology of the Sudbury Nickel Irruptive. Economic Geology 65, 122-155.

Naumov, M. V. (1993): Zonation of hydrothermal alteration in the central uplift of the Puchezh-Katunkiastrobleme. Metoritics 28, 408-409.

Newsom, H. E., Graup, G., Stewards, T., and Kiel, K. (1986): Fluidization and hydrothermal alteration of the suevite deposit at the Ries Crater, West Germany, and implications for Mars. Journal of Geophysical Research 91, E239-E251.

Niedermeier, D. R. D., Putnis, A., Geisler, T., Golla-Schindler, U. and Putnis, C. V.(2009): The mechanism of cation and oxygen isotope exchange in alkali feldspars under hydrothermal conditions. Contributions to Mineralogy and Petrology 157, 65-76.

O'Neil, J. R., and Taylor, H. P. Jr. (1967): The oxygen isotope and cation exchange chemistry of feldspars. The American Mineralogist 52, 1414-1437.

O'Sullivan, E. M., Goodhue, R., Ames, D. R., and Kamber, B. S. (2016): Chemostratigraphy of the Sudbury impact basin fill: Volatile metal loss and post-impact evolution of a submarine impact basin. Geochimica et Cosmochimica Acta 183, 198-233.

Osinski, G. R., Lee, P., Parnell, J., Spray, J. G., and Baron, M. (2005): A case study of impact-induced hydrothermal activity: The Haughton impact structure, Devon Island, Canadian High Arctic. Meteoritics and Planetary Science 40, 1859-1878.

Osinski, G. R., Spray, J. G., and Lee, P. (2001): Impact-induced hydrothermal activity within the Haughton impact structure, Srctic Canada: Generation of a transient, warm, wet oasis. Meteoritics and Planetary Science 36, 731-745.

Osinski, G. R., Tornabene, L. L., Banerjee, N. R., Cockell, C. S., Flemming, R., Izawa, M. R. M., McCutcheon, J., Parnell, J., Preston, L. J., Pickersgill, A. E., Pontefract, A., Sapers, H. M., and Southam, G. (2013): Impact-generated hydrothermal systems on Earth and Mars. Icarus 224, 347–363.

Pandur, K., Kontak, D. J., and Ansdell, K. M. (2014): Hydrothermal evolution in the Hoidas Lake vein-type RE deposit, Saskatchewan, Canada: Constraints from fluid inclusion microthermometry and evaporate mound analysis. The Canadian Mineralogist 52, 717-743.

Péntek, A., Molnár, F., Tuba, G., Watkinson, D. H., and Jones, P. C. (2013): The significance of partial melting processes in hydrothermal low sulfide Cu-Ni-PGE mineralization within the footwall of the Sudbury Igneous Complex, Ontario, Canada. Economic Geology 108, 59-78.

Péntek, A., Molnár, F., Watkinson, D. H., and Jones, P. C. (2008): Footwall-type Cu-Ni-PGE mineralization in the Broken Hammer Area, Wisner Township, North Range, Sudbury Structure. Economic Geology 103, 1005-1028.

Peredery, W. V. (1972): The origin of rocks at the base of the Onaping Formation, Sudbury, Ontario. Unpublished Ph.D. thesis, University of Toronto, Toronto, Ontario.

Peredery, W. V. and Morrison, G. G.(1984): Discussion of the Origin of the Sudbury Structure, in The Geology and Mineral Deposits of the Sudbury Structure, eds. E. G. Pye, A. J. Naldrett, P. Giblin, Ontario Geological Survey, Special Publication No. 1, 491-511.

Peretyazhko, I. S. (2010): Genesis of Mineralized Cavities (Miaroles) in Granitic Pegmatites and Granites. Petrology 18, 183-208.

Pesonen, L. J., Elming, S.-A., Mertanen, S., Pisarevsky, S., D'Agrella-Filho, M. S., Meert, J. G., Schmidt, P. W., Abrahamsen, N., and Bylund, G. (2003): Palaeomagnetic configuration of continents during the Proterozoic. Tecntonophysics 375, 289-324.

Pirajno, F. (2005): Hydrothermal processes associated with meteorite impact structures: evidence from three Australian examples and implications for economic resources. Australian Journal of Earth Sciences 52, 587-605.

Pirajno, F. (2009): Hydrothermal Processes and Mineral systems. Springer-Science and Business Media B. V.

Plumper, O. and Putnis, A. (2009): The Complex Hydrothermal History of Granitic Rocks: Multiple Feldspar Replacement Reactions under Subsolidus Conditions. Journal of Petrology 50, 967-987.

Pollard, P. J., Andrew, A. S., and Taylor, R. G. (1991): Fluid inclusion and stable isotope evidence for interaction between granites and magmatic hydrothermal fluids during formation of disseminated and pipe-style mineralization at the Zaaiplaats Tin Mine. Economic Geology 86, 121-141.

Putnis, A. (2002): Mineral replacement reactions: from macroscopic observations to microscopic mechanisms. Mineralogical Magazine 66, 689-708.

Puura, V., Karki, A., Kirs, J., Kirsimae, A., Konsa, M., Niin, M., Plado, J., Suuroja, K., and Suuroja, S. (2000): Impact-induced replacement of plagioclase by K-feldspar in granitoids and amphibolites at the Kardla Crater, Estonia. In: Gilmour, I. and Koeberl, C. (eds.). Impacts and the Early Earth, 417-445. Springer-Verlag, Berlin.

Puura, V., Koeberl, C., Karki A., Juvonen, R., Konsa, M., Plado, J., Suuroja, K., Kirs, J., and Huber, H. (2002): Geochemistry of K-enriched impactites, based on drillings into the Kardla Crater, Estonia. Geological Society of America Abstracts with Programs 34, 341.

Raharimahefa, T., Lafrance, B., and Tinkham, D. K. (2014): New structural, metamorphic, and U-Pb geochronological constraints on the Blezardian Orogeny and Yavapai Orogeny in the Southern Province, Sudbury, Canada. Canadian Journal of Earth Sciences 51, 750-774.

Reimold, U., Koeberl, W., Fletcher, P., Killick, A. M., and Wilson, J. D. (1999): Pseudotachylite breccias from fault zones in the Witwatersrand Basin, South Africa: evidence of

autometasomatism and post-brecciation alteration processes. Mineralogy and Petrology 66, 25-53.

Riciputi, L. R., Patterson, B., and Ripperdam, R. L.(1998): Measurement of light stable isotope ratios by SIMS: matrix effects for oxygen, carbon and sulfur isotopes in minerals. International Journal of Mass Spectrometry and Ion Processes 178, 81-112.

Riller, U., Schwerdtner, W. M., Halls, H. C., and Card, K. D.(1999):Transpressive tectonism in the eastern Penokean Orogen, Canada; consequences for Proterozoic crustal kinematics and continental fragmentation. Precambrian Research 93, 51-70.

Ripley, E. M., Lightfoot, P. C., Stifter, E. C., Underwood, B., Taranovic, V., Dunlop, M. III, and Donoghue, K. (2015): Heterogeneity of S isotope compositions recorded in the Sudbury Igneous Complex, Canada: significance to formation of Ni-Cu sulfide ores and host rocks. Economic Geology 110, 1125-1135.

Roedder, E. (1984): Fluid Inclusions, Reviews in Mineralogy 12. Mineralogical Society of America.

Rottier, B., Kouzmanov, K., Bouvier, A.-S., Baumgartner, L. P., Walle, M., Rezeau, H., Bendezu, R., and Fontbote, L. (2016): Heterogeneous melt and hypersaline liquid inclusions in shallow porphyry type mineralization as markers of the magmatic-hydrothermal transition (Cerro de Pasco district, Peru). Chemical Geology 447, 93-116.

Rousell, D. H. (1984a): Onwatin and Chelmsford formations. In The geology and ore deposits of the Sudbury Structure, (eds.) Pye, E. G., Naldrett, A. J., and Giblin, P. E. Ontario Geological Survey Special Volume 1, 211-218.

Rousell, D. H. (1984b): Mineralization in the Whitewater Group. In The geology and ore deposits of the Sudbury Structure, (eds.) Pye, E. G., Naldrett, A. J., and Giblin, P. E. Ontario Geological Survey Special Volume 1, 219-232.

Rusk, B. G., Reed, M. H., and Dilles, J. H. (2008): Fluid Inclusion Evidence for Magmatic-Hydrothermal Fluid Evolution in the Porphyry Copper-Molybdenum Deposit at Butte, Montana. Economic Geology 103, 307-334.

Rusk, B. G., Reed, M. H., Dilles, J. H., and Kent, A. J. R. (2006): Intensity of quartz Cathodoluminescence and trace-element content in quartz from the porphyry copper deposit at Butte, Montana. American Mineralogist 91, 1300-1312.

Schandl, E. S. (2004): The role of saline fluids base-metal and gold mineralization at the Cobalt Hill prospect northeast of the Sudbury Igneous Complex, Ontario: a fluid-inclusion and mineralogical study. The Canadian Mineralogist 42, 1541-1562.

Seedorf, E., Dilles, J. H., Proffett, J. M. Jr., Einaudi, M. T., Zurcher, L., Stavast, W. J. A., Johnson, D. A., and Barton, M. D. (2005): Porphyry deposits: characteristics and origin of hypogene features; in Hedenquist, J. W., Thompson, J. F. H., Goldfarb, R. J., and Richards, J. P., eds., Economic Geology, 100th Anniversary Volume, 251-298.

Sharpe, R., and Fayek, M. (2011): The World's oldest observed primary uraninite. The Canadian Mineralogist 49, 1199-1210.

Simmons, S. F., White, N. C., and John, D. A. (2005): Geological characteristics of epithermal precious and base metal deposits; in Hedenquist, J. W., Thompson, J. F. H., Goldfarb, R. J., and Richards, J. P., eds., Economic Geology, 100th Anniversary Volume, 485-522.

Smith, M. P., Savary, V., Yardley, B. W. D., Valley, J. W., Royer, J. J., Dubois, M. (1998): The evolution of the deep flow regime at Soultz-sous-Forets, Rhine Graben, eastern France:

evidence from a composite quartz vein. Journal of Geophysical Research – Solid Earth 103, 27223-27237.

Sterner, S. M., Hall, D. L., and Bodnar, R. J. (1988): Synthetic fluid inclusions. V. Solubility relations in the system NaCl-KCl-H2O under vapour-saturated conditions. Geochimica et Cosmochimica Acta 52, 989-1005.

Stewart, R. C. Kontak, D. J., Ames, D. E., and Fayek, M. (2014): A long lived mega-hydrothermal system preserved in the granophyre unit of the 1.85 Ga Sudbury impact-generated melt sheet Ontario, Canada [abs.]: Geological Association of Canada-Mineralogical Association of Canada Joint Annual Meeting, Abstracts, 265-266.

Taylor, H. P. Jr (1968): The oxygen isotope geochemistry of magmatic rocks. Contributions to Mineralogy and Petrology 19, 1-71.

Taylor, H. P. Jr (1977): 18O/16O, D/H, and 13C/12C studies of the Tertiary Igneous Complex of Skye, Scotland. American Journal of Science 277, 136-177.

Taylor, H. P. Jr (1979): Oxygen and hydrogen isotope relationships in hydrothermal mineral deposits. In: Geochemistry of Hydrothermal Ore Deposits, vol. 2, H. L. Barnes (eds.), John Wiley, New York, 236-277.

Taylor, H. P. Jr and Sheppard, S. M. F. (1986): Igneous rocks: I Processes of isotope fractionation and isotope systematics. In: Valley, J. W., Taylor, H. P. Jr (Eds.), Stable Isotopes in High-Temperature Geological Processes. Reviews in Mineralogy and Geochemistry 16, 227-271.

Thorne, W., Hagemann, S., Vennemann, T., and Oliver, N. (2009): Oxygen Isotope compositions of Iron Oxides from High-Grade BIF-Hosted Iron Ore Deposits of the

Central Hamersley Province, Western Australia: Constraints on the Evolution of Hydrothermal Fluids. Economic Geology 104, 1019-1035.

Tivey, M.K. (2007): Generation of seafloor hydrothermal vent fluids and associated mineral deposits. Oceanography 20, 50-65.

Tuba, G., Molnár, F., Ames, D. E., Péntek, A., Watkinson, D. H., and Jones, P. C. (2014): Multi-stage hydrothermal processes involved in "low-sulfide" Cu(-Ni)-PGE mineralization in the footwall of the Sudbury Igneous Complex (Canada): Amy Lake PGE zone, East Range. Mineralium Deposita 49, 7-47.

Tuba, G., Molnár, F., Watkinson, D. H., Jones, P. C., and Mogessie, A. (2010): Hydrothermal vein and alteration assemblages associated with low-sulfide footwall Cu-Ni-PGE mineralization and regional hydrothermal processes, North and East Ranges, Sudbury structure, Canada. SEG Special Publication 15, 573-598.

Tuttle, O. F. and Bowen, N. L. (1958): Origin of granite in light of experimental studies in the system $NaAlSi_3O_8$-KAl-Si_3O_8-H_2O. Geological Society of America Memoires 74, 153.

Tweedale, F., Hanley, J. J., Kontak, D. J., and Rogers, N. (2015): Petrographic observations and evaporate mound analysis of quartz-hosted fluid inclusions hosted by granitoid samples from the South Mountain Batholith, Nova Scotia: An exploration tool for vectoring towards mineralised areas in intrusive rocks.; in TGI4 – Intrusion Related Mineralisation Project: New Vectors to Buried Porphyry-Style Mineralisation, (ed.) N. Rogers. Geological Survey of Canada, Open File 7843, 79-99.

Valley, J. W. and Graham, C. M. (1996): Ion microprobe analysis of oxygen isotope ratios in quartz from Skye granite: healed micro-cracks, fluid flow and hydrothermal exchange. Contributions to Mineralogy and Petrology 124, 225-234.

Van Ruitenbeek, F. J. A., Cudahy, T. J., van der Meer, F. D., and Hale, M. (2012): Characterization of the hydrothermal systems associated with Archean VMS-mineralization at Panorama, Western Australia, using hyperspectral, geochemical and geothermometric data. Ore Geology Reviews 45, 33-46.

Versh, E., Kirsimae, K., Joeleht, A., and Plado, J. (2008): Fluid-rock interaction in hydrothermal system at Kardla impact structure, Estonia. In: Geochimica et Cosmochimica Acta. 18th Annual V M Goldschmidt Conference, Vancouver, Canada, (A981-A981). July, 2008.

Warren, J. K. (2006): Evaporites- sediments, resources, and hydrocarbons. New York, New York, Springer, 1035 p.

Webster, J. D. (1992): Fluid-melt interactions involving Cl-rich granites – experimental-study from 2 to 8 kbar. Geochimica et Cosmochimica Acta 56, 659-678.

Wenner, D. B. and Taylor, H. P. Jr (1976): Oxygen and hydrogen isotope studies of a Precambrian granite-rhyolite terrane, St. Francois Mountains, southeastern Missouri. Geological Society of America Bulletin 87, 1587-1598.

Whitehead, R. E. S., Davies, J. F., and Goodfellow, W. D. (1990): Isotopic evidence for hydrothermal discharge into anoxic seawater, Sudbury basin, Ontario, Canada. Chemical Geology 86, 49-63.

Wilkinson, J. J. (2001): Fluid inclusions in hydrothermal ore deposits. Lithos 55, 229-272.

Wilkinson, J. J. (2017): Metastable freezing: a new method for the estimation of salinity in aqueous fluid inclusions. Economic Geology 112, 185-193.

Yokoyama, E., Nedelec, A., Baratoux, D., Trindade, R. I. F., Fabre, S., and Berger, G. (2015): Hydrothermal alteration in basalts from Vargeao impact structure, south Brazil, and

implications for recognition of impact-induced hydrothermalism on Mars. Icarus 252, 347-365.

Zak, K., Pudilova, M., and Breiter, K. (2005): Oxygen isotope study of highly fractionated Podlesi granite system, Krusnehory mountains, Czech Republic. Bulletin of Geosciences 80, 139-143.

Zhao, G., Sun, M., Wilde, S. A., and Li, S. (2004): A Paleo-Mesoproterozoic supercontinent: assembly, growth and breakup. Earth-Science Reviews 67, 91-123.

Zhao, K.-D., Jiang, S.-Y., Nakamura, E., Moriguti, T., Palmer, M. R., Yang, S.-Y., Dai, B.-Z., and Jiang, Y.-H. (2011): Fluid-rock interaction in the Qitianling granite and associated tin deposits, South China: evidence from boron an oxygen isotopes. Ore Geology Reviews 43, 243-248.

Zieg, M. J. and Marsh, B. D. (2005): The Sudbury Igneous Complex: Viscous emulsion differentiation of a superheated impact melt sheet. Geological Society of America Bulletin 117, 1427-1450.

Zou, H., Zhang, S.-t., Chen, A.-q., Fang, Y., and Zeng, Z.-f. (2016): Hydrothermal Fluid Sources of the Fengjia Barite-fluorite Deposit in Southeast Sichuan, China: Evidence from Fluid Inclusions and Hydrogen Isotopes. Resource Geology 66, 24-36.

Zurcher, L. and Kring, D. A. (2004): Hydrothermal alteration at the core of the Yaxcopoil-1 borehole, Chicxulib impact structure, Mexico. Meteoritics and Planetary Sciences 38, 1199-1222.

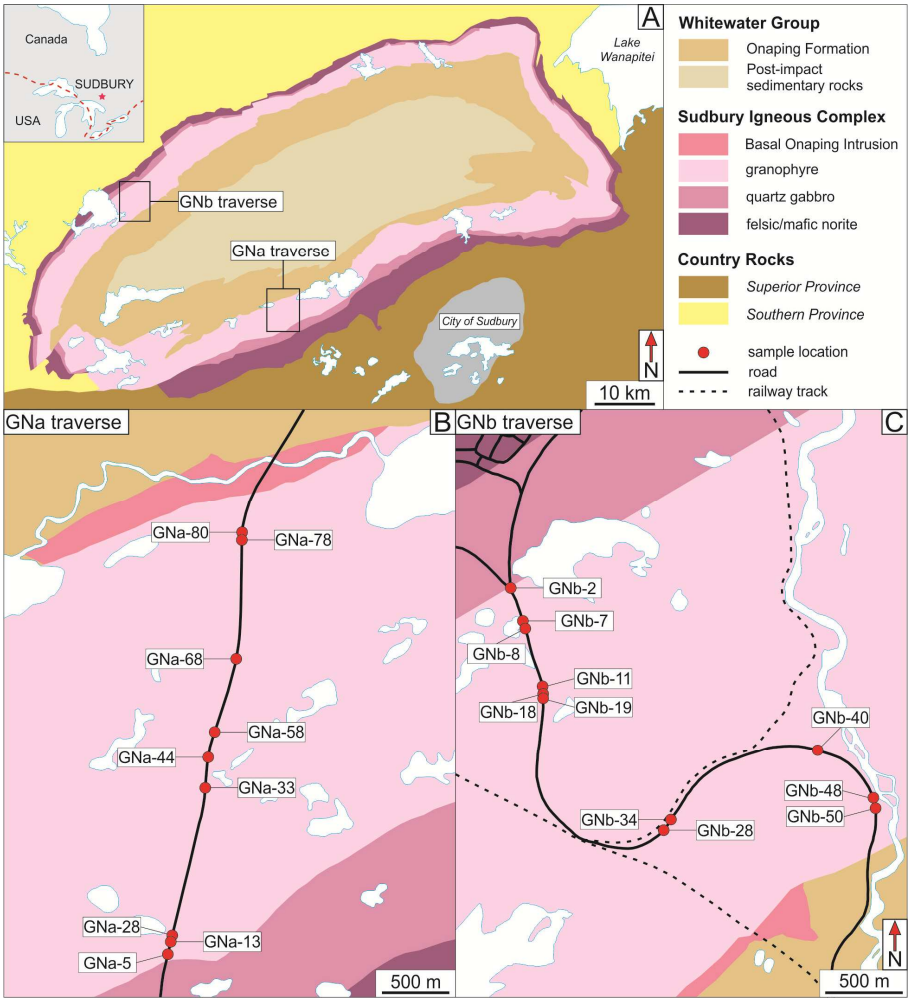

Figure 3-1. Geological setting of the area of study. (A) Regional geology of the Sudbury Structure and footwall rocks (modified after Ames and Farrow 2007). Inset map in upper left corner shows the location of the Sudbury Structure within Canada. The two black boxes indicate the locations of two traverses used for sample collection along highway #144 (shown in B and C). (B) South Range traverse (GNa, n = 9). (C) North Range traverse (GNb; n = 11). Sample locations from this study are indicated by blue boxes. Red dots indicate sample locations.

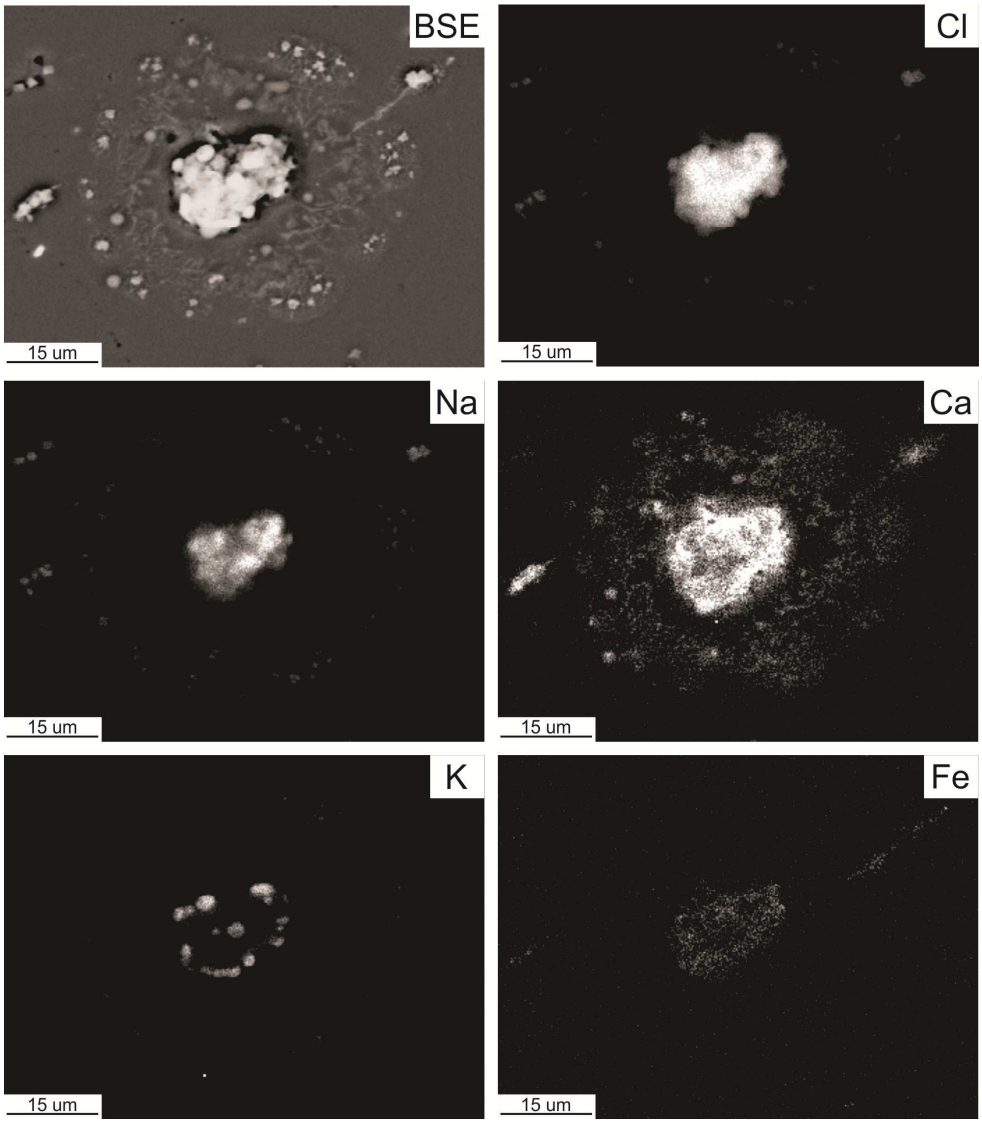

Figure 3-2. Back-scattered electron (BSE) image and X-ray maps (Cl, Na, Ca, K, and Fe) of a typical evaporate mound. These X-ray maps illustrate element fractionation and dispersion away from the inclusion that occurred during decrepitation.

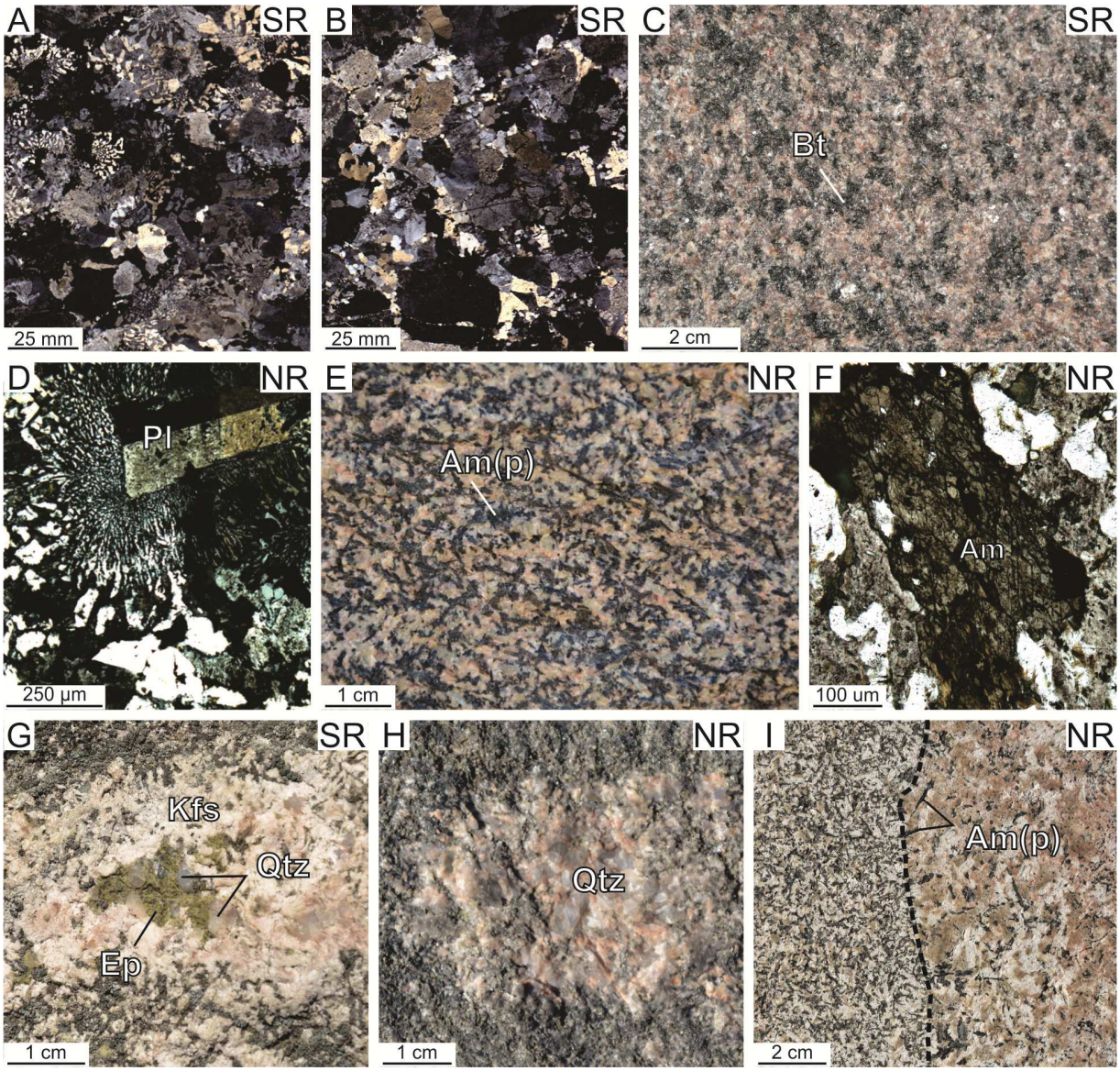
A
SR
25 mm
B
SR
25 mm
C
SR
Bt
2 cm
D
NR
Pl
250 µm
E
NR
Am(p)
1 cm
F
NR
Am
100 um
G
SR
Kfs
Qtz
Ep
1 cm
H
NR
Qtz
1 cm
I
NR
Am(p)
2 cm

Figure 3-3. Scanned polished thin section images (A, B), photographs (C, E, G, H, I) and photomicrographs (D, F) summarizing textural features of the granophyre unit (GR) in the North Range (NR) and South Range (SR). (A) Sample from GR with 34 vol. % granophyre. (B) Sample from GR that lacks granophyre. (C) GR outcrop from the SR containing biotite, quartz, K-feldspar, and plagioclase. (D) Plagioclase lath acting as a nucleus for granophyre. Notice the coarsening of quartz and K-feldspar away from plagioclase. (E) GR outcrop from the NR containing primary, acicular amphibole with quartz, K-feldspar, and plagioclase. (F) Primary amphibole with quartz and K-feldspar. (G) GR outcrop from the SR containing a miarolitic cavity with epidote and quartz-within a coarse-grained quartz-K-feldspar domain. (H) GR outcrop from the SR containing a miarolitic cavity filled with quartz. (I) GR outcrop from the NR showing a coarse-grained K-feldspar-quartz-amphibole felsic domain within a finer-grained amphibole-quartz-feldspar domain. Abbreviations: Am(p) – primary amphibole; Bt – biotite; Ep – epidote; Kfs – K-feldspar; Pl – plagioclase; Qtz – quartz.

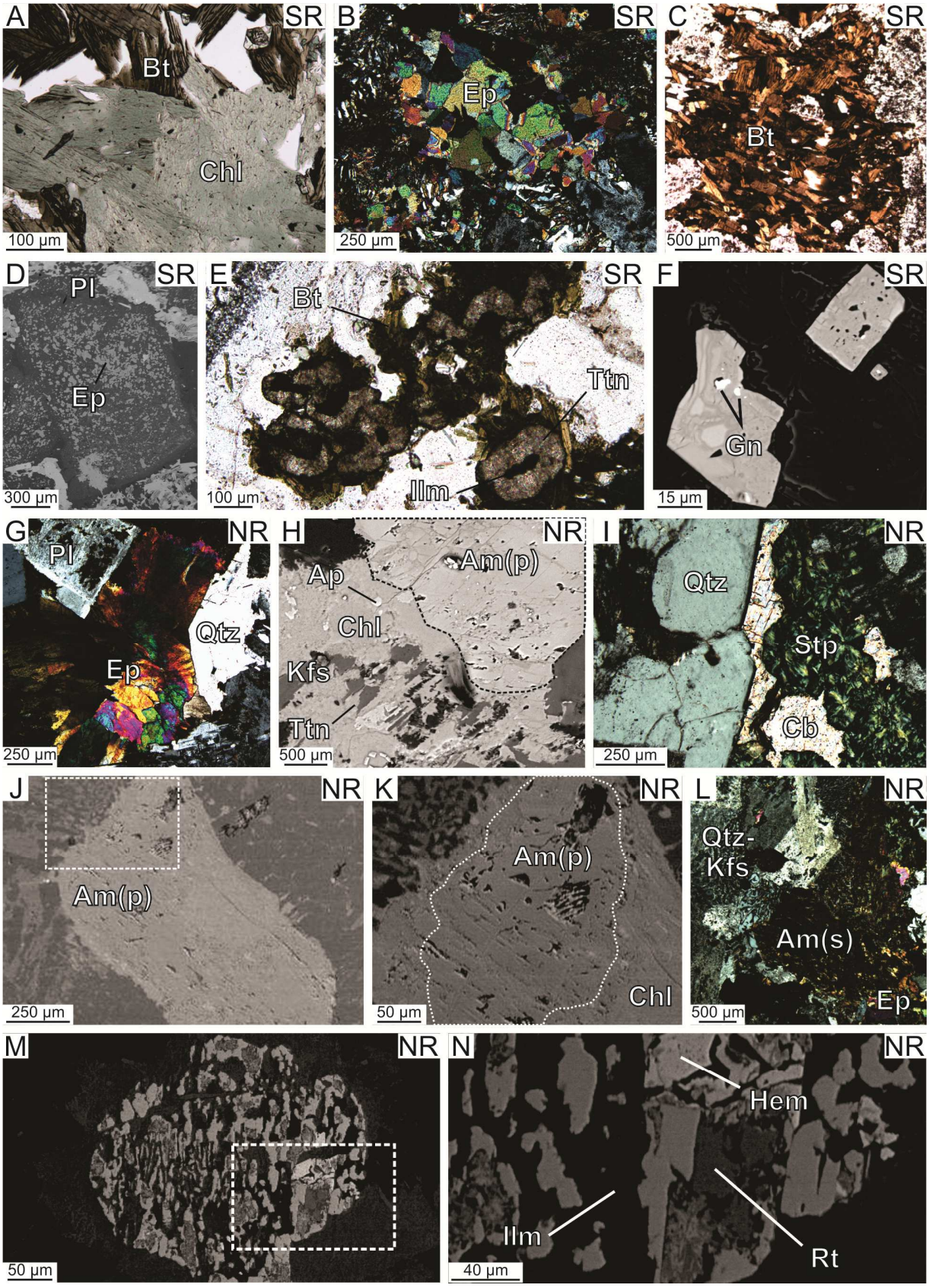
A
SR
Bt
Chl
100 µm
B
SR
Ep
250 µm
C
SR
Bt
500 µm
D
SR
Pl
Ep
300 µm
E
SR
Bt
Ttn
Ilm
100 µm
F
SR
Gn
15 µm
G
NR
Pl
Qtz
Ep
250 µm
H
NR
Ap
Am(p)
Chl
Kfs
Ttn
500 µm
I
NR
Qtz
Stp
Cb
250 µm
J
NR
Am(p)
250 µm
K
NR
Am(p)
Chl
50 µm
L
NR
Qtz-
Kfs
Am(s)
Ep
500 µm
M
NR
50 µm
N
NR
Hem
Ilm
Rt
40 µm

Figure 3-4. Photomicrographs (A, B, C, E, G, I,L) in plane-polarized (PPL) and cross-polarized (XPL) light and back-scattered electron (D, F, H, J, K, M, N) images summarizing the metasomatic textures of the granophyre unit (GR) in the North Range (NR) and South Range (SR). (A) PPL image of chlorite and biotite which is a common alteration assemblage in the SR. (B) XPL image of medium-grained epidote in fine-grained granophyre matrix. (C) PPL image of pervasive secondary biotite exhibiting moderate alignment of grains. (D) BSE image of a plagioclase grain exhibiting pit texture where epidote has precipitated in the pits. (E) PPL image showing ilmenite (core) being partially replaced by titanite (rim) with biotite. This style of replacement is unique to the SR (F) BSE image of zircon exhibiting zoning similar and pitted texture with thorite. (G) XPL image of a strongly altered sample containing coarse-grained epidote in a quartz-plagioclase matrix. (H) BSE image of an altered domain containing primary amphibole with chlorite, titanite, and K-feldspar with accessory apatite. (I) XPL image showing a stilpnomelane and carbonate alteration assemblage. (J) BSE image of primary amphibole in a quartz-K-feldspar matrix that has experienced partial re-equilibration producing pit texture (top and bottom of grain) and replacement (middle of grain). (K) BSE image of white dashed box from J. The image shows the pitted texture in greater detail of the primary amphibole domain that is now chemically secondary amphibole. The lower portion of the grain has been replaced by chlorite. (L) PPL image of secondary, acicular amphibole and epidote. (M) BSE image showing a complex replacement reaction of ilmenite to magnetite and rutile. (N) BSE image of white box inset from E. This image better shows the replacement of ilmenite by magnetite and ilmenite. Abbreviations: Am(p) – primary amphibole; Ap – apatite; Bt – biotite; Cb – carbonate; Chl – chlorite; Ep – epidote; Gn – galena; Hem – hematite; Ilm – ilmenite; Kfs – K-feldspar; Pl – plagioclase; Qtz – quartz; Rt – rutile; Stp – stilpnomelane; Ttn – titanite.

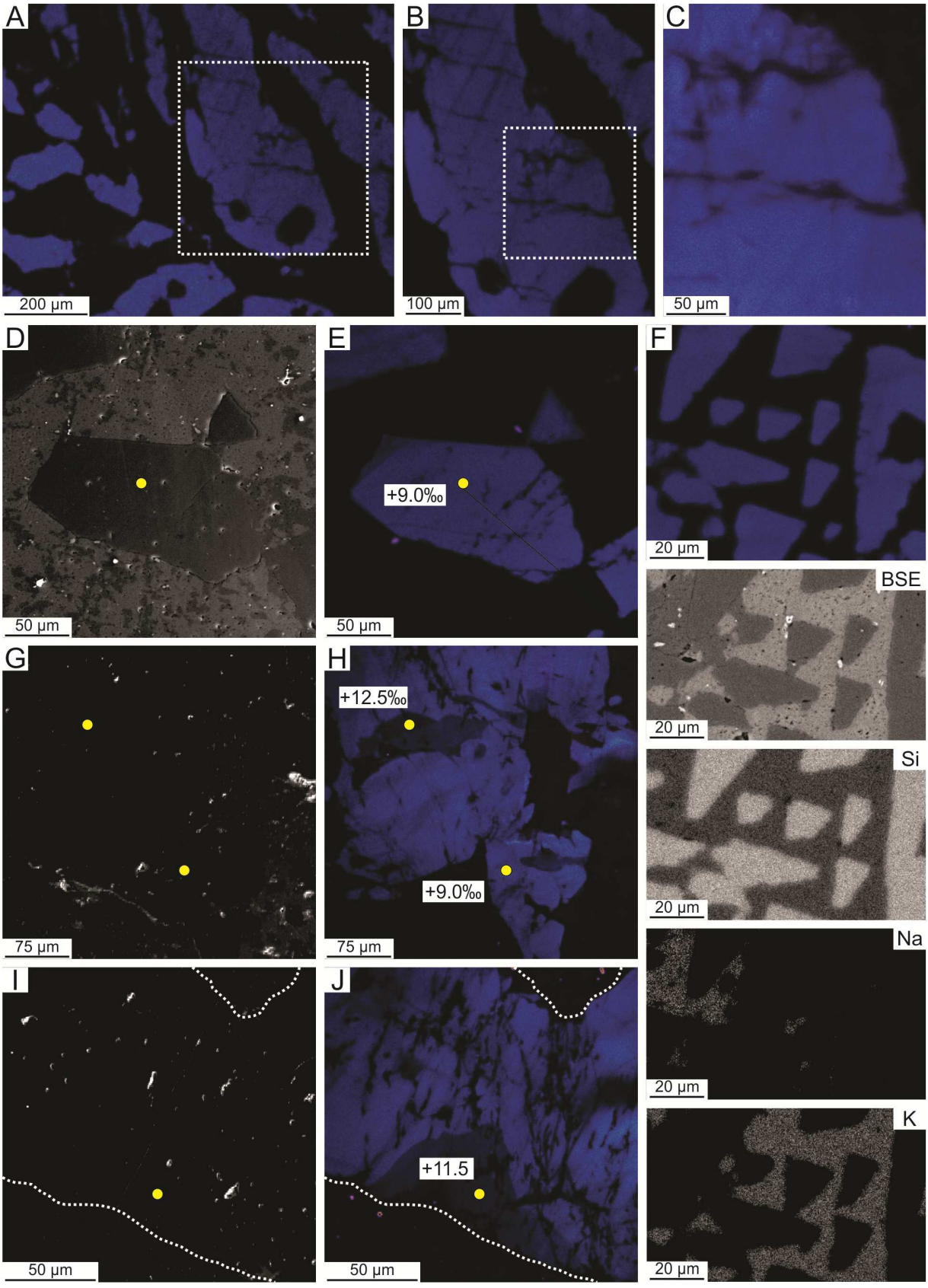
A
200 µm
B
100 µm
C
50 µm
D
50 µm
E
+9.0‰
50 µm
F
20 µm
BSE
20 µm
Si
20 µm
Na
20 µm
K
20 µm
G
75 µm
H
+12.5‰
+9.0‰
75 µm
I
50 µm
J
+11.5
50 µm

Figure 3-5. Cathodoluminescence (CL; A, B, C, D, F, H), back-scattered electron (BSE; E, G, I), and X-ray (J) images summarizing the characteristics of quartz in the granophyre unit (GR) from the North Range (NR) and South Range (SR). (A) CL image of granophyre-hosted quartz. Quartz within the white box exhibits textural evidence only visible by using CL of re-equilibration along two large fractures. (B) CL image of white box from A. (C) CL image of white box from figure B. Small microfractures related to the two larger fractures are visible only at such high magnification. (D) CL image of a granophyre-hosted quartz grain from the NR. This quartz grain contains few microfractures; however, the CL signal is strong (bright blue), indicating minimal re-equilibration. (E) BSE image of D. Notice how microfractures indicated by CL are not visible using BSE imaging. (F) CL image of re-crystallized quartz from the NR. Notice the moderate microfracturing in quartz and the change in variable CL single (brightness) indicating partial re-equilibration. Yellow dots indicate points of secondary ion mass spectrometry analysis and oxygen isotope values are noted. (G) BSE image of F. Notice how microfractures and textural evidence for re-equilibration and not visible by BSE alone, similar to D and E. (H) CL image of recrystallized quartz. Notice the very weak CL signal (dark blue) indicating the grain has experienced extensive re-equilibration. The white line outlines the extent of the quartz grain as it is indistinguishable using only CL imaging. (I) BSE image of H. Similar to the CL image, it is difficult to identify the quartz grain boundary using BSE imaging. (J) CL image and accompanying BSE and X-ray (Si, Na, K) maps of relatively unaltered granophyre-hosted quartz. Notice the strong (bright) signal in the CL image and the outline of Si X-ray map corresponding with the CL image.

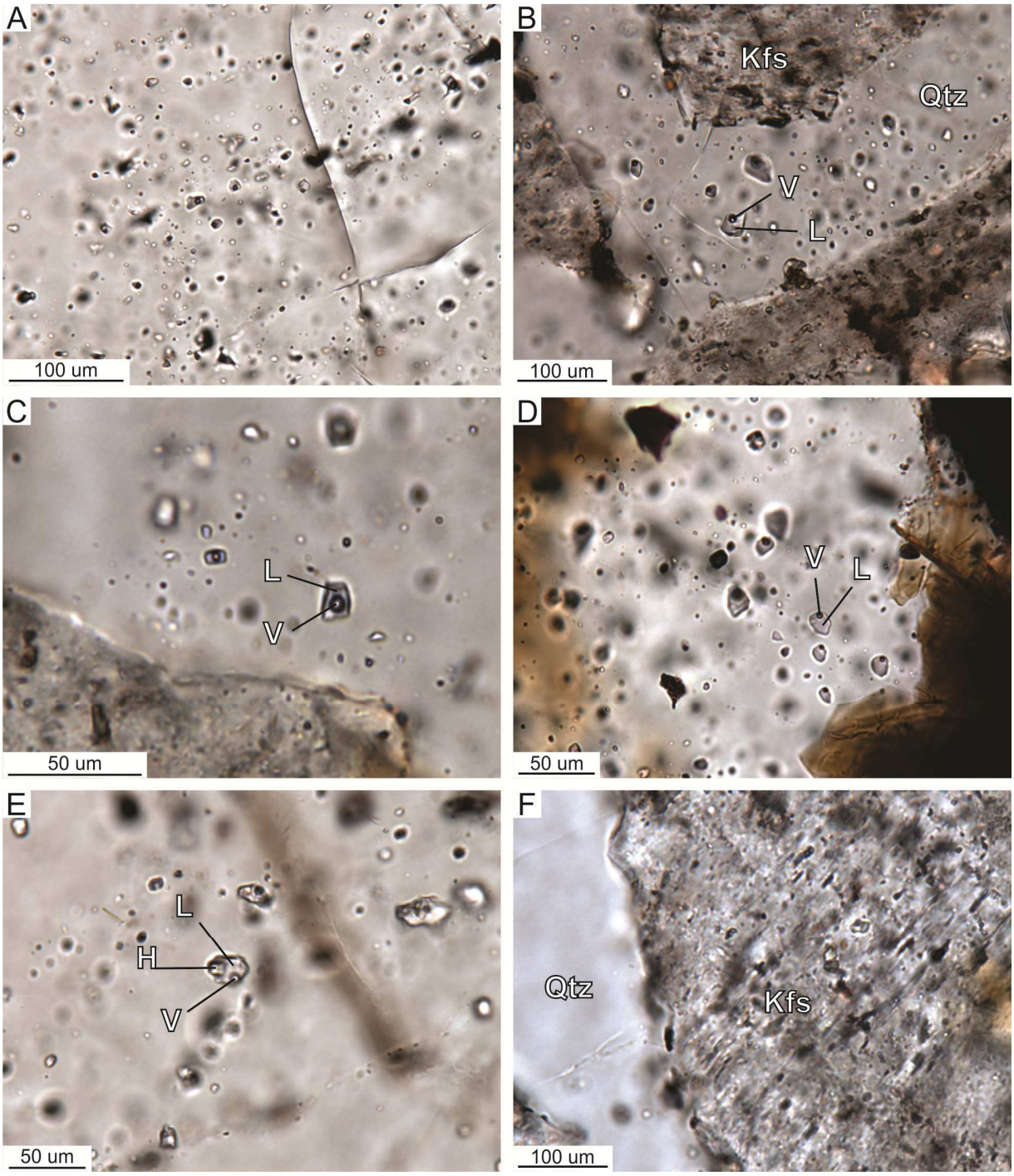
A
100 um
B
Kfs
Qtz
V
L
100 um
C
L
V
50 um
D
V
L
50 um
E
L
H
V
50 um
F
Qtz
Kfs
100 um

Figure 3-6. Photomicrographs of fluid inclusions from the granophyre unit. (A) Sample GNb-11 showing a granophyre-hosted quartz grain which contains abundant fluid inclusions. Notice the orientation of fluid inclusions along fracture planes. (B) Sample GNb-19 showing quartz and K-feldspar hosted in granophyre. Visible fluid inclusions comprise a fluid inclusion assemblage (FIA) containing liquid and vapour phases. (C) Sample GNa-44 containing an FIA of type 1, L-rich fluid inclusions with uniform L:V ratios which are smaller than type 1 inclusions. (D) Sample GNb-50 showing an FIA of type 2, L-rich fluid inclusions with near uniform liquid to vapour (L:V) ratios. (E) Sample GNb-7 containing an FIA of type 3, L-rich hypersaline fluid inclusions. Solid phase in inclusions is halite. (F) Sample GNa-68 showing quartz and K-feldspar hosted in granophyre with fluid inclusions hosted in K-feldspar. Abbreviations: Kfs – K-feldspar; Qtz – quartz; V – vapour; L – liquid; H – halite.

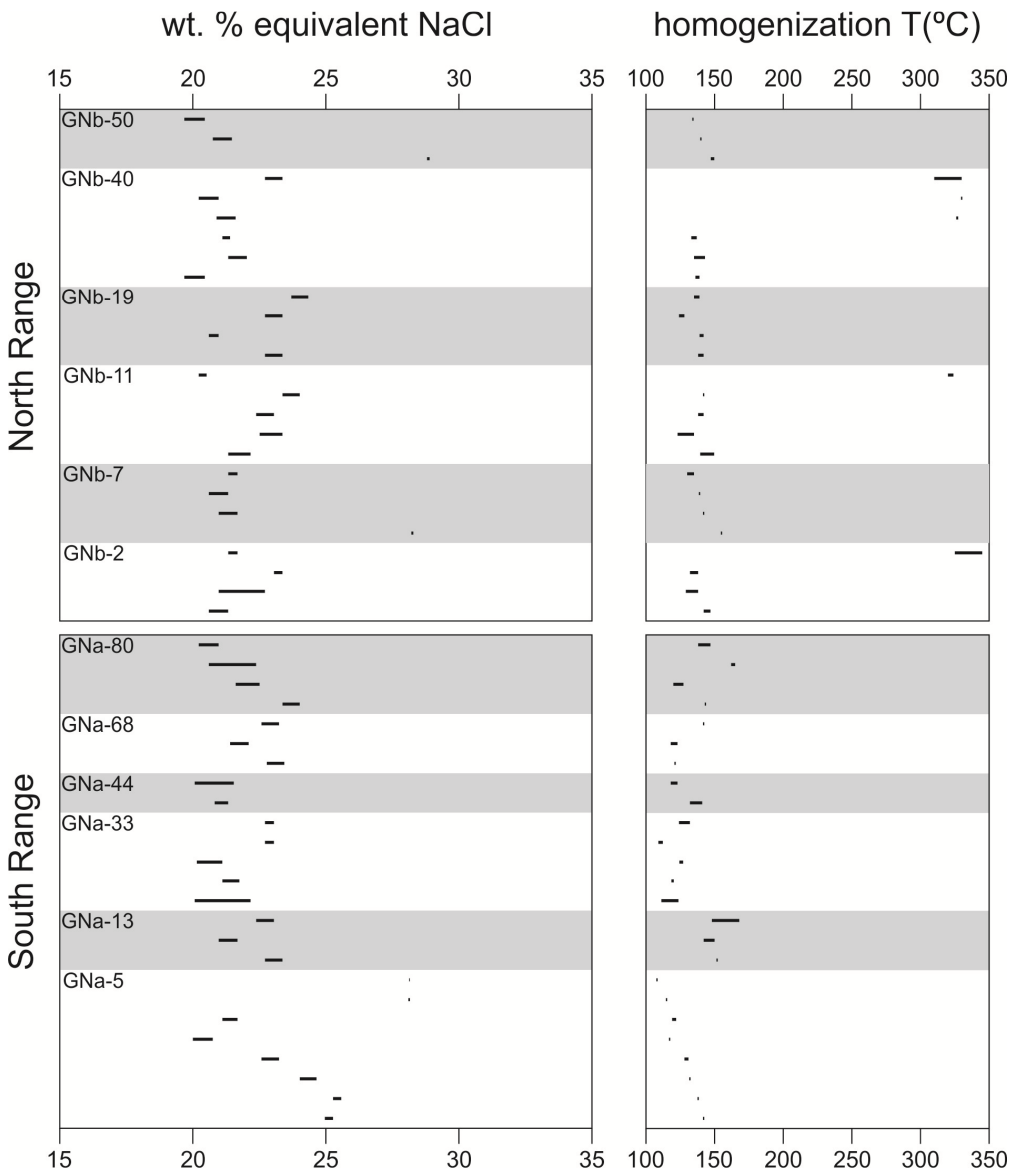

Figure 3-7. Summary of thermometric data for fluid inclusions from the granophyre unit (GR) from the North Range (NR) and South Range (SR) (see Table 2 for complete list of data). Figure shows the range in salinity (as wt. % equiv. NaCl) and homogenization temperature (in °C) for multiple fluid inclusions for each sample.

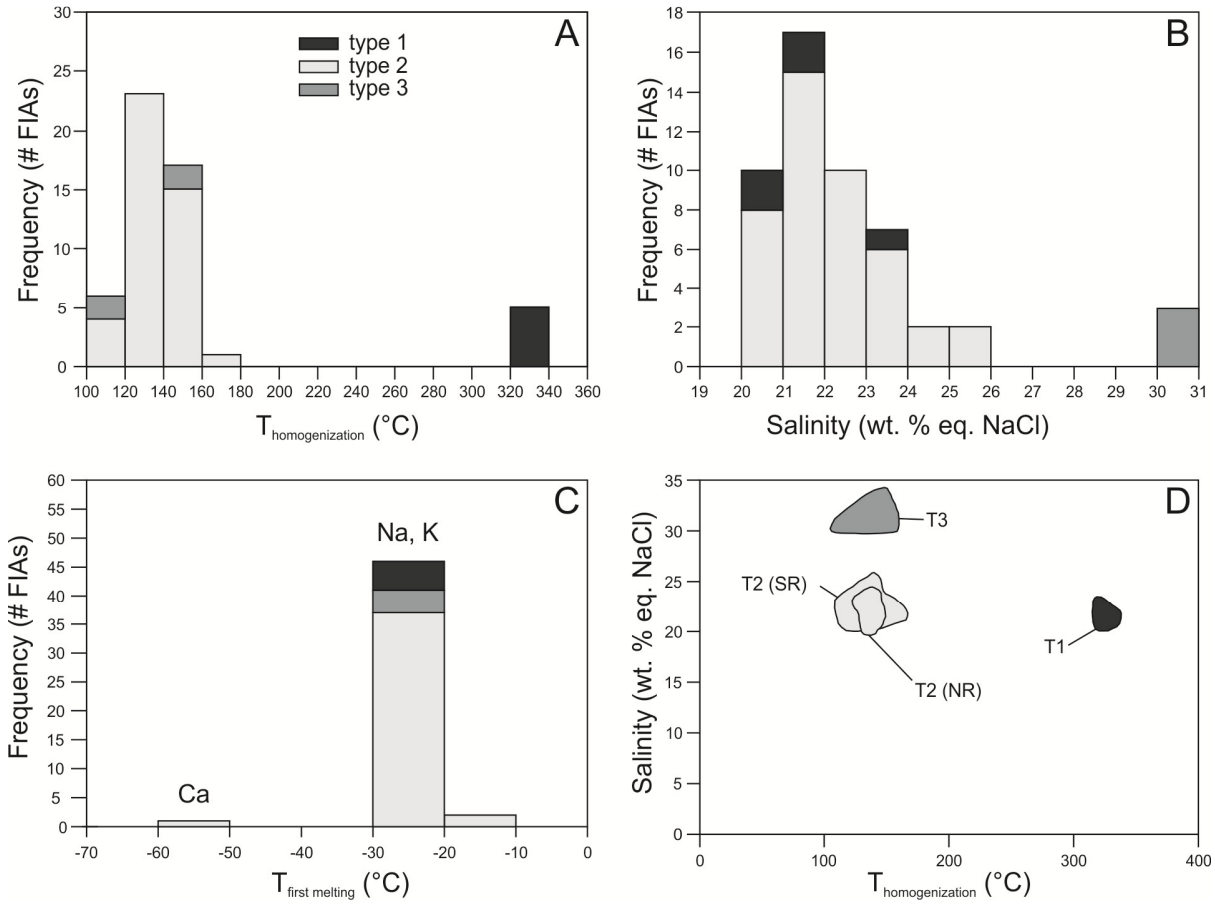

Figure 3-8. Histogram (A, B, C) and bivariate (D) plots summarizing microthermometric data for fluid inclusions hosted in quartz in the granophyre unit. (A) Homogenization temperatures. (B) Fluid inclusion salinity as expressed as wt. % equiv. NaCl. (C) Temperatures of first melting for fluid inclusions. (D) Plot of homogenization temperature and salinity showing fields for fluid inclusion types. Type 2 inclusions are subdivided into North Range (NR) and South Range (SR).

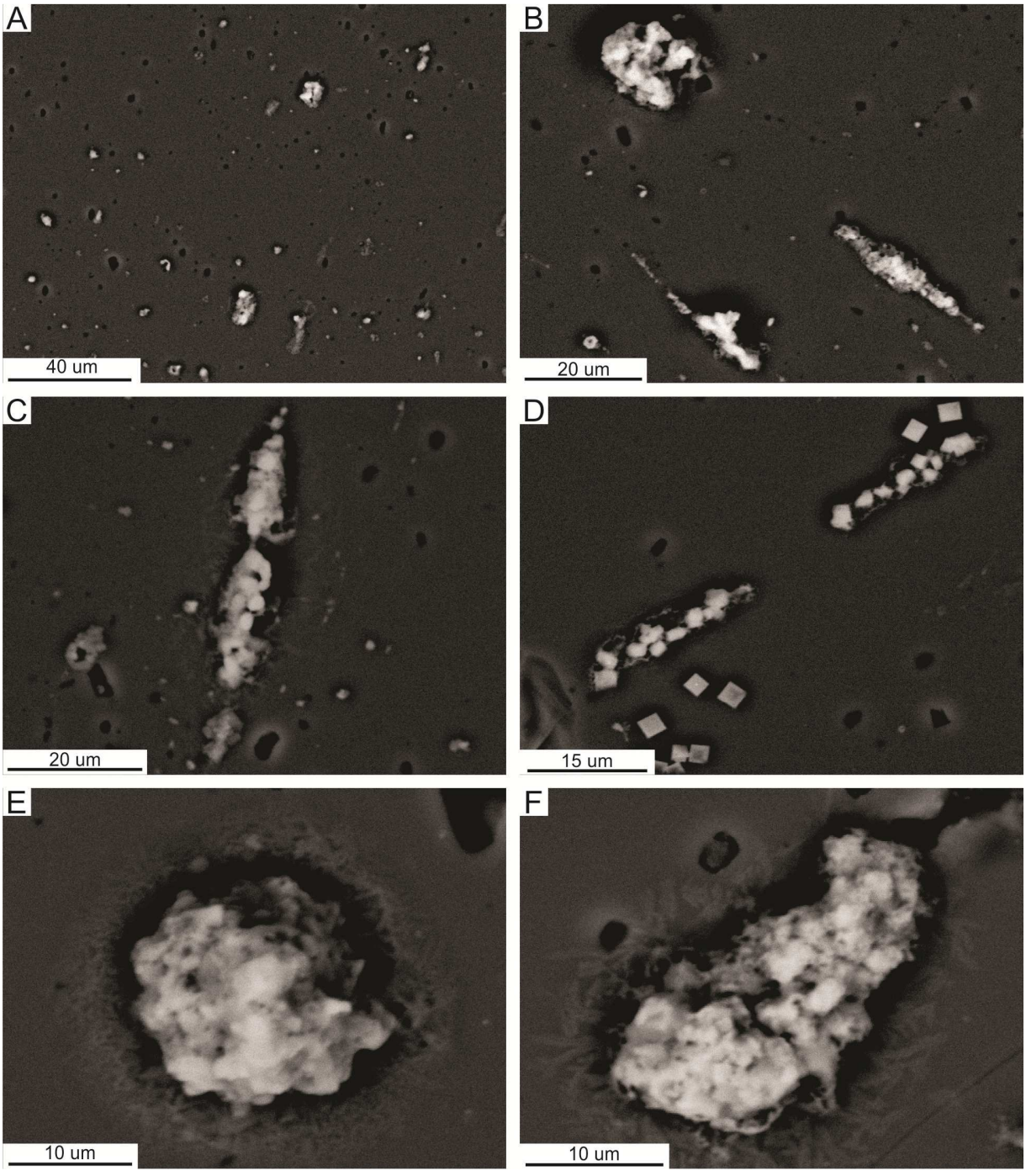
A
40 um
B
20 um
C
20 um
D
15 um
E
10 um
F
10 um

Figure 3-9. Back-scattered electron (BSE) images of evaporate mounds hosted in quartz. (A) Example of a evaporate mound mine field containing many mounds of various size and shape. (B) Example of two dominant mound types, circular and elongate. (C) An elongate mound formed by decrepitation and leakage of fluid inclusions along a fracture. (D) Example of elongate mound showing equant habit. (E) High magnification image of typical circular mound. Note the splattered ejecta material surrounding the mound. (F) High magnification image of partially elongate mound forming along a fracture. Note the splattered ejecta material surrounding the mound.

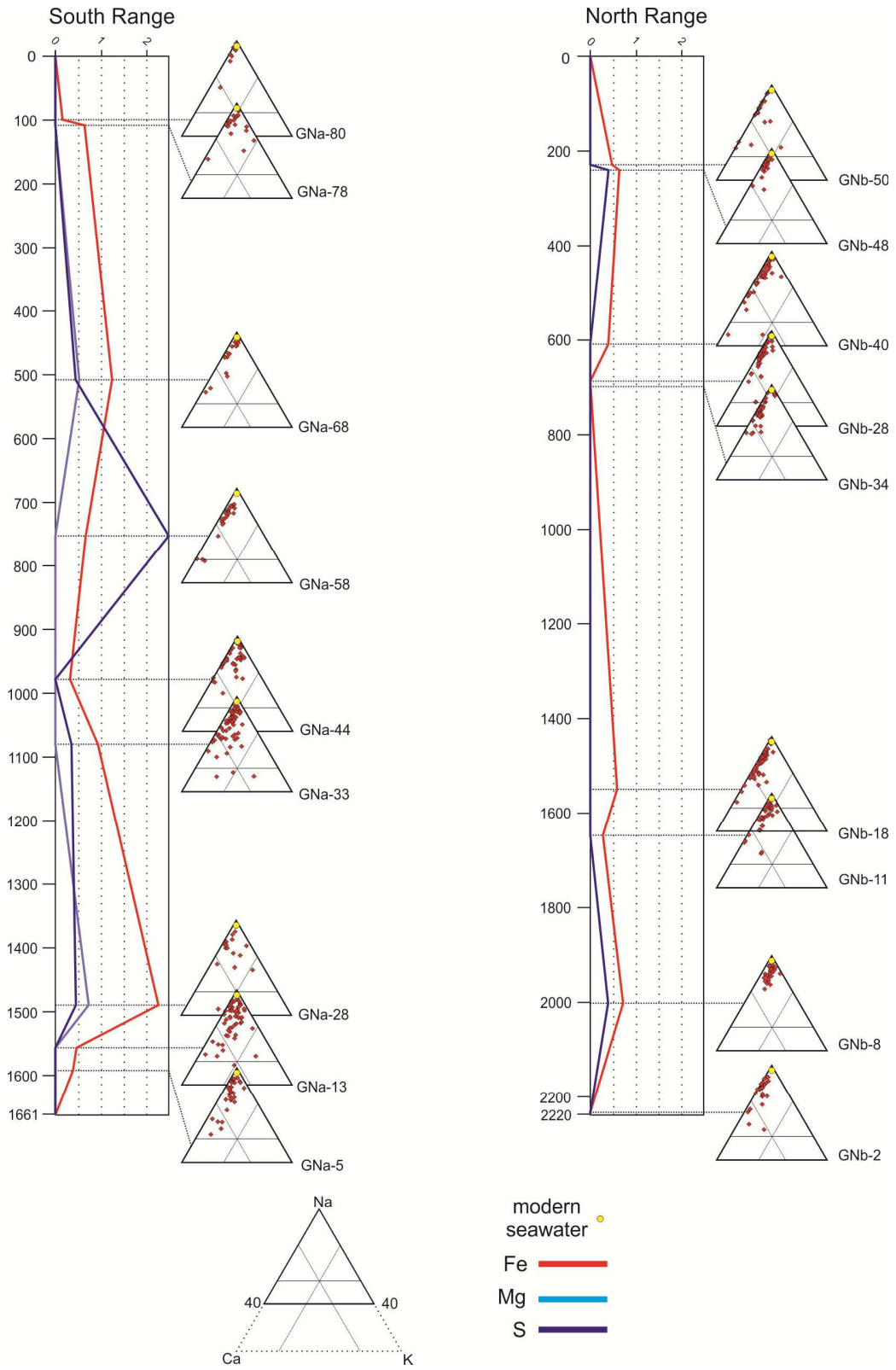
South Range
North Range
0
1
2
0
100
200
300
400
500
600
700
800
900
1000
1100
1200
1300
1400
1500
1600
1661
GNa-80
GNa-78
GNa-68
GNa-58
GNa-44
GNa-33
GNa-28
GNa-13
GNa-5
0
200
400
600
800
1000
1200
1400
1600
1800
2000
2200
2220
GNb-50
GNb-48
GNb-40
GNb-28
GNb-34
GNb-18
GNb-11
GNb-8
GNb-2
Na
40
40
Ca
K
modern seawater
Fe
Mg
S

Figure 3-10. Stratigraphic log showing chemistry of evaporate mounds in the South Range and North Range. Ternary diagrams show the major cations (Na, Ca, K) normalized to 100 %. The intersection of three lines superimposed on ternary diagrams represents 50 % Na, 25 % K and 25 % Ca. Stratigraphic logs show the abundance of minor cations (Fe, Mn, Mg) and sulfur normalized to 100 % (including Na, Ca, and K). Data for modern seawater composition from Millero (2003).

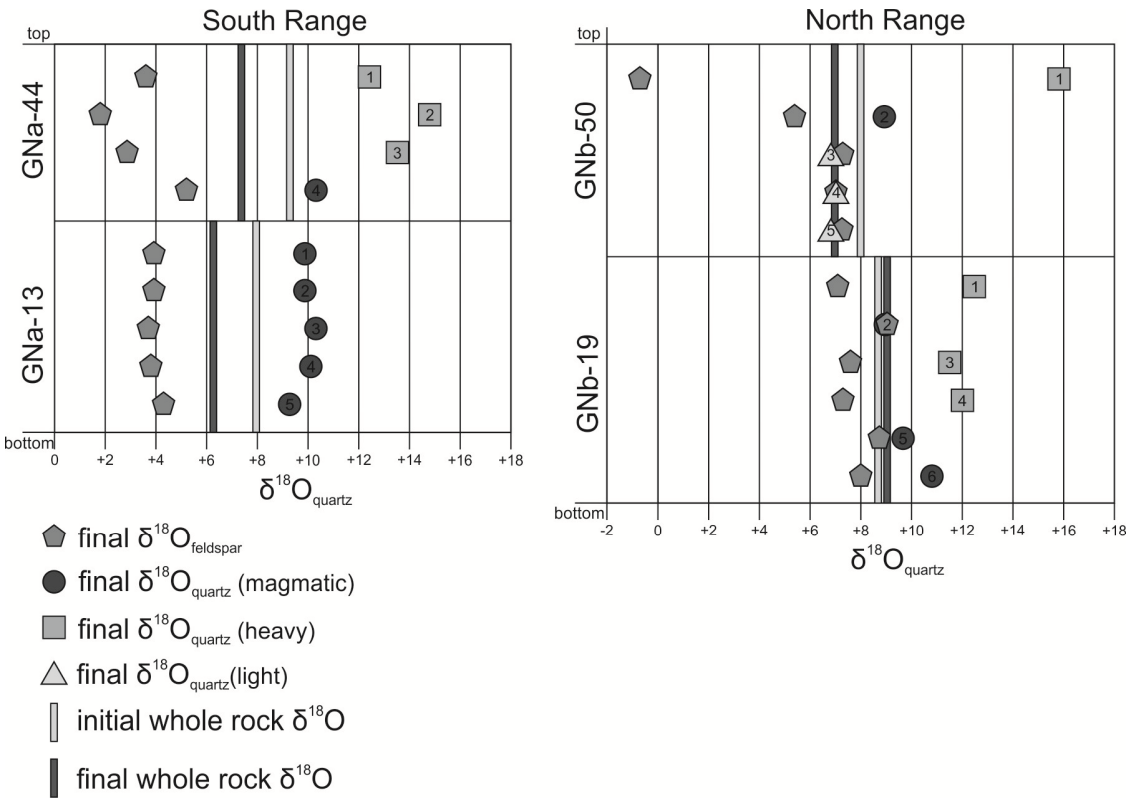

Figure 3-11. Summary of oxygen isotope values for the granophyre unit (GR) from the North Range (NR) and South Range (SR). Measured final whole rock $\delta^{18}O$ and quartz $\delta^{18}O$ values, calculated final feldspar $\delta^{18}O$, and calculated initial whole rock $\delta^{18}O$ oxygen isotope data are shown for four samples from the GR: two from the SR (GNa-13, GNa-44) and two from the NR (GNb-19; GNb-50). The figure shows the change in whole rock $\delta^{18}O$ from the calculated initial value (light grey line) to measured final value (dark grey line). Quartz values are subdivided into "magmatic" (+8 to +10‰; circles), "heavy" values (>+10‰; squares), and "light" values (<+8‰; triangles) in addition to final feldspar values (pentagons) for each analysis calculated based on the modal abundance of quartz and feldspar for each sample.

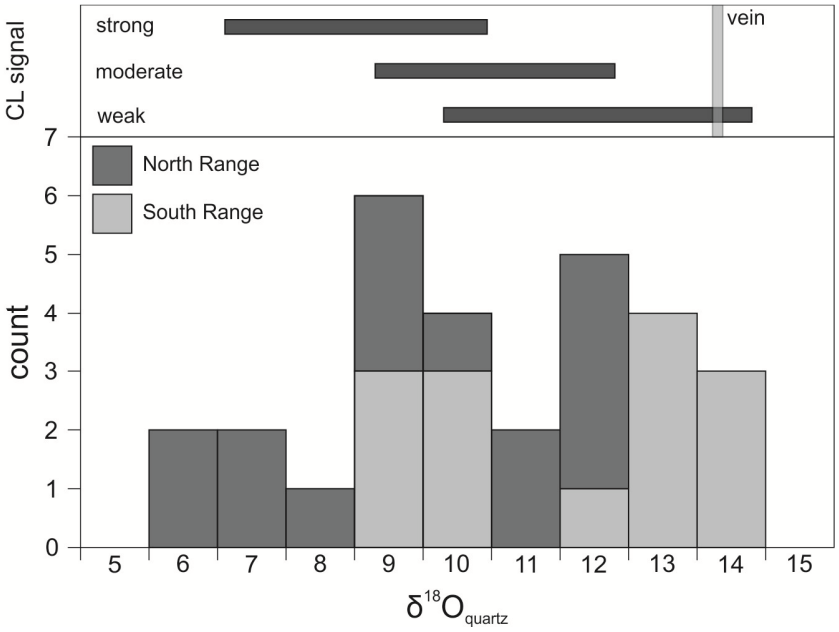

Figure 3-12. Frequency plot for oxygen isotope compositions of quart from the North Range (dark grey) and South Range (light grey) of the granophyre unit detected by secondary ion mass spectrometry (SIMS). Horizontal bars (dark grey) at top of the figure represent the range of $\delta^{18}O$ values of quartz coupled with the intensity of cathodoluminescence (CL) signal. The light grey vertical bar represents the $\delta^{18}O$ value for quartz from a vein. Notice that, on average, the South Range exhibits higher $\delta^{18}O_{quartz}$ values than the North Range.

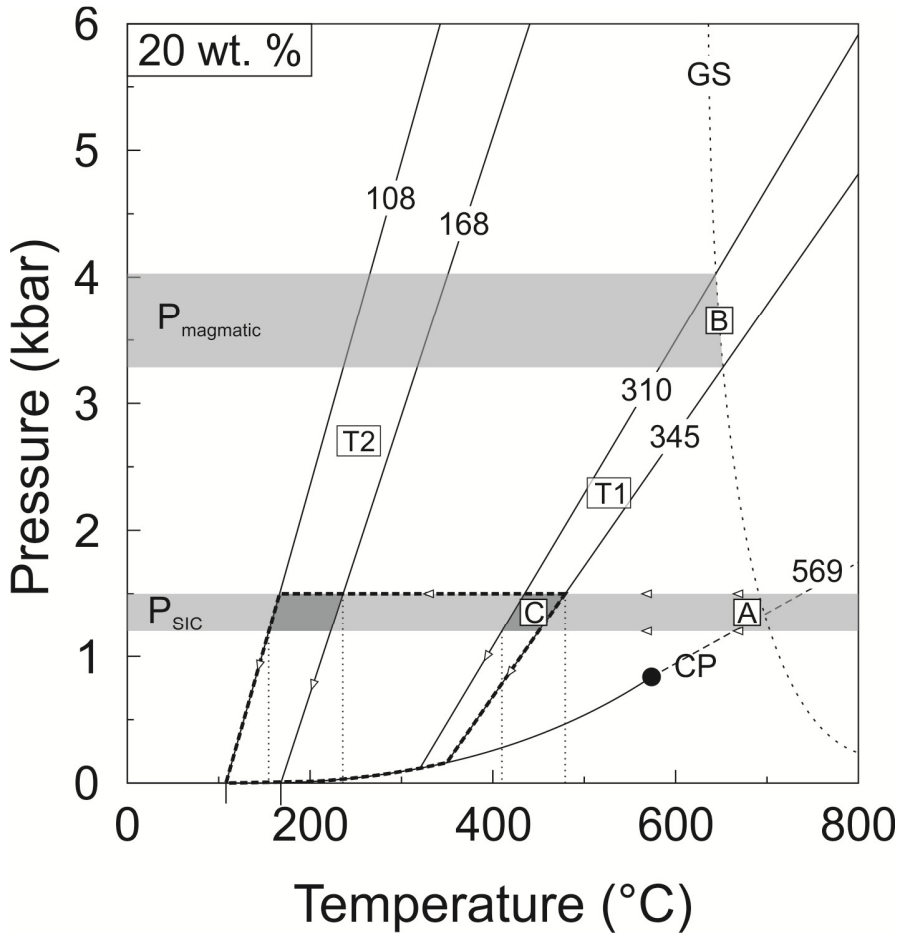

Figure 3-13. A pressure (kbar) versus temperature (°C) diagram showing the fluid path and inferred isochoric projections for types 1 and 2 fluid inclusions hosted in quartz from the granophyre unit (GR). Isochores were determined using microthermometric data (Th, salinity, and homogenization style) and are reported in T(°C). The vertical dotted lines projected to the X-axis (temperature) represent the trapping temperature (Tt) for type's 1 and 2 fluid inclusions. Curves representing phase boundaries (L+V) in the diagrams for 20 wt. % NaCl are from Bodnar (2003). The box labelled P_{SIC} represents the estimated lithostatic pressure of the SIC during trapping of fluid inclusions by Molnár et al. (1999) and Péntek et al. (2008). The dashed line labelled GS represents the solidus of H_2O-saturated granite (Tuttle and Bowen 1958). The arrows labelled "A" represent the pressure and temperature history for a magmatic fluid exsolved at

pressure reported for the GR and isobarically cooled to the trapping temperatures reported in this study ("C). The grey box labelled $P_{magmatic}$ is the trapping pressure required for type 1 fluid inclusions to be magmatic and trapped after exsolution ("B") from the melt according to measured Th data.

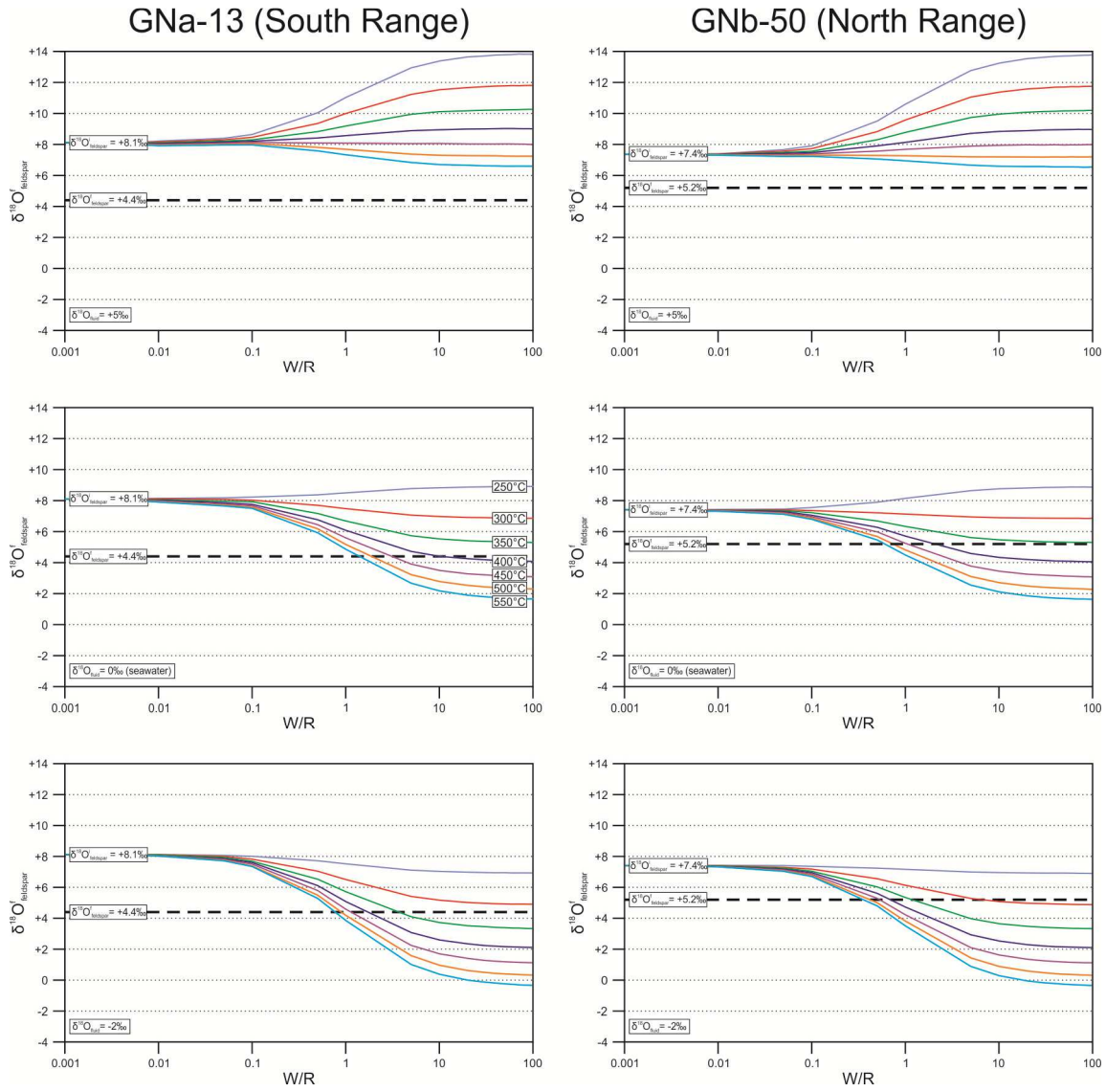

Figure 3-14. Bivariate plots of integrated water:rock ratio (W/R) and oxygen isotope ($\delta^{18}O$) composition of feldspar from the granophyre unit. The diagrams illustrate changes to the oxygen isotope composition of the feldspar phases ($\delta^{18}O^{f}_{feldspar}$) during oxygen isotopic exchange between the feldspar phases and fluids with compositions of +5‰, 0‰, and -2‰. Each diagram shows the evolution of oxygen isotope compositions of the rock (represented by feldspar isotopic composition) during interaction with fluids of different temperatures (250° to 550°C curves of

different colours) and W/R ratios. Each curve is calculated using water-rock fractionation equations representing orthoclase-water system (O'Neil and Taylor 1967). The black dashed line indicates the calculated final feldspar ($\delta^{18}O^{f}_{feldspar}$) value (discussed in text). The intersection of a temperature curve and the black dashed line indicates the W/R ratio required to alter $\delta^{18}O^{f}_{feldspar}$ to such a composition.

Table 3-1. Summary of data from previous fluid inclusion studies on the Sudbury Structure. List of abbreviations: NR – North Range; SR – South Range; L_{aq} – aqueous liquid, L_{CO2} – carbonic liquid; V – vapour; S – solid; nS – multiple solids; H – halite, BP – bubble point. References: 1 – Davies et al. 1990; 2 – Farrow and Watkinson 1992; 3 – Li and Naldrett 1993; 4 – Molnár et al. 1997; 5 – Marshall et al. 1999; 6 – Molnár et al. 1999; 7 – Molnár and Watkinson 2001; 8 – Molnár et al. 2001; 9 – Hanley et al. 2004; 10 – Schandl 2004; 11 – Péntek et al. 2008; 12 – Campos-Alvarez 2010; 13 – Hanley et al. 2011; 14 – Tuba et al. 2014.

Fluid Type	Character	Fluid Source	Range	Contents	V (%)	S (%)	Tf	T_c(ice)	T_m(HH)	T_m(ice)	T_h(V)	T_h(hal)	T_h(other)	T_m(CO2)	T_m(clath)	T_h(CO2)
1	Related to mineralization	saline Canadian groundwater + exsolved fluids from the SIC + fluids exsolved from the FWGR + solutions from crystallizing sulfide liquids	NR, SR	L_{aq}+V+nS (<5)	10 to 20	~10 to 40	~-100	-73 to -50	-50 to -10	-49 to -20	min. 280 to 500	140 to 420	min. 280 to 500			
2	Associated with footwall granophyre melt	saline groundwater + magmatic fluid derived from the FWGR	NR, SR	L_{aq}+V+H+nS	<10	<80					~110 to 175	215 to 500	90 to 400			
3	Associated with Sudbury basin SEDEX mineralization	normal seawater < isotopically positive hydrothermal fluid generated from seawater modified by heat and water-rock interaction in the substrate	Sudbury basin	n.d.												
4	Associated with Proterozoic seawater in Sudbury basin	weakly unmodified seawater	Sudbury basin	n.d.												
5	Basment-derived fluid that migrated to the upper portion of the SIC	Basement-derived fluids moving upwards through SIC + evolved Proterozoic seawater	NR	L_{aq}+V	15 to 20					-23 to -24.5	159 to 210					
6	Associated with deformation and metamorphism	derived from deformation and low-grade metamorphism + possibly magamtic FWGR fluids	SR	L_{aq}+L_{CO2}+V	60 to 70		~-100				decrep at 200 to 250			-61.3 to -56.6	-3.8 to -12.4	-14.8 to 28.9
7	Post-SIC, regional fluid (Ca-Na-rich)	Two end-members: exsolved SIC fluid and a regional groundwater/metamorphic fluid	NR, SR	L_{aq}+V												
8	Mobilization of Ca-rich "Shield brines"	neotectonic brine (5 to 13 Ma)	NR, SR	L_{aq}+V	~0.15		-60 to -90	-49 to -69		-12 to -44						

Table 3-2. Summary of microthermometric data measured fluid inclusions from the North (NR) and South (SR) ranges of the granophyre unit, Sudbury Igneous Complex. List of abbreviations: FIA – fluid inclusion assemblage; Tf – freezing temperature; Te – eutectic temperature; Tm(ice) ice melting temperature; Tm(halite) halite melting temperature; Th – homogenization temperature; homo. type – homogenization to dew point (DP; vapour) or bubble point (BP; liquid); Tt – trapping temperature; Pbulk – bulk density in g/cm^3; salinity is reported in wt. % equiv. NaCl.

Sample	Range	Depth % true (m)	Fluid Inclusion Type	# FIA	Tf mean ± σ range	Te mean ± σ range	Tm(ice) mean ± σ range	Tm(halite) mean ± σ range	Th mean ± σ range	Hom. Type V of H	Tt mean ± σ range	ρ_{bulk}	salinity (NaCl)
GNb-40	NR	72.8 1615	1	3	**-87.0 ± 7** -95 to -82	**-23.3 ± 2** -24.6 to -21	**-19 ± 1.8** -21 to -17.5	n.d.	**325 ± 5** 310 to 330	V	**414 ± 12** 405 to 421	**0.907**	**21.68** 20.6 to 23.5
GNb-11	NR	26.4 587	1	1	**-59.0** -59 to -58	**-20.8** -21 to -20.5	**-17** -17.4 to -17	n.d.	**322** 320 to 324	V	**412**	**0.896**	**20.22**
GNb-2	NR	0.2 6	1	1	**-82.0** -85 to -78	**-24.5** -25 to -24	**-18.8** -19 to -18.5	n.d.	**335** 325 to 345	V	**429**	**0.894**	**21.54**
GNa-80	SR	93.9 1653	2	4	**-69.5 ± 8.5** -81.3 to -58.7	**-23.7 ± 1.4** -25.3 to -21.5	**-19.5 ± 1.9** -22 to -17	n.d.	**142 ± 16** 119 to 165	V	**194 ± 19** 172 to 218	**1.088**	**22.0** 20.6 to 23.7
GNa-68	SR	69.3 1221	2	3	**-80.7 ± 1.1** -82 to -79.1	**-23.7 ± 0.2** -23.8 to -23.5	**-20 ± 0.9** -20.8 to -19.1	n.d.	**127 ± 12** 118 to 142	V	**177 ± 14** 168 to 193	**1.102**	**22.4** 21.8 to 22.9
GNa-44	SR	41.1 724	2	3	**-80.5 ± 0.7** -81 to -80	**-24.75 ± 0.4** -25 to -24.5	**-18.15 ± 5** -18.8 to -16.8	n.d.	**128 ± 11** 118 to 141	V	**177 ± 13** 168 to 187	**1.091**	**21.1** 20.8 to 21.3
GNa-33	SR	35.0 617	2	5	**-71.9 ± 5.9** -82 to -61.2	**-23.9 ± 1.9** -26.9 to -20.3	**-19 ± 1.7** -21 to -16.8	n.d.	**120 ± 7** 109 to 132	V	**168 ± 8** 157 to 177	**1.102**	**21.7** 20.5 to 22.9
GNa-13	SR	6.4 113	2	4	**-76.2 ± 9.3** -86 to -64	**-23.7 ± 2.3** -27.1 to -20.5	**-20 ± 1.3** -21 to -18	n.d.	**148 ± 9** 136 to 168	V	**200 ± 11** 186 to 211	**1.086**	**22.5** 21.3 to 23
GNa-5	SR	4.2 74	2	7	**-84.4 ± 7.5** -90 to -62	**-22.7 ± 2.2** -25.1 to -20.5	**-21.4 3.1** -25 to -17.2	n.d.	**130 ± 9** 117 to 142	V	**180 ± 11** 165 to 193	**1.107**	**23.3** 20.4 to 22.4
GNb-50	NR	89.8 1994	2	2	**-61.0 ± 1.4** -62 to -58	**-23.1 ± 0.6** -23.5 to -22.7	**-17.5 ± 1** -18.2 to -16.8	n.d.	**137 ± 4** 134 to 140	V	**188 ± 5** 184 to 191	**1.081**	**20.6** 20.1 to 21.1
GNb-40	NR	72.8 1615	2	3	**-70.5 ± 2.6** -75 to -67	**-24.3 ± 0.6** -24.7 to -23	**-18.1 ± 1.1** -19 to -16.8	n.d.	**137 ± 2** 133 to 143	V	**188 ± 2** 185 to 190	**1.084**	**21.0** 20.1 to 21.7
GNb-19	NR	31.0 688	2	4	**-82 ± 2.6** -87 to -78	**-24.1 ± 0.5** -24.5 to -23.5	**-20.6 ± 2** -22.5 to -17.5	n.d.	**136 ± 7** 124 to 142	V	**186 ± 8** 175 to 191	**1.099**	**22.7** 20.8 to 24
GNb-11	NR	26.4 587	2	4	**-78.4 ± 5.6** -86 to -69.5	**-22.9 ± 1.2** -24.6 to -21	**-20.6 ± 1.2** -22 to -18.5	n.d.	**139 ± 7** 123 to 150	V	**190 ± 8** 178 to 196	**1.097**	**22.8** 21.8 to 23.7
GNb-7	NR	10.1 226	2	3	**-79 ± 12.1** -90 to -63	**-31.9 ± 15.7** -50 to -22	**-18.4 ± 0.4** -19 to -18	n.d.	**138 ± 5** 130 to 142	V	**188 ± 6** 182 to 193	**1.085**	**21.3** 21 to 21.5
GNb-2	NR	0.2 6	2	3	**-67.2 ± 1.6** -70 to -65	**-19.5 ± 1.6** -21.5 to -17.5	**-19.5 ± 1.6** -21.5 to -17.5	n.d.	**138 ± 6** 129 to 147	V	**188 ± 7** 183 to 196	**1.092**	**22.0** 21 to 23.2
GNa-5	SR	4.2 74	3	2	**-72.5 ± 6.4** -78 to -68	**-24.6 ± 0.7** -25.1 to -24.1	**-19.4 ± 2.9** -22 to -17.1	**160 ± 1** 153 to 158	**112 ± 5** 108 to 115	H	**168** 165 to 170	**1.180**	**30.7** 30.4 to 30.9
GNb-50	NR	89.8 1994	3	1	**66.5** -68 to -65	**-24.6** -24.8 to -24.3	**-18.2** -18.5 to -17.9	**223** 218 to 227	**149** 147 to 150	H	**209**	**1.183**	**33.9**
GNb-7	NR	10.1 226	3	1	**-66.0** -68 to -64	**-23.8** -24.4 to -23.1	**-17.9** -18 to -17.7	**167** 163 to 170	**155** 155 to 156	H	**208**	**1.155**	**30.3**

Table 3-3. Summary of evaporate mound chemistry from decrepitated fluid inclusions from the North Range (NR) and South Range (SR) of the granophyre unit. Data are normalized to 100%. Abbreviation: b.d.l = below detection limit.

			Cl	F	S	Na	Ca	K	Fe	Mn	Mg	Pb	TOTAL
			mean ± σ	mean ± σ	mean ± σ	mean ± σ	mean ± σ	mean ± σ	mean ± σ	mean ± σ	mean ± σ	mean ± σ	
Sample	**Range**	**n=**	range	range	range	range	range	range	range	range	range	range	
GNa-80	SR	11	**50.0 ± 2.2** 45.6 to 53.2	**0.8 ± 1.5** b.d.l. to 4.2	b.d.l.	**46.0 ±5.0** 35.4 to 52.3	**2.6 ± 3.5** b.d.l. to 11.9	**0.4 ± 0.9** b.d.l. to 2.9	**0.1 ± 0.5** b.d.l. to 1.5	b.d.l.	b.d.l.	b.d.l.	**100**
GNa-78	SR	22	**51.8 ± 2.6** 46.9 to 55.7	**1.6 ± 3.7** b.d.l. to 13.5	b.d.l.	**40.3 ± 4.9** 26.2 to 46.8	**3.6 ± 3.0** b.d.l. 13.8	**2.5 ± 2.8** b.d.l. to 10.3	**0.2 ± 0.4** b.d.l. to 1.4	b.d.l.	b.d.l.	**0.1 ± 0.5** b.d.l. to 2.4	**100**
GNa-68	SR	21	**53.8 ± 4.5** 42.4 to 58.3	**0.3 ± 1.1** b.d.l. to 4.1	**0.1 ± 0.3** b.d.l. to 1.5	**39.1 ± 3.9** 30.8 to 45.0	**4.5 ± 5.4** b.d.l. to 20.3	**1.3 ± 1.2** b.d.l. to 4.1	**0.9 ± 2.9** b.d.l. to 13.3	**0.1 ± 0.3** b.d.l. to 1.2	**0.1** b.d.l. to 0.7	b.d.l.	**100**
GNa-58	SR	26	**48.5 ± 4.8** 35.8 to 56.8	b.d.l.	**3.7 ± 2.5** b.d.l. to 11.1	**37.9 ± 5.1** 23.8 to 48.9	**5.7 ± 3.0** b.d.l. to 13.7	**0.9 ± 0.8** b.d.l. to 2.8	**0.2 ± 0.6** b.d.l. to 2.3	**0.2 ± 0.4** b.d.l. to 1.2	b.d.l.	**2.0 ± 1.6** b.d.l. to 5.7	**100**
GNa-44	SR	49	**49.4 ± 3.8** 39.6 to 55.2	**1.8 ± 3.1** b.d.l. to 10.6	b.d.l.	**42.1 ± 5.1** 30.9 to 51.7	**4.1 ± 3.8** b.d.l. to 13.9	**1.8 ± 2.1** b.d.l. to 6.9	**0.5 ± 0.9** b.d.l. to 3.0	**0.3 ± 0.6** 2.2	b.d.l.	b.d.l.	**100**
GNa-33	SR	68	**54.6 ± 4.0** 48.4 to 69.4	b.d.l.	b.d.l.	**37.8 ± 5.5** 21.9 to 48.6	**5.0 ± 3.2** b.d.l. to 13.5	**2.1 ± 1.7** b.d.l. to 8.3	**0.2 ± 0.6** b.d.l. to 2.5	**0.3 ± 0.6** b.d.l. to 2.1	b.d.l.	b.d.l.	**100**
GNa-28	SR	16	**54.5 ± 2.6** 51.5 to 59.6	b.d.l.	b.d.l.	**37.7 ± 3.1** 31.5 to 42.4	**5.1 ± 2.4** 1.1 to 10.8	**2.6 ± 3.4** b.d.l. to 12.0	**0.1 ± 0.3** b.d.l. to 1.3	b.d.l.	b.d.l.	b.d.l.	**100**
GNa-13	SR	57	**51.4 ± 3.2** 44.2 to 59.3	**0.6 ± 1.2** b.d.l. to 4.3	b.d.l.	**39.1 ± 5.6** 20.8 to 50.7	**5.1 ± 4.9** b.d.l. to 20.1	**3.0 ± 2.2** b.d.l. to 9.2	**0.6 ± 1.0** b.d.l. to 4.3	**0.2 ± 0.4** b.d.l. to 1.7	b.d.l.	b.d.l.	**100**
GNa-5	SR	33	**50.5 ± 3.2** 38.3 to 55.9	**1.2 ± 1.6** b.d.l. to 6.4	b.d.l.	**39.7 ± 4.5** 26.1 to 46.6	**5.8 ± 4.3** b.d.l. to 18.5	**2.2 ± 1.6** b.d.l. to 5.2	**0.4 ± 1.0** b.d.l. to 4.3	**0.3 ± 0.6** b.d.l. to 3.0	b.d.l.	b.d.l.	**100**
GNb-50	NR	18	**45.7 ± 7.9** 33.9 to 54.5	**7.5 ± 7.7** b.d.l. to 23.8	b.d.l.	**37.5 ± 5.4** 26.8 to 44.2	**7.3 ± 4.1** 2.3 to 17.4	**1.1 ± 3.0** b.d.l. to 11.7	**0.9 ± 1.2** b.d.l. to 4.3	b.d.l.	b.d.l.	b.d.l.	**100**
GNb-48	NR	25	**51.9 ± 6.7** 40.7 to 69.6	**4.3 ± 4.8** b.d.l. to 14.0	b.d.l.	**38.9 ± 5.2** 27.3 to 47.0	**3.8 ± 2.7** b.d.l. to 10.6	**0.4 ± 0.8** b.d.l. to 3.4	**0.3 ± 0.6** b.d.l. to 2.2	b.d.l.	b.d.l.	**0.3 ± 0.8** b.d.l. to 2.1	**100**
GNb-40	NR	44	**52.6 ± 3.6** 44.9 to 58.2	b.d.l.	b.d.l.	**41.5 ± 3.3** 33.7 to 47.4	**5.2 ± 4.9** b.d.l. to 18.2	**0.6 ± 1.2** b.d.l. to 6.3	**b.d.l.**	b.d.l.	b.d.l.	**0.1 ± 0.4** b.d.l. to 2.4	**100**
GNb-34	NR	35	**50.0 ± 1.8** 44.8 to 53.0	**0.1 ± 0.4** b.d.l. to 1.7	b.d.l.	**42.4 ± 3.9** 32.4 to 49.6	**6.7 ± 3.6** b.d.l. to 15.1	**0.8 ± 1.0** b.d.l. to 2.6	**0.1 ± 0.3** b.d.l. to 1.8	b.d.l.	b.d.l.	b.d.l.	**100**
GNb-28	NR	47	**50.4 ± 2.2** 44.2 to 55.3	**1.0 ± 2.1** b.d.l. to 10.6	b.d.l.	**41.6 ± 5.0** 27.4 to 52.2	**6.0 ± 3.8** b.d.l. to 15.6	**1.0 ± 1.6** b.d.l. to 6.8	**0.1 ± 0.4** b.d.l. to 2.3	b.d.l.	b.d.l.	b.d.l.	**100**
GNb-19	NR	18	**49.5 ± 2.1** 46.2 to 54.2	**0.6 ± 1.2** b.d.l. to 3.8	b.d.l.	**41.7 ± 4.9** 31.6 to 49.2	**6.9 ± 2.5** b.d.l. to 10.2	**1.1 ± 1.7** b.d.l. to 5.6	**0.1 ± 0.4** b.d.l. to 1.2	b.d.l.	b.d.l.	b.d.l.	**100**
GNb-18	NR	29	**54.1 ± 6.4** 42.0 to 72.5	**0.7 ± 2.2** b.d.l. to 10.2	b.d.l.	**37.9 ± 5.3** 23.6 to 47.3	**6.7 ± 4.7** b.d.l. to 16.9	**0.6 ± 0.7** b.d.l. to 2.1	**0.1 ± 0.3** b.d.l. to 1.7	b.d.l.	b.d.l.	b.d.l.	**100**
GNb-11	NR	47	**50.2 ± 2.7** 39.3 to 54.5	**0.2 ± 0.9** b.d.l. to 4.6	**0.1 ± 0.5** b.d.l. to 2.3	**44.4 ± 5.4** 27.7 to 53.3	**3.7 ± 4.0** b.d.l. to 16.6	**0.7 ± 1.3** b.d.l. to 5.6	**0.5 ± 1.2** b.d.l. to 4.6	b.d.l.	**0.1 ± 0.4** b.d.l. to 2.2	b.d.l.	**100**
GNb-8	NR	44	**54.4 ± 3.0** 48.8 to 63.7	**0.5 ± 1.4** b.d.l. to 6.0	**0.1 ± 0.2** b.d.l. to 0.8	**39.9 ± 3.9** 30.8 to 46.7	**1.5 ± 1.7** b.d.l. to 4.9	**2.4 ± 2.0** b.d.l. to 10.8	**0.5 ± 1.0** b.d.l. to 4.4	b.d.l.	b.d.l.	**0.7 ± 1.1** b.d.l. to 3.0	**100**
GNb-2	NR	27	**48.8 ± 3.3** 39.7 to 54.1	**2.8 ± 3.4** b.d.l. to 13.9	b.d.l.	**40.9 ± 4.4** 30.6 to 49.4	**6.6 ± 3.0** 2.9 to 5.1	**0.8 ± 1.2** b.d.l. to 3.4	**0.1 ± 0.2** b.d.l. to 1.3	b.d.l.	b.d.l.	b.d.l.	**100**

Table 3-4. Summary of whole rock oxygen isotope data for the granophyre unit (GR) from six samples: three from the South Range (SR; GNa-13, GNa-44, GNa-80) and three from the North Range (NR; GNb-11; GNb-19; GNb-50). Oxygen isotope data for quartz ($\delta^{18}O_{quartz}$) is also summarized. Depth (%) is calculated using sample distance relative to the upper and lower contacts of the GR.

Sample	Depth (%)	Yield	$\delta^{18}O$ (‰)	1σ
GNa-80	93.9	15.3	7.0	0.030
GNa-44	41.1	14.0	7.4	0.021
GNa-38	39.0	15.4	7.5	0.021
GNa-13	6.4	13.6	6.2	0.019
GNb-50	89.5	15.0	7.1	0.021
GNb-43	73.3	15.1	8.9	0.019
GNb-19	30.6	14.6	9.0	0.029
GNb-11	26.1	15.1	8.2	0.030

Table 3-5. Summary of quartz oxygen isotope ($\delta^{18}O_{quartz}$) values and cathodoluminescence (CL) data for six samples from the granophyre unit (GR); three from the South Range (GNa-13, GNa-44, GNa-80) and three from the North Range (GNb-11, GNb-19, GNb-50). Signal strength is summarized in figure 5 and in text. Depth (%) is calculated using sample distance relative to the upper and lower contacts of the GR.

Sample	Depth (%)	Grain	Analysis	$\delta^{18}O_{quartz}$ (‰)	whole rock $\delta^{18}O$ (‰)
GNa-80	93.9	1	1	14.7	7.0
GNa-80	93.9	1	2	13.1	7.0
GNa-80	93.9	2	1	13.6	7.0
GNa-80	93.9	3	1	14.3	7.0
GNa-44	41.1	1	1	13.2	7.4
GNa-44	41.1	1	2	12.4	7.4
GNa-44	41.1	2	1	14.8	7.4
GNa-44	41.1	2	2	13.5	7.4
GNa-44	41.1	3	1	10.3	7.4
GNa-13	6.4	1	1	9.9	6.2
GNa-13	6.4	2	1	9.9	6.2
GNa-13	6.4	3	1	10.3	6.2
GNa-13	6.4	4	1	10.1	6.2
GNa-13	6.4	5	1	9.3	6.2
GNb-50	89.5	1	1	9.0	7.1
GNb-50	89.5	2	1	6.9	7.1
GNb-50	89.5	3	1	7.1	7.1
GNb-50	89.5	4	1	6.9	7.1
GNb-19	30.6	1	1	12.5	9.0
GNb-19	30.6	1	2	9.0	9.0
GNb-19	30.6	2	1	11.5	9.0
GNb-19	30.6	3	1	12.0	9.0
GNb-19	30.6	3	2	9.7	9.0
GNb-19	30.6	4	1	10.8	9.0
GNb-11	26.1	1	1	7.8	8.2
GNb-11	26.1	2	1	8.9	8.2
GNb-11	26.1	3	1	11.0	8.2
GNb-11	26.1	4	1	12.4	8.2
GNb-11	26.1	4	2	12.8	8.2

Chapter 4

Documenting the nature and implications of hydrothermal processes on a magmatic Ni-Cu-PGE deposit at Nickel Rim South, Sudbury, Ontario, Canada

4.1 Abstract

The Nickel Rim South (NRS) Cu-Ni-PGE deposit, located in the east range of the Sudbury Structure, Ontario, records textural and geochemical evidence of a complex, multi-stage hydrothermal history. The distal hydrothermal alteration footprint of NRS mineralized zones is dominated by epidote, chlorite, and amphibole with variable amounts of sericite, stilpnomelane, quartz, carbonate, albite, and K-feldspar. Alteration minerals do not vary systematically in abundance or composition with distance from the basal SIC contact.

Fluid inclusion petrography and microthermometry of select NRS samples reveal three fluid inclusion types: (1) aqueous inclusions showing L (liquid H_2O) + V (H_2O vapour) phase composition with 10 to 15 vol. % vapour at 20°C; (2) aqueous inclusions showing L + V + H (halite) phase composition with 10 to 15 vol. % V at 20°C; and (3) aqueous inclusions showing L + V phase composition with 30 vol. % vapour at 20°C. Type 1 inclusions are the most abundant and record total homogenization (Th) values ranging from 142° to 245°C with salinities of 20.5 to 21.4 wt. % equiv. NaCl. Type 2 inclusions are less abundant than type 1 and record vapour homogenization values (L+V+H → L+H) from 127° to 216°C, Th (L+H → L) values from 210° to 260°C, and salinities from 33.5 to 35.4 wt. % equiv. NaCl. Type 3 inclusions are rare and record Th values ranging from 315° to 329°C with salinities of 22.2 to 23.4 wt. %

equiv. NaCl. Analysis of evaporate mounds is most representative of type 1 fluid inclusions and the majority contain the following elements (normalized to 100 wt. %): 34% Na, 12% Ca, 1.8% K, 0.7 % Mn, and 0.3 % Fe. In situ SIMS $\delta^{18}O$ quartz values show large variability, ranging from +5.6 to +12.4‰, and a variation of up to 3.4‰ is recorded in a single grain.

Cathodoluminescence images do not show a relationship between the oxygen isotope values and features that may be related to this variability (e.g., microfractures, sector and concentric zoning). Trace element compositions of hydrothermal epidote exhibit three REE patterns, of which one type is associated with mineralized samples.

The combined results of this study indicate a complex hydrothermal history at NRS related to the cooling SIC and that there is a relationship between mineralization and hydrothermal alteration, suggesting that mineralization has a hydrothermal component. The hydrothermal fluid was likely a hybrid fluid containing variable contributions of magmatic, metamorphic, and possibly shield brine fluids. The NRS fluid inclusion record lacks high temperature, multi-solid inclusions identified in other mineralized footwall zones that have been interpreted to be necessary for redistribution of metals (Cu, Ni, PGEs). The absence of these inclusions therefore brings into question their necessity or role in ore remobilization.

4.2 Introduction

Recent advances in mineral exploration in the Sudbury mining camp have used various petrographic and analytical techniques to better understand footwall-type Cu-Ni-PGE deposits and develop potential vectors to mineralization. Hence, over the last 25 years, more

unconventional exploration techniques have been applied, such as the documentation and characterization of ore-related fluids using fluid inclusion methods (Farrow and Watkinson 1992, Li 1992, Li and Naldrett 1993, Farrow 1994, Molnár et al. 1997, Marshall et al. 1999, Molnár et al. 1999, Molnár et al. 2001, McCormick et al. 2002, Hanley and Mungall 2003, Hanley et al. 2005, Péntek et al. 2008, Hanley and Bray 2009, Tuba et al. 2010, Péntek et al. 2011, Stewart 2011), measuring the metal content and bulk composition of hydrocarbons and brines in fluid inclusions (Hanley et al. 2005, Kerr et al. 2015), stable isotopes (Marshall et al. 1999, Tuba et al. 2014), and characterizing the trace element (including ore metal) contents of alteration and ore-stage minerals such as epidote (Tuba 2012), biotite, amphibole, and chlorite (Li and Naldrett 1993, Farrow 1994, Magyarosi et al. 2002, Hanley and Mungall 2003, Hanley and Bray 2009, Stewart 2011, Tuba 2012, Ames and Kjarsgaard 2013, Warren et al. 2015).

Relative to magmatic processes, the importance of hydrothermal fluids for the genesis of footwall-type Cu-Ni-PGE deposits in the Sudbury district, and the sources of such fluids, is controversial. An integrated model involving both magmatic and hydrothermal stages has been proposed for some (Farrow and Watkinson 1992, Li and Naldrett 1993, Jago et al. 1994, Morrison et al 1994, Watkinson 1999, Molnár and Watkinson 2001, Hanley et al 2005). In particular, the relatively recent identification of a new style of mineralization defined as low-sulfide, PGE-rich mineralization (Farrow et al. 2005) stresses the importance of hydrothermal upgrading. The profusion of this ore style is not known because it is challenging to identify due to a combination of lack of established geochemical and mineralogical exploration indicators for detecting mineralization (e.g., diagnostic alteration assemblages), their relatively small size (individual ore zones no more than 10s of meters in spatial extent), and a lack of visible sulfides

despite their very high PGE-grades. These aspects make this ore style difficult to locate within regions of unmineralized footwall rocks.

The Nickel Rim South deposit(NRS), located in the East Range (ER) of the Sudbury Structure (SS), is an ideal location to study mineralization in the Sudbury camp and resolve some of the outstanding issues around the footwall ore deposits for several reasons: (i) it contains two of the three mineralization styles in the SS, those being Ni(-Cu)-rich contact-type and Cu-(Ni-) PGE-rich, footwall-type; (ii) it is currently producing which facilitates sampling; and (iii) it is located in the ER, where there have been relatively few studies completed, but where both "low-" and "high-sulfide" variants of the footwall-ore style have been reported, providing an excellent opportunity to compare its mineralized systems to those in the North Range (NR) and South Range (SR).

In this paper, we describe new aspects of the hydrothermal record preserved at NRS in the ER in order to build upon existing models that characterize footwall deposits. This is done through application of alteration petrography and mineral chemistry (major and trace elements), fluid inclusion petrography and microthermometry, fluid inclusion evaporate mound analysis, and in situ oxygen isotope analysis of mineralized and barren host rocks to the ores and their contained alteration assemblages. The combined results of these analytical techniques are used to: (i) describe the fluid(s) present in the hydrothermal system in this deposit, and compare them to fluids in the main mass of the SS; (ii) speculate on possible sources for these hydrothermal fluids, and (iii) evaluate the role of hydrothermal fluids in the development of mineralization and alteration within NRS.

4.3 Geological Setting

4.3.1 Regional geology

The SS is located in the southern region of the Canadian Shield (Fig. 1A) at the junction of three structural provinces: the Superior, Southern, and Grenville. It is defined as containing: (i) Archean and Proterozoic brecciated footwall rocks; (ii) the Whitewater Group; and (iii) the SIC main mass, which is broadly divided into the NR and SR. The NR is underlain by Archean-age para- and orthogneissic rocks (the Levack Gneiss Complex) and 2.6 Ga granitoids (Card et al. 1984; Dressler 1984; Lafrance et al. 2008), whereas the SR is underlain by early Proterozoic metavolcanics and metasedimentary rocks of the Huronian Supergroup (Dressler 1984) and the Creighton and Murray granites of the Paleoproterozoic Southern Province. A third range in the eastern margin of the SS, called the ER, is defined as spanning from the northeast corner of the Sudbury Basin (near Selwyn Lake) to its southeast corner (near Falconbridge). The footwall rocks of the ER include the Levack Gneiss Complex and Proterozoic granites that intrude the local country rock (e.g., mafic meta-volcanics and meta-sedimentary rocks as part of the Huronian Supergroup; Dressler 1984; James et al. 1992). Pseudotachylite breccia, known locally as “Sudbury breccia” and referred to as such herein, is a very common rock type in the ER footwall. Zones of Sudbury breccia occur as irregular veins varying in size from 10 to 100s of m and smaller, mm-size veinlets.

The complex geology of the SS is the result of various large-scale synchronous and later events (structural, thermal, metasomatic) relating to a 1.85 Ga impact event. The SIC itself consists of units that represent the in situ differentiation and crystallization of an impact melt sheet. These units are (from top to bottom): granophyre, quartz gabbro, and norite (Coats and Snajdr 1984;

Lightfoot et al. 1997). The granophyre contains variably developed granophyric texture (up to 65 volume %) with minor primary amphibole and ilmenite; the unit is characterized by a pervasive alteration relating to subsolidus metasomatism (Stewart and Kontak 2012, Stewart et al. 2013). The quartz gabbro is composed of cumulus plagioclase, clinopyroxene, amphibole, biotite, titanite, and variable amounts of magnetite. The norite unit is a medium- to coarse-grained, hypidiomorphic rock composed of cumulus plagioclase, orthopyroxene and clinopyroxene, quartz, K-feldspar, biotite, magnetite, and ilmenite (Naldrett and Hewins 1984). In the SR, the norite is underlain by a quartz-rich norite containing 5 to 20 vol. % quartz compared to <5 vol. % in the overlying norite. A mafic variety of the norite unit, located exclusively in the NR (mafic norite), occurs only at the base of the SIC and is composed of cumulate textured spinel, olivine and orthopyroxene with intercumulus plagioclase, sulfides, biotite, and accessory apatite and ilmenite (Naldrett and Hewins 1984; Lightfoot et al. 2001). Beneath the SIC but related to its formation are the following units: (i) the sublayer unit that is fine- to medium-grained and of noritic composition but contains clasts of country rock and xenoliths up to 10 m in diameter (Naldrett et al. 1984); (ii) the footwall breccia, a discontinuous heterolithic breccia comprised of fragments of country rocks, restite, and exotic fragments hosted in a variably textured igneous matrix (Stewart 2011), and (iii) the Sudbury breccia unit, a pseudotachylitic unit comprised of a dark grey, fine-grained to aphanitic matrix that hosts rounded lithic clasts and mineral fragments from country rocks (Thompson and Spray 1996; Rousell et al. 2003; Spray 2010; O'Callaghan et al. 2016).

Several studies (e.g., Dressler 1984; Coats and Snajdr 1984; Hanley and Mungall 2003; Boast and Spray 2006) have described a metamorphic aureole up to 2 km into the SS footwall produced

by contact metamorphism. The metamorphic sequence is defined by the following facies and distance from basal SIC contact: (i) a zone of assimilation and anatexis called the "footwall breccia" up to 25 m; (ii) a pyroxene hornfels facies zone up to 350 m; (iii) a hornblende hornfels facies zone up to 1100 m, and (iv) an albite-epidote hornfels zone up to 2 km.

The NRS occurs in the ER within the lower portion of the SIC main mass and into the footwall (Fig. 1B). The host rocks consist of mafic norite, sublayer, footwall breccia, and Sudbury breccia, as well as various gneisses of granitic and granodioritic composition that become increasingly foliated away from the basal SIC contact. The abundance of Sudbury breccia varies in the footwall but increases near the transition from granodiorite to gneissic-dominated footwall rocks. The host rocks to NRS also contain small bodies (i.e., ~1 m^2) footwall granophyre (FWGR) which are interpreted as injected melts from either the partially melted country rocks or from the crystallizing SIC (Hanley et al. 2011). Late diabase and gabbroic dike rocks cross-cut footwall lithologies.

The SS and its ore deposits environment has been affected by several pre-, syn-, and post-impact deformation events, including the 2.4 to 2.3 Ga Blezardian orogeny (Riller et al. 1999), the 1.89 to 1.83 Penokean orogeny (Hoffman 1989; Mukwakwami et al. 2012), a 1.45 Ga NW-thrusting event (Krough 1994), and the 1.0 Ga Grenvillian orogeny (Brocoum and Dalziel 1974).

4.3.2 Mineralization in the Sudbury Structure

Crystallization of the SIC and post-impact hydrothermal activity produced one of the world's most endowed Ni-Cu-PGE mining camps. Mineralization is subdivided into three types

(Morrison et al. 1994; Lightfoot and Farrow 2002; Ames and Farrow 2007): (i) contact-type deposits at or near the basal contact of the SIC with its basement rocks with Ni/Cu ~ 1; (ii) offset deposits hosted by SIC intrusive rocks (e.g., inclusion-rich quartz diorite offset dikes) cutting Archean basement rocks; these have variable Ni/Cu ratios and PGE contents; and (iii) footwall-type deposits with disseminations, stringers, and sheet-like veins in the basement up to 2 km from the SIC; these have Ni/Cu << 1. A genetic link between contact- and footwall-type deposits has been suggested (e.g., Farrow and Watkinson 1992, Watkinson 1999, Molnár et al. 1999, 2001, Hanley et al. 2005, Tuba et al. 2010, 2014).

Contact-type deposits are dominated by Ni-rich sulfide phases (pyrrhotite>pentlandite>chalcopyrite) and are most abundant along the SIC-basement contact. These deposits are often hosted within embayments or structurally complex depressions and slump features along the impact crater walls (Morrison et al. 1994). Offset-type deposits are hosted within quartz-diorite offset dikes that cross-cut stratigraphic layers of the footwall (Lightfoot et al. 2001; Tuchscherer and Spray 2002; O'Callaghan et al. 2016). The ore mineralization in this deposit type typically contains higher Cu and PGE contents than contact-type mineralization. Footwall-type deposits are dominantly hosted in Sudbury breccia (Coats & Snajdr 1984) and can occur up to 2 km outside of the SIC. Footwall-type deposits can be further divided into two subtypes: a) sharp-walled, high-sulfide footwall deposits which are dominantly magmatic in origin; and, b) low-sulfide, PGE-rich footwall deposits which are produced by hydrothermal activity (Péntek et al. 2008; Tuba et al. 2010; Nelles et al. 2010; Hanley et al. 2011; Tuba et al. 2014).

The sharp-walled, high-sulfide footwall deposits consist of massive veins (up to 7 m thick) composed mainly of chalcopyrite with variable amounts of pentlandite, pyrrhotite, cubanite, bornite and millerite. Though their origin is generally interpreted to be the product of fractional crystallization and differentiation of sulfide liquids at the basal SIC contact, there is still debate as to the contribution of hydrothermal fluids to this style of mineralization (e.g., Farrow and Watkinson 1992; Molnár et al. 2001; Hanley et al. 2005; Péntek et al. 2008; Hanley et al. 2011).

The low-sulfide, PGE-rich mineralization has received more attention over the last decade (Farrow et al. 2005; Ames and Farrow 2007, Péntek et al. 2008; Tuba et al. 2010, White et al. 2010, Péntek et al. 2013, Tuba et al. 2014). These deposits are dominated by veinlets (up to 30 cm thick) and disseminated sulfides with total sulfide contents less than 5 modal %. Total precious metal (Pt, Pd, Au) tenors can be as high in low-sulfide zones as in sharp-walled, high-sulfide deposits (up to 7.7 g/t; Farrow and Lightfoot 2002; Farrow et al. 2005). Low-sulfide deposits texturally pre-date the emplacement of sharp-walled vein deposits (Farrow et al. 2005).

A genetic link has been proposed between the two subtypes of footwall deposits (Farrow et al. 2005, Tuba et al. 2010, Péntek et al. 2013). Farrow et al. (2005) suggests that hydrothermal fluids enriched in metals migrated into the footwall after losing some of their initial metal content through cooling and, fluid-rock interaction. The resulting hydrothermal fluid is thus enriched in Pt and Pd relative to other base metals and forms the low-sulfide, PGE-rich mineralization.

4.3.3 Hydrothermal alteration in the Sudbury Igneous Complex footwall

Heterogeneously developed but locally pervasive alteration assemblages are present in the SIC footwall environment and reflect fluid circulation (Farrow and Watkinson 1992, Marshall et al. 1999, Molnár et al. 2001, Hanley et al. 2011). These assemblages, both related and unrelated to mineralization, contain variable amounts of actinolite + chlorite + epidote + albite + quartz ± carbonate ± scapolite ± magnetite ± K-feldspar ± biotite ± titanite (e.g., Farrow and Watkinson 1992, Hanley and Mungall 2003, Hanley et al. 2005, Tuba et al. 2014). Cavities occur in the footwall and are usually associated with FWGR bodies, in which case they may be considered miaroles. These features are often lined with K-feldspar ± quartz ± epidote ± chlorite ± amphibole (Molnár et al. 2001, Péntek et al. 2008, Péntek et al. 2009). Where mineralized veins occur, the assemblages include epidote + amphibole + chlorite (Farrow and Watkinson 1992; Li et al. 1992; Li and Naldrett 1993; Farrow 1994; Molnár et al. 2001; Hanley and Mungall 2003, Tuba et al. 2014) and they may occur in the wall rock a few hundred meters from mineralization. Petrographic, fluid inclusion, and stable isotope studies provide evidence for multiple generations of hydrothermal activity in the SIC footwall, including a hydrothermal cell generated by the cooling SIC and multiple post-SIC events (Marshall et al. 1999, Molnár et al. 2001, Molnár and Watkinson 2001).

4.3.4 Hydrothermal fluids and mineralization in the Sudbury Igneous Complex footwall

Characteristics of mineralization have been summarized in the following studies: Naldrett and Kullerud 1967, Farrow and Watkinson 1992, Li 1992, Li and Naldrett 1993, Farrow 1994, Farrow et al. 1994, Jago et al. 1994, Farrow and Watkinson 1996, Molnár et al. 1997, Marshall et al. 1999, McCormick and McDonald 1999, Molnár et al. 1999, Molnár and Watkinson 2001,

Molnár et al. 2001, McCormick et al. 2002, Hanley and Mungall 2003, Hanley et al. 2004, Hanley et al. 2005, , Ames and Farrow 2007, Péntek et al. 2008, Carter et al. 2009, Campos-Alvarez et al. 2010, Nelles et al. 2010, Tuba et al. 2010, Hanley et al. 2011, Péntek et al. 2011, Péntek et al. 2013, Tuba et al. 2014. Most studies on SS footwall mineralization conclude that base and precious metals (Cu, Ni, Au, PGE) were generated as fractionated sulfide liquids that migrated into the footwall rocks; however, the involvement of hydrothermal fluids and other volatiles in the mobilization and redistribution of contact-type deposits into the footwall has been explored using various techniques (e.g., petrography, fluid inclusions analysis, whole rock and mineral stable isotope). Metal remobilization by hydrothermal fluids is interpreted to be important for the generation of low-sulfide, PGE-rich mineralization, suggesting that metals were remobilized at or near the contact and migrated into the footwall environment. Several fluid sources are proposed by the above authors to have contributed to the SS footwall hydrothermal system in both barren and mineralized zones, including: (i) basement/saline "shield brines" of the Canadian Shield; (ii) orthomagmatic fluids exsolved from the crystallizing SIC; (iii) fluids exsolved from crystallizing sulfide liquids; (iv) fluids exsolved from FWGR bodies; and (v) molten salts exsolved from sulfide liquids. Fluid inclusion types identified in the SS footwall are interpreted to represent differing stages of hydrothermal activity resulting from various degrees of fluid mixing. This suggests that ore fluids involved in footwall-type deposits were hybrid fluids of saline groundwater and higher temperature, highly saline orthomagmatic fluids exsolved either from partial melts in the local footwall environment or from the crystallizing SIC.

Of particular importance is the ability and capacity of fluids to transport base (Cu, Ni) and precious (PGEs) metals within the SS footwall environment. The ability of an aqueous fluid to dissolve and transport PGEs is dependent on several factors, including the solubility of the PGE in the fluid phase, amount of PGE available to the fluid, presence and amount of saturated phases (e.g., PGMs), and flux and efficiency of the precipitation mechanism (Hanley et al. 2005). Thermochemical conditions (e.g., pH, $f(O_2)$, temperature, salinity, S content) will also control on the amount of PGEs dissolved in the fluid phase and the nature of metal complexation in solution (Hanley et al. 2005). In low-temperature hydrothermal environments (<500°C), it is most likely that bisulfide ion (HS^-) is responsible for PGE transport and chlorite complexation is primarily responsible for base metal (Cu, Fe), S, and precious metal (e.g., Ag) transport (Hanley et al. 2005). Conversely, in high-temperature magmatic-hydrothermal environments (>500°C), Cl-rich magmatic volatiles may contribute to the primary concentration and redistribution of PGE because the solubility of Pt in high-temperature (800° to 900°C), high-salinity brines has been proven to increase (up to ppm-level; Hanley et al. 2005). In the SS footwall, secondary mineral assemblages indicate the oxygen fugacity and pH values of the ore-forming fluid were not consistent with that of a low pH, oxidized system. Alternatively, bisulfide complexation has been proposed as a likely mechanism for PGE transportation within the SS footwall (Wood 2002; Hanley et al. 2005).

4.3.5 Mineralization and alteration at Nickel Rim South

The NRS was discovered in 2001 and contains two of the three mineralization styles in the SS, these being contact- and footwall types. Comprehensive summaries of the mineralization at NRS are provided by McLean et al. (2005) and information provided by Sudbury Integrated Nickel

Operations – A Glencore Company and what is presented below is extracted from these reports with some input based on our own observations and following the convention described by Farrow et al. (2005). As noted before, the Sudbury breccia is the primary host to ore in the NRS footwall. A summary of the geology of NRS is shown in Figure 2.

The contact mineralization is hosted in mafic norite, sublayer norite and footwall breccia units. In NRS it consists of finely disseminated blebby sulfides in the mafic norite that increase in abundance towards the sublayer norite and footwall breccia and can extend into the shallow footwall. Sulfide mineral assemblages consist of pyrrhotite-chalcopyrite-pentlandite and grades can vary from < 1% sulfides in disseminated zones to >65% sulfides in semi-massive and massive sulfide zones. The extent of contact-type mineralization into the footwall generally follows the SIC-footwall contact. The thickest sections of mineralization typically correspond with depressions, or embayment structures, in the SIC-footwall contact.

The footwall-style ore is similar to that in other systems (e.g., Fraser Deep Copper Zone, McCreedy East, McCreedy West in the NR and Lindsley 4B in the SR; Ames et al. 2008) and is hosted by zones of strongly brecciated footwall rocks grading from granodioritic gneiss to more coarse-grained felsic to intermediate foliated gneiss. At NRS this ore is subdivided into two types: (i) high-sulfide mineralization; and (ii) low-sulfide mineralization.

High-sulfide mineralization occurs 40 to 90 m below the SIC contact and is associated with strongly brecciated footwall rocks (e.g., Sudbury breccia). The breccia matrix varies from black- to light grey and the grain size coarsens with increasing proximity to mineralization.

Mineralization occurs as massive sulfide veins with associated stringers and disseminated sulfides. The sulfides consist of chalcopyrite with lesser pentlandite, cubanite, pyrrhotite, millerite, and bornite in addition to magnetite and PGMs. These veins have selvages and alteration haloes (up to 5 cm-wide) consisting of chlorite and actinolite with lesser epidote.

Low-sulfide mineralization is peripheral to high-sulfide mineralization and forms a broad zone consisting of disseminated and stringer sulfides and veins that are smaller (0.25 to 1.75 m in core) and less abundant than in the high-sulfide zone. Low-sulfide mineralization is characterized by a low total sulfide content (<2%) dominated by chalcopyrite, millerite, and pentlandite, with lesser bornite. Alteration is more intense than in the other mineralized zones and occurs mainly as sulfide vein selvages consisting of chlorite, epidote, and actinolite; quartz and carbonate occur within sulfide veins. Rocks hosting this mineralization often exhibit recrystallized textures (e.g., aggregates of recrystallized quartz). Low-sulfide, PGE-rich mineralization is present mainly in the distal extent of the fringe zone between 20 to 60 m below the high-sulfide zone. Mineral phases hosting precious metals and platinum group elements include maslovite (PtBiTe), sperrylite ($PtAs_2$), and hessite (Ag_2Te).

4.4 Methods

4.4.1 Sampling

Diamond drill core was provided by Sudbury Integrated Nickel Operations (A Glencore Company). Core from four drill holes was selected for detailed re-logging and sampling (n=220): NRS-104a (n=43), NRS-117 (n=58), NRS-124c (n=81), and NRS-170110 (n=38). Three of these drill holes are surface holes and intersect the contact zone, proximal footwall zone, and distal

footwall zone (NRS-104a, -117, -124c), and the fourth drill hole is an underground hole that intersects the contact zone and proximal footwall zone (Fig. 3). Each core was re-logged and sampled to characterize the mineralization, alteration, and host rocks in the footwall environment at NRS (Figs. 2 and 3). Samples were systematically selected in order to acquire good coverage, both stratigraphically and compositionally, and to sample within, near, and away from mineralization. Fifty-eight representative samples from this collection (DDH NRS-104a=16, NRS-117=14, NRS-124c=18, NRS-170110=10) were prepared as polished thin sections. Unfortunately, no drill core containing low sulfide, PGE-rich mineralization was available for sampling and is therefore omitted from further discussion.

Identification and characterization of petrographic features was carried out in plane-polarized, cross-polarized, and reflected light using a research-grade petrographic microscope. These observations were also used to determine a paragenetic sequence for the NRS environment.

4.4.2 Mineralogy and mineral chemistry

Silicate and sulfide minerals in representative samples (n=6) were identified and analyzed semiquantitatively by scanning electron microscope – energy dispersive X-ray spectroscopy (SEM-EDS) in the Department of Earth Sciences, Laurentian University. A solid-state (Oxford S-Sight) energy dispersive detector mounted on a JEOL 6400 SEM was utilized with a 15 kV accelerating voltage, a 1 nA beam current, acquisition times between 10 and 30 seconds, and at a working distance of 15 mm. Quantitative mineral chemical data were obtained using an electron microprobe at the Ontario Geoscience Laboratories (Sudbury).

Eight samples were selected for additional mineral chemical analysis using a Cameca SX-100 Electron Probe Micro Analyzer (EPMA) at the Ontario Geological Survey Geo Labs. The EPMA is equipped with 5 wavelength dispersive (WD) spectrometers. The instrument operating parameters were: a beam current of 20 nA, an accelerating voltage of 20 kV, a total count time of 40 seconds (20 seconds on peak, 10 seconds on each background), and a focused beam (1 μm) except where sample damage or grain size prohibited this and a defocused, 8 to 10 μm beam diameter was used. Detection limits for the major elements (e.g., SiO_2, TiO_2, Al_2O_3, FeO, Cr_2O_3, MnO, MgO, CaO, Na_2O, K_2O) and halogens (F, Cl) reported are on the order of 0.1 wt. %. Standards used for peak position calibration were pyxBRN and diopAST. X-ray lines measured for each element are as follows: Si *kα* (TAP1), Ti *kα* (LLiF3), Al *kα* (TAP1), Cr *kα* (LLiF3), Mg *kα* (TAP1), Ca *kα* (LiF4), Fe *kα* (LiF4), Na *kα* (LTAP2), K *kα* (LPET5), F *kα* (LTAP2), and Cl *kα* (LPET5). Mineral formula recalculations were calculated using software package MinPet.

4.4.3 Cathodoluminescence (CL) imaging

The SEM used for mineral identification is equipped with a cathodoluminescence (CL) detector allowing black and white CL images of quartz to be collected from carbon-coated polished thin sections. The CL system has an HKL Backscatter Diffraction unit and a GatanChromaCL mirror-type cathodoluminescence (CL) detector and a linear array photomultiplier tube with 16 separate photocathodes. The SEM-CL images were collected using an accelerating voltage of 20 kV and a beam current of 1nA.

4.4.4 Fluid inclusion petrography and thermometry

Fluid inclusions in quartz-bearing chips were first examined petrographically to assess the presence of suitable fluid inclusion assemblages (FIA), fluid inclusion types and determine if inclusions were suitable for further studies; this work followed methods and terminology of Goldstein (2003). Microthermometric analyses were conducted at Laurentian University on 100µm-thick, double-polished thin sections using a Linkham THMSG600 heating-freezing stage with an automated controller unit attached to an Olympus BX-51 microscope equipped with a Q-imaging digital capture system. Correction of the fluid inclusion microthermometric data for temperature bias was done using measurements on synthetic fluid inclusion standards through measuring the triple point of pure CO_2 (-56.6°C), the melting point of pure H_2O (0°C), and the critical point of pure H_2O (374.1°C). Bulk inclusion salinities were calculated using the final melting temperature of ice (Tm(ice)) and in the freezing point depression-salinity relationship from Bodnar (1994).

4.4.5 Evaporate mound analyses

Fluid inclusions were decrepitated by heating them above their Th to produce evaporate mounds containing solutes representative of fluid composition which can be used to qualitatively characterize fluid composition (e.g., Kontak 2004, 2013). Evaporate mounds were prepared for five samples following collection of the microthermometric data for these samples. Quartz chips were heated at a rate of 50°C/minute to about 500°C to induce decrepitation; samples were subsequently cooled to room temperature. The decrepitated quartz chips were then mounted on glass slides using double-sided adhesive tape and carbon coated prior to being analyzed with a SEM-EDS system (see above for details). During data collection, a raster beam was used, except

for small mounds (i.e., <5 μm) to acquire an average composition in order to preclude possible fractionation of the solute components during mound formation (e.g., Haynes et al. 1988, Kontak 2004). Data were collected for 15 to 20 seconds and the minimum detection limit was 0.2 wt. %. Mound compositions are reported normalized to 100 wt. %.

4.4.6 Oxygen isotopes and secondary ion mass spectrometry (SIMS)

Five samples (NRS-117-26, NRS-117-35, NRS-117-36b, NRS-124c-62, NRS-170110-31) were analyzed for in situ oxygen isotopes at the SIMS Laboratory, University of Manitoba. Samples were selected based primarily on the presence and quality of magmatic and vein-textured quartz. Detailed analytical protocol for SIMS analysis is described by Sharpe and Fayek (2011). After cleaning each sample in deionized water followed by ethanol in an ultrasonic bath, a gold coating was sputtered onto the sample surface to provide conductivity. Each sample was analyzed 8 to 12 times to ensure representative analyses and coverage. A ~7 nA primary ion beam of Cs, accelerated at 10 kV, was focused to a ~30 μm spot size. The entrance and exit slits were narrowed to obtain flat-top peaks. Oxygen ions (^{18}O and ^{16}O) were detected using a Balzers SEV 1217 electron multiplier coupled with an ion-counting system using a dead time of ~52 seconds. Each analysis typically lasted ~10 minutes and was comprised of 70 cycles. Counts were ~$1x10^6$ for ^{16}O. Additional discussion on this technique is provided by Riciputi et al. (1998). The data are reported as $\delta^{18}O$ referenced to standard mean ocean water (SMOW) and in units of per mil (‰). Replicate analyses of standards indicate a reproducibility of ± 0.4‰, whereas for unknown samples reproducibility was ± 1.2‰.

4.4.7 Laser ablation inductively-coupled plasma mass spectrometry

In situ laser ablation inductively-coupled plasma mass spectrometry (LA-ICP-MS) analysis of epidote was done at the Chemical Fingerprinting Laboratory at Laurentian University using a Resonetics Resolution M-50 laser ablation system. The study used 18 samples: 13 from NRS (NRS-104a-2b, NRS-104a-9, NRS-104a-33, NRS-117-1, NRS-117-29, NRS-117-46, NRS-124c-4, NRS-124c-11, NRS-124c-23, NRS-124c-70, NRS-170110-2, NRS-170110-9, NRS-170110-23) and 5 from a barren granophyre sample in the SR (GNa-26, GNa-52, GNa-74) and NR (GNb-13, GNb-28) of the SIC. Epidote samples were first examined using the SEM-EDS to characterize texturally and chemically. The instrument uses a193 nm Ar Fexcimer laser and two-volume Laurin Technic sample cell. Elemental analysis (S, Ca, Ti, V, Cr, Fe, Co, Ni, Cu, Zn, Ga, Sr, Sn, Ba, La, Ce, Pr, Sm, Eu, Gd, Ho, Yb, Lu, Hg, Pb, Th, and U) was done using a Thermo X Series II quadropole ICP-MS using helium as a carrier gas with a flow of 650 ml/min; nitrogen was also used as gas flow at a rate of 6 ml/min. The epidote grains were sampled using a 90 μm spot size, a fluence of 5 J/cm^2, and a laser pulse repetition rate of 6 Hz. The external standard used for calibration of analyte sensitivity was NIST610 and the internal standard used for quantification of trace elements in epidote was 23 wt. % CaO, based on the average Ca content of sample GNb-13 (22.9 to 23.8 wt. % CaO).

4.5 Results

4.5.1 Geology of the Nickel Rim South deposit

Samples were collected from drill core (n = 220; outlined in methods above) to characterize the geology of the NRS environment. The geology at NRS shows considerable variability in of rock types but is dominated by: (i) granitoids showing variable intensity of foliation (CBF; n = 115);

and (ii) Sudbury breccia (n = 35). In addition, there are also minor rock types, including diabase (n = 19), granodiorite (n = 13), mafic norite (n = 9), mafic gneiss (n = 3), footwall breccia (n = 3), sublayer norite (n = 1), felsic norite (n = 1), and Matachewan diabase (n = 1). Where mineralization is present, samples are divided into two categories based on total sulfide mineral content: (i) massive sulfide (MS; n = 7); (ii) disseminated to semi-massive sulfide zones (SMS; n = 11), and (iii) disseminated sulfide zones. Massive sulfide is defined here as > 50 modal % total sulfide minerals over an interval longer than 1 m. This mineralization style is most common in the contact zone but also occurs in the proximal footwall zone. Semi-massive sulfide is defined as <50 modal % total sulfide minerals per interval longer than 1 m. This mineralization style is most common in the contact and proximal footwall zones and also rarely occurs in the distal footwall zone.

4.5.1.1 Primary lithologies and textures

The dominant rock type at NRS is a granitoid characterized by highly variable proportions of felsic minerals (quartz: 8 to 75 vol. %; K-feldspar: 2 to 55%, and plagioclase: 1 to 65%), and minor amounts of amphibole, chlorite, biotite, apatite, zircon, titanite, and hematite (total sum less than 15 vol. %). There is a variable intensity of foliation present in this unit, resulting in a range from primary igneous to gneissic textures. This unit is also variably brecciated with little to no clast rounding or rotation, suggesting in situ brecciation with little breccias migration after formation. Despite the range in foliation intensity, host rock mineralogy and variation in breccia development, these host rock are been grouped into a single package referred to as coherent to in situ brecciated felsic igneous rocks (CBF). The foliation is typically weak to non-existent near the top of the stratigraphic package (Fig. 4A, B) and becomes increasingly developed near the

bottom (Fig. 4C, D); however there are localized zones with a well-developed foliation in areas where the foliation is otherwise lacking. This suggests that some transport of clasts may have locally occurred.

Where the rock is composed of greater than 40 volume % aphanitic, melanocratic to leucocratic, pseudotachylitic matrix material with clasts, it is classified as Sudbury breccia (e.g., Lafrance et al. 2008) rather than coherent to in situ brecciated felsic igneous rocks (Fig. 4E, F). The pseudotachylite domains occur in intervals ranging in thickness from 5 mm to 2.5 m and contain variable (10 to 40 vol. %) amounts of angular to subangular clasts 0.5 to 8 cm diameter. The clasts are locally derived from the basement and consist predominantly of CBF rocks. It is mainly composed of plagioclase, orthoclase, and quartz in proportions similar to the CBF (see above). The degree of crystallization of the clasts is also variable; however, the matrix becomes slightly more coarse-grained and contains increased amounts of recrystallized quartz into the footwall.

Footwall granophyre (FWGR) is a common minor rock type that is unique when compared to the other minor rock types at NRS. It consists of a granophyric to graphic intergrowth of quartz, near end-member K-feldspar, and near end-member albitic plagioclase (Fig. 4G, H). It is present as veinlets ranging from 1 to 15 cm in width that cut most rock types (e.g., granite, granodiorite, felsic gneiss, diabase), including Sudbury breccia (e.g., NRS-124c-64, NRS-117-36). It is important to note that this rock is free of recrystallization and deformation-related features (e.g., undulose extinction, subgrains).The FWGR is most abundant near the contact zone lessens in abundance in the proximal zone and is very rare in the distal footwall zone. The FWGR often

contains miarolitic cavities and voids lined by secondary phases (e.g., quartz, epidote) ranging from medium- to very coarse-grained. Bodies of FWGR are more abundant proximal to mineralization near the SIC contact, as noted elsewhere in the SIC environment (e.g., Hanley et al. 2011).

There are several minor rock types present at NRS, including felsic norite, mafic norite, sublayer norite, footwall breccia, gabbro, granodiorite, mafic gneiss, and diabase. Representative images of these lithologies are shown in Fig. 5. These rock types are variably distributed from the contact zone through to the distal footwall zone and their descriptions and distributions are summarized in Table 1.

4.5.1.2 Mineralization at Nickel Rim South

Contact- and footwall-style mineralization is present at NRS. Contact-type mineralization is hosted in predominantly footwall breccias and to a lesser extent felsic and mafic norite, and sublayer norite, and occurs as disseminated (in norites only) and massive ore (in all lithologies) intersections 2 to 35 m, and 1 to 13 m in width, respectively (Fig. 6A-C). This mineralization type consists of pyrrhotite-pentlandite (<45 modal %) with minor chalcopyrite (<25 modal %). Contact-style mineralization commonly transitions into net-textured and disseminated types of mineralization becoming chalcopyrite enriched (Fig. 6D). This textural transition can occur over ~1 cm to 1 m and depends on the thickness of the mineralized vein and forms massive chalcopyrite veins of 20 cm to 2 m thickness.

Footwall-type mineralization occurs in the proximal and rarely in the distal footwall zone and consists of disseminated to net-textured to vein-hosted chalcopyrite (<40 modal %) with minor bornite (<10 modal %), pyrrhotite (<5 modal %) pentlandite (<20 modal %), and millerite (<1 modal %). Chalcopyrite veins are 3 cm to up to 5 m wide (i.e., 100% chalcopyrite; Fig. 6E). In some areas this ore contains magnetite as 2 to 6 mm sub- to euhedral grains as disseminations. These veins can transition to net-textured and then to disseminated sulfides into the wall rock. Disseminated magnetite is often spatially associated with footwall-type mineralization. Semi-massive sulfide zones occur over larger intervals (50 cm to 35 m) and contain disseminated to blebby-net textured to vein-hosted chalcopyrite with minor bornite, pyrrhotite, and pentlandite. Rarely in areas proximal to the contact, chalcopyrite is present along grain boundaries within FWGR. This mineralization type is often spatially associated with Sudbury breccia. Areas devoid of SMS or MS often contain trace to 2 % disseminated chalcopyrite (Fig. 6F).

4.5.1.3 Alteration assemblages in the NRS ore zones and paragenesis

Hydrothermal alteration in the NRS mineralized zones, as identified petrographically and using the SEM-EDS, is dominated by epidote, chlorite, and amphibole with variable amounts of sericite, stilpnomelane, quartz, carbonate, re-equilibration of plagioclase and K-feldspar. The occurrence of these alteration minerals with respect to the host rock lithologies at NRS are summarized in Table 1 and representative textures displayed by these alteration phases are summarized in Figures 7 and 8.

Texturally, the alteration is present as selvages on barren and mineralized veins (epidote, chlorite, amphibole, stilpnomelane), a replacement of earlier mineral phases (saussuritization of

plagioclase by sericite and epidote, chloritization of biotite, albitization of plagioclase, and re-equilibration of K-feldspar), disseminations throughout the host rock matrix (epidote, chlorite, amphibole), void-space filling (epidote), and late veins that cross-cut all lithologies (chlorite, epidote, quartz, and carbonate). The three temporally and volumetrically dominant minerals in the NRS alteration assemblage (i.e., epidote, chlorite, and amphibole) have been subdivided based on their textural variety. Epidote exhibits five textural varieties (Fig. 7): (i) disseminated, fine- to medium-grained (type 1; Fig. 7A, B); (ii) vein, coarse-grained (type 2; Fig. 7C, D); (iii) vein, fine-grained (type 3; Fig. 7E, F); (iv) blocky/void-filling (type 4; Fig. G, H); and (v) pits in altered plagioclase (type 5; Fig. 8E). Amphibole exhibits two textural varieties: (i) euhedral (Fig. 8A); and (ii) fibrous (Fig. 8B). Chlorite exhibits two textural varieties: (i) replacement and disseminated (Fig. 8C); and (ii) as selvage to mineralized and unmineralized veins (Fig. 8D). Stilpnomelane was identified in one sample with chlorite as a selvage to a chalcopyrite (Fig. 8D). Sericite is present as part of saussuritized assemblages with epidote and rarely in veins (Fig. 8E). Biotite, where present, often exhibits poikilitic texture (Fig. 8F). Quartz is most commonly in granitic clasts in Sudbury breccia or CBF and often exhibits metamorphic (i.e., annealed) textures; however, it also occurs as late veins with carbonate (Fig. 8G). Orthoclase most often is present as a product of in situ re-equilibration (Fig. 8H) rather than part of a vein selvage or dissemination.

Of the alteration phases, types 1 and 2 epidote, type 2 chlorite, and type 2 amphibole are the only minerals that can be coeval with mineralization. However epidote and chlorite are much more commonly associated with mineralization than amphibole. Texturally these minerals form

selvages on mineralized veins and are disseminated within massive to net-textured mineralization.

An alteration assemblage paragenesis was constructed by integrating core logging, petrography, and SEM-EDS analysis (Fig. 9). This study characterized the genesis of NRS after impact and thus processes occurring prior to this are not discussed in this paragenesis. The hydrothermal stage at NRS is characterized by complex, multi-stage hydrothermal alteration events in the footwall during the prolong evolution of the footwall hydrothermal system. The alteration summarized for this stage is further divided into three stages and is based on the alteration noted in the many different lithologies present in the footwall rocks rather than a single lithology.

The first stage is characterized by an early stage of plagioclase, K-feldspar, and quartz development, followed by a pre-mineralization stage characterized by alteration of plagioclase by saussuritization (Fig. 8A) producing variable amounts of pitting in plagioclase and K-feldspar due to coupled dissolution-precipitation processes (e.g., Putnis 2002). In most instances these pits are filled with sericite and epidote. This stage also contains the early epidote types 1, 4 and 5 and minor biotite.

The third stage is coeval with mineralization however not all minerals show textural evidence of association with sulfides. This stage is characterized by types 1, 2, and 4 epidote, types 1 and 2 chlorite, type 2 amphibole, and stilpnomelane as veins and disseminations with and without associated footwall-type mineralization. Of these minerals, type 4 epidote is also texturally synchronous with type 2 chlorite and thus is also part of this stage. Epidote veins can contain

actinolite ± chlorite ± quartz vein selvages. Rare carbonate and quartz veins are also present. Mineralization (chalcopyrite ± cubanite) in this stage varies from massive to semi-massive to net-textured/vein to disseminated types. Importantly types 1 and 2 epidote, type 2 chlorite, type 2 amphibole, and stilpnomelane (one samples) are texturally associated with mineralization. Biotite is altered to various degrees and typically is intergrown with secondary phases such as epidote and chlorite.

The fourth stage consists of hydrothermal mineral assemblage that texturally post-dates mineralization. The majority of these minerals are contained within veins that crosscut the stage two assemblages. This mineral assemblage includes types 2 and 3 epidote, types 2 chlorite, type 1 amphibole, quartz, and carbonate.

4.5.2 Mineral Chemistry

4.5.2.1 Major and minor element composition of major alteration minerals

Semi-quantitative analyses by SEM-EDS show that plagioclase (n=170), an early alteration mineral (i.e., texturally early but modified hydrothermally to a new composition) has a composition that is similar in both the contact and distal footwall zones, ranging from end-member albite to a slightly calcic plagioclase (up to ~ 8% An). K-feldspar (n=88) analyses indicate, similarly, a relatively uniform composition of end-member orthoclase to slightly albitic K-feldspar (up to ~ 7% Ab) with no differences between ore zones.

Quantitative determinations of mineral chemistry for hydroxysilicate alteration phases (epidote, amphibole, chlorite and biotite) are presented in Tables 2 to 5. All five epidote textural varieties

from the various ore zones were analyzed (Table 2 and Fig. 10A). Ratios of FeO/CaO do not vary significantly with textural variety of epidote with type 5 epidote showing the lowest ratios overall. However, there is spatial variation in the range of FeO/CaO values seen in the contact zone (n=21; 0.50±0.06; 0.38 to 0.58), increasing in the proximal footwall zone (n=56; 0.53±0.09; 0.21 to 0.66), and highest in the distal footwall zone (n=50; 0.61±0.06; 0.50 to 0.79; Fig. 10A). Overall, FeO shows a weak inverse correlation to CaO over the entire range of epidote types and mineralized zones examined.

The amphibole analyses for all samples (n=44 from all zones; Table 3 and Fig. 10B) show predominantly actinolitic amphibole with some samples also containing some ferro-actinolite and magnesio-hornblende. Chlorine concentrations are negligible between euhedral (n=22; 0.07±0.08; 0.0 to 0.21) and fibrous (n=22; 0.03±0.06; 0.0 to 0.20) type. Fluorine is also similar in euhedral (0.20±0.17; 0.01 to 0.61) and fibrous (0.17±0.13; 0.03 to 0.54) types, whereas Cl/(Cl+F) is greater in euhedral (0.25±0.18; 0.0 to 0.69) than fibrous (0.11±0.12; 0.0 to 0.49) types. Halogen concentrations in amphibole exhibit a correlation to various zones sampled. Amphibole from the contact zone has low concentrations of Cl (n=11; 0.1±0.1; 0.0 to 0.2) and F (0.10±0.07; 0.01 to 0.26) and Cl/(Cl+F) (0.13±0.18; 0.0 to 0.62) compared to the proximal footwall zone (n=18; Cl 0.04±0.06; 0.0 to 0.20; F 0.19±0.13; 0.03 to 0.54; Cl/(Cl+F) 0.12±0.13; 0.0 to 0.49). The distal footwall zone is slightly enriched in Cl (n=15; 0.10±0.08; 0.0 to 0.21), F (0.24±0.19; 0.06 to 0.61) and Cl/(Cl+F) (0.27±0.17; 0.06 to 0.69).

Chlorite (n=76 from all three zones; Table 4 and Fig. 11A) analyses show compositions ranging from near end-member chamosite to clinochlore, reflecting significant variations in Fe#.

Disseminated and replacement chlorite exhibit a lower average Fe# (n=59; 0.54±0.13; 0.31 to 0.75) compared to vein-type chlorite (n=17; 0.73±0.02; 0.69 to 0.75). The chemistry of disseminated and replacement chlorite also varies with respect to its position within the deposit, with chlorite in the proximal footwall zone having the average in highest Fe# (n=53; 0.62±0.08; 0.45 to 0.75), and chlorite in the contact (n=17; 0.55±0.22; 0.31 to 0.75) and distal (n=6; 0.40±0.01; 0.39 to 0.41) footwall zones. The Fe# for chlorite was compared with the FeO/CaO ratios of all five textural varieties of epidote (Fig. 12). In the contact and distal footwall zones, no clear correlation is observed; however, in the proximal footwall zone (i.e., 117-46, 117-29) there is a good correlation between the Fe content of epidote and chlorite.

Biotite was analyzed in three samples only from the contact and proximal footwall zones because it is rare to absent in the distal footwall zone. The biotite results are summarized in Table 5 and Figure 11B. There is no significant variation in biotite chemistry with respect to its position in the deposit. The contact zone has lower Cl contents than the proximal footwall zone (0.12±0.04, 0.05 to 0.18 and 0.35±0.04, 0.29 to 0.41 respectively) and similar F (0.07±0.02, 0.05 to 0.09 and 0.07±0.01, 0.07 to 0.08, respectively) and overall a greater but more variable Cl/F ratio (0.65±0.24, 0.45 to 1.17 and 0.22±0.03, 0.18 to 0.27, respectively). Compositions plot between annite and phlogopite on the annite-phlogopite tie-line.

4.5.2.2 Trace element chemistry of epidote

A suite of 13 samples was selected from NRS it that contained representative textural variants of epidote. Representative samples of epidote-bearing granophyre from the main mass of the SIC were also selected. The epidote in these samples was analyzed by LA-ICP-MS to determine trace

element concentrations, including a variety of ore metals. Particular attention was paid to ore metals to assess the viability of using epidote chemistry as a pathfinder for mineralization.

Epidote samples were analyzed from the contact zone (n=5), proximal footwall zone (n=3), and distal footwall zone (n=5) at NRS, and from the granophyre unit of the SIC (n=5). Due to the rarity and small grain size of pit-hosted (type 5) epidote, only the other textural varieties were analyzed. The LA-ICP-MS results are summarized in Table 6. Based on REE chemistry, three different types of epidote were identified (see chondrite-normalized abundance patterns in Fig. 13):

1. strongly fractionated (i.e., $La_N > Lu_N$) with a positive Eu anomaly (type 1_{REE})
2. weakly fractionated pattern (i.e., $La_N \approx > Lu_N$) and lacking a Eu anomaly (type 2_{REE})
3. slight LREE enrichment but with the HREE fractionated (i.e., $Gd_N > Lu_N$) and with a variable Eu anomaly (type 3_{REE})

A summary of these classifications in relation to textural variety, host zone type, and host rock type is found in Table 7. Rare earth element patterns are consistent within individual epidote grains; however, the relationship between the epidote textural variety and the REE pattern is variable. Within an individual sample, epidote of the same textural variety exhibits a consistent REE pattern but the same textural variety can exhibit a different REE pattern in a different sample. Where multiple REE patterns are present within in a single sample, they are observed in different epidote textural varieties. There are no samples where definitive cross-cutting relationships between the various chemical types of epidote could be established.

A correlation between the REE pattern of epidote and its position within NRS it is observed. Type 1_{REE} epidote is the most common and is present in all samples analyzed and from all three zones at NRS. It is also the only chemical pattern observed in mineralized samples. Type 2_{REE} epidote was only identified in CBF in the distal footwall zone. Type 3_{REE} epidote occurs in the proximal and distal footwall zones.

There is a broad correlation between the epidote textural variety and its associated REE pattern. Epidote textural variety type 1 is the most consistent with respect to its chemistry and exhibits only pattern 1_{REE}. Epidote textural variety type 2 exhibits patterns 1_{REE} and 2_{REE} and this chemical variation does not appear to have a spatial control. Epidote textural variety type 3 exhibits only type 1_{REE} with the exception of two analyses (i.e., 124c-11) from one sample in the distal footwall zone, which exhibit type 3_{REE}. Epidote textural variety type 4 exhibits all three REE patterns. Individual grains of epidote textural variety type 5 were too small for trace element analysis.

Ore metal concentrations were also analyzed and are also presented in Table 7. No relationship between epidote textural variety and metal content was identified in single grains or within single samples.

The average Ni content of epidote is slightly enriched in samples from the contact zone (n=13; 19±11; 3 to 42 ppm). Of the two samples from the contact zone, one is barren of mineralization (sample 170110-36; n=9; 14±6; 3 to 25 ppm) whereas the mineralized sample is slightly enriched (sample 124c-73; n=4; 31±13; 18 to 42 ppm). The average Ni content of epidote in the proximal

footwall zone is similar to the contact zone (n=43; 8±13; 0 to 47 ppm) whereas the distal footwall zone is depleted (n=60; 2±2; 0 to 7 ppm).

The Cu contents of epidote from a mineralized sample in the contact zone are enriched (n=4; 41±30; 7 to 69 ppm) compared to the barren sample from the contact zone (n=9; 6±9; 0 to 28 ppm). The Cu contents of epidote are lower in the contact zone (n=13; 17±24; 0 to 69 ppm) compared to the proximal footwall zone (n=43; 14±22; 0 to 91 ppm) and are lowest in the distal footwall zone (n=60; 8±9; 1 to 31 ppm). Thus, there are only slight differences in the base metal contents of epidote between different mineralized zones.

4.5.3 Quartz-hosted Fluid Inclusions

4.5.3.1 Petrography

Fluid inclusions in quartz are present along healed fracture planes in samples of FWGR and metabreccia (Fig. 14A, B) and are therefore are secondary in origin. Important to note here is that the healed inclusions trails cross cut clear, undeformed quartz whose formation, in the case of the FWGR, post-dates the impact event and is therefore syn-footwall alteration or sometime thereafter.

The inclusions vary in terms of size (<4 to 20 μm) with most on the small size (<7 μm). Their shapes vary from equant to elliptical to irregular. As the inclusions are aqueous in nature, the terminology used below reflects this, thus L_{H2O}-V_{H2O} is simply referred to as L-V types. Petrographic investigation of all polished thin sections (n=58) prepared for this study indicates that the majority of fluid inclusions (>70 % based on point counting) have textures suggestive of

post-entrapment modification (e.g., necking; Fig 14C) and cannot be used for microthermometric analysis. Of the fluid inclusions that have not been modified after entrapment, three fluid inclusion types, that is fluid inclusion assemblages (FIA), are present: (1) L-V with about 10 to 15 % V (Fig. 14D); (2) L-V-solids with about 10 to 15% V and halite as the most common solid (Fig. 14E); and (3) L-V with about 20-30% V (Fig. 14F). The relative proportions of these fluid inclusion types are approximately 50 % type 1, 40 % type 2, and 10 % type three.

In terms of relative abundance and timing of entrapment, no cross-cutting relationships between FIAs were identified nor was any textural relationship to growth zones; therefore, no evidence was identified to differentiate relative timing of entrapment of each inclusion type. However, these inclusions must post-date the formation of the breccia hosts because they form trails in clasts of Sudbury breccia.

4.5.3.2 Microthermometry

Of the 58 thin sections used for petrographic study, only five contained appropriate FIAs with large enough fluid inclusions to collect microthermometric data. Of these five samples, two are from the proximal footwall zone (NRS-117-26, NRS-117-29), one from the near the transition between the proximal and core zones (NRS-124c-64), and two from the deep footwall zone (NRS-117-9, NRS-117-35). Thermometric data collected (Table 8) include: (i) temperature of freezing (Tf); (ii) the first melting or eutectic temperature (Te), which defines the bulk composition of the system (i.e., cations present in addition to Na; Davis et al. 1990); (iii) the ice melting temperature (Tm(ice)); (iv) the melting point of halite (Tm(halite)) in type 2 inclusions;

and (v) the final homogenization temperature (Th), either by disappearance of the vapour phase or halite.

Type 1 L-V inclusions

Data were measured on 17 inclusions for five FIAs in three samples with the following results: Tf ranges from -75° to -61°C, Te ranges from -27.1° and -17.9°C, Tm(ice) ranges from -19.8° to -16.1°C, and Th ranges from 142° to 245°C. In all cases, ice was observed as the last phase to melt during heating runs and due to the small size of the inclusions it was not possible to record the melting of hydrohalite and obtain the Na:Ca of the inclusions. The salinities of the inclusions range between 20.5 and 21.4 wt. % equiv. NaCl, but based on the low freezing values and the Te below -21.2°C another solute besides Na is inferred to be present.

Type 2 L-V-halite inclusions

Type 2 fluid inclusions with uniform phase proportions and large enough for microthermometry were only present in four samples (NRS-117-26, NRS-117-29, NRS-117-35, NRS-124c-64) and from these 15 inclusions for four FIAs were used for measurements. For these inclusions the following data were collected: Tf ranges from -81° to -61°C, Te ranges from -29.7° and -17.4°C, Tm(ice) ranges from -23.6° to -18.7°C, and Tm(halite) ranges from 210° to 260°C. In addition, the homogenization of the L-V component of these inclusions, which falls below Th(halite), was recorded and ranged from 127° to 216°C. Salinities, estimated using the dissolution temperature of halite, range between 33.5 and 35.4 wt. % equiv. NaCl, but based on the low freezing temperatures and Te values (i.e., <21.2°C) another solute in addition to Na is inferred to be present.

Type 3 L-V aqueous inclusions

Of these seven samples used for thermometric work, only two contained FIAs of type 3 inclusions large enough for measurement (NRS-117-9, NRS-117-29) and from these 7 inclusions from 2 FIAs were used for measurements. The following data were measured for these inclusions: Tf ranged from -79° to -68°C, Te ranged from -24.5° to 17.4°C, Tm(ice) ranged from -23.5° to -19.2°C, and Th ranged from 315° to 329°C. Fluid salinities range between 22.2 to 23.4 wt. % equiv. NaCl but based on the low freezing temperatures and Te values (i.e., <21.2°C) another solute in addition to Na is inferred to be present.

4.5.4 Evaporate mound analysis

The five samples used for microthermometry were also used for evaporate mound analysis (Table 9). Of these five samples, three are from the proximal footwall zone (n=51 mounds) and two are from the distal footwall zone (n=29 mounds). The inclusions in samples from the contact zone did not decrepitate and thus did not produce evaporate mounds. The size and shape of evaporate mounds varied considerably (Fig. 15), which is generally a function of the size, salinity and chemistry, in particular divalent cations, of the inclusions (Haynes et al. 1988, Kontak 2004). As seen in some of the mounds, it is common to see a central cubic phase which is halite that is covered with an amorphous looking material which is Ca-rich.

A summary of the major element chemistry of the mounds is presented in Figure 16, which highlights the enrichment in Na>Ca>>K (Na: 34.4±6.4, 21.7 to 46.6; Ca: 12.1±5.4, 2.6 to 32.4; K: 1.8±1.6, 0 to 7.0). Since the majority of fluid inclusions are type 1 and 2, it is likely that the evaporate mound chemistry reflects these inclusion types. In addition to the major cations noted,

Mn (0.7±0.8, 0 to 2.4) and Fe (0.3±0.5, 0 to 1.8) are also present in significant concentrations, but Mg was absent in all the evaporate mounds from both zones.

4.5.5 Oxygen isotopes

Results of in situ SIMS $\delta^{18}O$ quartz measurements are summarized in Figure 17 and in Table 10. Various styles of quartz were analyzed, including quartz aggregates in CBF, subhedral to anhedral quartz hosted in FWGR, and quartz veins cutting various lithologies. When considering which samples and where in these samples to analyse for $\delta^{18}O$, CL imaging was used to identify the best area for analysis. These areas were defined by bright CL signals, consistent signals that did not vary throughout a single grain, and a lack of fracture patterns indicative of re-equilibration of quartz. Grains that showed both dark and light CL signals were also analyzed in order to investigate the relationship between CL signal intensity and $\delta^{18}O$ value. Of the five samples used for analysis, three are Sudbury breccia, one is CBF, and one is from the SIC-footwall contact in brecciated mafic norite. In addition, samples selected came only came from two of the three in NRS (contact zone and proximal footwall zone) as suitable material was not available for the distal footwall zone.

The sample from the contact zone has an average $\delta^{18}O_{quartz}$ value of +9.0±1.6‰ and exhibits a range from +6.9 to +12.1‰. The $\delta^{18}O_{quartz}$ values in this sample vary between individual grains and within individual grains (up to 3.4‰ within a single grain). The sample from the proximal footwall zone near the contact zone (124c-62) has an average $\delta^{18}O_{quartz}$ value of +9.2±2.0‰ with range from +6.6 to +11.9‰. Individual quartz grains in this sample are also isotopically heterogeneous with a maximum range in $\delta^{18}O_{quartz}$ values of 5.3‰ within a single grain. Lastly,

the three samples from the proximal footwall zone have an average $\delta^{18}O_{quartz}$ value of +8.8±1.7‰ with data ranging from +5.6 to +12.4‰. The maximum variability of $\delta^{18}O_{quartz}$ values within a single grain for these samples is 3.8‰. With respect to the variability of $\delta^{18}O_{quartz}$ values within a single sample, the sample furthest from the contact zone (NRS-117-26) exhibits the least amount of variability (3.2‰). There is no apparent correlation between variability of $\delta^{18}O_{quartz}$ within a single sample. The other samples analyzed do not exhibit a correlation between the variability of $\delta^{18}O_{quartz}$ values within the sample and location relative to the contact zone.

Cathodoluminescence imaging data (Fig. 18) do not show any systematic variation or correlation with the oxygen isotopic data. No relationship was noted between intensity of the CL signal, and quartz texture (e.g., fractures, annealed textures).

4.6 Discussion

4.6.1 Estimates of fluid PT characteristics

Measured homogenization temperatures must be corrected for pressure to yield absolute fluid inclusion trapping temperatures since the homogenization temperature represents only a minimum trapping T, lying on the L+V curve (Roedder 1984; Bodnar 2003). Pressure constraints in the footwall environment during cooling of the SIC (and evolution of the footwall hydrothermal ores) have been estimated to range from 0.7 to 2.1 kbar based on the inferred thickness of SIC and crater fill sequence relative to the current depth of footwall ore deposit zones around the NR and ER (Molnár et al. 2001; Péntek et al. 2008). Thermobarometry of primary amphibole from footwall granophyre units confirm a pressure of 1.5±0.5 kbar for a

period of high temperature, SIC-related partial melting or melt injection into the footwall (Péntek et al. 2011). For correction of our microthermometric data, we used a pressure of 1.8 kbar based on an approximate thickness of 7 km at NRS. This pressure used in conjunction with calculated isochores (following method of Bodnar and Vityk 1994; Fig. 19) yields trapping temperature estimates of ~240º to 340°C, 220° to 300°C, and 455° to 462°C for types 1 and 3 inclusions, respectively.

The wide but similar range in estimated fluid temperature for types 1 and 2 inclusions, limited by a lack of evidence for their relative timing of entrapment, can be explained by two possibilities: (i) two fluids of similar temperature passed through the rocks at different times; or (ii) type 1 and 2 fluid inclusions contain a broadly similar fluid that contained a heterogeneous distribution of dissolved salts, resulting in trapping of inclusions with different salinities.

Type 1 fluid inclusions are two phase at 20°C (L + V) but have a salinity near halite saturation (20.5 to 21.5 wt. % equiv. NaCl), whereas type 2 fluid inclusions are halite saturated and of higher salinity (33.5 to 35.4 wt. % equiv. NaCl). The depressed Te values measured for the majority of both type 1 and 2 inclusions indicate that the fluid also contains a small amount of a cation in addition to Na as the dominant cation. It was not possible to determine the cation proportions by microthermometry because the small size of fluid inclusions did not allow for identification of hydrohalite (to determine the proportion of Ca to Na) or of other phases associated with cations other than Na (e.g., sylvite).

The fluid inclusion data for type 3 fluid inclusions are of a similar salinity to type 1 fluid inclusions (22 to 23 wt. % equiv. NaCl) but exhibit much higher trapping temperatures (estimated to be 455° to 462°C; Fig. 19). Type 3 inclusions are rare (only 5% of total fluid inclusions) but were identified in both the proximal and distal footwall zones and are not restricted to the contact zone. Given this distribution of type 3 inclusions within NRS, these high temperature fluids must have circulated at least 500 m from the SIC. Cross-cutting relationships between the three fluid inclusion types are not observed at NRS, and in order to investigate their relative timing, the PT regime of the footwall must be considered. A thermal aureole associated with the SIC has been documented in the footwall based on the contact metamorphic assemblages observed (Dressler 1984; Boast and Spray 2006). Pyroxene hornfels conditions dominate up to 350 m from the SIC contact, followed by hornblende hornfels conditions up to 1100 m from the contact, and albite-epidote hornfels conditions up to 2000 m from the contact. These zones correspond to temperatures of approximately 580° to 630°±20°C, 520° to 540°±20°C, and <400°C, respectively (Winkler 1967; Boast and Spray 2006). At NRS, the transition from the proximal to distal footwall zones ranges between 200 and 250 m away from the contact, indicating that the proximal footwall zone reached peak pyroxene hornfels conditions and the peak metamorphic conditions for the distal footwall zone varied from pyroxene to hornblende hornfels conditions. Partial melting also occurred at the contact and up to 25 m away from the contact (Boast and Spray 2006), and the contact zone at NRS therefore underwent partial melting. As outlined in the fluid inclusion petrography section above, all fluid inclusions must post-date the formation of the SIC because the inclusions form trails in clasts of Sudbury breccia, which represents impact-induced partial melting of the footwall rocks. Any inclusions that may have been present in these rocks at the time of impact would have been

destroyed by this partial melting event. Metamorphism associated with orogenic events post-impact was heterogeneously distributed throughout the SIC footwall, with the SR reaching up to amphibolite facies and the NR and ER only reaching sub- to low greenschist facies (Card 1978). Therefore, in the absence of any later high temperature events, fluid inclusion types 1, 2, and 3 must have been trapped during cooling of the SIC and the heat for the fluids was provided by the thermal aureole associated with the SIC. This also provides a relative timing for the inclusion types, as the high temperature type 3 inclusions must have been trapped earlier than the lower temperature type 1 and 2 inclusions. Furthermore, given that all three inclusion types exhibit trapping temperatures lower than the peak metamorphic temperatures for the rocks in which they were trapped, trapping must have occurred post-peak metamorphism and the fluids represent a retrograde, or post-hornfels, event.

4.6.2 Fluid sources contributing to the NRS hydrothermal system

Although the temperatures for fluid inclusion types 1, 2, and 3 are the product of the cooling SIC, these fluids are not necessarily sourced directly from the SIC. There are several possible sources for the fluids contributing to the NRS hydrothermal system that must be considered when evaluating the microthermometric and geochemical data presented here:

1. Magmatic (i.e., having been in equilibrium with melt) fluids, either exsolved directly from the cooling SIC or from liquids associated with FWGR bodies that have either been injected into the footwall or generated by partial melting of footwall rocks. The best estimate for the temperature and salinity of these fluids are derived from L-V-H±additional solids fluid inclusions hosted in FWGR bodies, interpreted to represent injections of melt from the SIC

into the footwall. Hanley et al. (2011) measured the Th of these inclusions to be 502°± 44°C based on the Tm(halite) and calculated the fluid salinity to be 60.5 ± 5.8 wt. % equiv. NaCl, which is consistent with the salinity range of 33 to 61 wt. % equiv. NaCl calculated for equivalent inclusions by Molnár et al. (2001). Fluid inclusions in FWGR bodies at Amy Lake are also consistent with the above temperature and salinity data, and are documented to have a Th value of 480° ±43°C and an average salinity of 54.3 ±8 wt. % equiv. NaCl (Tuba 2012).

2. Deep groundwaters also referred to as "crystalline shield brines". The temperature of this fluid is estimated to have been 40° to 160°C based on a thermal gradient of 15° to 20°C/km (Grasby et al. 2012) and depths ranging from 2.8 to 8 km. However, within the thermal aureole of the SIC these fluids would likely have been heated to ambient temperatures. The salinity is estimated to be up to 17 wt. % equiv. NaCl based on present day groundwater measurements (Frape and Fritz 1982; Pearson 1987, Frape and Fritz 1987). Pearson (1987) has shown that these fluids may have been at halite saturation but with the high $CaCl_2$ content, the common ion effect may produce a halite-undersaturated fluid. Although this salinity is below halite saturation for a pure NaCl system (26.5 wt. % equiv. NaCl), it is noted the high $CaCl_2$ content of these fluids resulted in halite saturation due to the common ion effect (Pearson 1987).
3. A metamorphic fluid produced in the contact aureole in the footwall to the SIC. There is no published data for the temperature and salinity of this fluid, although a contact metamorphic aureole has been documented in the footwall, as outlined above. The NRS underwent variable pyroxene to hornblende hornfels contact metamorphism corresponding to a range in maximum temperatures of 520° to 630°C (Winkler 1967; Boast and Spray 2006). Given that metamorphic dehydration of hydrous minerals begins around 200°C (e.g., Stevens et al.

1997), it is likely that this metamorphism generated a fluid; though it is not possible to estimate the volume proportion of this fluid given that the modal mineralogy of the protolith has been obscured by later hydrothermal alteration. These fluids would have been high temperature but low salinity, as is typical for metamorphic fluids (Yardley and Graham 2002). This is because they would have been produced by dehydration of minerals, which releases only H_2O from the crystal structure.

Given the measured salinities and calculated homogenization temperatures for fluid inclusion types 1, 2, and 3, it is apparent that none of the end-member fluid sources described above can account for these inclusions if modification or mixing with other fluids did not occur prior to trapping. The temperatures and salinities of the magmatic fluids are too high, whereas the temperature of the groundwater is appropriate for inclusion types 1 and 2 but the salinity of this fluid is lower than all three inclusion types. It is possible that the temperature and salinity of the metamorphic fluids are in the same range as all three inclusion types; however, it is unlikely that this fluid was volumetrically significant given that the dominantly felsic host rocks to NRS lack a significant proportion of hydrous mineral phases. Therefore, the fluid represented by the fluid inclusions at NRS must represent modification or mixing of one or more end-member fluids prior to trapping.

An alternative fluid source may be fluids exsolved directly from the mafic basal units of the SIC, for which fluid inclusion data has not been reported in previous studies. In order to consider the trapping conditions for such a fluid, the PT isochore diagram can be applied (Fig. 19). Of the three inclusion types, the type 3 fluid inclusions represent the highest temperature fluids and are

therefore closest to magmatic fluid temperatures. The point in PT space at which the isochore for type 3 inclusions intersects the basalt wet solidus represents the necessary trapping conditions if this fluid was trapped immediately after exsolution and represents an unmixed magmatic fluid. This corresponds to a pressure of ~4.7 to 5.0 kbar and a temperature of ~735° to 750°C ("A", Fig. 19). These pressures are significantly higher than the estimated footwall pressures of ~0.7 to 2.1 kbar (Molnár et al. 2001; Péntek et al. 2008) and are therefore unreasonable for NRS, indicating that type 3 inclusions do not represent end-member magmatic fluids derived from the basal SIC. Another option is that magmatic fluids were exsolved from the SIC at a reasonable pressure, which would correspond to a temperature of exsolution of approximately 950°C (Brown 1993). This temperature is significantly higher than that of type 3 inclusions, however, and requires that the magmatic fluid was cooled isobarically prior to trapping. This may have been achieved by one or a combination of circulation of the fluid throughout the footwall system during cooling or mixing of the magmatic fluid with a more saline and lower temperature fluid (e.g., shield brines from deeper in the footwall). Either mechanism requires that the overall footwall system had cooled enough prior to trapping to allow for the fluid to be trapped at the temperatures appropriate for type 3 (455° to 462°C; "B" and "C", Fig. 19).

Due to the very similar homogenization temperatures for inclusion types 1 and 2, these fluid types will be considered together on the isochore diagram. In order to compare these fluids with the type 3 fluid and because of the similarity in salinity between type 1 and 3 fluids, only the type 1 fluid is plotted on the diagram (Fig. 19). The trapping temperature of this fluid is too low for it to have been exsolved and trapped as a magmatic fluid, and, as stated above, the salinity is too high for groundwater and metamorphic fluids. Furthermore, these groundwater and contact

metamorphic fluids were likely to have been too volumetrically insignificant to account for a fluid that we observe abundantly and pervasively in the fluid inclusion record. Given the similar salinities for type 1 and 3 fluids, it is likely that this fluid represents a second trapping of the type 3 fluid following further isobaric cooling. Also noteworthy is the wide range (~220° to 340°C) in trapping temperatures of type 1 fluids in comparison with the limited range for type 3 fluids. This suggests that cooling of the fluid throughout the system was heterogeneous and that trapping occurred as the system cooled but long after peak contact metamorphic conditions.

Therefore, fluid inclusion microthermometric and salinity data does not unequivocally indicate which of the possible fluids are present in the NRS system and have been trapped as inclusions. However, these data does show that none of the fluid sources as end-members account for the fluid inclusion types directly without modification or mixing. Magmatic fluids, whether they be exsolved from FWGR bodies or directly from the SIC, must have been diluted, by groundwater and/or metamorphic fluids, and trapped after the thermal aureole produced by the SIC had cooled significantly. Furthermore, type 1 and 2 inclusions appear to represent a lower temperature of trapping of the hybrid fluid trapped as type 3 inclusions.

4.6.3 Comparison of fluid inclusion data with other systems

Fluid inclusion results from this study are notably different from what has been documented in other mineralized SS footwall systems. Although low-temperature fluid inclusions similar to the types 1 and 2 fluid inclusions at NRS have been identified in other footwall systems (e.g., McCreedy; Marshall et al. 1999), mineralized systems in the SS footwall typically contain multi-solid, hypersaline (≥ 35 wt. % equiv. NaCl), high-temperature (175º to 500°C) fluid inclusions

that pre-date or are coeval with Cu-Ni-PGE mineralization. These inclusions are interpreted to represent a high-salinity, moderate to high temperature fluid that was responsible for the remobilization and transport of Cu-Ni-PGE in the footwall and has been identified in the NR and SR, as well as in the only other ER deposit where fluid inclusions have been documented (Amy Lake; Tuba et al. 2014). The absence of fluid inclusions representing this fluid type at NRS suggests that the fluids were present but were not trapped as inclusions, the fluids were trapped but the inclusions were destroyed by later deformation, or the fluids were not present in the NRS hydrothermal system. One possibility for the absence of these fluid inclusions at NRS is that post-SIC deformation, unique to the ER (e.g., Lake Wanapitei impact event; Dence and Popelar 1972, Winzer et al. 1976, Rousell 1984), destroyed these fluid inclusions, and evidence for their existence has been lost. However, if this were the case we would expect to see strong, homogeneous deformation within all samples at NRS, and this is not observed. We have identified localized shearing and deformation in some areas of NRS but it is not extensive enough to account for complete destruction of this fluid inclusion type. Given that this fluid is trapped as inclusions throughout the rest of the SS footwall, it is unlikely that the fluid was present in the NRS system and not trapped. It is therefore most likely that the lack of high temperature, high salinity, multi-solid inclusions at NRS indicates that this fluid was not present in the NRS system.

If high-salinity fluids are necessary for metal remobilization in the footwall, especially in low-sulfide, PGE-rich deposits, we expect to see fluid inclusion evidence for a high-salinity fluid in a deposit like NRS, which contains both subtypes of footwall mineralization. An alternative explanation is that these fluids were not produced and/or did not circulate at NRS in the same

manner as in other SS footwall systems. This hypothesis brings into question the range in salinity and temperature required in the SS footwall to remobilize metals. While hypersaline fluids (≥35 wt. % equiv. NaCl) have been documented as the dominant metal transporting agents in SS footwall systems, fluids with much lower salinities have been shown to transport significant amounts of metals in other hydrothermal environments. For example, VMS-related hydrothermal fluids typically have salinities in the range of 4.2 to 21.3 wt. % equiv. NaCl (Shanks et al. 2012), and hydrothermal fluids circulating in porphyry systems have a range in salinity of 5 to 70 wt. % equiv. NaCl (John et al. 2010). Furthermore, geochemical reaction calculations show that fluids with seawater or higher salinity can transport metals and sulfides at temperatures above 200°C (Shanks et al. 2012) suggesting that, while the dominant mineralizing fluids in SS footwall systems have high salinities, extremely elevated fluid salinities may not necessarily be required for metal transport in the SS footwall.

The absence of evidence for high temperature, high salinity fluids at NRS also brings into question their source elsewhere in the SS footwall. Several studies have suggested that a high-salinity fluid was exsolved from crystallizing partial melts in the footwall that produced FWGR (Molnár et al. 2001, Péntek et al. 2008, Péntek et al. 2013). Péntek et al. (2013) speculated that these partial melts contributed significant volumes of saline fluids to the hydrothermal system driven by the cooling SIC. It is suggested that the high salinity of this fluid was a dominant source of cations to the hybrid hydrothermal fluid, providing the appropriate chemistry (ligands) to redistribute metals within the footwall environment. In other SS footwall systems containing FWGR, high temperature, hypersaline, multi-solid fluid inclusions are documented as being chemically and spatially related to FWGR bodies. At NRS, FWGR is distributed dominantly in

the contact zone and proximal footwall zone but, as outlined above, there is no evidence for the high temperature, hypersaline, multi-solid fluid inclusions. Miarolitic cavities in FWGR bodies at NRS provide evidence that there was some magmatic volatile exsolution, but a record of this fluid has not been preserved in inclusions. These observations bring into question the origin of the FWGR fluid and, on a larger scale, the mechanism by which FWGR originates. An alternative interpretation for the spatial association of FWGR and the high temperature, hypersaline, multi-solid fluid inclusions was presented by Hanley et al. (2011), who suggested that the timing of partial melt injection differed from the introduction of the mineralizing fluids. A possible explanation is that the partial melts in the footwall did not exsolve a significant volume of magmatic fluids, if at all, and the conduits formed from FWGR injection later acted as pathways for fluid infiltration. The volume and composition of the fluid transferred into the footwall along these FWGR pathways may have varied significantly between different footwall systems. In the case of NRS, either any fluid that may have migrated into the system along FWGR conduits has not been preserved as fluid inclusions or little to no fluid was introduced along these pathways.

4.6.4 Oxygen Isotopes and CL images

Oxygen isotope data for quartz has been proven to be a useful tool for characterizing hydrothermal processes, such as determining the composition of a reacting fluid or the temperature of reaction (Taylor 1979), calculating water to rock ratios (Larson and Taylor 1986), and mapping fluid flow in relict hydrothermal systems (Criss and Taylor 1986; Brauhart et al. 2000). However, these calculations are more useful if other factors pertaining to the system are known, such as modal mineralogy, whole rock oxygen isotope composition, and oxygen isotope

composition of unaltered minerals (e.g., feldspar, quartz). The NRS environment is composed of various lithologies that are present as individual units and as clasts within brecciated units, making it challenging to estimate the starting modal mineralogy and/or composition of a given sample. For this reason, whole rock oxygen isotopes cannot be accurately applied to this system and representative unaltered minerals are unidentifiable. Thus, the oxygen isotope values for individual quartz grains are examined and considered to be representative of the overall hydrothermal system at NRS.

Fluid inclusion microthermometric data indicates that end-member fluids available to the NRS hydrothermal system cannot account for the salinities and temperatures measured, and mixing of multiple end-member fluids likely occurred. Oxygen isotopes provide valuable information about the isotopic composition of the fluid(s) with which quartz equilibrated and can be used to determine fluid sources. There is an extreme range in oxygen isotope values for quartz at NRS (+5.6 to +12.4‰; Fig. 17), clearly showing that quartz has been re-equilibrated away from magmatic values (i.e., ~+8 to +10‰ in felsic rocks; Taylor 1968). The data are both enriched and depleted relative to these values, and this requires that more than one process altered the quartz isotopic compositions (e.g., fluid events, isotope resetting). There are two processes to enrich quartz isotopic values: (i) isotopic resetting via metamorphism; and (ii) interaction with an isotopically heavy fluid. Fluids with isotopic values heavy enough to increase the $\delta^{18}O$ values of quartz by up to 3‰ are typically metamorphic in origin, but there is no evidence that there was an abundance of such a fluid in the NRS system. Therefore, it is more likely that the increase in $\delta^{18}O$ values of quartz can be attributed to isotopic resetting by metamorphism. In order for the isotopic composition of quartz to be increased by up to 3‰, this isotopic resetting had to occur

prior to processes responsible for lowering the $\delta^{18}O$ values. It is therefore most likely that the increase in $\delta^{18}O$ values of quartz was due to contact metamorphism from the SIC aureole. This is further supported by the lack of zonation in quartz identified in CL images (Fig. 18), indicating that the quartz has not retained its magmatic characteristics.

Following isotopic resetting to enrich the $\delta^{18}O$ values of quartz, there was a process responsible for lowering the $\delta^{18}O$ values. This is most effectively achieved through fluid-mediated re-equilibration. The isotopic compositions of the available fluid reservoirs must be considered in order to determine the fluid(s) responsible for altering the isotopic composition of quartz. As outlined above, metamorphic fluids are isotopically heavy and this fluid type could therefore not have decreased the $\delta^{18}O$ values of quartz. For groundwater, Frape and Fritz (1982) calculated the $\delta^{18}O$ values in Sudbury to be -11.0 to -13.4‰ in the NR footwall and -10.3 to -12.8‰ in the SR footwall.

In order to calculate how this fluid would have affected the isotopic composition of quartz, the NR values are used because of the similarities in rock types for between the NR and ER and the lesser effect of post-SIC regional deformation and metamorphism in the NR (e.g., Card et al. 1984; Bailey et al. 2004). We use a reaction temperature of 460°C represented by the trapping temperature for type 3 fluid inclusions (Fig. 19) and have applied the oxygen isotope calculations of Zhang et al. (1989). For a $\delta^{18}O$ fluid composition of -11.0‰ the resulting quartz $\delta^{18}O$ values would be ~-7.2‰, and for a $\delta^{18}O$ fluid composition of -13.4‰ the resulting quartz $\delta^{18}O$ values would be -9.6‰. Both of these $\delta^{18}O$ values for quartz are significantly lighter than what is recorded at NRS. The isotope fractionation between quartz and the fluid increases with

decreasing temperature, and for a fluid temperature of 250°C the $\delta^{18}O$ values for quartz would range from -4.6 and -2.2‰, whereas at ~100°C, the resulting $\delta^{18}O$ values of quartz would range from +9.7 to +7.2. Although the $\delta^{18}O$ values for quartz at a reaction temperature of 100°C are similar to those recorded at NRS, it is not actually possible to modify quartz in this manner at such low temperatures (Matthews and Beckinsale 1979). It is noted that this calculation assumes that the isotopic range for groundwater was similar in the ER as in the NR, but it has been shown that groundwaters may be isotopically distinct over short distances. For example, Frape and Fritz (1987) provided data showing a difference up to ~+2‰ on either side of a major fault, indicating that these local controls have substantially altered compositions of groundwater in the Sudbury environment. These fluids may become isotopically distinct if isolated for a long period of time. For example, a volume of fluid that has been trapped or migrated through mafic gneiss would have a slightly different $\delta^{18}O$ value than a fluid in a fracture that is in equilibrium with granite or felsic gneiss. It is therefore possible that the isotopic composition of ER groundwater is significantly different from the NR, though this cannot be shown and this is not the case for the NR in comparison with the SR.

With respect to the isotopic composition of magmatic fluids, Tuba (2012) used the $\delta^{18}O$ composition of a fluid in equilibrium with epidote hosted in FWGR bodies at Amy Lake (ER), calculated to be +0.7 to +6.3‰ using the method of Zheng (1993), to represent the SIC-derived fluid. If we use this fluid composition to represent the composition of magmatic fluid in the NRS hydrothermal system, corresponding quartz compositions would be +4.5‰ to +10.2‰ at 410°C and +9.6 to +15.3‰ at 250°C. These quartz values are similar to what is recorded at NRS, but it is difficult to determine how much fluid was exsolved from the SIC and if it was volumetrically

significant enough to alter host rocks into the proximal footwall zone. Additionally, if this fluid mixed with shield brines, it would become significantly isotopically depleted. Therefore the most likely processes responsible for producing the observed $\delta^{18}O$ values and CL results for quartz are isotopic resetting during contact metamorphism followed by heterogeneous re-equilibration with a dominantly magmatic fluid in order to lower the $\delta^{18}O$ values and preserve some of the metamorphic quartz values.

The large variation (up to 3.1‰) in $\delta^{18}O$ values observed within single grains of quartz that do not show textural features of heterogeneous re-equilibration (e.g., dendritic fracture networks, changes in CL signal) is noteworthy. Wide ranges in primary $\delta^{18}O_{quartz}$ values for a single quartz crystal are thought to reflect a change in either the fluid composition or precipitation temperature during quartz precipitation if under equilibrium conditions (Taylor 1974). These changes can be reflected in features such as oscillatory or sector zoning in quartz crystals and a range in $\delta^{18}O_{quartz}$ values of up to 12.4 ± 0.3‰ within a single crystal has been attributed to this process (Tanner et al. 2013). Though typically associated with euhedral quartz in igneous rocks, zoning features are also documented in euhedral hydrothermal quartz (Penniston-Dorland 2001, Rusk et al. 2008, Jourdan et al. 2009, Muller et al. 2010, Tanner et al. 2013). However, evidence for zoning features is not observed in quartz from NRS, suggesting that the large range in $\delta^{18}O_{quartz}$ values is likely the result of post-crystallization processes that altered primary $\delta^{18}O_{quartz}$ values.

4.6.5 Additional constraints on fluid chemistry

Another means of understanding fluid mixing is through examination of the solute compositions of each fluid type. Evaporate mound data show a range in Ca:Na for each sample and in each

zone. This chemical range further supports a mixing of two fluids, but also allows us to qualitatively constrain the proportion of each fluid contributing to the hybrid fluid. Calcium to sodium ratios are useful in understanding these fluids due to the differences in fluid compositions, specifically between SIC-driven magmatic fluids with low Ca:Na (<<1) and groundwater with high Ca:Na ratio (~>1; Frape and Fritz 1982). Therefore, if the hydrothermal fluid was dominated by groundwater, we would expect the evaporate mound data to plot further towards the Ca apex on a Na-Ca-K ternary diagram (Fig. 16). Instead, there is little spread towards Ca and most of the data plots close to the Na apex, which is expected for a magmatic-dominated fluid. This is consistent with the isotope data that indicates the hydrothermal fluid was not dominated by groundwater. The limited spread towards Ca that is observed could be explained by mixing with a small proportion of groundwater; however, the Ca:Na ratio of the evaporate mounds is lower in the distal footwall zone than in the proximal footwall zone. If we assume a simple mixing model between magmatic fluids from the SIC region and groundwater from the deep footwall, we expect the distal samples to exhibit a stronger groundwater signature and therefore a larger Ca:Na ratio.

Alternatively, Ca in the hydrothermal fluid may be derived from pervasive equilibration of the fluid with plagioclase. There is sufficient evidence for this re-equilibration given the near end-member albitic composition and pitted texture of plagioclase observed throughout the NRS system. Therefore, evaporate mound data indicate that there was likely only a minor contribution of groundwater to the hybrid hydrothermal fluid and equilibration of the fluid with plagioclase provided a source of Ca.

4.6.6 Evidence for multiple fluid sources

Microthermometric and oxygen isotopic data indicate that a hybrid fluid produced by variable mixing of end-member fluids and dominated by magmatic fluids likely contributed to the hydrothermal system at NRS. Evidence for multiple fluid sources is also explored using epidote mineral chemistry. Five textural varieties and three distinct REE patterns of epidote were identified. The REE data for epidote in the NRS system reflects the effects of multiple fluid events and/or sources, and this is consistent with the fluid inclusion and oxygen isotopic data.

The REE pattern for epidote type 1_{REE} is strongly fractionated with a positive Eu anomaly. A possible process to generate this pattern is interaction with felsic (e.g., CBF) rocks containing plagioclase, with saussuritization of plagioclase providing a source for the Eu enrichment. Orthomagmatic fluids have been proposed as the source of saussuritization in the overlying granophyre unit (see Chapter 3), and it is possible that this is also the case at NRS. Therefore, it is possible that the fluid associated with the type 1_{REE} epidote was sourced at the SIC contact from SIC-derived orthomagmatic fluids. This is also consistent with the distribution of type 1_{REE} epidote, as it is the only chemical variation of epidote documented in the contact zone. This is especially significant because it is the only chemical variety of epidote associated with mineralization, and may indicate that fluids originating from the SIC were responsible for metal remobilization into the footwall. Furthermore, removal of Eu from plagioclase to produce the observed Eu anomaly in epidote type 1_{REE} requires that Eu remain in a reduced state (i.e., 2+) in order to promote Ca^{2+} exchange in plagioclase. The fluid may have remained reduced by maintaining equilibrium with sulfides, supporting the relationship between this fluid and sulfides and its derivation from the contact zone, where sulfides are the most abundant. Furthermore, this

chemical variety of epidote is the most common and is the only one present in all three zones at NRS. This may indicate that the fluid from which this chemical variety of epidote was formed was pervasive and a significant component of the NRS hydrothermal system. This is consistent with the fluid inclusion and oxygen isotopic data, which indicates that the hybrid fluid present at NRS was dominated by magmatically-derived fluids. This also indicates that fluids associated with ore bodies at the contact circulated several hundreds of metres into the footwall.

The model proposed above for the source of fluids that produced epidote type 1_{REE} requires a source for Ca in the fluid because magmatic fluids are characterized by low Ca concentrations. A magmatic fluid exsolved at high temperatures would be capable of producing rapid albitization of plagioclase resulting in Ca enrichment in the residual fluid. As previously stated, the measured temperature for magmatic fluids exsolved from footwall melts is approximately 500°C (Hanley et al. 2011) and the minimum temperature of a magmatic fluid exsolved directly from the mafic basal units of the SIC at pressures appropriate for the NRS system is approximately 950°C. Furthermore, the high temperature required for rapid albitization to occur suggests that this process happened early in the hydrothermal history when fluid temperatures were high due to the cooling SIC. It is noted, however, that if this process were responsible for Ca enrichment, the fluid must still have cooled prior to trapping in order to account for the lower temperatures of all fluid inclusion types observed at NRS(i.e., 220° to 300°C for types 1 and 2; ~460°C for type 3). If high temperature magmatic fluids are associated with mineralization, this suggests that metal mobility was also likely early due to the dependence of Cu solubility on temperature (e.g., Lydon 1988; Landtwing et al. 2005).

The REE pattern for epidote type 2_{REE} is characterized by weakly fractionated REEs with no Eu anomaly. This may indicate either that the fluid did not interact with plagioclase or possibly that the fluid was oxidized, not allowing for Eu^{2+} exchange with Ca^{2+} in plagioclase. It is also possible that the fluid was too low temperature to react with plagioclase (i.e., saussuritization). The type 3 REE pattern shows slight LREE enrichment, a fractionated HREE pattern, and a variable Eu anomaly. This REE pattern is similar to the type 2 pattern but lacks the HREE. It is therefore possible that the fluids responsible for this epidote type was derived at or near the basal SIC contact where garnet, a key constituent of altered contact-style ore bodies ("epidote zones"; Farrow and Watkinson 1996), could have removed or consumed the HREEs; however, this epidote chemical variety is not observed in the contact zone. Both epidote type 2_{REE} and 3_{REE} are only present in the proximal and distal footwall zones of NRS and are much less common than epidote type 1_{REE}. The source of these fluids is unclear from the epidote chemical data, but these fluids do not appear to be dominant components of the NRS hydrothermal system. The presence of these epidote chemical varieties does indicate that the fluid history at NRS is complex and involved multiple fluid sources.

The textural relationship to the REE pattern of epidote is also of interest. As was discussed above, type 1_{REE} epidote occurs in all textural types, type 2_{REE} epidote occurs only in epidote textural varieties 2 and 4, and type 3_{REE} epidote occurs only in textural variety 4. There are no samples where cross-cutting relationships of the epidote chemical types are observed, and the paragenesis of the epidote textural types is variable. It is also noteworthy that epidote textural variety 4 exhibits all 3 REE patterns. These data suggest that several textural varieties of epidote precipitated from the same fluid(s), that there is a relationship between type 1_{REE} epidote and

mineralization, and there is evidence for possible mixing of fluids due to the similarities between types 2_{REE} and 3_{REE} epidote. Metal concentrations do not correlate with textural variety and are not enriched in any epidote type unless it is in close proximity to mineralization (i.e., vein selvage or disseminated within sulfides).

Chemical data of other hydrosilicate phases within the alteration history are not as clear. The mineral paragenesis described in the results shows that the alteration history was complex, with certain assemblages (i.e., epidote + chlorite + amphibole) related to mineralization and other mineral assemblages unrelated to mineralization. This history is further complicated by multiple generations and styles of alteration phases (i.e., epidote, chlorite, amphibole). Only weak mineral-chemical correlations were identified and, where present, were unrelated to location in the NRS system. For example, disseminated chlorite exhibited the highest Fe# in the proximal footwall zone compared to the contact zone and distal footwall zone. There is also a slight increase in CaO/FeO in epidote from the contact zone to the proximal footwall zone and distal footwall zone. However, mineral chemistry cannot be used to distinguish mineralized and barren samples alone but the variability in chemistry also supports a complex hydrothermal history.

4.6.7 Comparison to mineralized and barren systems

The results presented for the hydrothermal system at NRS suggest that there are fundamental differences between the mineralizing environment at NRS and other SS footwall deposits. These differences may only be a reflection of variations in the preservation of mineralizing fluids as inclusions or they may be the result of variations in the composition and characteristics of the mineralizing fluids. A key difference between the environment at NRS and other SS footwall

systems is the geographic location, with NRS being located in the ER and all other documented footwall deposits being located in the NR or SR. Comparison of the NRS system to other ER footwall systems is difficult due to the small number of deposits and showings in the ER and the limited work done on these systems. A useful comparison to NRS is the Amy Lake showing, as it is also located in the ER of the SS and only ~7 km northwest of NRS. Tuba et al. (2014) performed a small fluid inclusion study at Amy Lake but comparison with this study for the purpose of determining geographic controls on SS footwall hydrothermal fluids may be misleading, as much of the microthermometric data was supplemented with results from the Wisner area in the NR. In order to assess the geographic controls on hydrothermal fluids in the SS footwall, more detailed fluid inclusion studies must be carried out on the other deposits and showings in the ER.

Results from the fluid inclusion study at NRS were also compared to the granophyre unit of the SIC – the uppermost portion of the crystallized SIC melt sheet and a unit barren of mineralization. Of significant interest is the striking similarity of fluid inclusion types identified in the granophyre unit to NRS. Three fluid inclusion types were identified in the granophyre unit (see Chapter 3): (i) type 1 L + V aqueous inclusions with an average salinity of 21 wt. % equiv. NaCl and trapping temperatures ranging from 405° to 430°C. ii) type 2 L + V aqueous inclusions with salinities of 20 to 24 wt. % equiv. NaCl and trapping temperature ranging from 168° to 218°C; and (iii) type 3 L + V + H inclusions with salinities of 30 to 34 wt. % equiv. NaCl and trapping temperatures 165° to 209°C. Type 1 fluid inclusions in the granophyre unit are very similar to type 3 fluid inclusions at NRS, whereas types 2 and 3 fluid inclusions in the granophyre are very similar to NRS fluid inclusion types 1 and 2, respectively. However,

decrepitate mound data for the granophyre unit indicate a much higher Ca content in the granophyre fluids (Fig. 16). Additionally, quartz $\delta^{18}O$ values for the granophyre unit are higher than at NRS overall (+6.9 to +14.8, mean 11.0 ±2.3 for the granophyre unit; +5.6 to +12.4, mean 8.9 ±1.7 for NRS), suggesting that the granophyre unit interacted and re-equilibrated with a lower temperature fluid for a longer period of time than the host rocks to NRS. Therefore, while the two systems share similarities, these appear to be mostly due to the common heat source for both hydrothermal systems, that being the cooling SIC.

4.6 Conclusions

Combined results from the mineralogical, mineral-chemical, fluid inclusion, isotopic, CL, and evaporate mound data indicate that the hydrothermal history of NRS is complex and likely involved multiple fluid sources. There is a relationship between mineralization and hydrothermal alteration, suggesting that there is a hydrothermal component to the mineralized zones. The fluid responsible for remobilizing metals from the SIC contact into the footwall appears to be dominated by orthomagmatic fluids derived at or near the contact, and these fluids circulated up to several hundred metres into the footwall. Fluid inclusion data indicates that the orthomagmatic fluids likely mixed with one or a combination of groundwater and metamorphic fluids, resulting in a dilution of the fluids prior to trapping. Furthermore, two trapping events of this hybrid fluid occurred, with the first ~460°C and the second between 220° to 340°C. The composition of the mineralizing fluid at NRS as reflected by fluid inclusions remains ambiguous; however, the absence of high-T multi-phase fluid inclusions identified in other mineralized footwall zones suggests that this fluid type was not the mobilizing agent for metals at NRS. These inclusions are inferred to be primary in the deposits where they are found; however insufficient evidence has

been provided to substantiate these interpretations (i.e., CL imaging showing inclusions along growth zones in quartz). The absence of these inclusions at NRS brings into question the necessity or role of these fluids in ore remobilization.

4.7 References

Ames, D. E. and Kjarsgaard, I. M. (2013): Sulfide and alteration mineral chemistry of low- and high-sulfide Cu-PGE-Ni deposits in the footwall environment, Sudbury, Canada. Geological Survey of Canada Open File 7331.

Ames, D. E., and Farrow, C. E. G.(2007): Metallogeny of the Sudbury Mining Camp, Ontario, in Goodfellow, W. D., ed., Mineral Deposits of Canada: A Synthesis of Major Deposit-Types, District Metallogeny, the Evolution of Geological Provinces, and Exploration Methods: Geological Association of Canada, Mineral Deposits Division, Special Publication 5, 329-350.

Ames, D. E., Davidson, A., and Wodicka, N. (2008): Geology of the Giant Sudbury Polymetallic Mining Camp, Ontario, Canada. Economic Geology 103, 1057-1077.

Bailey, S. W. (1984): Classification and structures of the micas. In Micas (ed. S. W. Bailey) Reviews in Mineralogy and Petrology 13, 1-12.

Bailey, J., Lafrance, B., McDonald, A. M., Fedorowich, J. S., Kamo, S., and Archibald, D. A. (2004): Mazatzal-Labradorian age (1.7-1.6 Ga) ductile deformation of the South Range Sudbury impact structure at the Thayer Lindsley mine, Ontario. Canadian Journal of Earth Sciences 41, 1491-1505.

Boast, M. and Spray, J. G. (2006): Superimposition of a thrust-transfer fault system on a large impact structure: implications for Ni-Cu-PGE exploration at Sudbury. Economic Geology 101, 1583-1594.

Bodnar, R. J. (1994): Synthetic fluid inclusions: XII. The system H2O-NaCl. Experimental determination of the halite liquidus and isochores for a 40 wt. % solution. Geochimica et Cosmochimica Acta 58, 1053-1063.

Bodnar, R. J. (2003): Introduction to aqueous fluid systems. In Samson, A., Anderson, A., and Marshall, D., eds, Fluid Inclusions L Analysis and Interpretation. Mineralogical Association of Canada Short Course 32, 81-99.

Bodnar, R. J. and Vityk, M. O. (1994): Interpretation of microthermometric data for H2O-NaCl fluid inclusions. In De Viro, B. and Frezzotti, M. L., eds., Fluid Inclusions in Minerals, Methods and Applications. Virginia Tech, Blacksburg, Virginia, 117-130.

Brauhart, C. W., Huston, D. L., and Andrew, A. S. (2000): Oxygen isotope mapping in the Panorama VMS district, Pilbara Craton, Western Australia: applications to estimating temperatures of alteration and to exploration. Mineralium Deposita 35, 727-740.

Brocoum, S. T. and Dalziel, I. W. D.(1974): The Sudbury Basin, the Southern Province, the Grenville Front and the Penokean Orogeny. Geological Society of America Bulletin 85, 1571-1580.

Brown, M. (1993): P-T-t evolution of orogenic belts. Journal of the Geological Society, London 150, 227-241.

Campos-Alvarez, N. O., Samson, I. M., Fryer, B. J., and Ames, D. E. (2010): Fluid sources and hydrothermal architecture of the Sudbury Structure: constraints from femtosecond LA-

ICP-MS Sr isotopic analysis of hydrothermal epidote and calcite. Chemical Geology 278, 131-150.

Card, K. D. (1978): Geology of the Sudbury-Manitoulin area, districts of Sudbury and Manitoulin. Ontario Geological Survey Report 166, p. 238.

Card, K. D., Gupta, V. K., McGrath, P. H. and Grant, F. S.(1984): The Sudbury Structure: Its regional Geological and Geophysical Setting: The Geology and Ore Deposits of the Sudbury Structure. O.G.S. Special Volume 1, 25-44.

Carter, W.M., Watkinson, D.H., Ames, D.E., and Jones, P.C. (2009): Emplacement of Quartz Dioritic Magmas and Cu–(Ni)–PGE Mineralization of the Whistle Offset, Sudbury Canada. Geological Survey of Canada Open File 6134, CD-Rom.

Coats, C. J. A. and Snajdr, P. (1984): Ore Deposits of the North Range, Onaping-Levack area, Sudbury, in The Geology and Mineral Deposits of the Sudbury Structure, eds. E. G. Pye, A. J. Naldrett, P. Giblin. Ontario Geological Survey, Special Publication 1, 328-346.

Criss, R. E. and Taylor, H. P. (1986): Meteoric-hydrothermal systems. *In* Stable isotopes in high temperature geological processes. *Eds*. Valley, J. W., Taylor, H. P., and O'Neil, J. R., Mineralogical Society of America, Washington D. C. Reviews in Mineralogy 16, 373-424.

Davis, D. W., Lowenstein, T. K., and Spencer, R. J. (1990): Melting behavior of fluid inclusions in laboratory-grown halite crystals in the systems NaCl-H_2O, NaCl-KCl-H_2O, NaCl+$MgCl_2$-H_2O, and NaCl-$CaCl_2$-H_2O. Geochimica et Cosmochimica Acta 54, 591-601.

Deer, W. A., Howie, R. A., and Zussman, J. (1966): An introduction to the rock-forming minerals. Longman, London, 528 p.

Dence, M.R., and Popelar, J. (1972): Evidence for an impact origin for Lake Wanapitei, Ontario. Geological Association of Canada Special Papers 10, 117–124.

Dressler, B. O. (1984): General Geology of the Sudbury Area, in The Geology and Mineral Deposits of the Sudbury Structure, eds. E. G. Pye, A. J. Naldrett, P. Giblin, Ontario Geological Survey, Special Publication 1, 57-82.

Farrow, C. E. G. (1994): Geology, alteration, and the role of fluids in Cu-Ni-PGE mineralization of the footwall rocks to the Sudbury Igneous Complex, Levack and Morgan Townships, Sudbury District, Ontario. Unpublished Ph.D. thesis, Carleton University, Ottawa, Canada, 373 p.

Farrow, C. E. G. and Watkinson, D. H. (1992): Alteration and the role of fluids in Ni, Cu and Platinum-group element deposition, Sudbury Igneous Complex Contact, Onaping-Levack area, Ontario. Mineralogy and Petrology 46, 67-83.

Farrow, C. E. G. and Watkinson, D. H. (1996): Geochemical evolution of the Epidote Zone, Fraser Mine, Sudbury, Ontario: Ni-Cu-PGE remobilization by saline fluids. Exploration and Mining Geology 5, 17-31.

Farrow, C. E. G., Everest, J. O., King, D. M., and Jolette, C. (2005): Sudbury Cu(-Ni)-PGE systems: refining the classification using McCreedy West Mine and Podolsky Project case studies. In: Mungall, J. E. (ed.) Mineral Association of Canada Short Course 35, 163-180.

Frape, S. K., and Fritz, P.(1982): The chemistry and isotopic composition of saline groundwaters from the Sudbury Basin, Ontario. Canadian Journal of Earth Sciences 19, 645-661.

Frape, S.K. and Fritz, P. (1987): Geochemical trends for groundwaters from the Canadian Shield. In: Fritz, P., Frape, S.K. (Eds.), Saline Waters and Gases in Crystalline Rocks. Geological Association of Canada, Special Paper, 33, 19–38.

Goldstein, R. (2003): Petrographic analysis of fluid inclusions. In: Samson, I., Anderson, A., and Marshall, D. (eds) Fluid inclusions: analysis and interpretation. Mineralogical Association of Canada Short Course 32, 9-54.

Grasby, S. E., Allen, D. M., Bell, S., Chen, Z., Ferguson, G., Jessop, A., Kelman, M., Ko, M., Majorowicz, J., Moore, M., Raymond, J., and Therrien, R. (2012): Geothermal Energy Resource Potential of Canada. Geological Survey of Canada Open File 6914, 301 p.

Hanley, J. J. and Mungall, J. E. (2003): Chlorine enrichment and hydrous alteration of the Sudbury breccia hosting footwall Cu-Ni-PGE mineralization at the Fraser mine, Sudbury, Ontario, Canada. The Canadian Mineralogist 41, 857-881.

Hanley, J. J., Ames, D. E., Barnes, J., Sharp, Z., and Guillong, M. (2011): Interaction of magmatic fluids and silicate melt residues with saline groundwater in the footwall of the Sudbury Igneous Complex, Ontario, Canada: new evidence from bulk rock geochemistry, fluid inclusions and stable isotopes. Chemical Geology 281, 1-25.

Hanley, J. J., Mungall, J. E., Bray, C. J., and Gorton, M. P. (2004): The origin of bulk and water-soluble Cl and Br enrichments in ore-hosting Sudbury breccia in the Fraser Copper zone, Strathcona embayment, Sudbury Ontario, Canada. The Canadian Mineralogist 42, 1777-1798.

Hanley, J. J., Mungall, J. E., Pettke, T., Spooner, E. T. C., and Bray, C. J. (2005): Ore metal redistribution by hydrocarbon-brine and hydrocarbon-halide melt phases, North Range footwall of the Sudbury Igneous Complex, Ontario, Canada. Mineralium Deposita 40, 237-256.

Hanley, J.J. and Bray, C. J. (2009): The trace metal content of amphibole as a proximity indicator for Cu-Ni-PGE mineralization in the footwall of the Sudbury Igneous Complex, Ontario, Canada. Economic Geology 104, 113-125.

Haynes, F. M., Sterner, S. M., and Bodnar, R. J.(1988): Synthetic fluid inclusions in natural quartz. IV. Chemical analyses of fluid inclusions by SEM/EDA: evaluation of method. Geochimica et Cosmochimica Acta 52, 969-977.

Hoffman, P. F.(1989): Precambrian geology and tectonic history of North America; in The geology of North America – An overview: eds. Bailey, A. W., and Palmer, A. R. Geological Society of America, Geology of North America, 447-512.

Jago, B. C., Morrison, G. G., and Little, T. L. (1994): Metal zonation patterns and microtextural and micromineralogical evidence for alkali- and halogen-rich fluids in the genesis of the Victor Deep and McCreedy East footwall copper orebodies, Sudbury Igneous Complex, in: Lightfoot, P. C., and Naldrett, A. J. (eds.) Proceedings of the Sudbury-Noril'sk Symposium. Ontario Geological Survey Special volume 5, 65-75.

James, R. S., Peredery, W., and Sweeny, J. M . (1992): Thermobarometric studies on the Levack gneisses – Footwall rocks to the Sudbury Igneous Complex. International Conference on Large Meteorite Impacts and Planetary Evolution Abstracts, Canada. August 31 to September 2 1992, p. 41.

John, D. A., Ayuso, R. A., Barton, M. D., Blakley, R. J., Bodnar, R. J., Dilles, J. H., Gray, Floyd, Graybeal, F. T., Mars, J. C., McPhee, D. K., Seal, R. R., Taylor, R. D., and Vikre, P. G. (2010): Porphyry copper deposit model, chapter B of Mineral deposit models for resource assessment. United States Geological Survey Scientific Investigations Report, 169 p.

Jourdan, A., Venneman, T., Mullis, J., and Ramseyer, K. (2009): Oxygen isotope sector zoning in natural hydrothermal quartz. Mineralogical Magazine 73, 615–632.

Kerr, M., Hanley, J. Morrison, G., Everest, J., and Bray, C. (2015): Preliminary evaluation of trace element hydrocarbon speciation and abundance as an exploration tool for footwall-style sulfide ores associated with the Sudbury Igneous Complex, Ontario, Canada. Economic Geology 110, 531-556.

Kontak, D. J. (2004): Analysis of evaporate mounds as a complement to fluid-inclusion thermometric data: case studies from granitic environments in Nova Scotia and Peru. The Canadian Mineralogist 42, 1315-1329.

Kontak, D. J. (2013): Fluid inclusion evaporate mound analysis: A rapid, efficient and informative means of determining fluid chemistry in hydrothermal systems. Atlantic Geology 49, 34.

Krough, T. E. (1994): Precise U-Pb ages for Grenvillian and pre-Grenvillian thrusting of Proterozoic and Archean metamorphic assemblages in the Grenville Front tectonic zone, Canada. Tectonics 13, 963-982.

Lafrance, B., Legault, D. and Ames, D. E.(2008): The formation of the Sudbury breccia in the North Range of the Sudbury impact structure. Precambrian Research 165, 107-119.

Landtwing, M. R., Pettke, T., Halter, W. E., Heinrich, C. A., Redmond, P. B., Einaudi, M. T., and Kunza, K. (2005): Copper deposition during quartz dissolution by cooling magmatic-hydrothermal fluids: The Bingham porphyry. Earth and Planetary Science Letters 235, 229-243.

Larson, P. B. and Taylor, H. P. (1986): An oxygen-isotope study of water-rock interaction in the granite of Cataract Gulch, western San Juan Mountains, Colorado. Geological Society of America Bulletin 97, 505-515.

Leake, B. E., Woolley, A. R., Arps, C. E. S., Birch, W. D., Gilbert, M. C., Grice, J. D., Hawthorne, F. C., Kato, A., Kisch, H. J., Krivovichev, V. G., Linthout, K., Laird, J., Mandarino, J. A., Maresch, W. V., Nickel, E. H., Rock, N. M. S., Schumacher, J. C., Smith, D. C., Stephenson, N. C. N., Ungaretti, L., Whittaker, E. J. W., and Youzhi, G. (1997): Nomenclature of amphiboles: Report of the Subcommittee on Amphiboles of the International Mineralogical Association, Commission on New Minerals and Mineral Names. American Mineralogist 82, 1019-1037.

Li, C. (1992): Quantitative model for the formation of sulfide ores at Sudbury and a study on the distributions of platinum-group elements in the Strathcona copper-rich zones, Sudbury, Ontario. Unpublished Ph.D. thesis, University of Toronto, Toronto, 436 p.

Li, C. and Naldrett, A.J. (1993): High chlorine alteration minerals and calcium-rich brines in fluid inclusions from the Strathcona Deep Copper zone, Sudbury, Ontario. Economic Geology 88, 1780–1796.

Lightfoot, P. C. and Farrow, C. E. (2002): Geology, geochemistry and mineralogy of the Worthington Offset Dike: a genetic model for offset dike mineralization in the Sudbury Igneous Complex. Economic Geology 97, 1419-1446.

Lightfoot, P. C., Doherty, W., Farrell, K., Keays, R. R., Moore, M. and Pekeski, D. (1997): Geochemistry of the main mass, sublayer, offsets, and inclusions from the Sudbury Igneous Complex, Ontario. Ontario Geological Survey, Open File Report 5959, 231.

Lightfoot, P. C., Keays, R. R., and Doherty, W. (2001): Chemical evolution and origin of nickel sulfide mineralization in the Sudbury Igneous Complex, Ontario, Canada. Economic Geology 96, 1855-1875.

Lydon, J. W. (1988): Ore Deposit Models #14. Volcanogenic Massive Sulphide Deposits Part 2: Genetic Models. Geoscience Canada 15, 43-65.

Magyarosi, Z., Watkinson, D. H., and Jones, P. C. (2002): Mineralogy of Ni-Cu-Platimun-group element sulfide ore in the 800 and 810 orebodies, copper cliff south mine, and P-T-X conditions during the formation of platinum-group minerals. Economic Geology 97, 1471-1486.

Marshall, D., Watkinson, D. H., Farrow, C. E. G., Molnár, F., and Fouillac, A.-M. (1999): Multiple fluid generations in the Sudbury Igneous Complex: fluid inclusion, Ar, O, H, Rb and Sr evidence. Chemical Geology 154, 1-19.

Matthews, A. and Beckinsale, R. D. (1979): Oxygen isotope equilibration systematics between quartz and water. American Mineralogist 64, 232-240.

McCormick, K. A. and McDonald, A. M. (1999): Chlorine-bearing amphiboles form the Fraser Mine, Sudbury, Ontario, Canada: description and crystal chemistry. The Canadian Mineralogist 37, 1385-1403.

McCormick, K.A., Lesher, C.M., McDonald, A.M., Fedorowich, J.S., and James, R.S. (2002b): Chlorine and Alkali Geochemical halos in the footwall breccia and Sublayer norite at the margin of the Strathcona embayment, Sudbury Structure, Ontario. Economic Geology 97, 1509–1519.

McLean, S. A., Straub, K. H., and Stevens, K. M. (2005): The discovery and characterization of the Nickel Rim South Deposit, Sudbury, Ontario. Mineralogical Association of Canada Short Course 35, 359-368.

Molnár, F. and Watkinson, D.H. (2001): Fluid-inclusion data for vein type Cu–Ni–PGE footwall ores and their use in establishing an exploration model for hydrothermal PGE-enrichment around mafic ultramafic intrusions. Exploration and Mining Geology 10, 125–141.

Molnár, F., Watkinson, D. H., Jones, P. C., and Gatter, I. (1997): Fluid inclusion evidence for hydrothermal enrichment of magmatic ore at the contact zone of the Ni-Cu-platinum group element 4b deposits, Linsley mine, Sudbury, Canada. Economic Geology 92, 674-685.

Molnár, F., Watkinson, D.H., Everest, J.O. (1999): Fluid–inclusion characteristic of hydrothermal Cu–Ni–PGE veins in granitic and metavolcanic rocks at the contact of the Little Stobie Deposit, Sudbury, Canada. Chemical Geology 154, 279–301.

Molnár, F., Watkinson, D.H., Jones, P.C. (2001): Multiple hydrothermal processes in footwall units of the North Range, Sudbury igneous complex, Canada, and implications for the genesis of vein-type Cu–Ni–PGE deposits. Economic Geology 96, 1645–1670.

Morrison, G. G., Jago, B. C., and White, T. L. (1994): Footwall mineralization of the Sudbury Igneous Complex, in: Lightfoot, P. C., Naldrett, A. J. (eds.) Proceedings of the Sudbury-Noril'sk symposium. Ontario Geological Survey Special Volume 5, 57-64.

Mukwakwami, J., Lafrance, B., and Lesher, C. M. (2012): Back-thrusting and overturning of the Southern Margin of the 1.85 Ga Sudbury Igneous Complex at the Garson Mine, Sudbury Ontario. Precambrian Research 196-197, 81-105

Muller, A., Herrington, R., Armstrong, R., Seltmann, R., Kirwin, D. J., Stenina, N. G., and Kronz, A. (2010): Trace elements and cathodoluminescence of quartz in stockwork veins of Mongolian porphyry-style deposits. Miner Deposita 45, 707–727.

Naldrett, A. J. and Kullerud, G. (1967): A study of the Strathcona mine and its bearing on the origin of nickel-copper ores in the Sudbury district, Ontario. Journal of Petrology 8, 453-531.

Naldrett, A. J. and Hewins, R. H. (1984): The Main Mass of the Sudbury Igneous Complex, in The Geology and Mineral Deposits of the Sudbury Structure, eds. E. G. Pye, A. J. Naldrett, P. Giblin. Ontario Geological Survey, Special Publication 1, 235-251.

Nelles E.W., Lesher C.M., and Lafrance, B. (2010): Mineralogy and textures of Cu–PPGE–Au-rich mineralization in the Morrison (Levack footwall) Deposit, Sudbury, Ontario (abs). SEG 2010 Conference, 2010, Keystone, USA Pearson 1985.

O'Callaghan, J. W., Osinski, G. R., Lightfoot, P. C., Linnen, R. L., and Weirich, J. R. (2016): Reconstructing the Geochemical Signature of Sudbury Breccia, Ontario, Canada: Implications for Its Formation and Trace Metal Content. Economic Geology 111, 1706-1729.

Pearson Jr., F. J. (1987): Geochemical and Isotopic Evidence on the Origin of Brines in the Canadian Shield. Report by INTERA Technologies, Inc., Texas for Atomic Energy of Canada, Ltd., Pinawa, Manitoba.

Penniston-Dorland, S. (2001): Illumination of vein textures in a porphyry copper ore deposit using scanned cathodoluminescence: Grasberg Igneous Complex, Irian Jaya, Indonesia. American Mineralogist 86, 652–666.

Péntek, A., Molnár F., Watkinson, D.H., Jones, P.C., and Mogessie, A. (2009): Partial melting and melt segregation in footwall units within the contact aureole of the Sudbury Igneous Complex (North and East Ranges, Sudbury structure), with implications for their relationship to footwall Cu-Ni-PGE mineralization. International Geology Review 53, 291–325.

Péntek, A., Molnár, F., Tuba, G., Watkinson, D. H., and Jones, P. C. (2013): The significance of partial melting processes in hydrothermal low sulfide Cu-Ni-PGE mineralization within the footwall of the Sudbury Igneous Complex, Ontario, Canada. Economic Geology 108, 59-78.

Péntek, A., Molnár, F., Watkinson, D. G., Jones, P. C., and Mogessie, A. (2011): Partial melting and melt segregation in footwall units within the contact aureole of the Sudbury Igneous Complex (North and East Ranges, Sudbury structure), with implications for their relationship to footwall Cu-Ni-PGE mineralization. International Geology Review 53, 291-325.

Péntek, A., Molnár, F., Watkinson, D. H., and Jones, P. C. (2008): Footwall-type Cu-Ni-PGE mineralization in the Broken Hammer Area, Wisner Township, North Range, Sudbury Structure. Economic Geology 103, 1005-1028.

Putnis, A. (2002): Mineral replacement reactions: from macroscopic observations to microscopic mechanisms. Mineralogical Magazine 66, 689-708.

Riciputi, L. R., Patterson, B., and Ripperdam, R. L.(1998): Measurement of light stable isotope ratios by SIMS: matrix effects for oxygen, carbon and sulfur isotopes in minerals. International Journal of Mass Spectrometry and Ion Processes 178, 81-112.

Riller, U., Schwerdtner, W. M., Halls, H. C., and Card, K. D. (1999): Transpressive tectonism in the eastern Penokean Orogen, Canada: consequences for Proterozoic crustal kinematics and continental fragmentation. Precambrian Research 93, 51–70.

Roedder, E. (1984): Fluid Inclusions, Reviews in Mineralogy 12. Mineralogical Society of America.

Rousell, D.H. (1984): Structural geology of the Sudbury basin. Ontario Geological Survey Special Volume 1, 83–96.

Rousell, D. H., Fedorowich, J. S., and Dressler, B. O. (2003): Sudbury breccia (Canada): a product of the 1850 Ma Sudbury event and host to footwall Cu-Ni-PGE deposits. Earth and Science Reviews 60, 147-174.

Rusk, B., Lowers, H., and Reed, M. (2008): Trace elements in hydrothermal quartz: relationships to cathodoluminescent textures and insights into vein formation. Geology 36, 546–550.

Shanks, W. C. Pat III and Thurston, Roland (2012): Volcanogenic massive sulfide occurrence model. United States Geological Survey Scientific Investigations Report 2010-5070-C, 345 p.

Sharpe, R., and Fayek, M.(2011): The World's oldest observed primary uraninite. The Canadian Mineralogist 49, 1199-1210.

Spray, J. G. (2010): Frictional melting processes in planetary materials: From hypervelocity impact to earthquakes. Annual Review of Earth and Planetary Sciences 38, 221-254.

Stevens, G., Boer, R., and Gibson, R.L. (1997): Metamorphism, fluid flow and gold remobilization in the Witwatersrand Basin: towards a unifying model. South African Journal of Geology 100, 363-375.

Stewart, R. C. (2011): Halogen geochemistry of footwall breccia and associated units of the Main Mass of the Sudbury Igneous Complex. Unpublished M.Sc. Thesis, Saint Mary's University, Halifax, 190 p.

Stewart, R. C., Kontak, D. J., and Ames, D. E. (2013): Petrography and fluid inclusions reflect a history of pervasive fluid-mediated metasomatism in the Granophyre Unit of the 1.85 Ga Sudbury Igneous Complex, Ontario. Geological Association of Canada – Mineralogical Association of Canada Joint Annual Meeting Abstracts, Winnipeg, Manitoba, Canada. May 22 to 24 2013, p. 183.

Stewart, R. C. and Kontak, D. J. (2012): Nature, origin, and role of fluids trapped in the Granophyre Unit of the 1.85 Ga Sudbury Igneous Complex. 11th Pan-American Current Research on Fluid Inclusions Conference Abstracts, Windsor, Ontario, Canada. June 18 to 20 2012, p. 89.

Sun, S. S. and McDonough, W. F. (1989): Chemical and isotopic systematics of oceanic basalts: implications for mantle composition and processes. *in* Magmatism in the ocean basins; Saunders, A. D. and Norry, M. J. (eds.). Geological Society of London: London, UK, Special Publications 42, 313-345.

Tanner, D., Henley, R. W., Mavrogenes, J. A., and Holden, P. (2013): Combining in situ isotopic, trace element and textural analyses of quartz from four magmatic-hydrothermal pre deposits. Contributions to Mineralogy and Petrology 166, 1119-1142.

Taylor, H. P. Jr (1968): The oxygen isotope geochemistry of magmatic rocks. Contributions to Mineralogy and Petrology 19, 1-71.

Taylor, H. P. Jr (1979): Oxygen and hydrogen isotope relationships in hydrothermal mineral deposits. In: Geochemistry of Hydrothermal Ore Deposits, vol. 2, H. L. Barnes (eds.), John Wiley, New York, 236-277.

Thompson, L. M. and Spray, J. G. (1996): Pseudotachylite petrogenesis: Constraints from the Sudbury impact structure. Contributions to Mineralogy and Petrology 125, 359-374.

Tuba, G. (2012): Multiple hydrothermal systems in the footwall of the Sudbury Igneous Complex: fluid characteristics, associated alteration, and the role in footwall-type "low-sulfide" Cu-(Ni-)-PGE sulfide mineralization (North and East Ranges, Sudbury Structure, Canada). Unpublished Ph.D. Thesis, Eotvos Lorand University, Budapest, 183 p.

Tuba, G., Molnár, F., Ames, D. E., Péntek, A., Watkinson, D. H., and Jones, P. C. (2014): Multi-stage hydrothermal processes involved in "low-sulfide" Cu(-Ni)-PGE mineralization in the footwall of the Sudbury Igneous Complex (Canada): Amy Lake PGE zone, East Range. Mineralium Deposita 49, 7-47.

Tuba, G., Molnár, F., Watkinson, D. H., Jones, P. C., and Mogessie, A. (2010): Hydrothermal vein and alteration assemblages associated with low-sulfide footwall Cu-Ni-PGE mineralization and regional hydrothermal processes, North and East Ranges, Sudbury structure, Canada. SEG Special Publication 15, 573-598.

Tuchscherer, M.G. and Spray, J.G. 2002. Geology, mineralization, and emplacement of the Foy offset Dike, Sudbury impact structure. Economic Geology 97, 1377-1397.

Warren, M. R., Hanley, J. J., Ames, D. E., and Jackson, S. E. (2015): The Ni-Cr-Cu content of biotite as pathfinder elements for magmatic sulfide exploration associated with mafic units of the Sudbury Igneous Complex, Ontario, Canada. Journal of Geochemical Exploration 153, 11-29.

Watkinson, D. H. (1999): Platinum-group-element enrichment in Cu-Ni-rich sulfides from footwall deposits, Sudbury Igneous Complex, Canada. Chronique de la Recherchemineire 535, 55-69.

White, C. J., Mungall, J. E., and Spooner, E. T. C. (2010): Low-sulfide PGE-Cu-Ni mineralization of the Sudbury Igneous Complex, Canada. In: Jugo, P. J., Lesher, C. M., and Mungall, J. E. (eds.) Abstracts, 11th International Platinum Symposium, Sudbury, Ontario, Canada. OGS Miscellaneous Release Data 269.

Winkler, H. G. F (1967): Die Genese der metamorphen Gesteine (second ed.). Springer-Verlag, Berlin, Germany.

Winzer, S.R., Lum, R.K.L., and Schuhmann, S. (1976): Rb, Sr and strontium isotopic composition, K/Ar age and large ion lithophile trace element abundances in rocks and glasses from the Wanapitei Lake impact structure. Geochimica et Cosmochimica Acta 40, 51–57.

Yardley, B. W. D and Graham, J. T. (2002): The origins of salinity in metamorphic fluids. Geofluids 2, 249-256.

Zhang, L., Jingxiu, L., Huanbo, Z., and Zhensheng, C. (1989): Oxygen Isotope Fractionation in the Quartz-Water-Salt System. Economic Geology 84, 1643-1650.

Zheng, Y.-F. (1993): Calculation of oxygen isotope fractionation in hydroxyl-bearing silicates. Earth and Planetary Science Letters 121, 247-263.

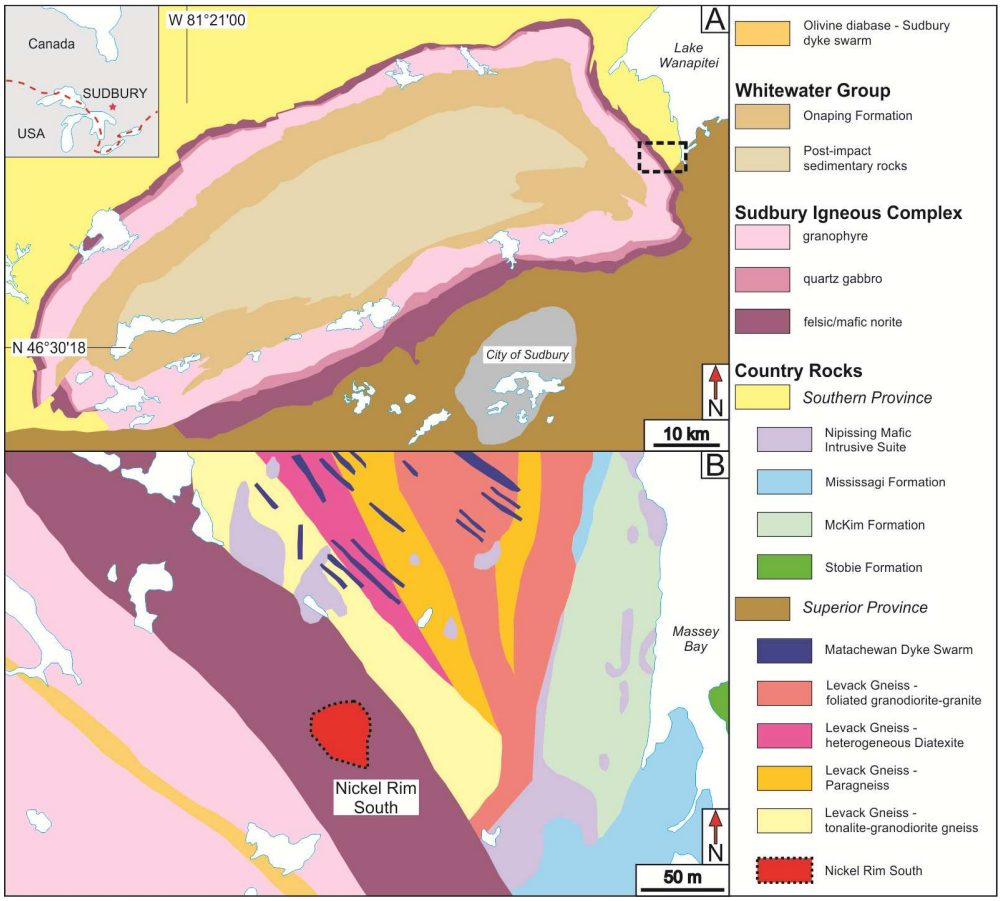

Figure 4-1. Geological setting of the area of study. (A) Sudbury Structure, Ontario, as modified after Ames and Farrow (2007), with inset map showing the location of the Sudbury Structure within Canada. Note that the Sudbury Igneous Complex (SIC) is located at the junction of the Superior and Southern provinces and is overlain by the Whitewater Group. The dashed box indicates the location of the Nickel Rim South deposit. (B) Detailed surface map of the Nickel Rim deposit area.

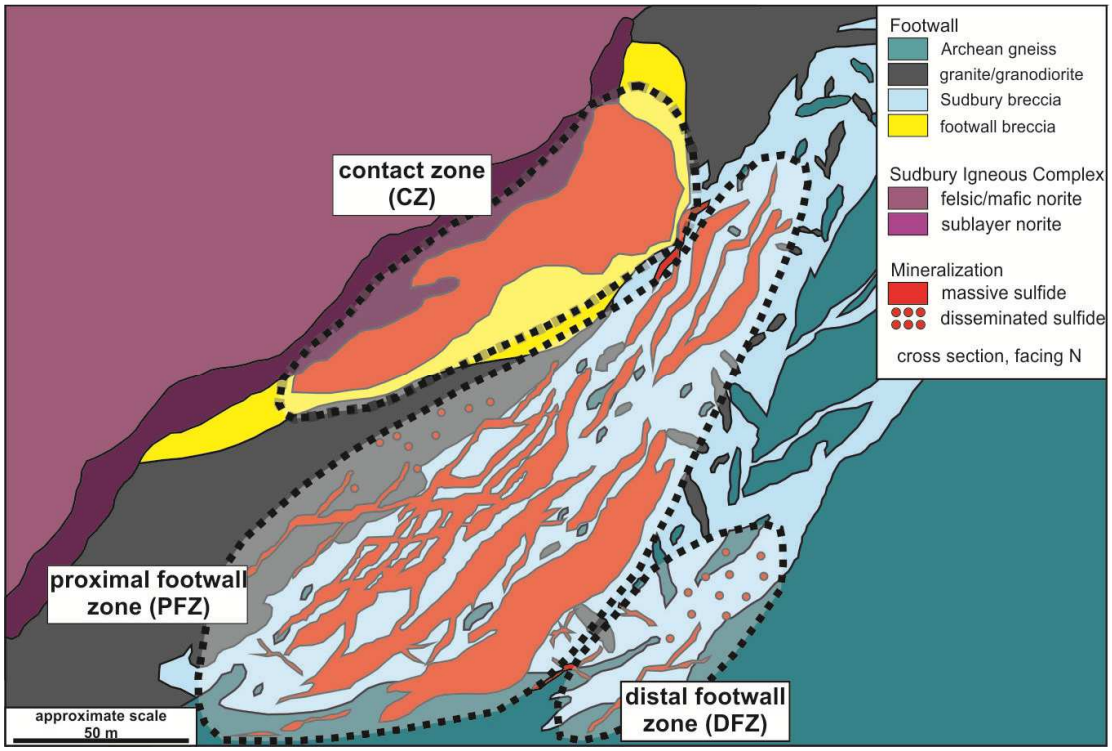

Figure 4-2. Schematic cross section facing north of the footwall environment at the Nickel Rim South deposit (after McLean et al. 2005). The figure shows the location of sublayer norite and felsic/mafic norite units of the Sudbury Igneous Complex, and footwall units which include Archean gneiss, granite/granodiorite, Sudbury breccia, footwall breccia, and general location of massive and semi-massive sulfide mineralization. The dashed ovoid outlines show the three subdivisions of the NRS environment used in this study: the contact, proximal footwall, and distal footwall zones.

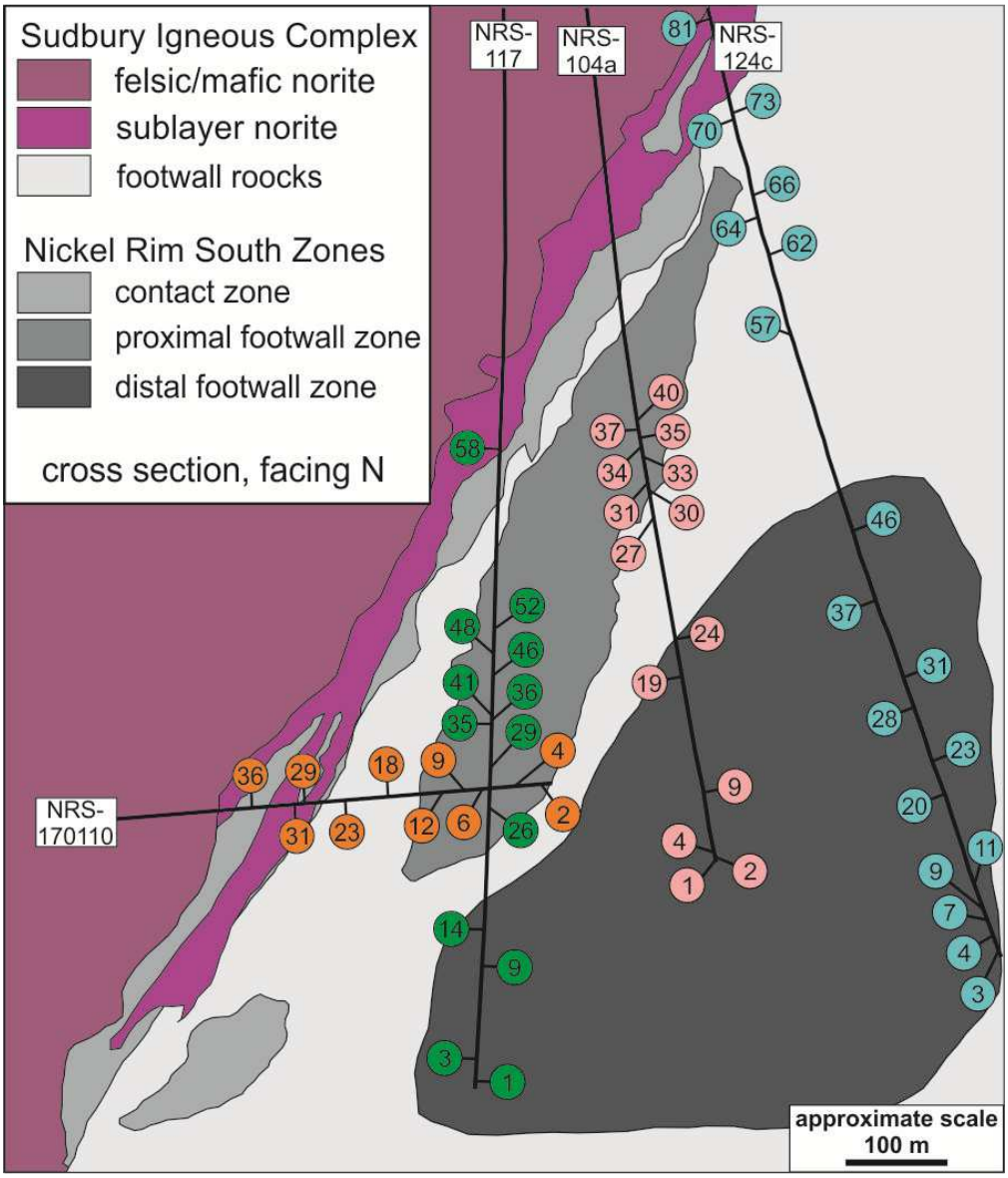

Figure 4-3. Schematic cross section of the footwall environment at the Nickel Rim South deposit showing the three subdivisions for the footwall environment: the contact, proximal footwall, and distal footwall zones, and locations of the four drill holes used in this study and samples collected.

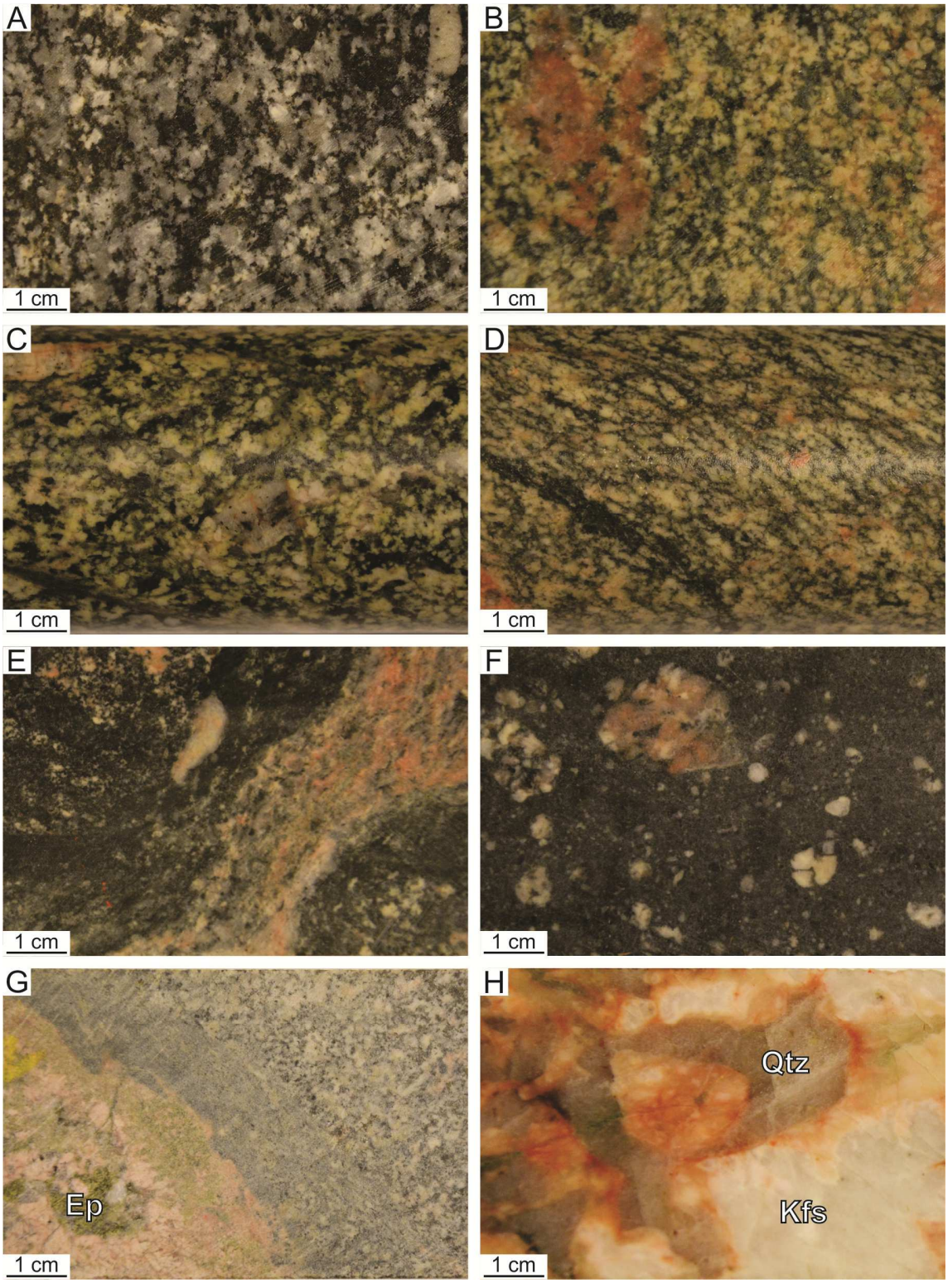
A
1 cm
B
1 cm
C
1 cm
D
1 cm
E
1 cm
F
1 cm
G
Ep
1 cm
H
Qtz
Kfs
1 cm

Figure 4-4. Photographs of drill core for major rock types at the Nickel Rim South deposit. (A) Coherent to in situ brecciated felsic igneous rock (CBF) of granitic affinity showing no alteration. (B) CBF showing no foliation. (C) CBF showing weak foliation. (D) CBF showing a strong foliation. (E) Sudbury breccia showing moderate contact metamorphism. (F) Image of unmetamorphosed Sudbury breccia containing sub-rounded clasts of CBF. (G) Footwall granophyre (FWGR) containing an epidote-filled miarolitic cavity. (H) FWGR containing coarse-grained K-feldspar and quartz. Abbreviations: Kfs – K-feldspar; Qtz – quartz.

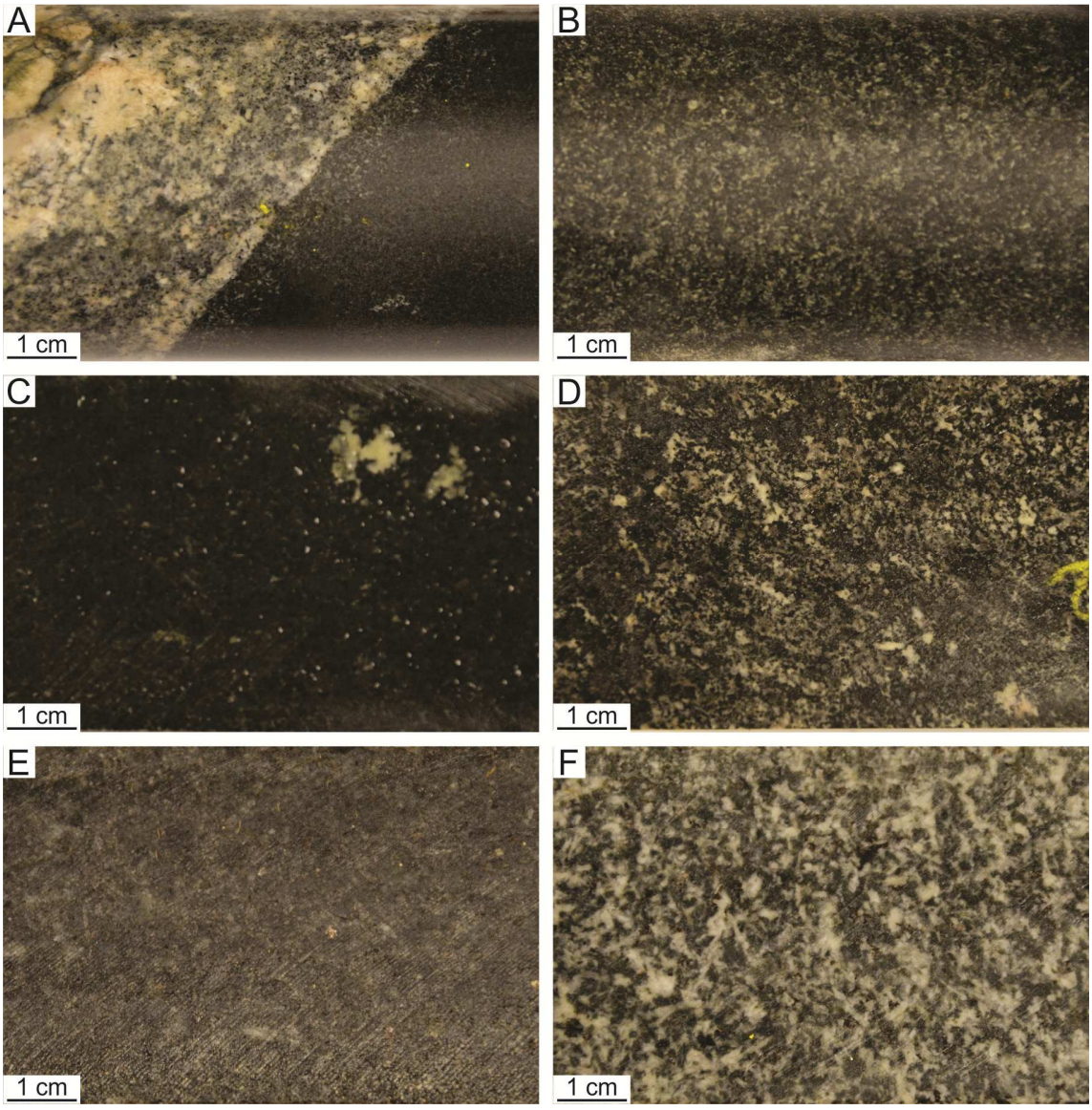

Figure 4-5. Photographs of drill core for minor rock types at the Nickel Rim South deposit. (A) Contact between very fine grained diabase dike and host coherent to in situ brecciated felsic igneous rock (CBF). (B) Representative image of fine-grained diabase dike. (C) Representative image of plagioclase-bearing Matachewan diabase dike. (D) Representative image of granodiorite. (E) Representative image of mafic norite. (F) Representative image of felsic norite

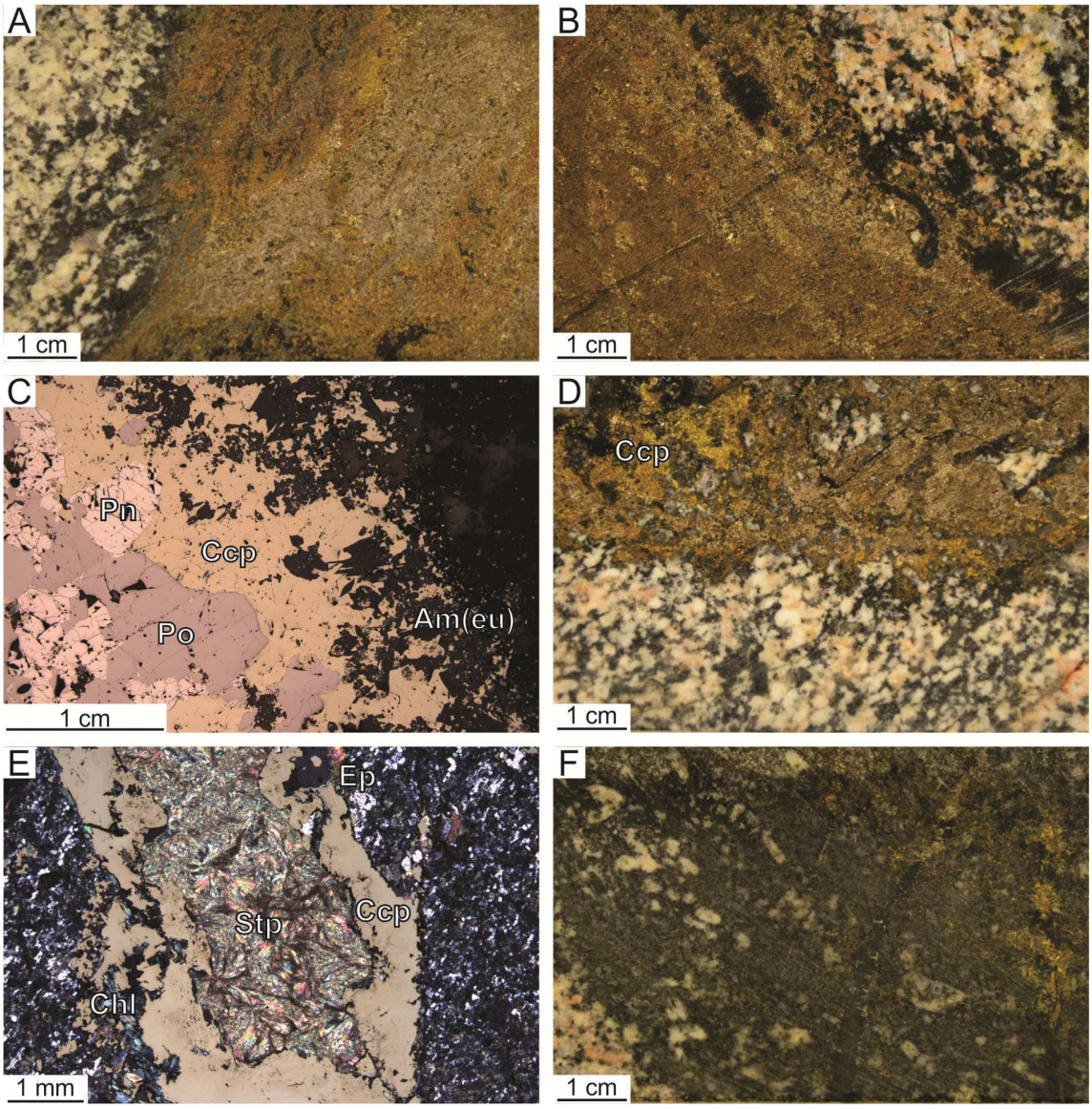

Figure 4-6. Photomicrographs (A, B, C, H) and scanned polished thin section images (D, E, F, G) in plane-polarized light (B, E, F, G) and cross-polarized light (A, C, D, H) summarizing the textural varieties of epidote at the Nickel Rim South deposit. (A) Type 1 (disseminated, fine to medium grained; highly birefringent phase) epidote disseminated in coherent to in situ brecciated felsic igneous rock (CBF). (B) Type 1 subhedral epidote intergrown with chlorite and surrounded by fine-grained epidote, and quartz. (C) Type 2 (vein, coarse-grained) epidote with carbonate.

(D) Type 2 epidote in CBF. (E) Type 3 epidote (vein, fine-grained) in footwall granophyre (FWGR). (F) Type 3 epidote in clast-rich Sudbury breccia. (G) Type 4 (blocky/miarole-hosted) epidote in FWGR. (H) Type 4 epidote and quartz in CBF. Abbreviations: Cb – carbonate; Chl – chlorite; Ep – epidote; Qtz – quartz.

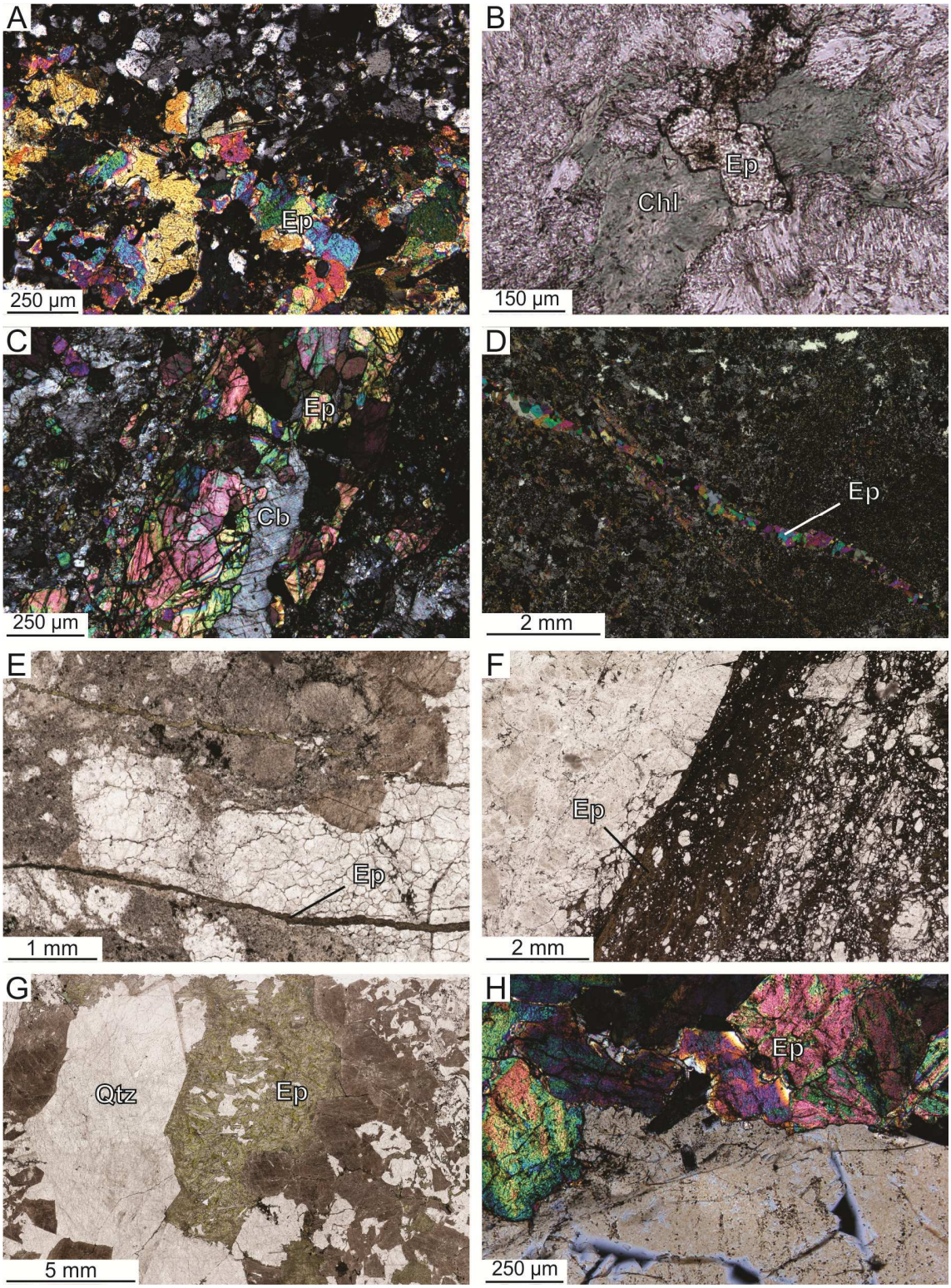
A
Ep
250 µm
B
Ep
Chl
150 µm
C
Ep
Cb
250 µm
D
Ep
2 mm
E
Ep
1 mm
F
Ep
2 mm
G
Qtz
Ep
5 mm
H
Ep
250 µm

Figure 4-7. Photomicrographs in cross-polarized light (XPL) and plane-polarized light (PPL) summarizing alteration minerals and textures in the Nickel Rim South deposit. (A) Chalcopyrite vein containing euhedral amphibole with an epidote-chlorite vein selvage. (B) Fibrous amphibole in quartz and K-feldspar. (C) Replacement style chlorite after biotite. (D) Chalcopyrite vein containing a chlorite and stilpnomelane assemblage. (E) Example of epidote and sericite saussurite assemblage replacing plagioclase. (F) Altered, poikilitic biotite altered to epidote and chlorite. (G) Quartz-carbonate vein cutting altered plagioclase and earlier coarse-grained epidote. (H) Quartz and K-feldspar within footwall granophyre. Notice the pits within K-feldspar caused by fluid re-equilibration. Abbreviations: Am(eu) – euhedral amphibole; Am(fib) – fibrous amphibole; Bt – biotite; Cb – carbonate; Ccp – chalcopyrite; Chl – chlorite; Ep – epidote; Kfs – K-feldspar; Pl – plagioclase; Qtz – quartz; Ser – sericite; Stp – stilpnomelane.

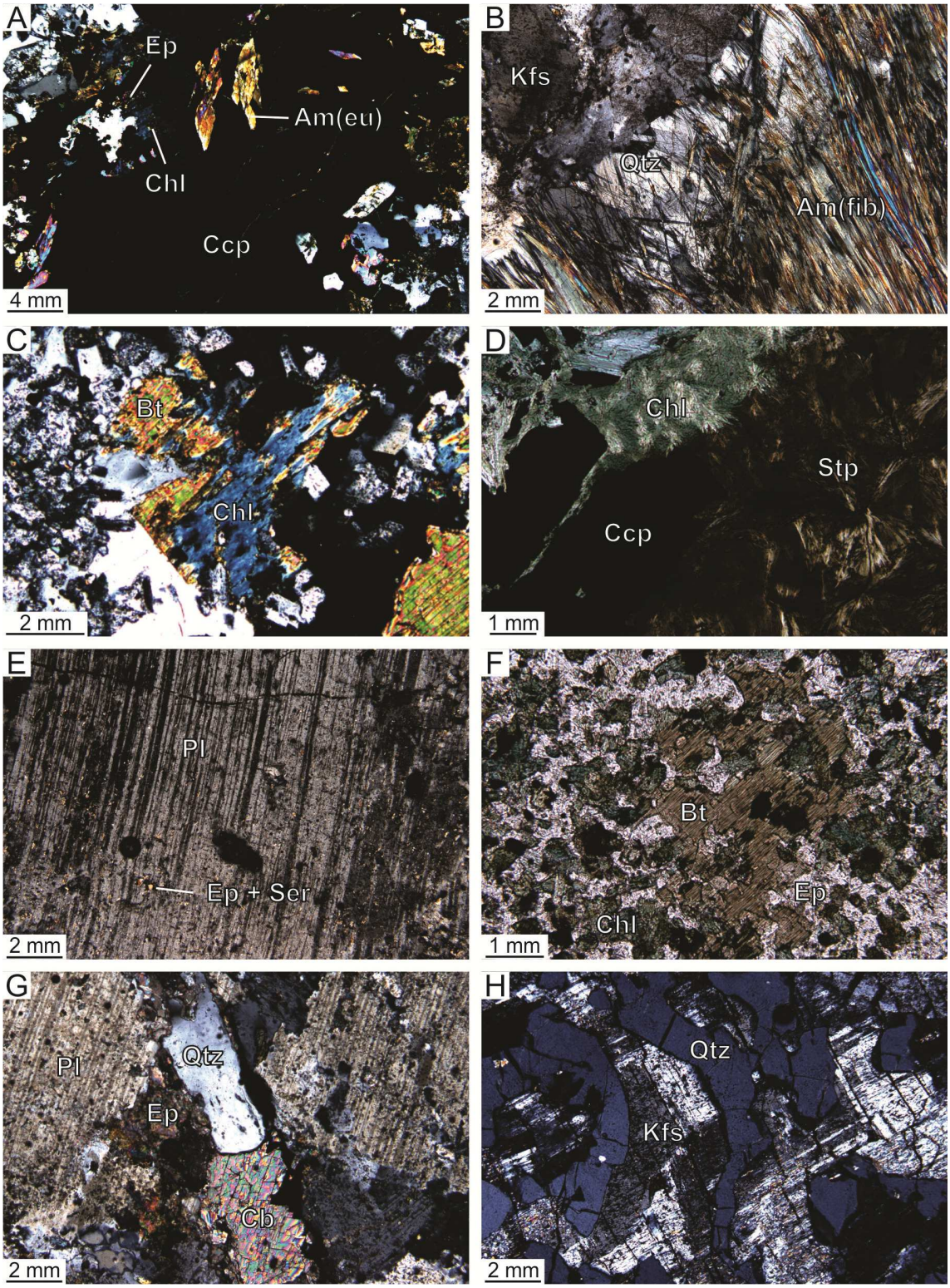
A
Ep
Am(eu)
Chl
Ccp
4 mm
B
Kfs
Qtz
Am(fib)
2 mm
C
Bt
Chl
2 mm
D
Chl
Stp
Ccp
1 mm
E
Pl
Ep + Ser
2 mm
F
Bt
Ep
Chl
1 mm
G
Pl
Qtz
Ep
Cb
2 mm
H
Qtz
Kfs
2 mm

Figure 4-8. Photographs of drill core (A, B, D, F) and photomicrographs in reflected light (C, E) and cross-polarized light (F) mineralization styles and textures and the Nickel Rim South deposit. (A) Representative image of contact-style mineralization hosted in coherent to in situ brecciated felsic igneous rock (CBF). (B) Contact-style mineralization with a chlorite selvage. (C) Contact-style mineralization showing the relationship between pyrrhotite, pentlandite, and chalcopyrite intergrown with euhedral amphibole. (D) Net-textured mineralization in CBF. (E) Representative image of footwall-style mineralization consisting of chalcopyrite and stilpnomelane with a chlorite and epidote selvage. (F) Representative image of disseminated footwall-style mineralization. Abbreviations: Am(eu) – euhedral amphibole; Ccp – chalcopyrite; Chl – chlorite; Pn – pentlandite; Po – pyrrhotite; Stp – stilpnomelane.

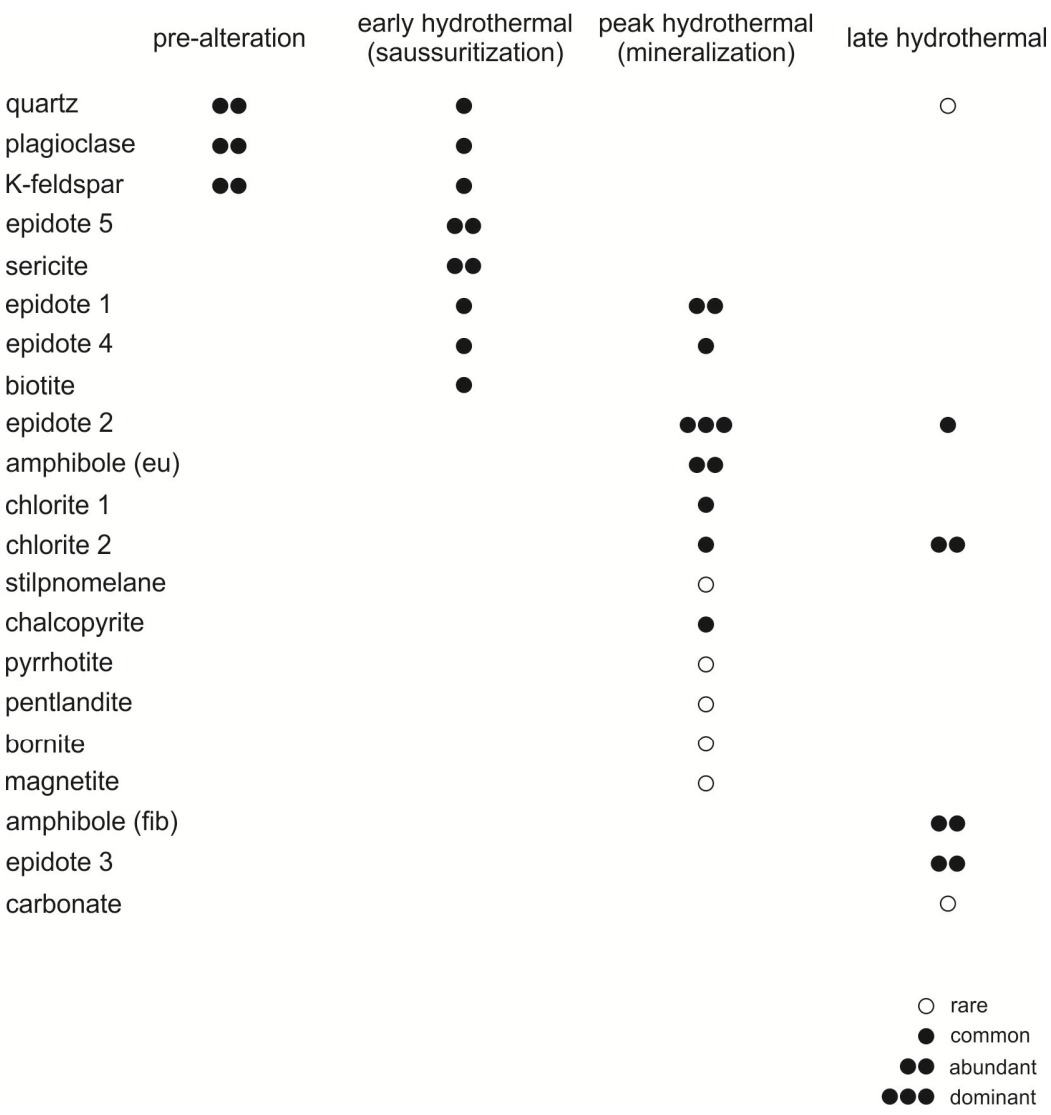

Figure 4-9. Figure which summarizes the mineral paragenesis and relative intensities of alteration types at Nickel Rim South. Note the paragenesis of the deposit is divided into four stages: 1) a pre-alteration stage, 2) an early saussuritization stage of the feldspars, 3) a peak hydrothermal stage associated with mineralization, and 4) a late hydrothermal stage. Minerals are listed in their approximate paragenetic order.

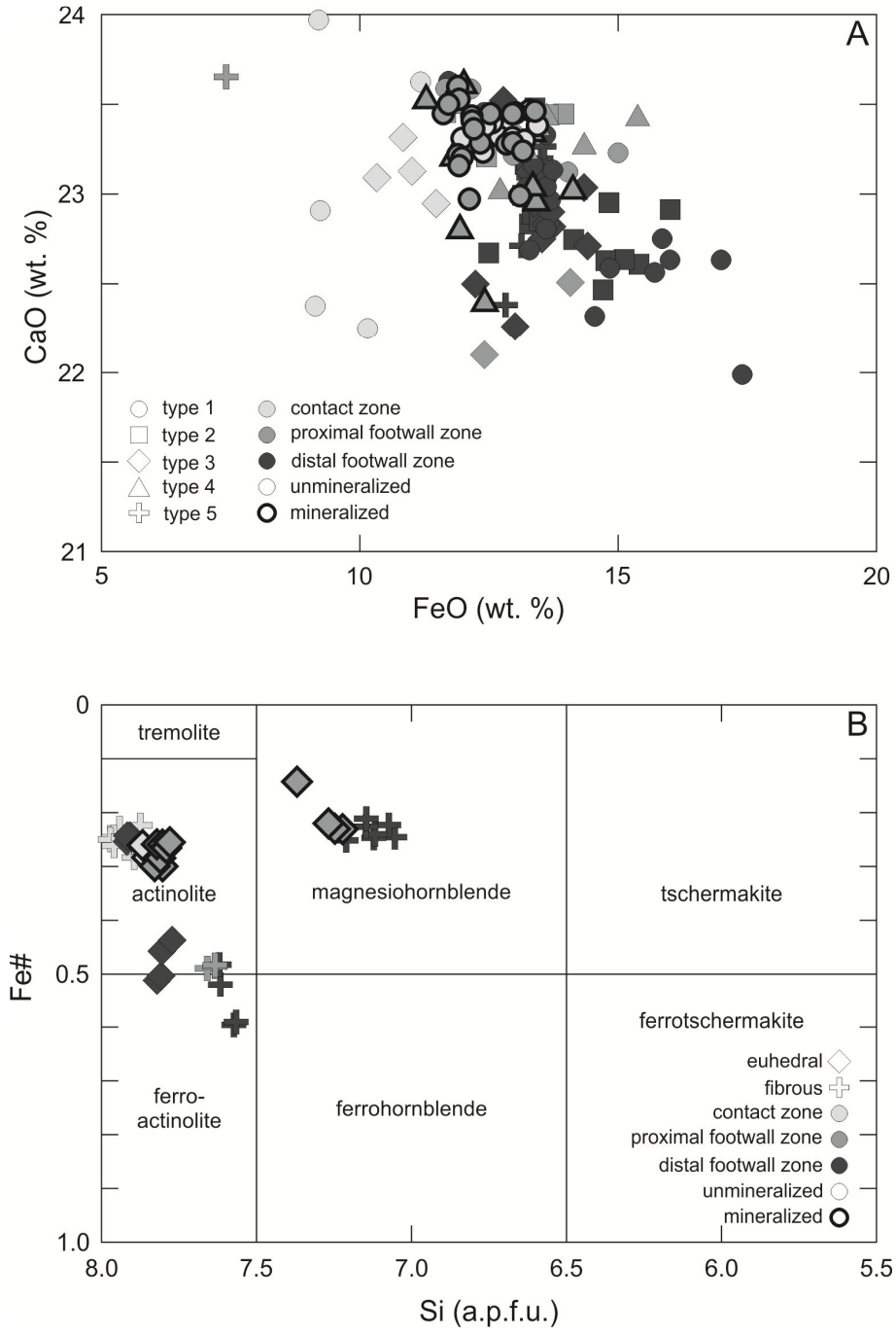

Figure 4-10. Mineral chemistry for samples from the Nickel Rim South deposit. (A) Plot of FeO (wt. %) against CaO (wt. %) for epidote data. (B) Plot of Si (atoms per formula unit) against Fe# (Fe/(Fe+Mg)) for amphibole data based on the classification criteria Leake et al. (1997).

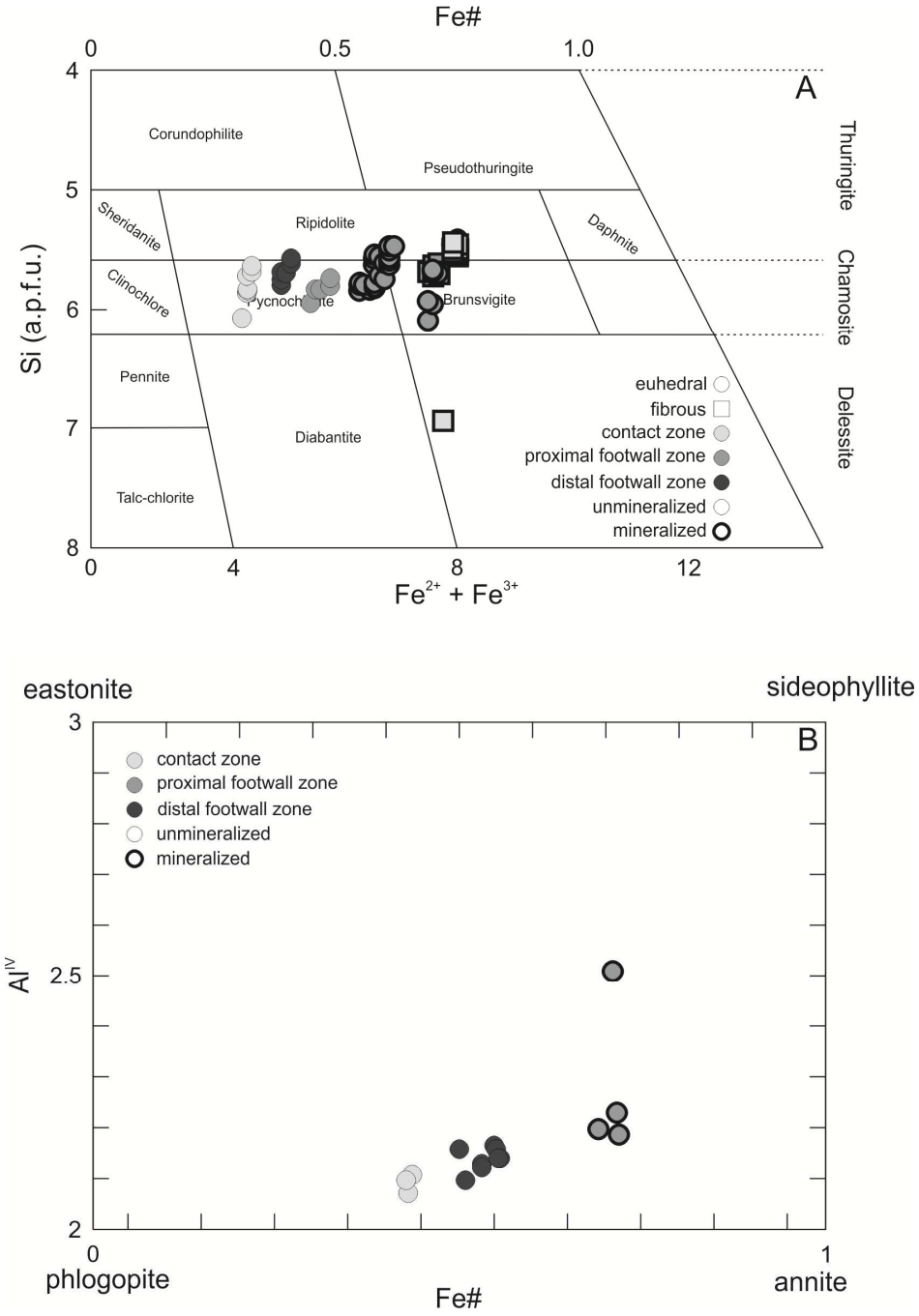

Figure 4-11. Mineral chemistry for samples from the GR from the NR and SR. (A) Plot of Fe# (Fe/(Fe+Mg)) and total Fe (Fe^{2+}+Fe^{3+}; atoms per formula unit) against Si (atoms per formula unit) for chlorite data (after Deer et al. 1966). (B) Plot of Fe# (Fe/(Fe+Mg)) against Al^{IV} for mica data (after Bailey 1984).

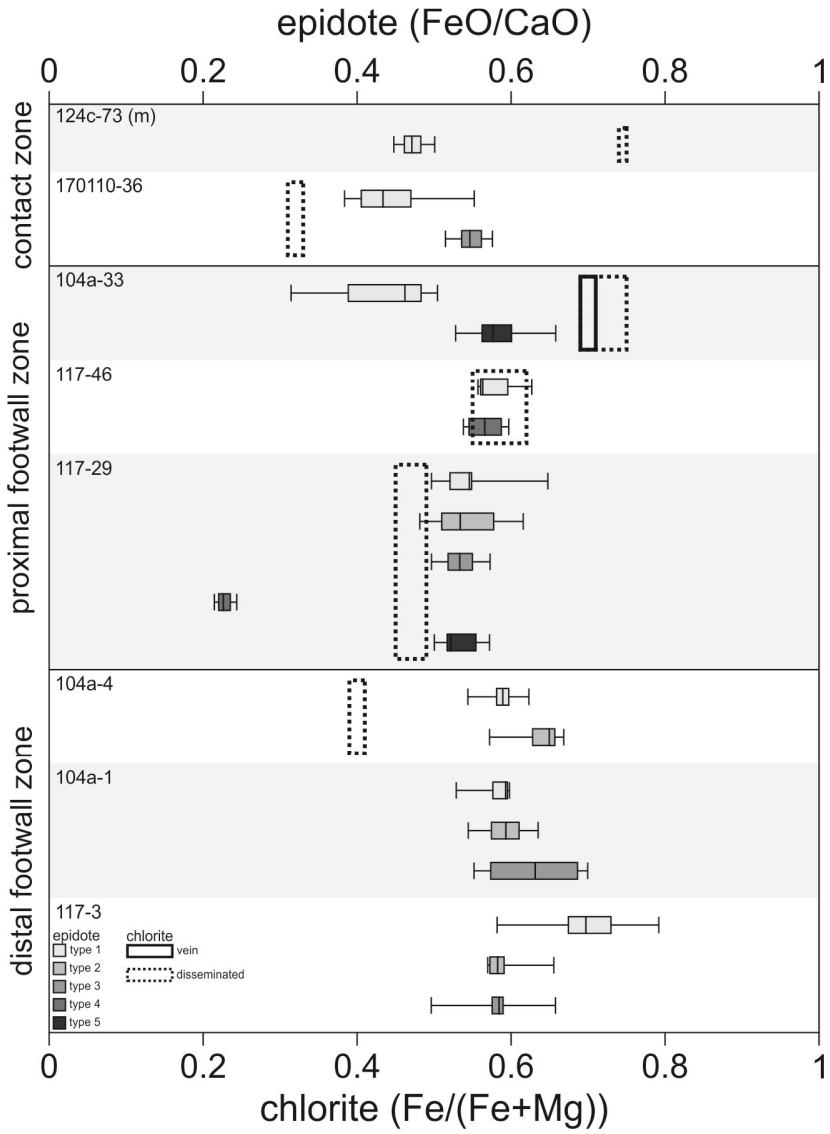

Figure 4-12. Comparison of epidote and chlorite mineral chemical data for the Nickel Rim South deposit. Figure shows box plots for epidote (FeO/CaO) and ranges for chlorite (Fe/(Fe+Mg)) of texturally coeval secondary grains to characterize the variation in Fe content for each mineral.

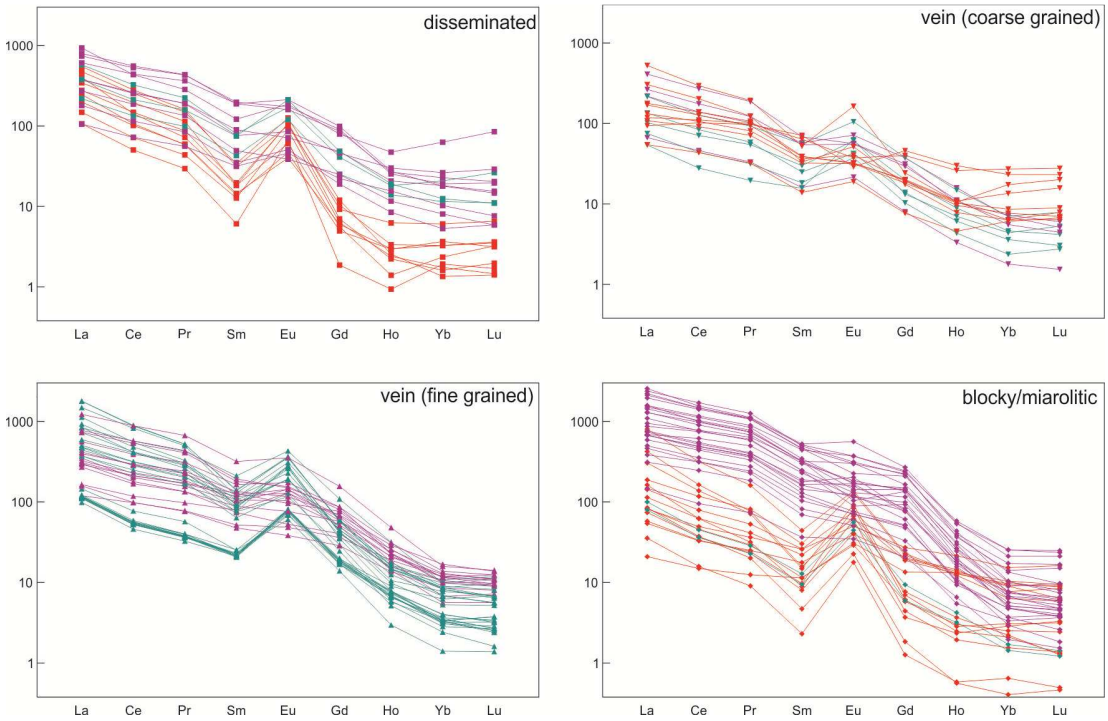

Figure 4-13. Chondrite-normalized (values from Sun and McDonough 1989) rare earth element (REE) diagrams summarizing the in situ LA ICP-MS data for different epidote types from the Nickel Rim South deposit. Each diagram represents one textural variety of epidote, these being 1) disseminated, 2) vein, coarse-grained, 3) vein, fine-grained, and 4) blocky/miarolitic. Note that the different colours are used for each separate plot in order to highlight the variability within each epidote type. The colours used also indicate the different REE patterns that are recognized and discussed in the text: red represents type 1_{REE} pattern, purple represents type 2_{REE} pattern, and blue represents type 3_{REE} pattern.

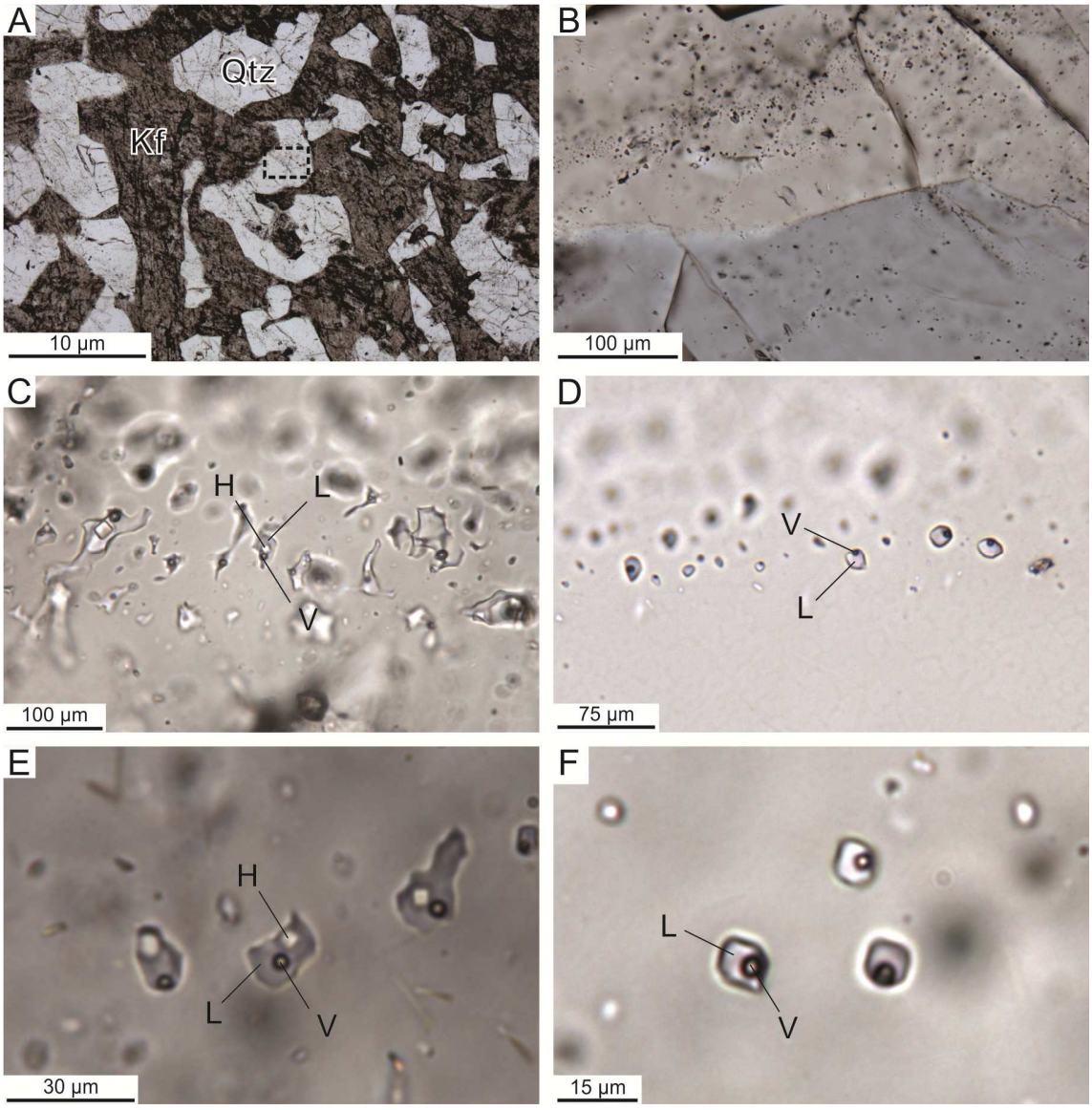

Figure 4-14. Photomicrographs in plane-polarized light of quartz-hosted fluid inclusions from the Nickel Rim South deposit. (A) Image at low magnification showing abundant secondary fluid inclusions hosted in quartz of the footwall granophyre. Note the dark lines in the quartz are linear to curvilinear fluid inclusion trails (i.e., healed fractures). (B) Close up image of the dashed black box from image a showing fluid inclusions decorating healed fracture planes. (C) A FIA of type 2 L-V-H fluid inclusions showing evidence for post-entrapment modification in the form of necking; also note their irregular shapes. (Abbreviations: Kfs – K-feldspar; Qtz – quartz; L –

liquid (H_2O) phase; V – vapour (H_2O) phase, H – halite. (D) A secondary fluid inclusion assemblage (FIA) of type 1, low-temperature, L-rich fluid inclusions with uniform L:V ratios. (E) A FIA of type 2 L-V-H fluid inclusions having uniform phase ratios. (F) A FIA of type 3, L-rich fluid inclusions with uniform L:V ratios. Note that the L:V phase ratios of these inclusions reflect a higher homogenization temperature (i.e., lower density) than type 1 inclusions in image C.

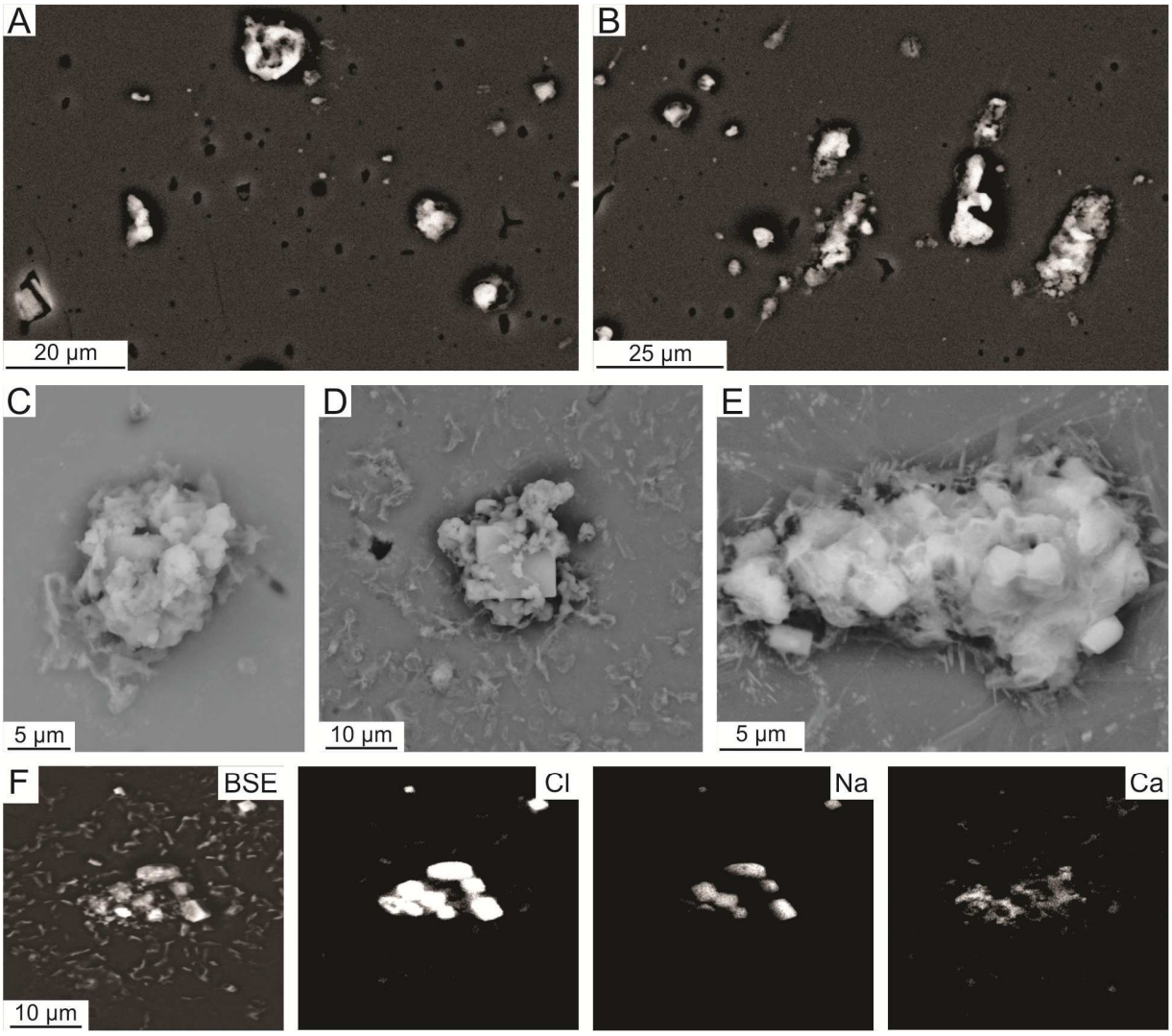

Figure 4-15. Back-scattered electron (BSE) images of evaporate mounds hosted in quartz from samples in the footwall zone of the Nickel Rim South deposit. (A) Example of a evaporate mound field containing predominantly sub-rounded mounds. Notice the presence of abundant pits on the quartz surface which were produced during the artificial decrepitation of the fluid inclusions. (B) Example of a evaporate mound field with elongate-shaped mounds. Again notice the pitted surface of the quartz. (C) Close-up of a typical circular mound which has a Na:Ca:K composition of~70:25:5. (D) Close-up image of a composite-type mound which has a cubic-

shaped core of halite which is overgrown by irregular material that is Ca-rich. Also note the presence of the ejecta material surrounding the mound which is a common feature of mounds. (E) Close-up image of a composite ovoid-shaped mound which can be seen to have many cubic-shaped phases with amorphous looking internal matrix material. (F) A BSE image and accompanying X-ray maps (Cl, Na, Ca) of a typical decrepitate mound with an internal mound area and surrounding ejecta material. These images illustrate the reality of potential elemental fractionation that can occur during fluid inclusions decrepitation, in particular for larger mounds. The X-ray maps highlight the partial decoupling of Na and Ca in the mounds.

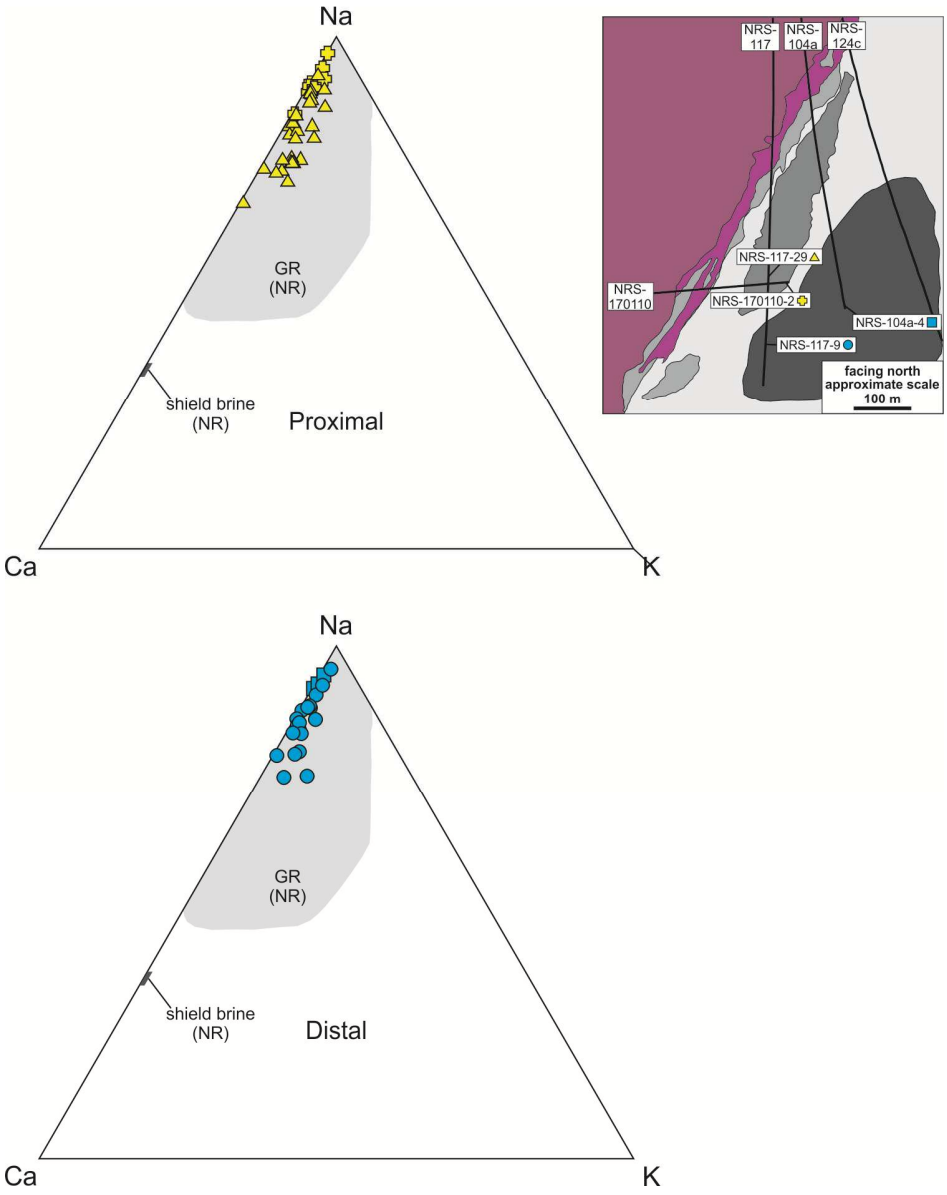

Figure 4-16. Ternary plots which summarize the major element chemistry (Na, Ca, K) of evaporate mounds from Nickel Rim South. Shield brine composition from Frape and Fritz (1982).

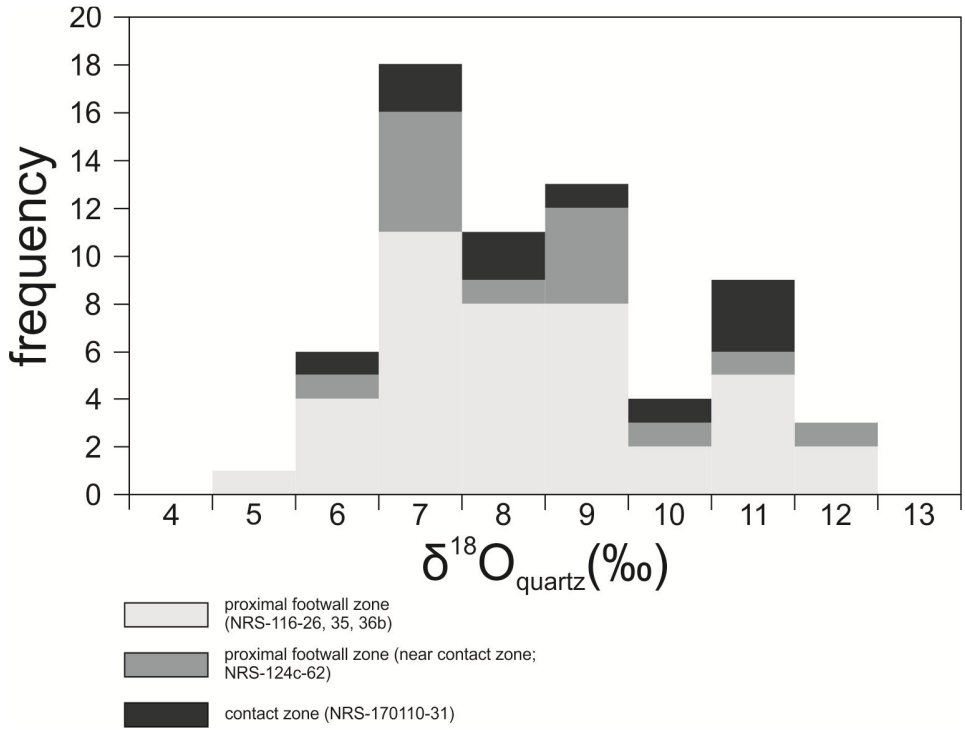

Figure 4-17. Frequency plot for oxygen isotope data of quartz from Nickel Rim South as determined using secondary ion mass spectrometry (SIMS). The samples are separated into deep proximal footwall (n=3), shallow footwall zone (n=1), and contact zone (n=1).

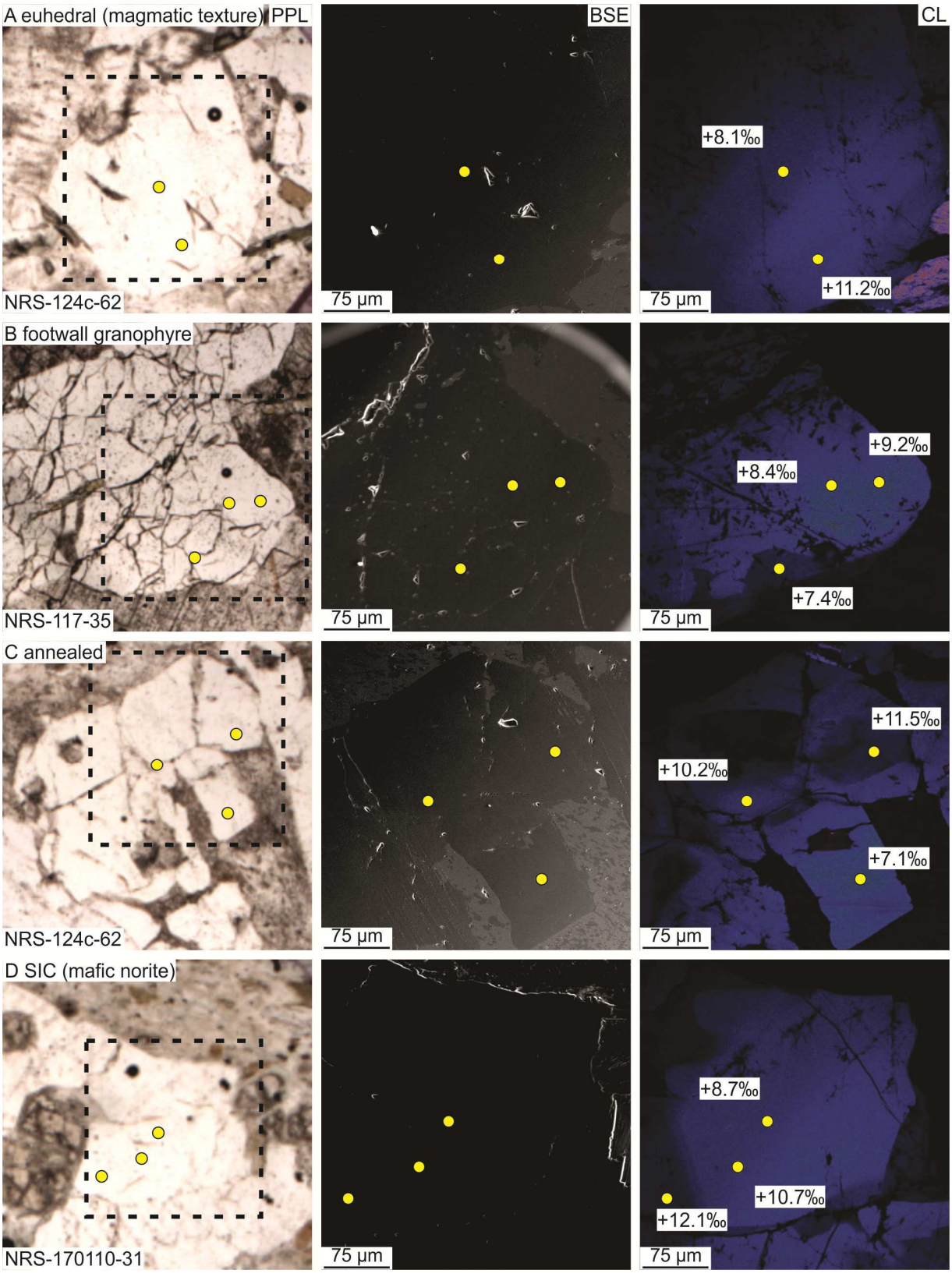
A euhedral (magmatic texture)
PPL
BSE
CL
+8.1‰
+11.2‰
NRS-124c-62
75 µm
75 µm
B footwall granophyre
+9.2‰
+8.4‰
+7.4‰
NRS-117-35
75 µm
75 µm
C annealed
+11.5‰
+10.2‰
+7.1‰
NRS-124c-62
75 µm
75 µm
D SIC (mafic norite)
+8.7‰
+10.7‰
+12.1‰
NRS-170110-31
75 µm
75 µm

Figure 4-18. Plane-polarized light (PPL), back-scattered electron (BSE), and cathodoluminescence (CL) images which summarize the petrographic and chemical features of quartz in the Nickel Rim South (NRS) deposit environment. The images show various styles of quartz identified at NRS, including: (a) euhedral quartz hosted in coherent to in situ brecciated felsic igneous rock, (b) footwall granophyre-hosted; (c) annealed quartz in the Sudbury breccia; and (d) quartz in the mafic norite unit of the Sudbury Igneous Complex. Note the dashed black boxes in the first column (PPL images) indicate the visible areas in the BSE and CL images whereas the yellow dots indicate the points where secondary ion mass spectrometry (SIMS) analysis for oxygen isotopes were acquired. In addition, the strong (blue) and weak (dark blue to black) CL signals indicate areas of least-altered (blue) and moderate- to strongly altered (dark blue to black) quartz and presence or absence of microfractures within quartz not visible by PPL or BSE imaging alone.

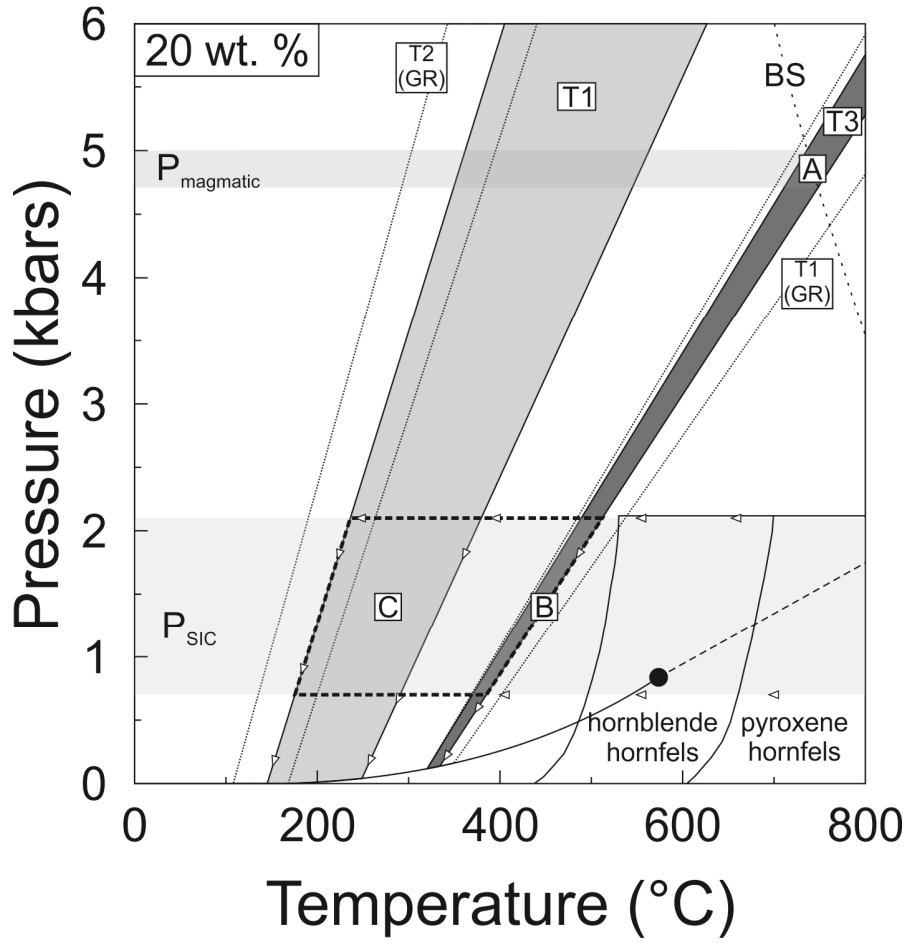

Figure 4-19. A pressure (kbar) versus temperature (°C) diagram showing the fluid path and inferred isochoric projections for types 1 and 2 fluid inclusions hosted in quartz from the Nickel Rim South deposit (NRS). Isochores were determined using microthermometric data (Th, salinity, and homogenization style) and are reported in T(°C). The vertical dotted lines projected to the X-axis (temperature) represent the trapping temperature (Tt) for type's 1 and 3 fluid inclusions. Curves representing phase boundaries (L+V) in the diagrams for 20 wt. % NaCl are from Bodnar (2003). The box labelled P_{SIC} represents the estimated lithostatic pressure of the SIC during trapping of fluid inclusions by Molnár et al. (1999) and Péntek et al. (2008). The dashed line labelled BS represents the solidus of H_2O-saturated basalt (Brown 1993). The arrows labelled "A" represent the pressure and temperature history for a magmatic fluid exsolved at

pressure reported for NRS and isobarically cooled to the trapping temperatures reported in this study (“C). The grey box labelled $P_{magmatic}$ is the trapping pressure required for type 1 fluid inclusions to be magmatic and trapped after exsolution (“B” and "C") from the melt according to measured Th data.

Table 4-1. Summary of rock types and alteration assemblage characteristics at Nickel Rim South. Abbreviations: CZ - contact zone; PFZ - proximal footwall zone; DFZ - distal footwall zone.

Rock Type	Description	Distribution	Dominant Alteration Assemblage	Accessory Alteration Phases
footwall granophyre	Present as dikes and veins ranging from 1 to 25 cm width that cut most other rock types. Most abundant near CZ and lessens into the PFZ and vary rare in the DFZ. Contains granophyric intergrowth of quartz and K-feldspar with plagioclase. Absent of recrystallization and deformation related features (e.g., undulose extinction, subgrains). Sometimes contains cavities (miaroles). Occasionally associated with mineralization near the basal SIC contact.	PFZ	Blocky epidote (T4)	
diabase	Fine-to medium-grained, green to grey, and contains plagioclase (needle texture). Contains clasts of primary felsic (e.g., CBF) that are mm scale and subrounded. Exhibits both sharp and irregular contact with the host (most often CBF). Cross-cuts all primary footwall lithologies.	PFZ, DFZ	chlorite within fractures and weak perfasive chloritization	carbonate+/-chlorite veins (up to 5 mm width)
Matachewan diabase	Similar to diabase but contains anhedral to subhedral plagioclase (trace to 3 modal %) as individual phenocrysts or clots. Cross-cuts all primary footwall lithologies.	PFZ	sericite-chlorite	epidote (T1)
granodiorite	Fine- to medium-grained and consists of quartz, plagioclase, and K-feldspar. Occasionally brecciated. Some intervals exhibit weak compositional layering and locally it grades into the CBF rock type.	PFZ	patchy epidote (T1) and epidote veins (T2) with lesser chlorite veins	muscovite, amphibole after micas. Rare ilmenite-titanite reaction rims.
mafic gneiss	Similar to CBF but contains strong compostiional layering with a greater proportion of mafic constituents (i.e. biotite, amphibole).	PFZ, DFZ	Weak to moderate chloritization of biotite and amphibole	chlorite, epidote veinlets

Table 4-1 (cont'd). Summary of rock types and alteration assemblage characteristics at Nickel Rim South. Abbreviations: CZ - contact zone; PFZ - proximal footwall zone; DFZ - distal footwall zone.

Rock Type	Description	Distribution	Dominant Alteration Assemblage	Accessory Alteration Phases
felsic norite	Plagioclase (40 to 62 modal %) and amphibole (30 to 53 modal %)	CZ (SIC)	Quartz-chlorite-carbonate veins	Weak saussuritization of plagioclase and minor chlorite in fractures
mafic norite	Fine- to medium-grained hypidiomorphic rock composed of plagioclase, biotite, and pyroxene consisting of cumulus orthopyroxene with lesser augite.	CZ (SIC)	Epidote veining, patchy chloritization	chlorite veining
sublayer norite	Fine- to medium-grained rock composed of plagioclase, orthopyroxene, with lesser clinopyroxene. Contains mafic to ultramafic clasts.	CZ	minor epidote and chlorite veins	
footwall breccia	Heterolithic breccia containing locally-derived clasts of footwall rocks (primarily CBF) in a fine-grained igneous matrix. Margins of clasts are irregular, suggesting that clasts have undergone partial melting.	CZ	chlorite veining	epidote (T1)
coherent to in situ brecciated felsic igneous rock (CBF)	Granitoid rock exhibiting variable foliation (absent to strong), characterized by K-feldspar (2 to 55 %), quartz (8 to 75 %), and plagioclase (1 to 65 %) with minor biotite, amphibole, apatite, zircon, titanite, and hematite. Variably brecciated and, where developed, typically in situ with minimal clast rotation.	PFZ, DFZ	Strong coarse-grained epidotitization, coarse-grained secondary amphibole	minor carbonate-chlorite veining. Minor disseminated epidote in the DFZ
Sudbury breccia	Consists of >40 vol. % aphanitic, melanocratic to leucocratic, irregularly-formed pseudotachylitic materia. Occurs in intervals from 5 mm to 2.5 m and contains variable (10 to 40 %) amounts of angular to subangular fragments 0.5 to 8 cm in diameter. Fragments locally derived from basement and predominantly CBF.	PFZ, DFZ	pervasive epidote (T1)-chlorite+/-muscovite. Alteration increases with proximity to mineralized veins	Biotite, amphibole, choritization of biotite

Table 4-2. Average EMPA data for epidote from the Nickel Rim South deposit.

	124c-73 n=11 CZ T1 avg	170110-36 n=6 CZ T1 avg	104a-33 n=20 PFZ T1 avg	117-29 n=6 PFZ T1 avg	117-46 n=6 PFZ T1 avg	104a-4 n=10 DFZ T1 avg	117-3 n=4 DFZ T1 avg	117-29 n=4 PFZ T2 avg	104a-4 n=13 DFZ T2 avg
SiO_2	37.54	37.75	37.41	37.51	37.59	37.50	37.30	37.32	37.44
Al_2O_3	23.42	25.47	22.61	23.06	23.68	22.60	22.74	22.95	22.36
FeO	12.79	10.31	13.53	13.05	12.47	13.39	13.36	13.24	13.83
MgO	0.01	0.08	0.00	0.01	0.00	0.10	0.00	0.05	0.04
CaO	23.35	23.08	23.04	23.33	23.38	23.07	23.10	23.39	22.92
Total	97.11	96.70	96.59	96.97	97.12	96.66	96.51	96.95	96.59
FeO/CaO	0.55	0.45	0.59	0.56	0.53	0.58	0.58	0.57	0.60
Si	2.98	2.98	2.99	2.98	2.98	2.99	2.98	2.97	2.99
Al	2.19	2.37	2.13	2.16	2.21	2.12	2.14	2.15	2.10
Fe^{3+}	0.85	0.68	0.90	0.87	0.83	0.89	0.89	0.88	0.92
Mg	0.00	0.01	0.00	0.00	0.00	0.01	0.00	0.01	0.01
Ca	1.98	1.95	1.97	1.99	1.99	1.97	1.98	2.00	1.96
cations	8.00	7.99	7.99	8.00	8.00	7.99	8.00	8.01	7.99
O	12.50	12.50	12.50	12.50	12.50	12.50	12.50	12.50	12.50
Ps	0.30	0.22	0.33	0.30	0.30	0.30	0.30	0.30	0.31

Mineral formula based on 12.5 oxygens

Table 4-2 (cont'd). Average EMPA data for epidote from the Nickel Rim South deposit.

	117-3 n=4 DFZ T2 avg	170110-36 n=4 CZ T3 avg	117-29 n=3 PFZ T3 avg	104a-1 n=4 DFZ T3 avg	117-3 n=8 DFZ T3 avg	117-29 n=7 PFZ T4 avg	117-46 n=11 PFZ T4 avg	104a-33 n=3 PFZ T5 avg	117-29 n=3 PFZ T5 avg	104a-1 n=5 DFZ T5 avg
SiO_2	37.08	38.45	37.19	37.46	37.35	37.40	37.60	38.77	39.45	37.79
Al_2O_3	21.85	24.28	22.70	22.63	22.47	22.74	23.63	29.17	25.99	22.74
FeO	14.48	10.93	13.17	13.36	13.53	13.59	12.57	5.32	9.65	13.21
MgO	0.00	0.23	0.00	0.04	0.03	0.05	0.04	0.01	0.01	0.00
CaO	22.80	23.12	22.65	22.57	23.01	23.30	23.18	23.35	22.71	22.96
Total	96.22	97.00	95.70	96.07	96.39	97.09	97.01	96.62	97.81	96.71
FeO/CaO	0.64	0.47	0.58	0.59	0.59	0.58	0.54	0.23	0.42	0.58
Si	2.98	3.03	2.99	3.00	2.99	2.98	2.98	3.01	3.06	3.01
Al	2.07	2.25	2.15	2.14	2.12	2.13	2.21	2.67	2.37	2.13
Fe^{3+}	0.97	0.72	0.89	0.89	0.90	0.90	0.83	0.35	0.63	0.88
Mg	0.00	0.03	0.00	0.01	0.00	0.01	0.00	0.00	0.00	0.00
Ca	1.97	1.95	1.95	1.94	1.97	1.99	1.97	1.94	1.89	1.96
cations	7.99	7.98	7.98	7.98	7.99	8.00	7.99	7.98	7.94	7.98
O	12.50	12.50	12.50	12.50	12.50	12.50	12.50	12.50	12.50	12.50
Ps	0.30	0.23	0.30	0.30	0.30	0.30	0.29	0.10	0.23	0.30

Mineral formula based on 12.5 oxygens

Table 4-3. Average EMPA data for amphibole from the Nickel Rim South deposit.

	124c-73		170110-36		117-46		117-29	
	n=3		n=8		n=8		n=3	
	eu	CZ	fib	CZ	eu - in sulf	PFZ	fib	PFZ
	avg	1σ	avg	1σ	avg	1σ	avg	1σ
SiO_2	54.91	0.19	55.67	0.42	54.39	0.32	50.90	0.23
TiO2	0.01	0.00	0.01	0.00	0.02	0.01	0.02	0.00
$Al2O_3$	1.19	0.11	0.58	0.24	1.49	0.16	3.13	0.06
FeO	11.57	0.58	10.85	0.71	12.04	0.74	18.62	0.20
Cr_2O_3	0.00	0.00	0.01	0.01	0.01	0.01	0.00	0.00
MnO	0.41	0.02	0.41	0.07	0.36	0.03	0.36	0.01
MgO	16.60	0.26	17.26	0.52	16.26	0.57	10.82	0.04
CaO	12.77	0.05	12.82	0.20	12.59	0.28	12.33	0.11
Na_2O	0.24	0.03	0.19	0.10	0.29	0.08	0.34	0.03
K_2O	0.04	0.01	0.03	0.01	0.07	0.01	0.14	0.01
F	0.09	0.03	0.10	0.08	0.13	0.06	0.09	0.00
Cl	0.01	0.00	0.01	0.01	0.01	0.01	0.02	0.00
Subtotal	97.82	0.08	97.93	0.33	97.65	0.31	96.76	0.30
O = Cl, F	0.04	0.01	0.05	0.03	0.06	0.02	0.04	0.00
Total	97.78	0.09	97.88	0.34	97.59	0.31	96.72	0.30
Si (p.f.u.)	7.85	0.02	7.92	0.04	7.81	0.02	7.65	0.01
Al	0.15	0.02	0.07	0.04	0.19	0.02	0.36	0.01
Fe^{3+}	0.00	0.00	0.00	0.01	0.00	0.00	0.00	0.00
Ti	0.00	0.00	0.00	0.00	0.00	0.00	0.00	0.00
T sites	8.00	0.00	8.00	0.00	8.00	0.00	8.00	0.00
Al	0.05	0.03	0.02	0.02	0.06	0.03	0.20	0.01
Cr	0.00	0.00	0.00	0.00	0.00	0.00	0.00	0.00
Fe^{3+}	0.08	0.05	0.06	0.04	0.12	0.02	0.05	0.01
Ti	0.00	0.00	0.00	0.00	0.00	0.00	0.00	0.00
Mg	3.54	0.05	3.66	0.10	3.48	0.11	2.42	0.02
Fe^{2+}	1.30	0.07	1.22	0.09	1.31	0.08	2.29	0.02
Mn	0.03	0.00	0.03	0.01	0.03	0.00	0.04	0.01
Ca	0.00	0.00	0.00	0.00	0.00	0.00	0.00	0.00
C sites	5.00	0.00	5.00	0.00	5.00	0.00	5.00	0.00
Mg	0.00	0.00	0.00	0.00	0.00	0.00	0.00	0.00
Fe^{2+}	0.00	0.00	0.00	0.00	0.01	0.01	0.00	0.00
Mn	0.02	0.00	0.02	0.01	0.02	0.00	0.01	0.01
Ca	1.96	0.01	1.95	0.02	1.94	0.04	1.98	0.02
Na	0.02	0.01	0.02	0.01	0.03	0.02	0.01	0.01
B sites	2.00	0.00	2.00	0.00	2.00	0.00	2.00	0.00
Ca	0.00	0.00	0.00	0.00	0.00	0.00	0.00	0.00
Na	0.04	0.01	0.03	0.02	0.05	0.01	0.09	0.01
K	0.01	0.00	0.00	0.00	0.01	0.00	0.03	0.00
A sites	0.05	0.01	0.04	0.02	0.06	0.01	0.12	0.01
cations	15.05	0.01	15.03	0.02	15.06	0.01	15.12	0.01
Cl	0.00	0.00	0.00	0.00	0.00	0.00	0.01	0.00
F	0.04	0.01	0.05	0.04	0.06	0.03	0.04	0.00
Cl/F	0.03	0.04	0.05	0.05	0.05	0.07	0.11	0.01
Cl/(Cl+F)	0.03	0.04	0.04	0.04	0.05	0.06	0.10	0.01
oxygen	23.00	0.01	23.01	0.01	23.01	0.01	23.00	0.00
Mg#	0.27	0.01	0.25	0.02	0.27	0.02	0.49	0.00
Fe#	0.73	0.01	0.75	0.02	0.73	0.02	0.51	0.00

Cations calculated on the basis of 23 (O, F, Cl) p.f.u. and the average ferric iron constraint (values obtained from the average 15eNK and 13eCNK)

Table 4-3 (cont'd). Average EMPA data for amphibole from the Nickel Rim South deposit.

	104a-4 n=7 eu - in sulf avg	DFZ 1σ	117-3 n=4 eu avg	DFZ 1σ	104a-4 n=4 fib avg	DFZ 1σ	104a-1 n=7 fib-vein avg	DFZ 1σ
SiO_2	52.83	2.65	52.06	0.39	50.22	0.39	49.26	0.45
TiO2	0.40	0.37	0.01	0.01	0.02	0.02	0.90	0.09
$Al2O_3$	2.89	2.11	2.19	0.18	3.36	0.06	5.50	0.29
FeO	11.30	1.12	18.32	1.09	20.80	2.20	12.81	0.53
Cr_2O_3	0.06	0.08	0.01	0.01	0.01	0.01	0.12	0.03
MnO	0.33	0.12	0.34	0.05	0.33	0.02	0.20	0.02
MgO	16.87	0.83	11.16	0.87	9.42	1.21	15.59	0.30
CaO	12.10	0.82	12.30	0.07	12.26	0.05	11.45	0.06
Na_2O	0.64	0.45	0.24	0.02	0.31	0.04	1.18	0.10
K_2O	0.26	0.22	0.08	0.02	0.25	0.14	0.56	0.04
F	0.29	0.15	0.09	0.03	0.09	0.01	0.42	0.11
Cl	0.08	0.09	0.01	0.01	0.10	0.09	0.16	0.03
Subtotal	97.97	0.30	96.81	0.31	97.17	0.80	98.02	0.34
O = Cl, F	0.14	0.08	0.04	0.01	0.06	0.02	0.21	0.05
Total	97.83	0.26	96.77	0.31	97.11	0.79	97.81	0.31
Si (p.f.u.)	7.55	0.34	7.80	0.02	7.60	0.03	7.12	0.05
Al	0.45	0.33	0.20	0.02	0.40	0.03	0.87	0.05
Fe^{3+}	0.01	0.01	0.00	0.00	0.00	0.00	0.01	0.01
Ti	0.00	0.00	0.00	0.00	0.00	0.00	0.00	0.00
T sites	8.00	0.00	8.00	0.00	8.00	0.00	8.00	0.00
Al	0.04	0.02	0.18	0.02	0.20	0.03	0.07	0.02
Cr	0.01	0.01	0.00	0.00	0.00	0.00	0.01	0.00
Fe^{3+}	0.25	0.19	0.02	0.02	0.07	0.03	0.41	0.05
Ti	0.04	0.04	0.00	0.00	0.00	0.00	0.10	0.01
Mg	3.59	0.15	2.49	0.17	2.13	0.26	3.36	0.06
Fe^{2+}	1.04	0.21	2.28	0.17	2.57	0.26	1.04	0.07
Mn	0.03	0.01	0.03	0.01	0.04	0.00	0.01	0.00
Ca	0.00	0.00	0.00	0.00	0.00	0.00	0.00	0.00
C sites	5.00	0.00	5.00	0.00	5.00	0.00	5.00	0.00
Mg	0.00	0.00	0.00	0.00	0.00	0.00	0.00	0.00
Fe^{2+}	0.05	0.05	0.00	0.00	0.00	0.00	0.09	0.00
Mn	0.01	0.01	0.01	0.01	0.01	0.01	0.01	0.00
Ca	1.85	0.12	1.97	0.02	1.99	0.01	1.77	0.01
Na	0.07	0.06	0.01	0.01	0.01	0.01	0.12	0.00
B sites	2.00	0.01	2.00	0.00	2.00	0.00	2.00	0.00
Ca	0.00	0.00	0.00	0.00	0.00	0.00	0.00	0.00
Na	0.10	0.07	0.05	0.01	0.09	0.01	0.21	0.03
K	0.05	0.04	0.02	0.00	0.05	0.03	0.10	0.01
A sites	0.15	0.11	0.07	0.01	0.13	0.02	0.31	0.03
cations	15.15	0.11	15.07	0.01	15.13	0.02	15.31	0.03
Cl	0.02	0.02	0.00	0.00	0.03	0.02	0.04	0.01
F	0.13	0.07	0.04	0.01	0.04	0.01	0.19	0.05
Cl/F	0.13	0.19	0.08	0.04	0.58	0.53	0.20	0.04
Cl/(Cl+F)	0.10	0.13	0.07	0.03	0.31	0.22	0.17	0.03
oxygen	23.00	0.00	23.03	0.01	23.00	0.00	23.00	0.00
Mg#	0.22	0.04	0.48	0.04	0.55	0.06	0.24	0.01
Fe#	0.78	0.04	0.52	0.04	0.45	0.06	0.76	0.01

Cations calculated on the basis of 23 (O, F, Cl) p.f.u. and the average ferric iron constraint (values obtained from the average 15eNK and 13eCNK)

Table 4-4. Average EMPA data for chlorite from the Nickel Rim South deposit.

	170110-36		124c-73		104a-33		117-46		117-29	
	n=7		n=9		n=10		n=8		n=5	
	CZ	diss	CZ	vein (m)	PFZ	diss	PFZ	diss	PFZ	diss
	avg	1σ	avg	1σ	avg	1σ	avg	1σ	avg	1σ
SiO_2	28.94	0.76	24.66	0.21	25.49	1.35	25.56	0.34	27.90	0.52
TiO_2	0.01	0.02	0.03	0.01	0.12	0.09	0.02	0.01	0.04	0.03
Al_2O_3	19.40	0.94	19.07	0.28	18.67	1.15	19.56	0.38	18.32	0.36
FeO	18.10	0.32	37.34	0.25	35.16	0.90	29.20	0.37	25.63	0.89
MnO	0.20	0.01	0.80	0.03	0.38	0.04	0.45	0.03	0.39	0.02
MgO	21.32	0.41	7.09	0.20	7.77	0.75	11.54	0.22	16.06	0.76
CaO	0.02	0.02	0.02	0.01	0.07	0.03	0.02	0.02	0.05	0.01
Na_2O	0.00	0.00	0.00	0.01	0.01	0.03	0.00	0.00	0.00	0.00
K_2O	0.07	0.06	0.09	0.06	0.19	0.26	0.02	0.01	0.01	0.01
H_2O	11.94	0.56	10.89	0.45	12.14	0.42	13.62	1.21	11.61	0.53
Total	100.00	0.00	100.00	0.00	100.00	0.00	100.00	0.00	100.00	0.00
Si	5.81	0.14	5.49	0.04	5.68	0.25	5.60	0.02	5.83	0.08
Al^{IV}	2.19	0.14	2.51	0.04	2.32	0.25	2.40	0.02	2.17	0.08
T sites	8.00	0.00	8.00	0.00	8.00	0.00	8.00	0.00	8.00	0.00
Al^{VI}	2.40	0.10	2.50	0.04	2.58	0.10	2.65	0.03	2.34	0.03
Ti	0.00	0.00	0.00	0.00	0.02	0.02	0.00	0.00	0.01	0.00
Fe^{2+}	3.04	0.06	6.96	0.05	6.55	0.24	5.35	0.04	4.48	0.19
Mn	0.03	0.00	0.15	0.01	0.07	0.01	0.08	0.01	0.07	0.00
Mg	6.39	0.11	2.36	0.06	2.58	0.22	3.77	0.04	5.00	0.20
Ca	0.00	0.00	0.01	0.00	0.02	0.01	0.01	0.00	0.01	0.00
Na	0.00	0.00	0.00	0.00	0.00	0.01	0.00	0.00	0.00	0.00
K	0.02	0.02	0.02	0.02	0.05	0.07	0.01	0.00	0.00	0.00
cations	19.89	0.02	20.00	0.02	19.87	0.05	19.87	0.02	19.91	0.03
F	0.02	0.03	0.07	0.04	0.10	0.03	0.03	0.03	0.03	0.03
Cl	0.05	0.01	0.02	0.01	0.01	0.00	0.02	0.01	0.02	0.01
OH	0.00	0.00	0.00	0.00	0.00	0.00	0.00	0.00	0.00	0.00
O	36.00	0.00	36.00	0.00	36.00	0.00	36.00	0.00	36.00	0.00
Fe#	0.32	0.01	0.75	0.01	0.72	0.02	0.59	0.00	0.47	0.02
Mg#	0.68	0.01	0.25	0.01	0.28	0.02	0.41	0.00	0.53	0.02

Cation calculated on the basis of 36 (O, OH, F, Cl)

Table 4-4 (cont'd). Average EMPA data for chlorite from the Nickel Rim South deposit.

	117-46 n=8 PFZ avg	diss 1σ	117-46 n=14 PFZ avg	massive 1σ	104a-33 n=8 PFZ avg	vein 1σ	104a-4 n=3 DFZ avg	diss 1σ	104a-4 n=3 DFZ avg	repl. Bt 1σ
SiO_2	26.05	0.62	25.93	0.57	25.65	0.23	27.97	0.20	27.39	0.66
TiO_2	0.07	0.15	0.23	0.18	0.02	0.01	0.04	0.03	0.06	0.01
Al_2O_3	19.20	0.68	18.95	0.81	18.96	0.15	19.36	0.45	19.70	0.62
FeO	28.63	1.04	30.13	0.75	34.87	0.18	21.64	0.25	22.21	0.29
MnO	0.42	0.02	0.44	0.03	0.47	0.03	0.48	0.02	0.50	0.02
MgO	12.03	0.62	11.38	0.48	8.21	0.24	18.78	0.17	18.18	0.62
CaO	0.04	0.06	0.09	0.05	0.02	0.01	0.08	0.04	0.05	0.02
Na_2O	0.00	0.00	0.00	0.00	0.00	0.00	0.00	0.00	0.00	0.00
K_2O	0.02	0.02	0.05	0.06	0.01	0.01	0.01	0.01	0.01	0.01
H_2O	13.55	1.11	12.80	1.06	11.80	0.28	11.64	0.61	11.91	0.63
Total	100.00	0.00	100.00	0.00	100.00	0.00	100.00	0.00	100.00	0.00
Si	5.68	0.12	5.66	0.13	5.67	0.04	5.72	0.06	5.64	0.09
Al^{IV}	2.32	0.12	2.34	0.13	2.33	0.04	2.28	0.06	2.36	0.09
T sites	8.00	0.00	8.00	0.00	8.00	0.00	8.00	0.00	8.00	0.00
Al^{VI}	2.61	0.07	2.52	0.06	2.60	0.03	2.39	0.03	2.43	0.09
Ti	0.01	0.02	0.04	0.03	0.00	0.00	0.01	0.00	0.01	0.00
Fe^{2+}	5.22	0.17	5.49	0.12	6.45	0.06	3.70	0.03	3.83	0.07
Mn	0.08	0.00	0.08	0.00	0.09	0.01	0.08	0.00	0.09	0.00
Mg	3.91	0.21	3.70	0.17	2.70	0.07	5.73	0.04	5.58	0.16
Ca	0.01	0.01	0.02	0.01	0.01	0.00	0.02	0.01	0.01	0.00
Na	0.00	0.00	0.00	0.00	0.00	0.00	0.00	0.00	0.00	0.00
K	0.01	0.01	0.01	0.02	0.00	0.00	0.00	0.00	0.00	0.00
cations	19.84	0.03	19.87	0.03	19.85	0.02	19.93	0.02	19.95	0.01
F	0.02	0.02	0.04	0.04	0.03	0.03	0.09	0.06	0.07	0.03
Cl	0.01	0.01	0.01	0.01	0.06	0.02	0.00	0.01	0.01	0.01
OH	0.00	0.00	0.00	0.00	0.00	0.00	0.00	0.00	0.00	0.00
O	36.00	0.00	36.00	0.00	36.00	0.00	36.00	0.00	36.00	0.00
Fe#	0.57	0.02	0.60	0.02	0.70	0.01	0.39	0.01	0.40	0.01
Mg#	0.43	0.02	0.40	0.02	0.30	0.01	0.61	0.01	0.60	0.01

Cation calculated on the basis of 36 (O, OH, F, Cl)

Table 4-5. Average EMPA data for biotite from the Nickel Rim South deposit.

	170110-36 n=3 CZ		124c-73 n=4 CZ		104a-33 n=8 PFZ	
	avg	σ	avg	σ	avg	σ
SiO_2	38.47	0.06	35.59	0.96	37.39	0.23
TiO_2	4.59	0.14	2.15	0.76	3.63	0.29
Al_2O_3	12.99	0.06	13.92	0.56	13.37	0.16
Cr_2O_3	0.05	0.02	0.03	0.01	0.02	0.01
FeO	17.39	0.18	28.07	0.73	21.23	0.77
MnO	0.16	0.01	0.39	0.03	0.23	0.01
MgO	12.89	0.11	6.49	0.37	10.39	0.52
BaO	0.00	0.00	0.00	0.00	0.00	0.00
CaO	0.01	0.01	0.10	0.08	0.03	0.02
Na_2O	0.02	0.01	0.03	0.02	0.01	0.02
K_2O	9.70	0.15	8.61	0.68	9.76	0.12
F	0.32	0.04	0.19	0.08	0.70	0.09
Cl	0.33	0.02	0.22	0.02	0.28	0.02
H_2O	3.06	0.02	4.22	0.05	2.96	0.04
Subtotal	100.00	0.27	100.00	0.82	100.00	0.15
O = F, Cl	0.21	0.02	0.13	0.04	0.36	0.04
Total	99.79	0.25	99.87	0.78	99.64	0.11
Si	6.02	0.01	5.92	0.10	5.99	0.02
Al^{IV}	1.98	0.01	2.08	0.10	2.01	0.02
Al^{VI}	0.41	0.02	0.65	0.06	0.51	0.03
Ti	0.54	0.02	0.27	0.09	0.44	0.03
Fe^{2+}	2.28	0.02	3.91	0.14	2.84	0.11
Cr	0.01	0.00	0.00	0.00	0.00	0.00
Mn	0.02	0.00	0.05	0.00	0.03	0.00
Mg	3.01	0.03	1.61	0.10	2.48	0.12
Ba	0.00	0.00	0.00	0.00	0.00	0.00
Ca	0.00	0.00	0.02	0.01	0.00	0.00
Na	0.01	0.00	0.01	0.01	0.00	0.01
K	1.94	0.03	1.83	0.13	2.00	0.03
cations	16.21	0.00	16.35	0.05	16.31	0.03
F	0.32	0.04	0.20	0.08	0.71	0.09
Cl	0.18	0.01	0.12	0.01	0.15	0.01
Cl/F	0.16	0.02	0.06	0.04	0.35	0.04
Cl/(Cl+F)	0.09	0.00	0.06	0.01	0.07	0.00
OH	1.75	0.02	1.84	0.05	1.57	0.04
Fe#	0.43	0.00	0.71	0.01	0.53	0.02
Mg#	0.57	0.00	0.29	0.01	0.47	0.02

Cations calculated on the basis of 24 (O, OH, F, Cl)

Table 4-6. Average trace element chemistry for epidote from the Nickel Rim South deposit.

	NRS-170110-36				NRS-124c-73 cpy vein selvage				NRS-104a-33 massive sulfide			
Zone	CZ				CZ				PFZ			
Lithology	FNOR				GAB				CBF			
Mineralized	y				y				y			
Textural Variety	1				2				1			
REE pattern	1				1				1			
n=	9				4				3			
	avg	1σ	min	max	avg	1σ	min	max	avg	1σ	min	max
Ca	7158889	477243	6400000	8050000	9267500	548718	8610000	9730000	9472857	278670	8960000	9720000
Ti	654	278	323	1191	222	31	195	259	229	96	134	399
V	122	32	92	190	382	52	307	418	33	42	10	128
Cr	9.3	3.1	5.1	14.0	28.9	16.3	16.9	53.0	4.2	1.4	2.6	6.7
Fe	63800	4314	57400	71200	91225	2347	88000	93600	82600	2379	79000	86300
Co	0.54	0.17	0.27	0.83	0.42	0.38	0.15	0.98	0.41	0.54	0.15	1.62
Ni	14.4	6.3	3.3	24.7	30.8	12.8	17.6	42.4	14.3	9.4	7.6	25.0
Cu	6.3	9.1	0.2	28.0	41.0	30.3	7.0	69.0	50.5	44.7	2.5	91.0
Zn	17.0	24.9	1.2	76.0	18.5	17.1	2.7	37.0	26.1	16.9	3.2	46.0
Ga	40.8	5.8	35.4	52.3	48.8	2.1	46.5	51.5	65.3	7.1	54.9	72.9
Sr	1784	370	1147	2295	2531	585	1855	3229	2637	769	1583	4033
La	110	64	25	221	41	28	14	78	71	39	25	130
Ce	178	95	44	324	78	45	29	133	96	55	31	172
Pr	20.7	11.8	5.3	40.9	8.5	4.1	3.3	12.6	8.7	4.9	2.8	15.3
Sm	14.8	9.4	4.8	30.2	4.9	1.8	2.3	6.4	3.0	1.5	0.9	5.2
Eu	6.7	4.0	2.2	12.3	2.1	0.8	1.2	3.2	4.9	1.7	2.3	7.3
Gd	10.7	6.2	3.9	20.3	3.5	1.2	1.7	4.3	1.4	0.7	0.4	2.5
Ho	1.3	0.7	0.5	2.7	0.5	0.2	0.3	0.6	0.1	0.0	0.1	0.2
Yb	3.6	2.9	0.9	10.7	1.8	1.0	1.1	3.2	0.4	0.1	0.2	0.6
Lu	0.59	0.63	0.15	2.16	0.30	0.17	0.18	0.55	0.06	0.03	0.04	0.09
^{204}Pb	4.8	2.3	2.4	8.7	49.6	8.7	37.4	56.2	337.2	316.9	125.0	1020.0
^{206}Pb	8.5	2.8	4.4	12.7	42.7	7.0	34.1	49.9	293.7	279.4	102.7	900.0
^{207}Pb	4.6	1.4	3.1	7.1	47.0	8.1	36.9	54.9	333.7	324.9	117.9	1040.0
^{208}Pb	4.6	2.0	2.3	8.5	46.3	7.8	36.2	53.7	323.3	304.4	113.8	980.0
Th	1.3	1.1	0.0	3.6	0.8	1.0	0.1	2.2	0.4	0.5	0.0	1.1
U	3.6	1.9	1.1	6.9	0.5	0.2	0.3	0.8	1.0	0.9	0.1	2.5

Table 4-6 (cont'd). Average trace element chemistry for epidote from the Nickel Rim South deposit.

	NRS-170110-2				NRS-170110-9				NRS-170110-9			
Zone	PFZ				PFZ				PFZ			
Lithology	CBF				CBF				CBF			
Mineralized	n				n				n			
Textural Variety	4				4				4			
REE pattern	3				1				3			
n=	15				2				11			
	avg	1σ	min	max	avg	1σ	min	max	avg	1σ	min	max
Ca	8852000	408765	8140000	9420000	9945000	106066	9870000	10020000	9391818	464819	8820000	10250000
Ti	19	13	5	48	29	10	22	36	27	39	7	143
V	198	109	41	414	34	4	31	36	174	144	51	555
Cr	3.1	0.7	1.9	4.6	4.1	0.1	4.0	4.2	15.9	39.9	2.7	136.0
Fe	89540	5036	83400	101300	91350	71	91300	91400	98527	7855	84700	114200
Co	0.12	0.09	0.06	0.45	0.06	0.02	0.05	0.07	0.98	2.86	0.06	9.60
Ni	0.4	0.2	0.1	0.8	0.7	0.1	0.7	0.8	1.2	1.6	0.3	5.7
Cu	3.8	5.2	0.1	21.0	0.9	0.0	0.9	0.9	11.1	16.4	0.4	56.0
Zn	16.9	36.4	0.9	140.0	2.7	0.2	2.5	2.8	19.5	21.2	1.5	68.0
Ga	82.5	9.1	71.1	96.0	61.0	1.3	60.1	61.9	65.4	7.1	50.1	75.4
Sr	6652	1471	4824	9980	6312	1146	5501	7122	7742	2379	4185	13280
La	282	183	74	604	21	3	19	24	248	133	35	462
Ce	520	303	151	1039	25	4	22	28	455	244	58	863
Pr	60.8	34.3	17.5	119.2	2.4	0.4	2.2	2.7	53.8	28.3	7.0	101.0
Sm	43.4	25.2	10.6	80.1	1.7	0.4	1.5	2.0	36.9	19.1	5.6	70.0
Eu	12.3	8.3	3.0	32.5	2.9	0.5	2.6	3.2	7.9	4.5	2.0	17.5
Gd	27.1	17.4	5.2	55.2	1.6	0.5	1.2	1.9	22.4	11.7	4.2	42.9
Ho	1.5	1.0	0.3	3.3	0.2	0.0	0.2	0.2	1.3	0.7	0.4	2.5
Yb	1.8	1.3	0.6	4.3	0.3	0.0	0.2	0.3	1.1	0.6	0.3	2.3
Lu	0.26	0.20	0.09	0.63	0.03	0.00	0.03	0.04	0.13	0.07	0.04	0.25
^{204}Pb	6.7	1.5	4.7	9.0	11.9	0.4	11.6	12.1	15.3	19.1	5.6	71.0
^{206}Pb	8.1	3.9	3.4	17.1	9.6	0.4	9.4	9.9	13.7	17.1	4.4	63.0
^{207}Pb	6.3	1.7	3.3	9.3	10.2	0.1	10.1	10.3	14.7	18.7	4.8	69.0
^{208}Pb	6.0	1.5	3.3	8.6	10.4	0.3	10.2	10.6	15.0	18.2	5.0	68.0
Th	1.4	1.6	0.1	5.8	0.0	0.0	0.0	0.0	0.7	1.6	0.0	5.6
U	2.3	2.5	0.3	9.1	0.1	0.0	0.1	0.1	0.2	0.2	0.1	0.6

Table 4-6 (cont'd). Average trace element chemistry for epidote from the Nickel Rim South deposit.

	NRS-117-29				NRS-117-46				NRS-124c-23			
Zone	PFZ				PFZ				DFZ			
Lithology	CBF				SUDBX				CBF			
Mineralized	n				n				n			
Textural Variety	3				3				2			
REE pattern	1				1				1			
n=	8				4				9			
	avg	1σ	min	max	avg	1σ	min	max	avg	1σ	min	max
Ca	9457500	560274	8880000	10380000	9535000	184300	9390000	9790000	6418889	347507	5750000	6890000
Ti	470	373	62	1157	271	270	98	673	352	323	122	940
V	120	71	53	263	18	8	8	25	401	42	348	483
Cr	8.0	6.3	2.5	18.6	4.0	1.8	2.6	6.7	573.6	211.1	248.3	1032.0
Fe	85675	5458	76800	91400	85425	3197	81000	88300	86822	3095	82500	93400
Co	1.45	0.82	0.40	2.46	0.62	0.24	0.32	0.90	0.29	0.20	0.18	0.80
Ni	16.4	12.5	5.5	44.9	36.2	13.3	17.3	46.9	4.1	2.1	1.9	7.4
Cu	11.2	11.8	0.8	30.0	43.8	25.4	22.1	76.0	14.9	10.4	2.5	31.0
Zn	19.2	19.6	2.4	61.0	43.5	19.5	19.0	62.0	36.1	26.9	11.0	100.0
Ga	67.4	6.8	51.9	73.8	34.8	3.6	29.8	37.6	90.2	7.5	83.2	107.8
Sr	2013	1205	790	4449	2821	106	2669	2913	6078	660	4790	6950
La	41	30	14	105	86	79	14	190	145	65	77	290
Ce	66	52	18	178	88	78	21	193	266	125	140	541
Pr	7.4	5.6	2.0	19.1	7.0	6.0	2.3	15.3	31.4	14.5	17.5	63.5
Sm	5.9	3.5	2.6	11.2	3.0	2.5	1.4	6.8	24.1	10.6	14.7	48.6
Eu	3.6	1.6	1.3	6.6	5.0	2.0	3.5	8.0	10.2	4.2	6.0	20.5
Gd	4.7	2.7	1.8	8.3	2.1	1.7	0.9	4.7	15.8	6.9	9.3	32.1
Ho	0.5	0.3	0.2	1.0	0.3	0.3	0.1	0.7	1.5	0.5	0.9	2.7
Yb	0.9	0.4	0.3	1.3	0.6	0.6	0.3	1.5	2.1	0.4	1.5	2.9
Lu	0.12	0.06	0.04	0.21	0.07	0.06	0.03	0.16	0.29	0.05	0.21	0.36
^{204}Pb	9.6	5.3	5.0	17.9	32.2	15.1	15.7	50.8	12.5	4.6	6.8	19.8
^{206}Pb	9.3	4.6	4.4	16.6	27.9	17.9	12.3	52.9	11.5	4.0	6.6	17.1
^{207}Pb	8.5	4.9	4.4	16.5	27.6	15.1	12.5	47.6	11.1	4.1	6.5	17.7
^{208}Pb	8.6	5.0	4.4	16.6	26.7	14.4	11.8	45.4	11.9	5.0	6.5	19.1
Th	0.8	0.9	0.0	2.4	1.2	1.0	0.1	2.6	5.2	13.4	0.2	40.9
U	1.1	0.7	0.3	2.4	2.6	3.5	0.2	7.7	0.9	0.3	0.7	1.6

Table 4-6 (cont'd). Average trace element chemistry for epidote from the Nickel Rim South deposit.

	NRS-104a-2b				NRS-104a-2b				NRS-104a-9			
Zone	DFZ				DFZ				DFZ			
Lithology	CBF				CBF				CBF			
Mineralized	n				n				n			
Textural Variety	4				4				2			
REE pattern	1				2				2			
n=	5				4				9			
	avg	1σ	min	max	avg	1σ	min	max	avg	1σ	min	max
Ca	10820000	151162	10660000	11020000	10722500	68007	10650000	10790000	7101111	341703	6630000	7630000
Ti	194	44	143	250	148	23	124	175	279	65	159	360
V	583	158	388	774	342	47	306	410	82	14	63	115
Cr	43.0	29.9	12.9	84.8	57.0	7.7	49.2	64.1	4.2	1.4	1.8	6.4
Fe	92940	1195	91600	94600	94475	4814	88000	99100	82378	2028	78600	85200
Co	0.11	0.09	0.04	0.23	0.05	0.02	0.04	0.08	0.07	0.06	0.02	0.20
Ni	2.2	1.8	0.9	5.3	1.5	0.6	1.0	2.4	1.1	0.7	0.5	2.1
Cu	9.7	7.6	1.4	19.0	6.1	4.1	0.6	10.3	6.0	7.9	1.8	27.0
Zn	14.6	8.5	2.5	26.0	18.3	8.6	13.0	31.0	17.8	27.0	3.4	85.0
Ga	104.4	12.6	91.4	120.0	85.0	5.0	80.2	91.3	43.0	2.0	39.3	45.7
Sr	6528	602	5655	7240	7765	1261	6650	9070	4137	354	3861	5016
La	13	5	5	19	30	13	13	45	5	8	1	25
Ce	24	9	9	30	45	22	20	72	10	15	3	49
Pr	3.2	1.2	1.2	4.2	4.8	2.3	2.4	7.7	1.3	1.9	0.4	6.3
Sm	5.3	2.5	1.7	7.8	3.7	0.8	2.7	4.6	1.6	1.9	0.6	6.5
Eu	2.6	0.5	1.8	2.9	4.4	2.2	2.3	7.5	0.4	0.4	0.1	1.3
Gd	7.7	3.5	2.8	11.5	4.1	0.3	3.9	4.5	1.5	1.3	0.6	4.9
Ho	1.8	0.9	0.8	2.9	0.8	0.1	0.7	0.8	0.3	0.1	0.1	0.5
Yb	3.9	1.8	1.8	6.4	1.4	0.3	1.1	1.6	0.7	0.2	0.3	1.0
Lu	0.56	0.25	0.24	0.86	0.21	0.04	0.15	0.23	0.10	0.03	0.04	0.14
^{204}Pb	13.4	5.0	9.2	21.0	17.8	6.1	12.7	25.4	28.9	3.7	23.0	34.4
^{206}Pb	12.3	5.0	8.1	20.3	15.8	5.6	11.4	23.3	25.4	2.5	20.9	29.0
^{207}Pb	11.9	5.0	7.8	19.7	15.2	5.7	10.5	22.7	27.4	2.5	22.8	30.6
^{208}Pb	11.9	5.0	7.9	19.8	15.4	5.9	10.4	23.2	26.7	2.9	21.8	31.3
Th	0.0	0.0	0.0	0.1	0.1	0.1	0.0	0.3	0.0	0.0	0.0	0.0
U	0.6	0.1	0.4	0.8	0.7	0.3	0.4	1.1	0.3	0.1	0.1	0.5

Table 4-6 (cont'd). Average trace element chemistry for epidote from the Nickel Rim South deposit.

	NRS-117-1				NRS-124c-4				NRS-124c-11			
Zone	DFZ				DFZ				DFZ			
Lithology	CBF				CBF				CBF			
Mineralized	n				n				n			
Textural Variety	3				3				2			
REE pattern									1			
n=	9				16				6			
	avg	1σ	min	max	avg	1σ	min	max	avg	1σ	min	max
Ca	7331111	422328	6450000	7690000	9385625	718498	7770000	10810000	8625000	227662	8330000	9010000
Ti	176	135	41	433	176	135	41	433	119	30	82	167
V	274	65	209	426	274	65	209	426	221	35	190	265
Cr	17.7	10.3	5.5	35.3	17.7	10.3	5.5	35.3	26.3	4.9	21.2	33.1
Fe	79160	6268	69200	88400	79160	6268	69200	88400	86317	1656	83100	87800
Co	0.26	0.11	0.13	0.43	0.26	0.11	0.13	0.43	0.10	0.03	0.07	0.14
Ni	2.3	0.8	1.0	3.6	2.3	0.8	1.0	3.6	1.1	0.3	0.8	1.5
Cu	8.3	11.1	1.1	31.0	8.3	11.1	1.1	31.0	7.1	10.2	0.6	23.0
Zn	23.1	35.3	2.7	114.0	23.1	35.3	2.7	114.0	16.7	22.4	2.1	52.0
Ga	79.3	15.9	61.2	109.6	79.3	15.9	61.2	109.6	110.0	4.1	102.8	114.1
Sr	4886	978	3587	6448	4886	978	3587	6448	7293	785	6180	8160
La	69	49	20	172	69	49	20	172	314	99	200	423
Ce	114	69	42	256	114	69	42	256	411	132	253	546
Pr	13.5	7.4	5.3	27.9	13.5	7.4	5.3	27.9	38.5	11.4	24.9	49.6
Sm	13.6	5.7	4.7	19.6	13.6	5.7	4.7	19.6	17.0	3.8	13.2	21.6
Eu	8.4	6.6	2.5	20.9	8.4	6.6	2.5	20.9	16.2	4.0	11.2	21.2
Gd	10.6	3.6	3.8	15.7	10.6	3.6	3.8	15.7	9.8	1.7	7.9	12.0
Ho	1.0	0.3	0.7	1.5	1.0	0.3	0.7	1.5	0.7	0.1	0.6	0.9
Yb	2.0	1.0	1.0	4.4	2.0	1.0	1.0	4.4	1.2	0.2	0.9	1.4
Lu	0.29	0.14	0.14	0.62	0.29	0.14	0.14	0.62	0.15	0.02	0.13	0.18
^{204}Pb	14.9	11.5	4.5	41.1	14.9	11.5	4.5	41.1	9.1	0.9	8.3	10.6
^{206}Pb	16.4	11.1	5.6	39.3	16.4	11.1	5.6	39.3	10.1	0.8	9.3	11.0
^{207}Pb	13.9	11.0	4.6	39.1	13.9	11.0	4.6	39.1	8.9	1.0	7.5	10.3
^{208}Pb	13.3	10.4	4.3	37.2	13.3	10.4	4.3	37.2	8.1	1.2	6.4	9.9
Th	0.2	0.2	0.0	0.6	0.2	0.2	0.0	0.6	0.1	0.2	0.0	0.4
U	3.0	2.2	0.7	7.8	3.0	2.2	0.7	7.8	2.1	0.3	1.7	2.6

Table 4-6 (cont'd). Average trace element chemistry for epidote from the Nickel Rim South deposit.

	NRS-124c-11			
Zone	DFZ			
Lithology	CBF			
Mineralized	n			
Textural Variety	3			
REE pattern	3			
n=	2			
	avg	1σ	min	max
Ca	8775000	190919	8640000	8910000
Ti	124	37	98	151
V	342	18	329	354
Cr	39.9	6.7	35.1	44.6
Fe	88600	283	88400	88800
Co	0.22	0.04	0.19	0.24
Ni	3.7	3.6	1.1	6.3
Cu	4.5	4.5	1.3	7.7
Zn	10.4	2.5	8.6	12.2
Ga	94.6	12.7	85.6	103.5
Sr	5025	884	4400	5650
La	51	19	37	64
Ce	82	30	60	103
Pr	10.0	3.9	7.2	12.7
Sm	10.4	4.4	7.3	13.5
Eu	3.3	1.6	2.2	4.4
Gd	8.9	4.2	5.9	11.8
Ho	1.1	0.5	0.8	1.5
Yb	1.7	0.4	1.5	2.0
Lu	0.24	0.05	0.20	0.27
^{204}Pb	35.3	8.1	29.5	41.0
^{206}Pb	36.0	9.4	29.3	42.6
^{207}Pb	36.4	10.0	29.3	43.5
^{208}Pb	39.2	9.3	32.6	45.7
Th	0.1	0.1	0.0	0.1
U	2.0	0.1	1.9	2.1

Table 4-7. Textural, chemical, and spatial characteristics of epidote at the Nickel Rim South deposit.

Lithology	REE Pattern	Textural Variety	Zone	n=
CBF	1, 2, 3	1, 2, 3, 4, 5	P, D	154
Sudbury breccia	1	4, 5	P, D	9
gabbro	1	1, 2	C	9
felsic norite	1	1	C	12

Zone	Lithology	REE Pattern	Textural Variety	n=
Contact zone	CBF, GAB	1	1, 2, 5	21
Proximal footwall zone	CBF, SUDBX	1, 3	1, 4, 5	55
Distal footwall zone	CBF	1, 2, 3	1, 2, 3, 4, 5	63

Textural Variety	Lithology	REE Pattern	Zone	n=
1	CBF, FNOR, GAB	1	C, P, D	26
2	CBF, GAB	1, 2	C, D	30
3	CBF, GAB	1, 3	D	28
4	CBF, SUDBX	1, 2, 3	P, D	55
5	CBF, SUDBX	n/a	C, P, D	n/a

REE Pattern	Lithology	Textural Variety	Zone	n=
1	CBF, SUDBX, GAB, FNOR	1, 2, 3, 4	C, P, D	87
2	CBF	2, 4	D	12
3	CBF	3, 4	P, D	29

Legend

Textural Variety	Description
1	disseminated, mg to cg
2	vein (cg)
3	vein (fg)
4	open space fill, cg, blocky
5	pit-hosted (in plagioclase)

REE Pattern	
1	Steep slope, +Eu*
2	Flat slope, no Eu*
3	Shallow slope LREE, steep slope Gd-Yb

Zone	
C	contact zone
P	proximal footwall zone
D	distal footwall zone

Table 4-8. Summary of microthermometric data measured fluid inclusions from the Nickel Rim South deposit. List of abbreviations: FIA – fluid inclusion assemblage; Tf – freezing temperature; Te – eutectic temperature; Tm(ice) ice melting temperature; Tm(halite) halite melting temperature; Th – homogenization temperature; homo. type – homogenization to dew point (DP; vapour) or bubble point (BP; liquid); Tt – trapping temperature; Pbulk – bulk density in g/cm^3; salinity is reported in wt. % equiv. NaCl.

Zone	Sample	Fluid Inclusion Type	# FIA (FIs)	Tf mean range	Te mean range	Tm(ice) mean range	Tm(halite) mean range	Th(L-V) mean range	Th(total) mean range	Hom. Type V of H	Tt mean range	ρ_{bulk}	Salinity (NaCl)
PFZ	NRS-124c-64	T1	2	-66.5 -72 to -61	-23.2 -27.1 to -20.7	-18.6 -19.6 to -17.9		222 189 to 243	222 189 to 243	V	321	1.012	21.37
PFZ	NRS-117-26	T1	1	-70.5 -71 to -67	-19.5 -22.8 to -18.2	-17.4 -19.8 to -16.1		237 226 to 245	237 226 to 245	V	342	0.99	20.52
PFZ	NRS-117-29	T1	2	-70 -75 to -64	-18.5 -21.5 to 17.9	-17.4 -19.5 to -16.5		158 142 to 169	158 142 to 169	V	239	1.06	20.49
PFZ	NRS-124c-64	T2	1	-72 -79 to -66	-22.2 -23.5 to -21.3	-19.7 -21.6 to -18.7	247 231 to 251	164 158 to 169	247 231 to 251	H	285	1.071	35.38
PFZ	NRS-117-26	T2	1	-74 -81 to -68	-18.4 -19.8 to -17.4	-21.5 -22.8 to -20.6	253 235 to 260	208 190 to 216	253 235 to 260	H	295	1.043	35.44
PFZ	NRS-117-29	T2	1	-76 -78 to -70	-26.4 -29.7 to -23.1	-22 -23.6 to -20	218 210 to 224	158 145 to 174	218 210 to 224	H	241	1.089	33.54
PFZ	NRS-117-35	T2	1	-71 -75 to -61	-19.8 -21.6 to -18.9	-20.6 -21.7 to -19.3	239 233 to 248	131 127 to 139	239 233 to 248	H	271	1.103	34.82
PFZ	NRS-117-26	T3	1	-75 -79 to -72	-22.1 -24.5 to -20.5	-21.5 -23.5 to -20.2		323 315 to 329		V	455	0.926	23.37
DFZ	NRS-117-9	T3	1	-70 -71 to -68	-18.5 -19.7 to -17.4	-19.7 -21.2 to -19.2		321 316 to 327		V	455	0.917	22.17

Table 4-9. Summary of evaporate mound chemistry from decrepitated fluid inclusions from the Nickel Rim South deposit. Data are normalized to 100%. Abbreviation: b.d.l = below detection limit.

Sample	Analysis	Lithology	Zone	Cl	Na	Ca	K	Mn	Fe	SUM
170110-2	1	CBF	PFZ	52.7	34.6	12.7	0.0	0.0	0.0	100
170110-2	2	CBF	PFZ	50.8	46.4	2.8	0.0	0.0	0.0	100
170110-2	3	CBF	PFZ	51.0	41.1	7.9	0.0	0.0	0.0	100
170110-2	4	CBF	PFZ	49.5	40.6	9.4	0.5	0.0	0.0	100
170110-2	5	CBF	PFZ	54.8	40.2	4.4	0.6	0.0	0.0	100
170110-2	6	CBF	PFZ	51.5	40.2	8.3	0.0	0.0	0.0	100
170110-2	7	CBF	PFZ	50.5	40.0	7.9	1.1	0.5	0.0	100
170110-2	8	CBF	PFZ	50.1	40.4	7.9	1.1	0.5	0.0	100
170110-2	9	CBF	PFZ	49.1	43.3	5.7	1.9	0.0	0.0	100
117-29	1	CBF	PFZ	52.8	25.4	21.8	0.0	0.0	0.0	100
117-29	2	CBF	PFZ	50.7	43.2	6.1	0.0	0.0	0.0	100
117-29	3	CBF	PFZ	50.1	26.3	20.2	3.4	0.0	0.0	100
117-29	4	CBF	PFZ	52.0	26.8	15.4	5.0	0.9	0.0	100
117-29	5	CBF	PFZ	54.8	21.7	18.1	4.8	0.6	0.0	100
117-29	6	CBF	PFZ	50.7	32.5	10.9	3.9	1.3	0.6	100
117-29	7	CBF	PFZ	56.4	26.2	10.0	4.5	2.2	0.8	100
117-29	8	CBF	PFZ	50.7	28.3	17.3	3.7	0.0	0.0	100
117-29	9	CBF	PFZ	53.7	24.7	16.1	3.6	1.3	0.5	100
117-29	10	CBF	PFZ	51.5	25.2	20.6	2.7	0.0	0.0	100
117-29	11	CBF	PFZ	55.2	36.5	7.6	0.6	0.0	0.0	100
117-29	12	CBF	PFZ	53.2	32.3	14.0	0.5	0.0	0.0	100
117-29	13	CBF	PFZ	49.2	36.9	13.3	0.6	0.0	0.0	100
117-29	14	CBF	PFZ	51.6	32.8	14.5	0.0	1.1	0.0	100
117-29	15	CBF	PFZ	47.0	34.3	13.9	1.8	2.2	0.7	100
117-29	16	CBF	PFZ	51.5	31.2	15.0	1.3	1.0	0.0	100
117-29	17	CBF	PFZ	50.6	39.3	8.7	0.8	0.6	0.0	100
117-29	18	CBF	PFZ	51.0	37.0	8.8	1.5	0.8	0.8	100
117-29	19	CBF	PFZ	53.0	34.4	8.7	1.4	1.6	0.9	100
117-29	20	CBF	PFZ	44.7	22.9	32.4	0.0	0.0	0.0	100
117-29	21	CBF	PFZ	53.1	33.3	6.9	3.8	2.0	0.9	100
117-29	22	CBF	PFZ	50.5	40.1	6.3	2.6	0.0	0.6	100
117-29	23	CBF	PFZ	50.1	26.3	16.8	4.3	1.8	0.8	100
117-29	24	CBF	PFZ	51.8	31.1	13.2	2.1	1.2	0.8	100
117-29	25	CBF	PFZ	51.3	26.1	16.8	4.1	1.2	0.6	100
117-29	26	CBF	PFZ	50.7	27.5	18.6	2.4	0.8	0.0	100
117-29	27	CBF	PFZ	50.2	31.5	15.0	2.6	0.8	0.0	100
117-29	28	CBF	PFZ	52.4	32.9	13.5	0.8	0.5	0.0	100
104a-4	1	CBF	DFZ	45.5	46.6	7.9	0.0	0.0	0.0	100
104a-4	2	CBF	DFZ	48.4	45.2	6.4	0.0	0.0	0.0	100
104a-4	3	CBF	DFZ	50.4	44.6	4.5	0.6	0.0	0.0	100
117-9	1	CBF	DFZ	48.7	39.9	11.4	0.0	0.0	0.0	100
117-9	2	CBF	DFZ	44.4	41.5	14.2	0.0	0.0	0.0	100
117-9	3	CBF	DFZ	52.0	39.7	7.2	1.2	0.0	0.0	100
117-9	4	CBF	DFZ	50.8	34.6	12.6	1.0	0.0	1.0	100
117-9	5	CBF	DFZ	45.5	32.1	19.9	0.6	0.6	1.3	100
117-9	6	CBF	DFZ	48.6	26.6	16.0	7.0	0.6	1.2	100
117-9	7	CBF	DFZ	47.3	36.0	13.8	2.3	0.0	0.6	100
117-9	8	CBF	DFZ	49.1	38.4	9.3	1.4	0.7	1.1	100
117-9	9	CBF	DFZ	47.5	34.3	12.9	1.7	1.8	1.8	100
117-9	10	CBF	DFZ	52.0	34.4	9.1	3.0	0.9	0.6	100
117-9	11	CBF	DFZ	52.9	32.6	11.3	1.0	1.7	0.6	100
117-9	12	CBF	DFZ	52.1	36.0	8.6	1.1	2.1	0.0	100
117-9	13	CBF	DFZ	50.4	24.8	18.5	3.3	2.4	0.5	100
117-9	14	CBF	DFZ	52.2	31.8	12.3	2.2	1.5	0.0	100
117-9	15	CBF	DFZ	50.8	29.3	14.2	3.5	2.2	0.0	100
117-9	16	CBF	DFZ	48.9	29.9	15.6	3.1	2.4	0.0	100
117-9	17	CBF	DFZ	53.7	30.5	12.8	0.9	2.0	0.0	100
117-9	18	CBF	DFZ	51.6	37.4	9.3	1.0	0.7	0.0	100
117-9	19	CBF	DFZ	53.4	41.5	2.6	1.1	0.6	0.8	100
117-9	20	CBF	DFZ	51.3	40.0	5.2	1.2	1.1	1.1	100

Table 4-10. Summary of quartz oxygen isotope ($\delta^{18}O_{quartz}$) values for five samples from the Nickel Rim South deposit. Abbreviations: SUDBX – Sudbury breccia; CBF - coherent to in situ brecciated felsic igneous rock; MNOR – mafic norite; CZ – contact zone; PFZ – proximal footwall zone.

Sample	Rock Type	Zone	Grain	Analysis	$\delta^{18}O_{qtz}$ (‰)	1σ	Reproducibility
NRS-117-26	SUDBX	PFZ	1	1	8.6	1.2	0.7
NRS-117-26	SUDBX	PFZ	2	1	9.8	1.2	0.7
NRS-117-26	SUDBX	PFZ	2	2	8.0	1.2	0.7
NRS-117-26	SUDBX	PFZ	3	1	7.6	1.2	0.7
NRS-117-26	SUDBX	PFZ	3	2	9.5	1.2	0.7
NRS-117-26	SUDBX	PFZ	3	3	6.5	1.2	0.7
NRS-117-26	SUDBX	PFZ	4	1	6.3	1.2	0.7
NRS-117-26	SUDBX	PFZ	4	2	7.9	1.2	0.7
NRS-117-26	SUDBX	PFZ	4	3	7.5	1.2	0.7
NRS-117-26	SUDBX	PFZ	5	1	7.3	1.2	0.7
NRS-117-26	SUDBX	PFZ	5	2	9.0	1.2	0.7
NRS-117-35	SUDBX	PFZ	1	1	8.1	1.2	0.7
NRS-117-35	SUDBX	PFZ	1	2	7.3	1.2	0.7
NRS-117-35	SUDBX	PFZ	2	1	9.2	1.2	0.7
NRS-117-35	SUDBX	PFZ	2	2	8.4	1.2	0.7
NRS-117-35	SUDBX	PFZ	2	3	7.4	1.2	0.7
NRS-117-35	SUDBX	PFZ	3	1	10.0	1.2	0.7
NRS-117-35	SUDBX	PFZ	3	2	11.9	1.2	0.7
NRS-117-35	SUDBX	PFZ	3	3	8.9	1.2	0.7
NRS-117-35	SUDBX	PFZ	4	1	8.5	1.2	0.7
NRS-117-35	SUDBX	PFZ	4	2	9.6	1.2	0.7
NRS-117-35	SUDBX	PFZ	5	1	6.6	1.2	0.7
NRS-117-36b	SUDBX	PFZ	1	1	11.7	1.2	0.5
NRS-117-36b	SUDBX	PFZ	1	2	9.1	1.2	0.5
NRS-117-36b	SUDBX	PFZ	1	3	11.2	1.2	0.5
NRS-117-36b	SUDBX	PFZ	2	1	11.0	1.2	0.5
NRS-117-36b	SUDBX	PFZ	2	2	9.7	1.2	0.5
NRS-117-36b	SUDBX	PFZ	3	1	8.5	1.2	0.5
NRS-117-36b	SUDBX	PFZ	3	2	6.9	1.2	0.5
NRS-117-36b	SUDBX	PFZ	3	3	7.2	1.2	0.5
NRS-117-36b	SUDBX	PFZ	3	4	10.0	1.2	0.5
NRS-117-36b	SUDBX	PFZ	4	1	7.8	1.2	0.5
NRS-117-36b	SUDBX	PFZ	4	2	5.6	1.2	0.5
NRS-117-36b	SUDBX	PFZ	4	3	7.7	1.2	0.5
NRS-117-36b	SUDBX	PFZ	5	1	11.5	1.2	0.5
NRS-117-36b	SUDBX	PFZ	5	2	12.4	1.2	0.5
NRS-117-36b	SUDBX	PFZ	6	1	12.1	1.2	0.5
NRS-117-36b	SUDBX	PFZ	6	2	8.3	1.2	0.5
NRS-117-36b	SUDBX	PFZ	7	1	9.8	1.2	0.5
NRS-117-36b	SUDBX	PFZ	7	2	7.0	1.2	0.5
NRS-117-36b	SUDBX	PFZ	7	3	7.9	1.2	0.5

Table 4-10 (cont'd). Summary of quartz oxygen isotope ($\delta^{18}O_{quartz}$) values for five samples from the Nickel Rim South deposit. Abbreviations: SUDBX – Sudbury breccia; CBF - coherent to in situ brecciated felsic igneous rock; MNOR – mafic norite; CZ – contact zone; PFZ – proximal footwall zone.

Sample	Rock Type	Zone	Grain	Analysis	$\delta^{18}O_{qtz}$ (‰)	1σ	Reproducibility
NRS-124c-62	CBF	PFZ	1	1	9.9	1.2	0.6
NRS-124c-62	CBF	PFZ	1	2	8.3	1.2	0.6
NRS-124c-62	CBF	PFZ	1	3	7.1	1.2	0.6
NRS-124c-62	CBF	PFZ	2	1	7.1	1.2	0.6
NRS-124c-62	CBF	PFZ	2	2	10.2	1.2	0.6
NRS-124c-62	CBF	PFZ	2	3	11.5	1.2	0.6
NRS-124c-62	CBF	PFZ	3	1	6.6	1.2	0.6
NRS-124c-62	CBF	PFZ	3	2	11.9	1.2	0.6
NRS-124c-62	CBF	PFZ	4	1	11.2	1.2	0.6
NRS-124c-62	CBF	PFZ	4	2	8.1	1.2	0.6
NRS-170110-31	MNOR	CZ	1	1	7.9	1.2	0.6
NRS-170110-31	MNOR	CZ	1	2	9.4	1.2	0.6
NRS-170110-31	MNOR	CZ	1	3	9.8	1.2	0.6
NRS-170110-31	MNOR	CZ	1	4	7.4	1.2	0.6
NRS-170110-31	MNOR	CZ	1	5	7.3	1.2	0.6
NRS-170110-31	MNOR	CZ	2	1	6.9	1.2	0.6
NRS-170110-31	MNOR	CZ	2	2	7.9	1.2	0.6
NRS-170110-31	MNOR	CZ	3	1	9.7	1.2	0.6
NRS-170110-31	MNOR	CZ	3	2	9.3	1.2	0.6
NRS-170110-31	MNOR	CZ	4	1	7.4	1.2	0.6
NRS-170110-31	MNOR	CZ	4	2	11.2	1.2	0.6
NRS-170110-31	MNOR	CZ	5	1	8.7	1.2	0.6
NRS-170110-31	MNOR	CZ	5	2	12.1	1.2	0.6
NRS-170110-31	MNOR	CZ	5	3	10.7	1.2	0.6

Chapter 5

5.1 Conclusions

This thesis provides the first detailed examination and characterization of the granophyre unit (GR) of the SIC and first description of its contained hydrothermal system. The GR of the SIC has experienced pervasive metasomatism via fluid-induced re-equilibration and the only primary component preserved in the GR is the granophyre itself. The textural and geochemical evidence for metasomatism in the GR indicates an influx and circulation of a large volume of fluid, and the hydrothermal history can be subdivided into two main stages. The first is an early magmatic-hydrothermal stage resulting from exsolution of an orthomagmatic fluid from the GR itself, and the second was dominated by modified seawater derived from the hydrothermal system in the overlying Onaping Formation. This overlying hydrothermal system was driven by heat from the GR, and progressive cooling resulted in collapse of this hydrothermal system into the GR, overprinting the earlier magmatic-hydrothermal event and likely resulting in mixing between the orthomagmatic fluids and modified seawater. The hydrothermal fluids that circulated throughout the GR transported significant amounts of Ca from re-equilibrated plagioclase to form epidote and derived external Fe from the Onaping Formation, resulting in the formation of abundant Fe-enriched secondary mineral phases (i.e., chlorite, epidote, stilpnomelane, amphibole). The results of this thesis indicate that the hydrothermal system previously documented in the Onaping Formation was vertically extensive and related to the hydrothermal system in the GR, providing an important link between the ore-forming hydrothermal system in the Onaping Formation and the barren hydrothermal system in the GR.

The format of the thesis also provided a means of comparing hydrothermal and alteration characteristics of the barren granophyre environment to a mineralized footwall environment (the Nickel Rim South deposit; NRS) in order to establish the nature of the fluids responsible for alteration, both related and unrelated to mineralization. This study has shown that, although the hydrothermal alteration assemblages and intensity vary between the GR and NRS, the fluid inclusion record is quite similar. Of particular importance are the differences between the fluid inclusions recorded at NRS and those in other footwall deposits, and NRS shares more similarities with the GR. Whereas mineralized footwall systems typically contain high-salinity, multi-solid fluid inclusion assemblages inferred to be related to metal remobilization, these inclusions are absent from the fluid inclusion record at NRS. This brings into question the necessity of these fluids in the remobilization of base and precious metals in the footwall and/or indicates a different post-impact history for the ER compared to the rest of the SS.

5.2 Future Work

In Chapter 2, we completed a detailed petrological study of the GR, which contributes to our understanding of the genesis of the SIC. However, in the scope of this thesis, this description was only used as a means of establishing the hydrothermal history of the GR and its implications for SIC formation were not explored. We have provided insight into what the results may indicate (e.g., differences in volume % granophyre in relation to melt volatile content), but more work is required. Importantly, future work must establish how these findings support or contradict previous interpretations for SIC genesis.

Miaroles were previously identified in the GR (e.g., Ames 1999) and this thesis provided additional constraints on their distribution. The identification of miaroles is important because it provides a means of quantifying volatile exsolution and identifying areas where this occurred. We have identified a concentrated zone of miaroles towards the centre of the unit, but this was established on surface and needs to be further explored and correlated at depth. Furthermore, only two transects through the GR were used for this thesis, and work must be done to correlate these transects at depth and provide additional coverage at surface. Whereas this thesis focused on comparison between the GR in the North Range versus the South Range future work should investigate lateral variability in textures and the volume proportion of primary and alteration minerals.

In Chapter 3 of this thesis, an unusual relationship between CL signals and oxygen isotopic values in quartz was identified. Variations in CL signal are not consistent with variations in oxygen isotope values and these inconsistencies do not appear to be the result of sector zoning or heterogeneous re-equilibration with hydrothermal fluids. To our knowledge, this type of relationship has not been previously identified and brings into question mechanisms for resetting the oxygen isotopic values in quartz. More work is needed to identify the cause of this relationship.

The fluid inclusion study completed for NRS in Chapter 4 was limited by the number of samples collected and the low abundance of fluid inclusions observed in these samples. The purpose of this study was to provide a complement to the work completed in the GR, and a more extensive fluid inclusion study would be beneficial at NRS. Additionally, we did not have access to

samples from the PGE zone at NRS, and a fluid inclusion study of this zone is necessary. Furthermore, this is only the second fluid inclusion study completed on footwall systems in the east range and more work is needed in this area. We have mostly compared our data to previous studies in the North Range because we believe this is a more appropriate comparison than the South Range, but there may be intrinsic differences in the East Range that have not yet been identified.